Crystal structure, martensitic transformation crystallography, mechanical and magnetocaloric performance of Ni(Co)MnIn multifunctional alloys

Haile Yan

UNIVERSITÉ DE LORRAINE

NORTHEASTERN UNIVERSITY

DISSERTATION

Presented at

Université de Lorraine and Northeastern University

Haile YAN 闫海乐

To obtain the doctor's degree of
University of Lorraine and Northeastern University

SPECIAL FIELD: Engineering Sciences
OPTION: Materials Science

Crystal structure, martensitic transformation crystallography, mechanical and magnetocaloric performance of Ni(Co)MnIn multifunctional alloys

Defended on the 29th July, 2016 in front of the jury:

José Luis SANCHEZ LLAMAZARES	Doctor	Instituto Potosino de Investigación Científica y Tecnológica, Mexico	Reviewer& Jury member
Zhidong ZHANG	Professor	Institute of Metal Research, Chinese Academy of Sciences, China	Reviewer& Jury member
Werner SKROTZKI	Professor	Technische Universität Dresden, Germany	Jury member
Zheng LIU	Professor	Shenyang University of Technology, China	Jury member
Claude ESLING	Professor	Université de Lorraine, France	Invited
Liang ZUO	Professor	Northeastern University, China	Invited
Xiang ZHAO	Professor	Northeastern University, China	Supervisor
Yudong ZHANG	Doctor HDR	Université de Lorraine, France	Supervisor

Laboratoire d'Étude des Microstructures et de Mécanique des Matériaux, LEM3
Ile du Saulcy 57012 Metz Cedex 1

Abstract

Ni-Mn-In based alloys have attracted considerable attention due to their multifunctional properties since its discovery in 2004, such as metamagnetic shape memory effect (MMSME), magnetocaloric effect (MCE) and magnetoresistance (MR) effect. However, some fundenmental knowledge on these alloys is still missing until now, such as crystal structure of martensite, crystallographic features of microstructure and magnetostructural transition. In this dissertation, the crystallographic features, mechanical behaviors and magnetic properties of Ni-Mn-In based alloys were studied theoretically and experimentally.

First, the crystal structures of Ni-Mn-In alloys were accurately determined by Rietveld method in the frame of superspace theory (Chapter 3). Then, the microstructure of martensite (Chapter 4), such as variant organization and interface structure, and the crystallographic features of martensitic transformation, such as orientation relationship (*OR*), transformation strain path and geometrical compatibility between austenite and martensite, were systematically studied (Chapter 5). Finally, with this fundamental knowledge on Ni-Mn-In alloys, the behaviors and mechanisms of martensite variant rearrangement/ selection under two kinds of mechanical loading strategies, *i.e.* loading at martensite state and loading across the structural transition, and the effects of annealing on MCE and its related hysteresis loss were explored (Chapter 6).

The main results are as follows. The modulated martensite has an incommensurate 6M crystal structure with superspace group $I2/m(\alpha 0\gamma)00$ that can be approximated by a three-fold superstructure model in the three-dimensional space. The microstructure of martensite is in plate shape and self-organized in colonies. Each colony has four distinct orientation variants. The maximum of 6 distinct colonies and 24 variants can be generated within one austenite grain. Although as many as 14 kinds of twin relations are suggested in the frame of crystallographic theories of martensitic transformation, only three types of twin relations are generally detected, *i.e.* type-I, type-II and compound twin. Variant interfaces are defined by their corresponding twinning plane K_1 at mesoscopic scale. However, at atomic scale, the type-I twin has a coherent interface, whereas type-II and compound twins have “stepped” interfaces. Both the *K-S* and *Pitsch ORs* are appropriate to describe the lattice correspondence between austenite and martensite in Ni-Mn-In alloys. However, the strain path related to the *Pitsch* relation is evidenced to be the effective for the structural distortion. With the determined transformation path, the underlying mechanism of

variant organization is revealed. Across the martensitic transformation, despite the existence of a relative wide stressed layer (around 20 nm), the *habit plane* is bordered by single martensite variant with austenite rather than the generally observed “sandwich-like” structure, implying a relative good geometrical compatibility between the corresponding phases.

For compressive loading at martensite, variant arrangement is realized by the detwinning process. It is evidenced that a single variant state in some colonies can be obtained when the loading orientation is located in the common positive Schmid factor (*SF*) zone of the three detwinning systems. For loading across the structural transition, the prestrain is obtained by variant selection in which the number of colonies is significantly reduced and the variant organization within colony is greatly changed. The *SF* for transformation strain path is introduced to evaluate the possible selection of variants.

Heat treatment can significantly enhance the magnetic entropy change ΔS_M but simultaneously increase the magnetic hysteresis loss. For ΔS_M, the chemical ordered degree should play a prominent role. The treatments that increase chemical ordered degree should be effective to enhance the ΔS_M. The hysteresis loss might be closely related to the crystal perfectness of austenite. Crystal defects, such as grain boundaries, could be favorable to promote the nucleation for structural transition and then result in a low hysteresis loss.

The present work provides fundamental knowledge to understand the underlying mechanisms of multifunctional properties of Ni-Mn-In based alloys and to guide subsequent performance optimizations.

Keywords: Ni-Mn-In; shape memory alloy; incommensurate modulated martensite; variant organization; martensitic transformation strain path; variant arrangement; magnetocaloric effect; hysteresis loss.

Résumé

Les alliages à base de Ni-Mn-In ont attiré une attention considérable en raison de leurs propriétés multifonctionnelles depuis leur découverte en 2004, telles que effet de mémoire de forme métamagnétique (Metamagnetic shape memory effect MMSME), l'effet magnétocalorique (MCE) et l'effet de magnétorésistance (MR). Cependant, certaines connaissances fondamentales sur ces alliages manquent toujours jusqu'à présent, telles que la structure cristalline de la martensite, les caractéristiques cristallographiques de microstructure et de transition magnétostructurale. Dans cette thèse, les caractéristiques cristallographiques, les comportements mécaniques et les propriétés magnétiques des alliages Ni-Mn-In base ont été étudiés théoriquement et expérimentalement.

Tout d'abord, les structures cristallines des alliages Ni-Mn-In ont été déterminées avec précision par la méthode de Rietveld dans le cadre de la théorie du superespace (Chapitre 3). Ensuite, la microstructure de la martensite (Chapitre 4), notamment l'organisation et l'interface des variantes, ainsi que les caractéristiques cristallographiques de la transformation martensitique, telles que les relations d'orientation (*OR*), le chemin de déformation de la transformation et la compatibilité géométrique entre l'austénite et la martensite, ont été systématiquement étudiés (Chapitre 5). Enfin, avec cette connaissance fondamentale sur les alliages Ni-Mn-In, les comportements et les mécanismes de sélection /réarrangement des variantes de martensite sous deux types de stratégies de chargement mécanique, à savoir le chargement à l'état martensitique et le chargement durant la transition structurelle, et les effets du recuit sur l'effet MCE et les pertes d'hystérésis associées ont été explorées (Chapitre 6).

Les principaux résultats sont les suivants. La martensite modulé a une structure cristalline incommensurable avec la structure cristalline 6M et le groupe de superespace *I2/m(α0γ)00* qui peut être approximée par un modèle de superstructure de multiplicité 3 dans l'espace à tridimensionnel. La microstructure de martensite est en forme de plaques et auto-organisée en colonies. Chaque colonie a quatre variantes d'orientations distinctes. Le maximum de 6 colonies distinctes et 24 variantes peut être généré à l'intérieur d'un grain austénitique. Bien que jusqu'à 14 types de relations de maclage sont proposées dans le cadre des théories cristallographiques de transformation martensitique, seuls trois types de relations de maclage sont généralement observés, à savoir des macles de type I, type II et composées. Les interfaces des variantes sont définies à l'échelle mésoscopique par leur plan de maclage K_1 correspondant. Cependant, à l'échelle atomique, la

macle de type I a une interface cohérente, alors que celles de type-II et les macles composées ont des interfaces étagées. Les deux relations d'orientations *K-S* et *Pitsch* sont appropriés pour décrire la correspondance de réseau entre austénite et martensite dans les alliages Ni-Mn-In. Cependant, le chemin de déformation lié à la relation de *Pitsch* est mis en évidence pour être efficace pour la déformation de la structure. Avec le chemin de transformation déterminé, le mécanisme sous-jacent de l'organisation des variantes est révélé. À travers la transformation martensitique, en dépit de l'existence d'une relativement large couche contrainte (de l'ordre de 20 nm), le plan d'habitat est bordé par une variante de martensite simple avec l'austénite plutôt que la structure généralement observée "en sandwich", ce qui suggère une relativement bonne compatibilité géométrique entre la phases correspondantes.

Pour le chargement en compression à l'état martensitique, l'arrangement des variantes est réalisé par des processus de démaclage. Il est démontré que l'état de variante unique dans certaines colonies pourrait être obtenu lorsque l'orientation de chargement est situé dans la zone de Facteur de Schmid (*SF*) positif commune pour les trois systèmes de démaclage. Pour le chargement au cours de la transition de structure, la précontrainte est obtenue par la sélection de la variante dans laquelle le nombre de colonies est considérablement réduit et l'organisation de variantes à l'intérieur de la colonie est considérablement modifiée. Le *SF* pour le chemin de déformation de transformation est introduit pour évaluer la sélection possible de variantes.

Le traitement thermique peut améliorer considérablement le changement d'entropie magnétique ΔS_M mais augmente simultanément la perte par hystérésis magnétique. Pour ΔS_M, le degré d'ordre chimique devrait jouer un rôle déterminant. Les traitements qui augmentent l'ordre chimique devraient être efficaces pour améliorer le terme ΔS_M. La perte d'hystérésis pourrait être étroitement liée à la perfection cristalline de l'austénite. Des défauts cristallins, tels que des joints de grains, pourrait être propices pour favoriser la nucléation pour la transition de la structure, puis entraîner une faible perte d'hystérésis.

Le présent travail fournit des connaissances fondementales pour comprendre les mécanismes sous-jacents de multiples propriétés fonctionnelles des alliages à base Ni-Mn-In et pour guider l'optimisation des performances ultérieures.

Mots-clés: Ni-Mn-In; alliage à mémoire de forme; martensite modulée incommensurable; organisation de variantes; chemin de déformation de transformation martensitique; arrangement de variantes; effet magnétocalorique; pertes d'hystérésis.

摘要

自 2004 年 Ni-Mn-In 合金被首次报道以来，因其优异的多功能磁控性能（变磁形状记忆效应，磁热效应和磁阻效应等），引起了广泛的关注。但到目前为止，关于该合金很多基础知识仍不清楚，例如，马氏体相晶体结构，微观组织和磁结构转变的晶体学特征。本论文从理论预测和实验研究两个方面，对 Ni-Mn-In 基合金的晶体结构、微观组织、马氏体相变、力学行为和磁性能等进行了系统的研究。

首先，利用 Rietveld 方法并结合超空间理论，对 Ni-Mn-In 合金的晶体结构进行了精确解析（第 3 章）。然后，对该合金调幅马氏体的微观组织（第 4 章）及马氏体相变的晶体学特征（第 5 章），如，取向关系、相变路径以及奥氏体和马氏体间几何兼容性，进行了研究。最后，对马氏体变体在外加机械载荷下（在马氏体状态及相变过程中加载）的重排机制以及退火对磁热效应及磁滞损耗的影响进行了探索（第 6 章）。

主要结果如下：调幅马氏体具有非公度 6M 晶体结构，空间群为 $I2/m(\alpha 0\gamma)00$。该非周期性晶体结构在三维空间里可近似描述为具有 3 个平均结构晶胞沿 $\boldsymbol{c}$ 方向排列的超结构。调幅马氏体的微观组织呈板条状并自发组合以马氏体变体团的形式存在。每个变体团内部包含四种具有不同晶体学取向的变体。一个奥氏体晶粒内部最多可相变产生 6 种变体团和 24 种变体。马氏体相变晶体学理论表明不同马氏体变体间存在 14 种孪生关系，但只有 3 种孪生关系在实验中被广泛观察到，即，I 型、II 型和复合型孪生。研究发现，在介观尺度，不同变体界面与它们的孪生面相重合。在原子尺度，I 型孪晶为共格界面，II 型和复合型孪晶为“台阶”型界面。尽管 *K-S* 和 *Pitsch* 取向关系都可被用来描述奥氏体和马氏体间晶格对应关系，但只有 *Pitsch* 关系对应的相变路径可用来描述相变过程中的结构转变。根据确定的相变路径，进一步揭示了 Ni-Mn-In 合金马氏体相变过程中变体组合机制。此外，尽管相变过程中存在一个相对较宽的应变层（约 20 nm），惯析面是由单个马氏体变体与奥氏体组成而不是通常观察到的“三明治”结构，表明奥氏体与马氏体之间存在一个相对较好的几何兼容性。

在马氏体状态对材料进行外部机械加载时，马氏体变体间通过去孪生的方式实现重新排列。沿着对三种去孪生关系均为正值的 Schmid 因子方向加载，在某些变体团内可获得

单变体状态。在相变过程中对材料进行外部机械加载时，马氏体变体团的数量明显减少，变体团内部的自协调组织也发生了显著变化。通过马氏体变体在相变过程中的选择性产生可有效的获得预应变。本研究中，相变路径的 Schmid 因子被引入来分析变体选择的可能机制。

热处理能够显著的提高磁熵变ΔS_M，但同时也增加了磁结构转变中的磁滞损耗。对于磁熵变，合金的化学有序度起主要作用，而磁滞损耗则与奥氏体相的晶体完整度密切相关。晶体学缺陷（晶界等）能够有效的促进马氏体相变的进行从而降低磁滞损耗。

本论文对 Ni-Mn-In 合金的晶体结构、微观组织、马氏体相变、力学行为及磁性能进行了研究。为理解该合金的多功能磁控行为提供了一定的理论基础，对后续的性能优化起一定的指导作用。

关键词：Ni-Mn-In；形状记忆合金；非公度调幅结构；变体组合；马氏体相变路径；变体重排；磁热；滞损耗。

Contents

目录

Chapter 1 Literature review

1.1 Introduction

Conventional shape memory effect (SME), associated with the thermoelastic martensitic transformation, is known to be the unique behavior that the deformed low-temperature phase can recover its original shape upon heating by reverse martensitic transformation [1-4]. This effect was first reported in Au-Cd alloys [5] in 1951 and become well known with the discovery of Ni-Ti alloys [6] in 1963. Since the output strains and output stresses of SMEs are much larger than those generated in piezoelectric and magnetostrictive materials, during the last half-century, the shape memory alloys (SMAs) have attracted considerable attention and many kinds of commercially available SMAs have been fabricated, such as Ni-Ti [7, 8], Cu-Al-Ni [9, 10], and Fe-Mn-Si [11-13]. So far, the SMAs have been successfully applied in many fields such as smart actuators, sensors and medical guidewires [7, 14, 15]. However, due to the intrinsically low conductivity of thermal flux that is needed to trigger the conventional SME, the work frequency of conventional SMAs is generally lower than 5 Hz [16]. This drawback greatly restricts the application scope of the conventional SMAs.

Magnetic shape memory effect (MSME) that has a large output strain as well as the fast work frequency was first reported in Heusler-type Ni_2MnGa alloy in 1996 [17], and quickly became a focus in the field of condensed matter [18]. Different from the conventional SME, the MSME is triggered by a magnetic field that can be applied instantaneously. At present, the output strain as large as 12 % have been obtained in the off-stoichiometric compounds under the magnetic field of 1 T [19, 20]. The large magnetic-field-induced strain (MFIS) in Ni-Mn-Ga alloys was expained as the rearrangement of martensite variants through interface movement driven by the magnetic field [21-23]. When the magnetocrystalline anisotropic energy (MAE) of some favoured variants are larger than their interface movement resistances, they will grow at the expense of other unfavoured variants and thus generate giant macroscopic strains. Unfortunately, due to the quick saturation of the magnetization, the output magnetostress is restricted to only a few MPa [24, 25]. Thus, the applications of Ni-Mn-Ga alloys are limited to the low environment resistant conditions. Moreover, due to the strong orientation dependence of MAE, the large MFIS only observed in single crystal

alloys. The significant brittleness of materials is another serious drawback that prevents the application of these materials.

In 2004, a novel MSME, metamagnetic shape memory effect (MMSME), was observed in Mn enriched Heulser-type Ni-Mn-X (X = In, Sn and Sb) alloys [26]. With the discovery of giant recoverable prestrain of 3 % under magnetic field in Co-doped Ni-Mn-In alloy in 2006 [27], the MMSME quickly become known. Different from Ni-Mn-Ga alloys in which the saturation magnetization of austenite is comparable to that of martensite, the magnetism of austenite in these alloys is significantly larger than that of martensite. Due to the giant difference of magnetization between the corresponding phases, the Zeeman energy (ZE) could significantly influence phase stability and result in magnetic-field-induced (inverse) martensitic transformation (MFIMT) [4, 27]. This magnetoresponsive property can make the deformed martensite resume its initial form *via* field induced reverse martensitic transformation, and thus realize the MMSME. Moreover, since the ZE increases continuously with the external magnetic field, a large output magnetostress can be achieved [21, 25]. In addition, unlike the MAE, the ZE does not strongly depend on crystal orientation. This character would allow utilizing polycrystalline alloys for actuator/ sensor applications.

In addition to the MMSME [25, 27], due to the strong coupling interactions between crystal structure and magnetic structure across the magnetostructural transition in Ni-Mn-X (X = In, Sn and Sb) based alloys, many magnetoresponsive behaviors were activated, such as giant magnetocaloric effect [28, 29], barocaloric effect [30, 31], elastocaloric effect [32, 33], exchange bias effect [34, 35], magnetoresistance effect [36, 37], Hall effect [38, 39] and kinetic arrest effect [40, 41]. All these properties bring about potentials for technological applications in many magnetic and electric field control devices, such as magnetically controlled dampers [42], high-performance actuators [25] and environment-friendly magnetic refrigerators [28, 43].

1.2 State of the art

This dissertation work focuses on Ni-Mn-In based alloys. From the first report of MFIMT in Ni-Mn-In based alloys twelve years ago (in 2004), these alloys have been largely investigated experimentally and theoretically. Before the presentation of this Ph.D. work, the published literature on Ni-Mn-In alloys was first overviewed.

1.2.1 Crystal structure

Crystal structure of a material is the prerequisite parameter for microstructural analyses and property investigations. The determination of crystal structure is generally considered as the first step of material characterization. So far, the crystal structures of Ni-Mn-In based alloys with various alloy compositions have been largely investigated by means of X-ray diffraction (XRD), selected area electron diffraction (SAED) and neutron diffraction (ND) [26, 43-54]. It is clear now that the high-temperature phase, austenite, has a cubic $L2_1$ or B2 structure, depending on different fabrication or post-treatment processes. The low-temperature phase, martensite, generally possesses a complicated crystal structure. For easy consultation, some results reported in the literature are summarized in Table 1. 1. It is seen that there are two kinds of martensite, namely non-modulated martensite and modulated martensite. For the latter, the reported modulation types include 5M (or 10 M), 6M (or 3M) and 7M (or 14M) under the notation of Otsuka [55], where "M" stands for "monoclinic".

Despite numerous progresses in advancing the recognitions of the crystal structures in Ni-Mn-In based alloys, ambiguities remain to be clarified, especially for the modulated martensite. As shown in Table 1. 1, different structures have been reported for some alloys with the same composition under similar experimental environments. For example, the martensite structures at room temperature were respectively suggested to be 4O, 10M and orthorhombic for ternary $Ni_{50}Mn_{35}In_{15}$ alloy and 10M, 14M, 6M and $L1_0$ for quaternary $Ni_{45}Co_5Mn_{36.7}In_{13.3}$ alloy. Furthermore, the complete crystal structure information including the fractional atomic coordinates has never been reported so far. All these bring about difficulties for detailed crystallographic analyses and physical property investigations through experimental measurements or theoretical simulations. Thus, a profound crystal structure determination is in great need.

Table 1. 1 Crystal structures of martensite phases in Ni-Mn-In alloys retrieved from literature.

Composition	Reference	Temperature*	Method	Sample	Crystal structure
$Ni_{50}Mn_{45}In_5$	[44]	*RT*	XRD	Powder	$L1_0$
$Ni_{50}Mn_{40}In_{10}$	[44]	*RT*	XRD	Powder	14M
$Ni_{50}Mn_{36}In_{14}$	[45]	150 K	XRD	Ribbon	10M
	[44]	*RT*	XRD	Powder	10M
$Ni_{50}Mn_{35}In_{15}$	[46], [47]	*RT*	XRD	Powder	Orthorhombic
	[26]	*RT*	SAED	Bulk	4O
$Ni_{50}Mn_{34.5}In_{15.5}$	[48]	*RT*	XRD	Powder	10M
$Ni_{49.7}Mn_{34.3}In_{16}$	[48]	5 K	ND	Powder	10M
$Ni_{49}Co_1Mn_{37}In_{13}$	[50]	*RT*	XRD	Ribbon	5M
$Ni_{48}Mn_{41}In_{13}$	[49]	83 K	SAED	Bulk	10M and 14M
$Ni_{46}Mn_{41}In_{13}$	[52]	*RT*	XRD	Powder	6M
$Ni_{45}Co_5Mn_{37}In_{13}$	[50]	*RT*	XRD	Ribbon	7M
	[51]	*RT*	SAED	Ribbon	7M
$Ni_{45}Co_5Mn_{36.7}In_{13.3}$	[53]	*RT*	SAED	Bulk	10M and 14M
	[54]	200 K	SAED	Bulk	$L1_0$ or 6M
Ni_{45} $Co_5Mn_{36.5}In_{13.5}$	[25]	180 K	High-Energy XRD	Single crystal	6M
$Ni_{40}Mn_{50}In_{10}$	[43], [45]	150 K	XRD	Ribbon	14M

* *RT* represents room temperature.

1.2.2 Microstructure

In addition to crystal structure, almost all the mechanical and physical properties of materials are also closely related to their microstructure [56, 57]. Thus, a comprehensive knowledge on the microstructure features of Ni-Mn-In based alloys should be helpful for understanding their multifunctional properties. Until now, a large of investigations have been carried out to explore the microstructure features of Ni-Mn-In based alloys by means of optical microscope (OM), scanning electron microscope (SEM), transmission electron microscope (TEM) and atomic force microscope (AFM) [43-45, 51, 53, 58-69]. The microstructure features of bulk [44, 53, 58, 59], ribbon [43, 45, 51, 60], particle [61] and film [62-65] samples in single-phase and dual-phase (even multi-phase) [66-69] Ni-Mn-In based alloys have been investigated. Unfortunately, the reported investigations mainly focus on the morphological features of Ni-Mn-In based alloys. There is little information available in the literature on the crystallographic characteristics of microstructural constituents,

such as martensite variant types, crystallographic orientation relationships between martensite variants, variant organization manner and variant interfaces. This brings about difficulties to further understand the underlying mechanism of the associated properties and to the subsequent performance optimization. Consequently, systematic characterization of crystallographic features in Ni-Mn-In based alloys is still required.

1.2.3 Performance

1.2.3.1 Metamagnetic shape memory effect

Metamagnetic shape memory effect (MMSME) depicts the phenomenon that the SME is realized by the MFIMT that is driven by the Zeeman energy under the external magnetic field due to the difference in magnetization between austenite and martensite [25, 27, 48, 70-75]. This effect becomes well known with the report of a 3 % recovered prestrain in $Ni_{45}Co_5Mn_{36.7}In_{13.3}$ single crystal at room temperature under magnetic field of 4 T by Kainuma *et al.* in 2006 [27], as shown in Fig. 1. 1. With the Clausius-Clapeyron relation, a magnetostress of more than 100 MPa was theoretically predicted in this material. Very quickly, a single magnetic field pulse of 200 Hz accompanying with almost perfect MMSME was experimentally evidenced by their research group [72]. All their work triggered numerous studies on the MMSME and its related superelastic effect in Ni-Mn-In based alloys [25, 48, 70-75].

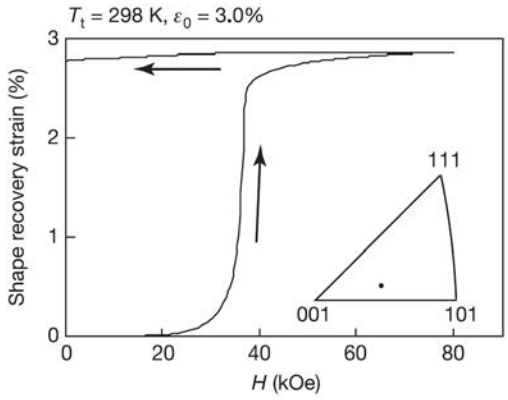

Fig. 1. 1 Strain cycle during the inverse martensitic transformation induced by a magnetic field for the $Ni_{45}Co_5Mn_{36.7}In_{13.3}$ single crystal in which a compressive prestrain of about 3 % was applied and the magnetic field was applied vertically to the compressive axis of the specimen and length change parallel to the compressive axis was measured [27].

During the last ten years, the studies on MMSME in Ni-Mn-In based alloys have mainly focused on quaternary Mn enriched Co-doped single crystal alloys [25, 70, 71, 74]. At present, a fully recoverable transformation strain up to 3.10 % has been detected in a [100]-oriented $Ni_{45}Co_5Mn_{36.5}In_{13.5}$ single crystal under compressive loading up to 125 MPa [71]. Moreover, a fully reversible superelastic response with the strain level more than 6 % has been detected in the same composition single crystal alloy under compressive loading along [100] orientation [25, 74]. The magnetic work output was determined to be more than $1MJ \cdot m^{-3} \cdot T^{-1}$, which is one order of magnitude higher than that obtained in Ni-Mn-Ga alloys. Besides, the behaviors of transformation strain and stress against crystal orientation were also studied [25], as shown in Fig. 1. 2. It is seen that the [111]-oriented crystal can produce a magnetostress of 140 $MPa \cdot T^{-1}$ with 1.2 % axial strain under compression, which is much higher than that observed in Ni-Mn-Ga alloys (a few MPa) [24, 25].

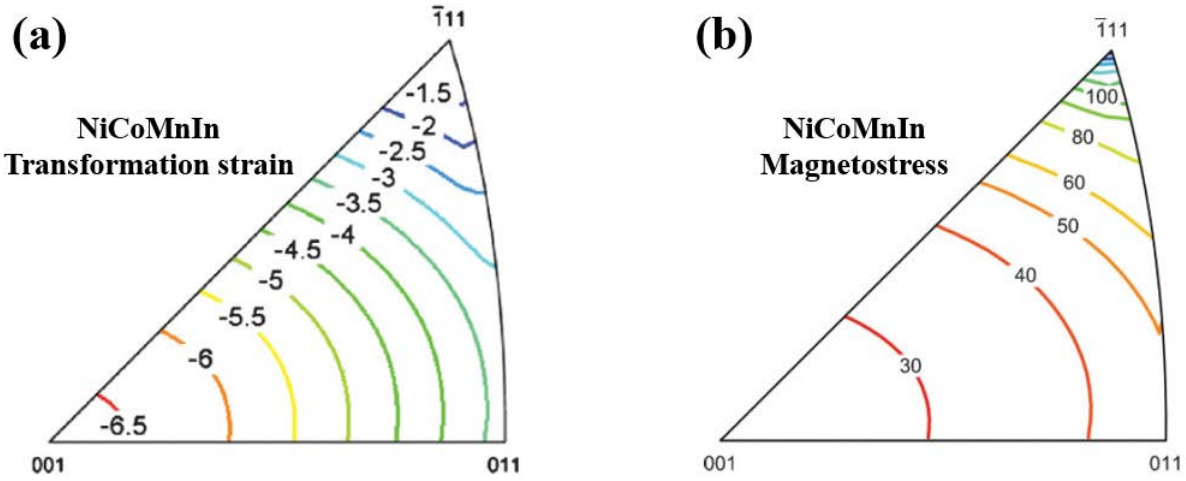

Fig. 1. 2 Theoretical transformation strain (a) and magnetostress level (b) in $Ni_{45}Co_5Mn_{36.5}In_{13.5}$ single crystal as a function of crystal orientation presented in a standard stereographic triangle [25].

In addition to the MMSMEs in single crystal Ni-Mn-In based alloys, some efforts have also been devoted to polycrystalline samples. Using *in-situ* X-ray diffraction technique, Wang *et al.* first experimentally confirmed the occurrence of MFIMT in $Ni_{45}Co_5Mn_{36.6}In_{13.4}$ polycrystalline sample under 50 MPa compression loading [73]. Across the magnetostructural transition, a magnetic superelastic strain of 0.12 % was observed in $Ni_{50}Mn_{34}In_{16}$ polycrystalline alloy in the absence of applied stress [48]. Moreover, a large magnetostrain of 0.25 % at 310 K has been detected in a textured $Ni_{45.2}Co_{5.1}Mn_{36.7}In_{13}$ sample under a magnetic field of 5 T after training [75].

Despite the stress and strain level are lower than those obtained in single crystal samples, they are still significantly higher than those generated from the existing piezoelectric and magnetostrictive actuators.

As summarized above, both of single crystalline and polycrystalline samples of Ni-Mn-In based alloys possess excellent MMSMEs, making them promising candidates for magnetic actuators or sensors. Until now, most of investigations on MMSMEs were concentrated on properties characterization with different alloy compositions and/ or under different external circumstances. There is little information in the literature on the details of the underlying mechanism of these effects. For example, it is clear that the SME is closely related to the microstructure features of martensite, such as martensite variant organization and variant interface, but comprehensive studies on MMSME and its related microstructure evolution have rarely been reported so far. Comprehensive knowledge on the underlying mechanisms of MMSME would be very useful for further performance optimization.

1.2.3.2 Magnetocaloric effect

Magnetocaloric effect (MCE) is a change in temperature of a material when it is exposed to an external magnetic field [76, 77]. The MCE was first discovered by Warburg in 1881 that the temperature of iron changes under a magnetic field [78]. Until a half-century later, Debye (1926) [79] and Giauque (1927) [80] independently proposed a thermodynamic interpretation and indicated a possibility of obtaining ultralow temperatures by adiabatic demagnetization. The first magnetic refrigeration experiment was quickly performed by Giauque and MacDougall in 1933 in which the temperatures below 1 K were achieved by demagnetization of $Gd_2(SO_4)_3 \cdot 8H_2O$ [81]. Since then, the MCE in low temperature refrigeration have been well developed and many magnetic refrigerants have been discovered, such as $Gd_2(SO_4)_3 \cdot 8H_2O$ [81], $R_3M_5O_{12}$(R = Nd, Gd, and Dy; M = Ga and Al) [82], $Dy_3Al_5O_{12}$ (DAG) [83] and $Gd_3Ga_5O_{12}$ (GGG) [84].

Magnetic refrigeration near room temperature was first realized by Brown in 1976 in Gd alloy [85]. Until twenty years later, another important breakthrough was made with the discovery of giant MCE in $Gd_5(Si_2Ge_2)$ by Pecharsky and Gschneidner Jr. in 1997 [86]. An entropy change of around 18 $J \cdot kg^{-1} \cdot K^{-1}$ was observed around 280 K under a magnetic field variation of 5 T, which is much higher than that of Gd (10 $J \cdot kg^{-1} \cdot K^{-1}$) under similar conditions. Since then, motivated by the huge potential applications in household refrigerators or air-conditioners, research on room

temperature magnetocaloric materials experienced an explosive growth [76, 77, 87]. So far, a variety of advanced magnetocaloric materials have been found, such as $Gd_5Si_{4-x}Ge_x$ [86, 87] , $LaFe_{13-x}Si_xH$ [88] and MnFeP(As, Ge) [89].

Since the discovery of MFIMT in Ni-Mn-In based alloys, this kind of alloys have been considered as one of the most promising magnetic refrigerants and been largely investigated [4, 25, 77, 90-97]. Although Ni-Mn-In based alloys was first reported as a novel metamagnetic SMA, the MCEs of these materials have attracted much more attention than that of MMSME. Some results reported in the literature, for easy consultation, are summarized in Table 1. 2. So far, most of investigations on MCE have focused on performance optimizations *via* modification of alloy composition by tuning the relative contents of the constituent elements [44, 47, 49, 98-100] and/ or adding a fourth (even a fifth) elements, such as Co [27, 101], Cr [102, 103], Fe [104, 105], Cu [106], Si [107, 108], Ga [109], Sn [110, 111], Sb [112], Ge [113], Pd [114], B [115, 116], and Ti [117]. The routes to enhance the MCE-related properties in Ni-Mn-In based alloys consist of: (i) increasing the Curie temperature of austenite and further the magnetization change across the magnetostructural transition; (ii) adjusting the critical temperatures of the magnetostructural transition near room temperature; (iii) decreasing the hysteresis loss across the magnetostructural transition. The basic principles to improve these properties, in origin, are the adjustment of the alloy electron concentration, lattice parameters and magnetic spin structures.

During the twelve-year development, as summarized by Liu *et al.* [28], Ni-Mn-In based alloys have become one of the most promising magnetic refrigerants near room temperature. These materials have the highest cooling capacity under a moderate magnetic field of 2 T but do not contain rare earth elements, as shown in Fig. 1. 3. Several ternary or quaternary Ni-Mn-In based alloys with excellent MCEs have been discovered, such as $Ni_{45}Co_5Mn_{50-x}In_x$ (x = 13 - 13.5) [27, 28], $Ni_{50}Mn_{34}In_{16}$ [118-120], $Ni_{50}Mn_{35}In_{15}$ [121-123], and $Ni_{48}Mn_{39}In_{12}Si_1$ [108]. At present, a reversible adiabatic temperature change of -3 K (the irreversible adiabatic temperature change of -8 K) has been obtained in $Ni_{45.7}Mn_{36.6}In_{13.5}Co_{4.2}$ alloy under the static magnetic field variation of 1.95 T [59]. A maximum of temperature change of -12.8 K has been detected in $Ni_{45}Co_5Mn_{36.7}In_{13.3}$ alloys with a pulsed fields of up to 15 T [124].

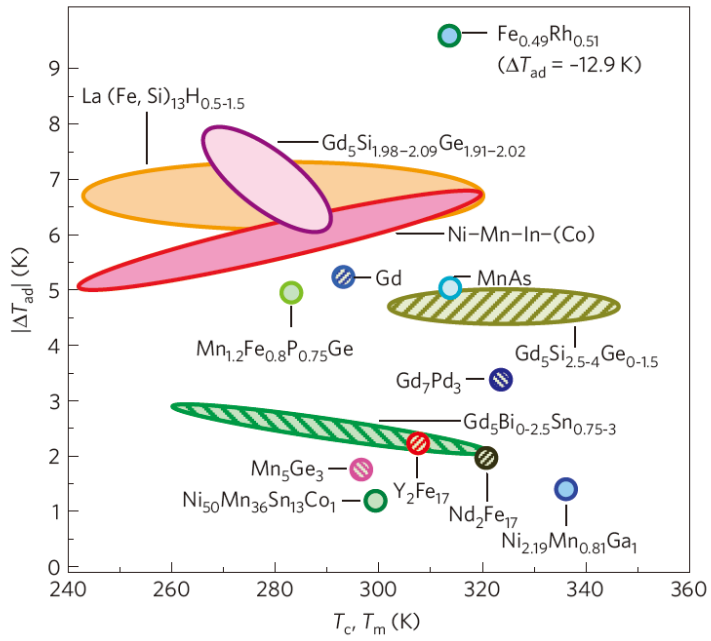

Fig. 1. 3 Adiabatic temperature change (ΔT = 2 T) of several most studied ambient magnetic refrigerants at either a purely magnetic transition temperature T_C (second-order transition, marked by hatched pattern) or magnetostructural coupling transition temperature T_M (first-order transition, solid fill-pattern) [28].

Different from the MMSME of which the single crystal sample has much more prominent performance than the polycrystalline sample, as shown in Table 1. 2, the polycrystalline sample of Ni-Mn-In based alloys also possess excellent MCEs. Due to the intrinsic brittleness of Heusler-type alloys and thus difficult to be processed, in recent years, the melt spun technique has been well accepted as an alternative processing route for the preparation of Heusler-type alloys [125, 126]. Apart from bulk samples, the MCE in Ni-Mn-In based polycrystalline ribbon samples have also been studied [43, 45, 50, 51, 60, 108, 127-136]. At present, the positive maximum magnetic entropy change of 20.2 and 23.1 $J \cdot kg^{-1} \cdot K^{-1}$ have been respectively observed in the as-spun $Ni_{48}Mn_{39}In_{13}$ [108] and the annealed $Ni_{48}Mn_{39}In_{12}Si_1$ ribbon [134] with a magnetic field variation of 5 T.

Despite the excellent magnetic refrigeration capacity of Ni-Mn-In based alloys, there are two aspects that need to be improved before their technological applications. One is the relative high actuating magnetic field. The other is the relative large hysteresis loss across the magnetostructural transition [28, 59, 137, 138]. The former greatly increases the cost and restrict the application range

of these materials. The latter not only reduce the refrigeration capacity but also result in a further degradation or even failure of MCE after limited cycles [77, 139, 140]. As a consequence, in view of practical applications, it is critical to decrease or even eliminate these two negative effects, especially the hysteresis loss. Although numerous efforts have been devoted and several approaches have been proposed [51, 104, 141-143], such as alloying [104], heat treatment [51] and the electron field control [141], these two negative effects have not been well tackled so far.

For the hysteresis loss, it is clear that this effect is not mandated in the framework of thermodynamics since the first-order derivative of the *Gibbs* free energy of the correlated magnetostructural transition is discontinuous with respect to temperature, magnetic field, or any other free thermodynamic variable [144]. At the thermodynamic equilibrium state, *i.e.* the *Gibbs* free energies of the parent and product phases are equal and then the driving force is 0. Thermal or magnetic hysteresis may occur since the transformation driving force should be sufficiently large to overcome the transformation resistances [56, 140, 145]. Consequently, based on the mechanism of hysteresis generation, two routes would be effective to optimize the hysteresis loss. One is to reduce the resistance of phase transition. Decreasing the geometrical incompatibility between the parent and product phases is one of the most successful case [1, 56, 140]. The other is to increase the driving force to promote the phase transition, such as introducing appropriate defects as the nucleation sites for phase transformation.

Table 1. 2 Magnetocaloric effect in Ni-Mn-In based alloys retrieved from literature. ΔS_M, ΔT, RC_{EFF} represent the magnetic entropy change, adiabatic temperature change and effective refrigerant capacity, respectively. $\boldsymbol{\Delta H}$ and T denote the variation of magnetic field and the measured temperature, respectively. PB indicates the polycrystalline bulk sample.

Year	Ref.	Alloy composition at %	State	Representative parameters			$\boldsymbol{\Delta H}$	T
				ΔS_M J·kg^{-1}·K^{-1}	ΔT K	RC_{EFF} J·kg^{-1}	T	K
2006	[27]	$Ni_{45}Co_5Mn_{36.6}In_{13.4}$	Single crystal	28.4	–	–	7	292
2006	[49]	$Ni_{46}Mn_{41}In_{13}$	PB	13	–	–	9	190
2007	[48]	$Ni_{50}Mn_{34}In_{16}$	PB	12	–	–	5	190
2007	[146]	$Ni_{50}Mn_{34}In_{16}$	PB	19	–	–	8	240
2007	[118]	$Ni_{50}Mn_{34}In_{16}$	PB	19	–	–	5	240
2007				–	–	219.51	8	214-242
2007	[147]	$Ni_{50}Mn_{33.13}In_{13.90}$	Single crystal	28.6	–	–	5	295-315
2007				-6.6	–	–	5	315-325
2008	[99]	$Ni_{44}Mn_{44}In_{12}$	PB	7.6	–	–	1	230
2009	[130]	$Mn_{50}Ni_{40}In_{10}$	As-spun ribbon	–	–	60	3	210-234
2009	[112]	$Ni_{48.3}Mn_{36.1}In_{10.1}Sb_{5.5}$	PB	8	–	–	2	160
				21	–	–	5	160
2010	[131]	$Ni_{51.1}Mn_{31.2}In_{17.7}$	As-spun ribbon	-1.7	–	–	2	275
				–	–	132	2	213-291
2010	[148]	$Ni_{50}Mn_{36.5}In_{13.5}$	PB	24	–	–	5	349
2010	[101]	$Ni_{50}CoMn_{34}In_{15}$	PB	–	–	167(net)	5	277-293
			PB	–	–	229	5	305-354
2010	[102]	$Ni_{50}Mn_{33.66}Cr_{0.34}In_{16}$	PB	17.7	–	–	8	270
				–	–	254	8	255-275

Table 1. 2 (continued)

Year	Ref.	Alloy composition at %	State	Representative parameters			ΔH	T
				ΔS_M J·kg^{-1}·K^{-1}	ΔT K	RC_{EFF} J·kg^{-1}	T	K
2011	[129]	$Ni_{50.4}Mn_{34.9}In_{14.7}$	As-spun ribbon	7.2	–	–	3	255
				–	–	60	3	251-265
				-2.6	–	–	3	285
2011	[149]	$Ni_{48}Co_2Mn_{35}In_{15}$	PB	–	–	95	3	270-315
				20.5	–	–	5	270
				–	–	268	5	250-274
				-5.4	–	–	5	350
2011	[103]	$Ni_{50}Mn_{33.32}Cr_{0.68}In_{16}$	PB	–	–	243	5	311-376
				24.4	–	–	5	294
2011	[108]	$Ni_{48}Mn_{39}In_{12}Si_1$	Annealed ribbon	23.1	–	–	5	195
2012	[133]	$Ni_{50.0}Mn_{35.5}In_{14.5}$	Annealed ribbon	13	–	–	3	260
				-5	–	–	3	305
2012	[104]	$Ni_{45}Co_{4.75}Fe_{0.25}Mn_{36.6}In_{13.4}$	PB	18.7	–	–	5	281
				–	–	228	5	270-290
2012	[150]	$Ni_{50}Mn_{34}Sn_8In_8$	PB	17.0	–	–	8	283
				–	–	64	5	278-299
				3.4	–	–	8	252.5
				–		26	5	243-268
				-6.5	–	–	8	315
				–	–	47	5	309-319
2012	[105]	$Ni_{50}Mn_{34}In_{14}Fe_2$	PB	26.5	–	–	5	306
				53.6	–	–	8	306
2012	[113]	$Ni_{50}Mn_{35}In_{15}$	PB	–	2	–	1.8	321
		$Ni_{50}Mn_{35}In_{14}Ge$	PB	–	-2	–	1.8	309
2012	[151]	$Ni_{52}Mn_{31.5}In_{16.5}$	PB	22.3	–	–	1.5	270
2012	[28]	$Ni_{45.7}Co_5Mn_{36.3}In_{13}$	PB	–	-6.2	–	2	317
2012	[134]	$Ni_{48}Mn_{39}In_{13}$	As-spun ribbon	20.2	–	–	5	235

Table 1. 2 (continued)

Year	Ref.	Alloy composition at %	State	Representative parameters			ΔH	T
				ΔS_M J·kg^{-1}·K^{-1}	ΔT K	RC_{EFF} J·kg^{-1}	T	K
2013	[110]	$Ni_{45}Co_5Mn_{40}In_2Sn_8$	PB	22.5	–	–	3	355
			PB	–	–	306.7	3	339-359
2014	[152]	$Ni_{50}Mn_{36}In_{14}$	PB	24	–	–	9	247
2014	[153]	$Ni_{43}Mn_{37.9}In_{12.1}Co_7$	PB	–	-3.3	–	8	273
2014	[124]	$Ni_{45}Co_5Mn_{36.7}In_{13.3}$	PB	–	-12.8	–	15	300
2015	[122]	$Ni_{50}Mn_{35}In_{15}$	PB	–	-17	–	6	250
2015	[59]	$Ni_{45.7}Mn_{36.6}In_{13.5}Co_{4.2}$	PB	–	-8	–	1.95	287
2015	[127]	$Mn_{50}Ni_{41}In_9$	As-spun ribbon	–	–	184.2	3	276-296
2015	[114]	$Ni_{45}Co_{4.5}Pd_{0.5}Mn_{37}In_{13}$	PB	25	–	–	3	364
2015	[107]	$Ni_{45.32}Mn_{29.27}In_{25}Si_{0.41}$	PB	35	–	–	1.5	273
2015	[115]	$Ni_{50.51}Mn_{33.08}Cu_{1.26}In_{14.14}B_{1.01}$	PB	23	–	–	5	195
2015	[116]	$Ni_{50}Mn_{35}In_{14.5}B_{0.5}$	PB	–	-2.5	–	1.8	305
2015	[154]	$Mn_{50}Ni_{40}In_{10}$	Unidirectional bulk	–	–	246.79	3	236-253
2015	[155]	$Ni_{50}Mn_{35}In_{15}$	PB	–	-11	–	14	314
2015	[117]	$Ni_{49}Mn_{32.83}In_{16.17}Ti_2$	PB	17	–	–	6	240
2015	[111]	$Ni_{43}Mn_{46}Sn_8In_3$	PB	–	–	172.6	3	260
2016	[106]	$Ni_{48.5}Mn_{34.3}In_{14.5}Cu_{2.7}$	PB	21.7	–	–	6	272
2016	[109]	$Ni_{48.4}Co_{1.9}Mn_{34.2}In_{13.8}Ga_{1.7}$	PB	18	–	–	7	290
2016	[156]	$Ni_{47.74}Mn_{37.06}In_{15.20}$	PB	30.7	–	–	5	282

1.2.3.3 Mechanical caloric effect

Mechanical caloric effect is a mechanical analogue of MEC that has received considerable attention in recent years owing to its potential use for environmentally friendly refrigeration [31, 157, 158]. Like MCE, it is defined as an isothermal change of entropy or an adiabatic change of temperature that takes place when a mechanical field is applied or released in a given material. The origin of mechanical caloric effect has been related to the interaction between the crystal structure lattice and an external applied mechanical field. With respect to loading manners, the mechanical caloric effect can be classified into barocaloric [30, 31, 158, 159] and elastocaloric effect [157, 160, 161]. For the former, the mechanical field is the hydrostatic pressure that is applied *via* compression or expansion of gases. For the latter, the mechanical field is a strain or a stress that is directly applied or released in the refrigeration materials. At present, a giant temperature rise of 25 K has been observed in Ni-Ti wires upon stretching [162], and a large temperature change of 6 ~ 7 K has been detected by compressing Cu-Zn-Al polycrystalline bulk samples over a large temperature span of 130 K [163].

Barocaloric effect in Ni-Mn-In based alloys was first reported by Mañosa *et al.* in 2010 [31]. A giant barocaloric effect of 24.4 $J \cdot kg^{-1} \cdot K^{-1}$ was observed in $Ni_{49.26}Mn_{36.08}In_{14.66}$ alloy around room temperature under a moderate hydrostatic pressure of 2.6 kbar, which is comparable to the magnitude of the giant MCE reported in this kind of alloys, and predicting that a similar barocaloric effect will occur in many giant-magnetocaloric materials undergoing magnetostructural transitions involving a volume change [31, 164]. After that, comparative studies on the barocaloric and MCE in Ni-Mn-In based alloys were carried out by their research group [30]. They found that these two caloric effects exhibit opposite trends. The barocaloric is larger for samples with martensitic transformation from the paramagnetic austenite to the weak-magnetic martensite. When the martensitic transition occurs below the Curie temperature, all quantities start to decrease. Such a decrease was explained as the lowering of the transition entropy change, arising from the magnetic contribution to the entropy. With respect to the MCE, the entropy change attains a maximum for those samples with martensitic and magnetic transitions close to each other. However, the adiabatic temperature change and refrigeration capacity are larger for samples with martensitic transformation slightly below the Curie temperature.

Elastocaloric effect in Ni-Mn-In based alloys was first reported in 2014 [33]. A reversible temperature change of ± 3.5 K was experimentally detected in a [001]-textured $Ni_{45.7}Co_{5.1}Mn_{36.6}In_{13.3}$ polycrystalline sample under a relative low stress of 100 MPa [33]. The lattice vibration was thought to play a dominant role in this large elastocaloric effect. In addition, the cycle behaviors of the elastocaloric effect in $Ni_{45}Co_5Mn_{36.4}In_{13.6}$ polycrystalline alloy were studied [165]. A large temperature range of about 3 ~ 4 K was generated under a moderate stress of around 150 MPa and no significant degradation of the elastocaloric effect was observed after 15 cycles. This excellent cyclic elastocaloric behavior was explained as the full reversibility of transformation as well as the reproducible stress-strain response in transformation. Very recently, a temperature decrease of - 4 K was detected in a directionally solidified $Ni_{48}Mn_{35}In_{17}$ alloy under a stress of 300 MPa [32].

Compared with MCE, the barocaloric and elastocaloric effect exhibit some obvious advantages, such as low cost, relatively low driving forces, large and reversible adiabatic temperature change and wide temperature window [157]. However, like the MCE, the large hysteresis loss across the structural transition is still one of the biggest obstacle to technological applications. Moreover, due to the refrigeration features of these two mechanical caloric effects, their required mechanical properties of the magnetic refrigerants should be much higher than that of MCE. The intrinsic brittleness of the Heusler alloys is another problem that prevents the application of mechanical caloric effects in these materials.

1.2.3.4 Magnetoresistance effect

Magnetoresistance (MR) effect is the variation of the electrical resistivity (ρ) of materials under an external magnetic field (H) [166-170], as demonstrated in Eq. 1-1.

$$MR = \frac{\rho(H) - \rho(0)}{\rho(0)} \quad (1\text{-}1)$$

This effect was first discovered in Fe/ Cr multilayer material where the resistivity is lowered by almost a factor of 2 in a magnetic field of 2 T at 4.2 K in 1988 [166]. Since then, stimulated by the engineering applications in the magnetoresistive reading heads and similar devices, the MR effect has been largely investigated and many multilayer materials with large MR effect, composed of magnetic and nonmagnetic layers, have been fabricated, such as Co/ Ru [167], CoFe/ Al_2O_3/ Co [171] and Fe/ MgO [170]. The origin of MR effect in multilayer materials was explained as the

magnetic-field-induced magnetism transition from an antiferromagnetic arrangement of the consecutive ferromagnetic layers to a complete ferromagnetic arrangement of the corresponding ferromagnetic layers. Due to the spin dependence of electron scattering both at layer boundaries and within each layer, the overall resistivity in a parallel spin system is lower than that in an antiparallel arrangement of the moments in the layers [169, 172, 173]. Apart from the artificial magnetic multilayer materials, in recent years, the large MR effect was also observed in the ferromagnetic and antiferromagnetic coexisting bulk metallic or intermetallic compounds, particularly in those alloys that undergo first-order phase transformations, such as FeRh [169], GdSiGe [174], and MnAs [175].

The MR effect in Ni-Mn-In based alloys was first reported in 2006 [36, 98]. At first, researches mainly focused on ternary Mn enriched Ni-Mn-In alloys with the structural transition from weak-magnetic martensite to ferromagnetic austenite, such as $Ni_{50}Mn_{50-x}In_x$ ($14 \leq x \leq 16.2$) and $Ni_{46}Mn_{41}In_{13}$ alloys [36, 98, 100, 176]. A giant MR of over 60 % was observed in $Ni_{50}Mn_{35}In_{15}$ single crystal alloy under a moderate strength magnetic field of 3.5 T around room temperature. Under the magnetic field of 5 T, a MR effect of 80 % was detected in $Ni_{50}Mn_{34}In_{16}$ alloy around 125 K [100]. In addition, the MR effect associated with the structural transition from weak-magnetic martensitic to paramagnetic austenite was also studied. A MR effect of 8 % was experimentally detected in $Ni_{50}Mn_{36.5}In_{13.5}$ polycrystalline alloys. Although the obtained MR effect was much lower compared with that of the Ni-Mn-In based alloys having large magnetization change during martensitic transformation, this kind of alloys was found to possess a significantly smaller hysteresis loss accompanied with the structural transition.

Later, the influence of alloying, *via* adding a fourth element such as Fe [104], Ge [113], Co [109], Si [177], B [37], Al [113] and Ga [109], on MR effects were largely studied. It was reported that the appropriate Fe-doping is effective to reduce the hysteresis loss of $Ni_{45}Co_5Mn_{36.6}In_{13.4}$ alloy, which leads to an enhancement of effective RC by 15 % [104]. A giant MR effect of 66 % was observed in Ga-doped $Ni_{48.4}Co_{1.9}Mn_{34.2}In_{13.8}Ga_{1.7}$ alloy under a magnetic field of 7 T around room temperature [109]. Furthermore, a novel physical phenomenon, a large unusual asymmetric switchinglike magnetoresistance between the forward (isothermal) and the reverse (athermal) metamagnetic transitions, was detected in the B-doped $Ni_{50}Mn_{35}In_{14}B_1$ bulk alloy in the vicinity of the phase coexistence region (304 K) at a low applied field of 0.25 T [37]. This observation provided us new information regarding the magnetostructural transition.

Different from the mechanism of MR effect in multilayered materials, the significant change of electrical resistivity in Ni-Mn-In based alloy should be ascribed to the altered electronic structure across the magnetostructural transition. Thus, to obtain a large MR effect with lower magnetic field intensity, composition modification to increase the magnetization and to reduce the entropy change should work. Like MCE and mechanical caloric effect, a large hysteresis loss across the magnetostructural transition again significantly reduce the work efficiency of the MR effect. Although low hysteresis loss in the alloys with the structural transition from the weak-magnetic martensite to the paramagnetic austenite has been reported, the extremely small temperature window greatly restricts their application range. Consequently, composition modification or other approaches to decrease hysteresis loss as well as to keep large magnetization difference and low entropy change is still in great need.

1.2.3.5 Exchange bias effect

Exchange bias (EB) effect is associated with the "unidirectional anisotropy" of magnetic coupling interaction [178, 179]. When a system consisting of ferromagnetic-antiferromagnetic, ferromagnetic-spin glass, antiferromagnetic-ferromagnetic, and ferromagnetic-ferrimagnetic interfaces is cooled under an external magnetic field through the Néel temperature (T_N) of the antiferromagnetic or the glass temperature (T_{SG}) of the spin glass, this effect is induced that shows a negative shift of the hysteresis loop along the magnetic field axis [34, 178-181]. Since the discovery of EB effect in 1956 by Meiklejohn and Bean [182], it has been extensively studied during the last half of century due to its technological applications in the ultrahigh-density magnetic recording and the spin valve devices [34, 183]. The EB effect within a ferromagnetic (light blue) and antiferromagnetic (orange) system is demonstrated in Fig. 1. 4. The process of field cooling from higher temperature (above T_N in Fig. 1. 4) is generally used to obtain the magnetic unidirectional anisotropy in the EB system [178, 179]. The strength of EB effect, indicated by H_E, is characterized by the amount of the hysteresis loop shift along the magnetic field axis, as shown in Fig. 1. 4b.

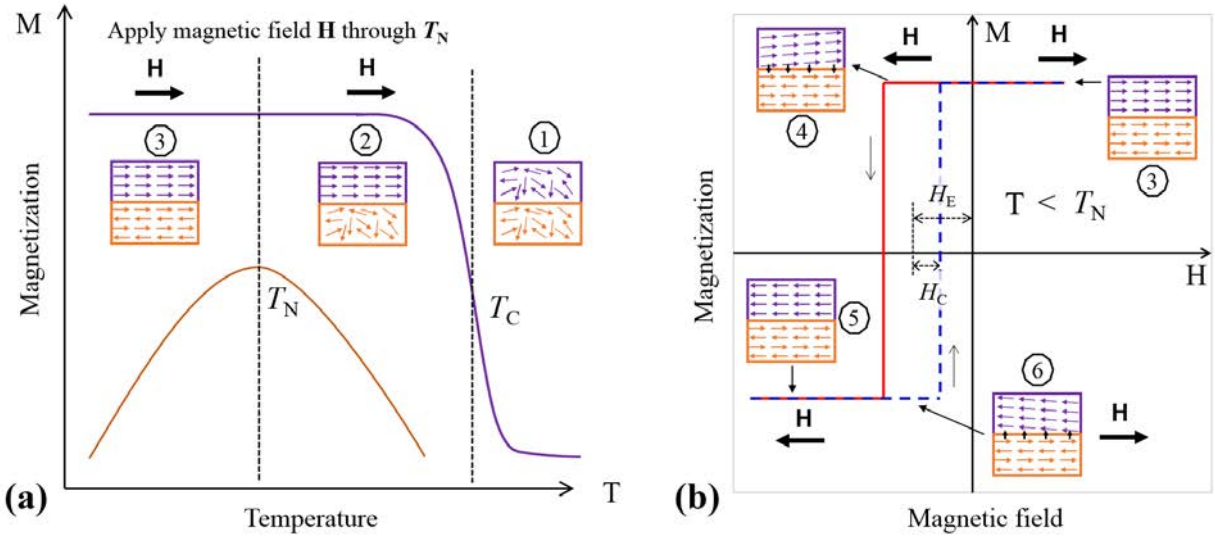

Fig. 1. 4 Illustration of exchange bias (EB) effect within a ferromagnetic (light blue) and antiferromagnetic (orange) system. (a) Magnetization curve against temperature. The magnetic field H is applied through the Néel temperature (T_N) of the antiferromagnetic. (b) Magnetic hysteresis loop curve at the temperature below T_N. H_E and H_C indicate the EB effect and coercivity, respectively. The small black arrows in EB systems of ④ and ⑥ demonstrate the interactions between ferromagnetic and antiferromagnetic domains under external magnetic field (**H**).

The EB effect in Ni-Mn-In based alloys was first studied in bulk polycrystalline samples with alloy composition of $Ni_{20}Mn_{50-x}In_x$ ($14.5 \leq x \leq 15.2$) in 2009 by Pathak *et al.* [35]. It was found that the EB effects in the samples with $14.8 < x < 15.2$ are almost constant. The maximum shift of the hysteresis loops up to 120 Oe was observed under the field cooling of 5 T. However, for the materials with compositions of $x \leq 14.5$ or $x \geq 15.2$, their EB effects sharply decrease to about 20 Oe. Later, an EB effect of around 170 Oe was detected by their research group in Si-doped $Ni_{50}Mn_{35}In_{11}Si_4$ bulk polycrystalline sample at 5 K under a field cooling of 5 T [184].

In addition to bulk samples, the EB effect in melt-spun ribbon samples of Ni-Mn-In based alloys were also explored [132, 135, 136]. An EB effect of around 150 Oe was observed in $Mn_{49.5}Ni_{40.4}In_{10.1}$ melt-spun ribbon at 5 K under a field cooling of 5 T [132]. Besides, it was found that the EB effect has a great temperature dependence. It drastically decreases with the increase of temperature. When the temperature is above 30 K, no obvious EB effect was observed in this material. Furthermore, the influence of annealing and Si-doping on EB effects in Ni-Mn-In ribbons was explored [135, 136]. Heat treatments were found to be favorable to improve the EB effect in

melt-spun ribbons. The maximum EB of 456 Oe was observed in an annealed $Ni_{48}Mn_{39}In_9Si_4$ ribbon at 10 K under a magnetic field cooling of 2 T.

Different from the conventional EB effect of which magnetic unidirectional anisotropy is obtained by the field cooling across the Néel or glass temperature (Fig. 1. 4), very interesting, an unusual large EB effect, a novel physical phenomenon, has been observed in Ni-Mn-In bulk alloys after the zero-field cooling from an unmagnetized state [34]. The origin of this unusual phenomenon has been related to the newly formed interface between different magnetic phases during the initial magnetization process. This observation clearly shows that the magnetic unidirectional anisotropy can be created isothermally below the blocking (Néel or glass) temperature, and might open a new direction to realize EB effect.

Despite the large EB effects in Ni-Mn-In based alloys, they are generally observed in very low temperatures (below 10 K), which greatly restrict their application range. Thus, in view of technological applications, it is critical to increase the work temperatures of EB effect in these materials. It is clear now that EB effect originates from the coupling interactions between the ferromagnetic and antiferromagnetic domains. In Ni-Mn-In based alloys, the spin structures of the ferromagnetism and antiferromagnetism should be closely related to the modulated atomic spacing between magnetic atoms (Mn and Ni). Thus, the accurate determination of the crystal structures of modulated martensites should be essential to quantitatively analyze and understand the EB effect in these materials for subsequent property optimization.

1.2.3.6 Hall effect

When a magnetic field is applied on an electrical conductor with the field direction perpendiculars to the electric current, a voltage will be generated across the electrical conductor with the direction perpendiculars to both the electric current and the magnetic field [185]. This phenomenon is the so-called Hall effect. Since its revelation in ferromagnetic materials in 1879 [186] and especially its counterpart anomalous Hall effect (AHE) [187, 188], *i.e.* the generation of a voltage difference without external magnetic field, it has been a subject of intense theoretical and experimental studies due to its wide potential applications in electric and magnetic field-effect devices [38]. The Hall effect in ferromagnets is generally characterized by Hall resistivity ρ_H that can be written as a sum of two terms, as shown in Eq. 1-2.

$$\rho_H = R_0 B_z + R_s 4\pi M_Z \quad (1\text{-}2)$$

where R_0 and R_S represent the coefficients of Hall effect and AHE respectively. B_Z and M_Z indicate magnetic induction and magnetization components, respectively. The first term in Eq. 1-2 describes the ordinary Hall effect that is related to the Lorentz force and is proportional to the applied magnetic field, and the second one is the AHE resistivity and is proportional to the magnetization of materials.

The Hall effect in Ni-Mn-In based alloys was first reported in 2009 [38]. An unusual field dependence of Hall resistivity ρ_H was observed in $Ni_{50}Mn_{34.8}In_{15.2}$ alloy in the vicinity of martensitic transformation that ρ_H sharply increases up to 50 μΩ cm under a magnetic field of 1.5 T that is comparable to the giant Hall resistivity in magnetic nanogranular alloys [38]. Associated with ρ_H, the Hall angle reaches a giant value of $\tan^{-1}0.5$, which is the highest value for known magnetic materials [38, 189]. Later, the Hall effect in quaternary Co-doped $Ni_{48}Co_2Mn_{35}In_{15}$ alloy was explored under the temperature range of 77 ~ 300 K in magnetic fields up to 1.5 T [190]. It was found that the sign of R_0 changes across the magnetostructural transition, which implies a strong change in electronic structure during martensitic transformation, while the R_S is positive in both austenite and martensite. Furthermore, the influence of Si-doping on Hall effect and AHE in $Ni_{50}Mn_{35}In_{15-x}Si_x$ (x = 1.0, 3.0, 4.0) alloys were explored [39]. It was reported that the R_0 is negative that is higher than that of nickel by an order of magnitude at 80 K, decreases monotonically with increasing temperature, approaches zero in austenite, and does not undergo sharp changes in the vicinity of martensitic transformation. So far, studies on Hall effect and AHE in Ni-Mn-In based alloy is still on going. The details of the underlying mechanism, especially for AHE, is still indistinct. However, it is clear that these two effects are closely related to the martensitic transformation. Thus, the study on martensitic transformation could be expected to provide some fundamental knowledge for deep understanding on these two effects.

1.2.3.7 Kinetic arrest effect

Kinetic arrest (KA) effect of martensitic transformation describes the phenomenon that part of austenite is frozen in the equilibrium martensite matrix when the material is cooled below the finishing temperature of martensitic transformation under an external magnetic field beyond a certain critical value or below a certain critical temperature [40, 41, 128, 132, 191, 192]. The

supercooled austenite phase, termed as “glass formers”, experiences a viscous retardation of nucleation and growth, and results in the formation of the so-called nonergodic glasslike state [193]. At present, it is still a great challenge to fully understand the nature of this kind of glass transition [194, 195]. The correlated KA effect has been considered as one of the deepest and most important unsolved problems in condensed matter physics [196].

The KA effect in Ni-Mn-In based alloys was first reported in bulk samples of $Ni_{50}Mn_{34}In_{16}$ polycrystalline alloy in 2007 [40]. It was found that the magnetostructural transition is partially kinetically arrested when the applied magnetic field is larger than 4 T, and the material shows a typical nonergodic glasslike dynamical response. Later, the influence of alloying (Fe and Cr) on KA effect was studied. Unlike the KA effect in the parent $Ni_{50}Mn_{34}In_{16}$ alloy that takes place under a high external magnetic field (larger than 4 T), the KA effect in the Fe doped alloy occurs even in zero magnetic field. The Cr-doped alloy, on the other hand, shows no signature of KA effect during martensitic transformation [191]. Apart from the magnetic field, the influence of the temperature field on KA effect was also explored [41, 192]. It was reported that the martensitic transformation in $Ni_{45}Co_5Mn_{36.7}In_{13.3}$ single crystal is interrupted at about 150 K during field cooling and does not proceed with further cooling [41]. Later, a critical temperature of around 100 K was observed in polycrystalline $Ni_{50}Mn_{34}In_{16}$ alloy [192]. The temperature influence on KA effect in these alloys has been related to the extremely low mobility of the phase interfaces (*habit plane*) and an abnormal behavior in transformation entropy change at low temperatures [41, 192].

In addition to bulk samples, the KA effects in ribbon samples of Ni-Mn-In based alloys were also studied [128, 132]. A progressive KA effect was observed in $Mn_{49.5}Ni_{40.4}In_{10.1}$ ribbon when the external magnetic field is larger than 10 T [132]. The amount of austenite frozen in the martensite matrix was found to increase with the enhancement of the intensity of the external magnetic field. The metastable character of the supercooled austenite phase was experimentally verified. Apart from the KA effect of martensitic transformation, very interestingly, the KA effect during inverse martensitic transformation was also found in the $Mn_{49.5}Ni_{40.4}In_{10.1}$ ribbon. The frozen martensite phase decreases with the increases of temperature.

The existence of KA effect in Ni-Mn-In based alloys is obviously unfavorable to some magnetoresponsive properties, such as MMSME, MCE and MR effect. It could significantly restrict the range of applied magnetic field or temperature field, and decrease their work efficiency.

However, if we use it reasonably, the KA effect might become a positive property in some cases. For example, the frozen austenite within martensite matrix could be utilized as nuclei to decrease the resistance and thus hysteresis loss during MFIMT. In addition, the broad coexisting two-phase temperature range, consists of both ferromagnetic and antiferromagnetic interactions, generated by KA effect might open a perspective to enlarge the work temperature range of EB effect (even at room temperature). So far, the underlying mechanism of KA effect in Ni-Mn-In based alloys is still unclear, although the temperature influence on KA effect was related to the lower interface mobility at low temperature [41, 192]. In origin, the KA effect is associated with the incompleteness of martensitic transformation, and it should thus be related to the martensitic transformation path. Consequently, the investigations on the influences of magnetic and temperature field on material parameters associated with martensitic transformation path, such as lattice parameters and elastic modulus, should provide some useful knowledge to deeply understand this effect.

1.3 Crystal structure determination of modulated martensite

Until now, several approaches have been proposed to determine the crystal structure of modulated martensite [197-200]. At the early attempts [197, 198], the modulated martensite structure was depicted by a supercell containing certain number of unit cells of the basic structure in the three-dimensional space. The number of unit cells in the supercell was deduced by counting the number of satellite reflections between two main reflections in SAED patterns. To achieve structural modulation, a sinusoidal function [197] or a simple uniform shear [198] was applied on individual atoms in the supercell. Such structural models are feasible to describe the atomic arrangements revealed by high-resolution transmission electron microscopy (TEM) or diffraction analysis for some Ni-Al and Ni-Mn-Ga alloys [201-204]. However, it is not rigorous to specify the number of unit cells in a supercell according to the number of observed satellite reflections, as pointed out in Ref. [205]. Moreover, a simple unique shear or a sinusoidal function is, in general, not enough to accurately represent the structural modulation features. Considering the fact that these structural models require a predetermination of the unit cell in the three-dimensional space depicting the crystal structure, they can only be applied to describe the so-called commensurate modulated structure. In fact, in many cases, modulated martensite refers to the so-called incommensurate modulated structure, *i.e.* the translational symmetry of crystal lattice may not exist

in the three-dimensional space. Therefore, one cannot accurately define incommensurate modulated structure in the three-dimensional basis, like the cases encountered for quasicrystals [206] and composite crystals [207].

An advanced approach to the crystal structure determination of modulated martensite involves the superspace theory [199, 200]. The basic idea of this theory is to add dimensions of space to render the aperiodic structure to be periodic in mathematics. In this approach, the crystal structure of modulated martensite is solved and refined in high-dimensional space, *e.g.* a (3+1)-dimensional space. The modulation wave vector $\boldsymbol{q}$ is introduced to describe the periodicity of structural modulation. If the coefficients of the modulation wave vector are rational, the structural modulation is commensurate; otherwise, it is incommensurate. Thus, both incommensurate and commensurate cases can be treated equally under this scheme, which is considered as the most appropriate and elegant option for determining the complete crystal structure of modulated martensite. So far, the validity of this general approach has been demonstrated in Heusler-type alloys with different kinds of modulated martensite [205, 208-210]. The details of the superspace theory are referred to the books of Janssen [199] and Van Smaalen [200].

1.4 Crystallography of martensitic transformation

Martensitic transformation is a diffusionless, military, first-order solid-solid structural transition [1, 3, 7, 211-220]. Since the crystal structure of the parent and product phase generally differ from each other, the elastic strain should be generated due to the crystal lattice misfit between the corresponding phases, as well as between differently oriented variants of martensite [221]. As a consequence, the microstructure of martensite should be determined by the minimization of the elastic strain energy and the interface energy.

With the assumption that the interface between austenite and martensite (*habit plane*) is invariant across the structural transition to keep a low transformation energy, the so-called phenomenological theories of martensitic transformation (PTMTs) were independently proposed by Wechsler, Leiberman and Read (WLR) in 1953 [222] and by Bowles and Mackenzie (BM) [223-226] in 1954. In spite of different mathematical descriptions, these two theories were verified to be equivalent [1-3]. The common feature of these two PTMTs is that both of them are formulated in a simple pure geometrical terms, and Bain distortion model is generally exploited to determine

the *transformation stretch tensors* for various martensite variants [1-3]. The lattice parameters of the corresponding phases are the only input parameters. The twinning systems, *habit plane* and crystallographic orientation relationship between austenite and martensite can be predicted. The details of PTMTs have been well summarized by Wayman [1], Nishiyama [2] and Christian [3].

With the consideration of elastic strain energy, the so-called nonlinear elasticity theory of martensitic transformation was developed by Ball and James on the basis of the PTMTs [213, 227]. The essential features of this theory are that it views microstructure to result from energy minimization and strain compatibility [228]. An energy function dependent on atomic positions and temperature is postulated, where this function has multiple energy wells for different phases [228-231]. Such an energy description permits a change of stability between the corresponding phases upon either a change in temperature or an application of stress [232]. The detailed information is described in books of Bahattachaya [56], Pitteri and Zanzotto [233], Dolzmann [234] and Müller [235].

1.5 Content of the present work

During the past twelve years, Ni-Mn-In based alloys have been well developed in both mechanism explorations and performance characterizations. Despite the revelation of many excellent properties, such as large MFIS, giant MCE and giant MR, some fundamental knowledge on Ni-Mn-In based alloys is still not available, such as the accurate crystal structure information of modulated martensite, the crystallographic features of microstructure and martensitic transformation, and variant rearrangement mechanism. Moreover, some properties of Ni-Mn-In based alloys still need to be improved, such as the hysteresis loss across the magnetostructural transition. This situation greatly hinders the development of this kind of promising multifunctional alloys.

Based on such a situation, the present work was carried out, as illustrated in Fig. 1. 5. It consists of three parts. First, the crystal structures and microstructures of Ni-Mn-In based alloys were systematically characterized. Then, the crystallographic features of martensitic transformation were studied. Finally, with the determined crystal structure, microstructure and martensitic transformation information, the behaviors and mechanisms of variant rearrangement under external

mechanical loadings and the influences of annealing on MCE and its related hysteresis loss were explored. The main contents are summarized as follows:

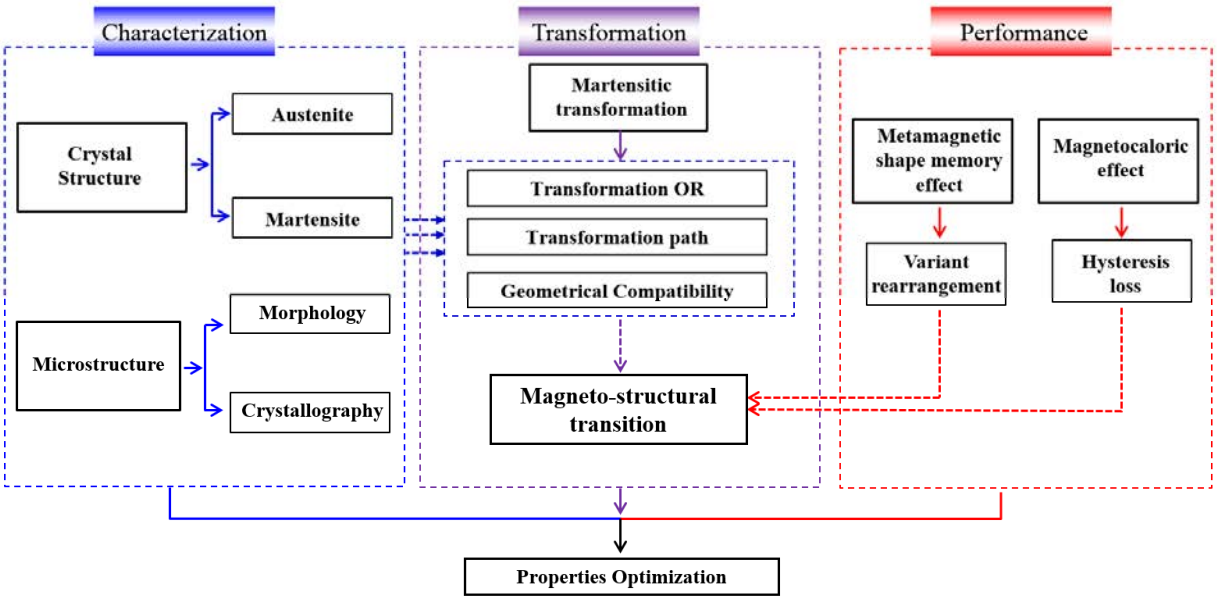

Fig. 1. 5 Framework of the present dissertation.

(1) Crystal structure determinations of austenite and martensite (non-modulated and modulated) by means of Rietveld method in the frame of superspace theory (Chapter 3).

(2) Microstructure investigations by means of crystallographic theories of martensitic transformation (CTMT), electron backscatter diffraction (EBSD) and high resolution transmission electron microscopy (HRTEM) (Chapter 4).

(3) Crystallographic studies on orientation relationship (*OR*) between austenite and martensite, martensitic transformation strain path and geometrical compatibility between austenite and martensite by means of CTMT, EBSD and HRTEM (Chapter 5).

(4) Behaviors and mechanisms of martensite variant rearrangement/ selection under mechanical loadings in martensite state and across the structural transition by Schmid factor (*SF*) analysis, *in-situ* neutron diffraction investigation and *ex-situ* microstructure examination (Chapter 6).

(5) Effects of heat treatment on MCE and its related hysteresis loss (Chapter 6).

The present work was expected to provide some fundamental information on crystal structure, microstructure, martensitic transformation crystallography, variant rearrangement/ selection

behavior, and mechanism of hysteresis loss in Ni-Mn-In based alloys for the understanding of their multifunctional properties and the further performance optimizations.

Chapter 2 Experimental and calculation methods

2.1 Experimental details

2.1.1 Alloy preparations and heat treatments

The polycrystalline alloys with nominal compositions of $Ni_{50}Mn_{50-x}In_x$ ($0 \leq x \leq 25$) and $Ni_{45}Co_5Mn_{50-x}In_x$ ($13 \leq x \leq 13.5$) were prepared by arc-melting pure constituent elements Ni (99.97 wt. %), Co (99.9 wt. %), Mn (99.95 wt. %) and In (99.995 wt. %) under Ar atmosphere in a water-cooled copper crucible. The alloys were remelted for four times to ensure composition homogeneity. The ingots were further remelted and injected into a copper mould to obtain a cylindrical rod of 8 mm in diameter and ~ 50 mm in length. The as-cast rods were further annealed in a sealed quartz tube under Ar atmosphere at 1173 K for 24 hours followed by water quenching. The ribbon samples were melt spun using a single copper roller with a wheel-rotating speed of 15 $m \cdot s^{-1}$, followed by annealing at 1173 K for 24 hours in a sealed quartz tube.

2.1.2 Martensitic transformation temperature measurements

Disk sample with the diameter of 3 mm and the thickness of 1 mm was cut out from the center of the annealed rod. The critical temperatures of martensitic transformation were determined using the differential scanning calorimeter (DSC, TA-Q100) in heating and cooling modes at a rate of 5 $K \cdot min^{-1}$.

2.1.3 Crystal structure measurements

Powder samples with particle diameter around 74 μm were prepared by mechanically grinding the bulk sample. To release the stresses induced by mechanical grinding, they were annealed at 823 K for 6 hours in vacuum quartz tube. The crystal structures of the alloys were first examined with an X-ray diffractometer (XRD, Rigaku, Smartlab) with a 9 kW rotating anode using *Cu-Kα* radiation and graphite monochromater at room temperature. The “step” mode was used with a scanning step of 0.02° (2θ).

To accurately determine the crystal structure, such as the space group and atomic positions, of the austenite and the martensite of Ni-Mn-In alloys, neutron diffraction and synchrotron X-ray

diffraction techniques were utilized. The high-resolution neutron diffraction experiments were performed at room temperature using the structure powder diffractometer (SPODI) [236] at FRM II. For each powder sample, it was filled into a thin-walled (0.15 mm) vanadium container. Monochromatic neutrons (λ = 1.54832(2) Å) were obtained using the (5 5 1) reflection of vertically focused composite Ge monochromator at 155^{o} take-off angle. Two-dimensional diffraction data were collected using the SPODI position-sensitive ^{3}He detector and then corrected for geometrical aberrations under the procedure described in Ref. [236]. The synchrotron X-ray diffraction experiments were conducted with the high energy materials science beam line (HEMS) at PETRA III. The transmission method with pinhole technique was chosen, where the primary slit system guided a highly brilliant beam of 500 μm × 500 μm on the samples. In order to get good resolution, one Mar345 area detector with a pixel distance of 100 μm was positioned 1110 mm behind the samples. The Debye-Scherrer rings up to 7.7° in 2θ were recorded. To increase the signal-to-noise ratio of spectra, an exposure time of 4 seconds was selected. The experimental parameters for the neutron and synchrotron diffraction measurements are summarized in Table 2. 1.

Table 2. 1 Experimental parameters for neutron and synchrotron diffraction measurements.

Radiation source	Research neutron reactor	High-energy synchrotron radiation
Wavelength (Å)	1.5483	0.1423
2θ range (°)	20~110	2.10~7.10
Step (°)	0.05	0.0051
Temperature (K)	298	298

2.1.4 Microstructural characterizations

Rectangular parallelepiped samples with a dimension of 5.5 mm × 5.5 mm × 7.5 mm were cut out of the middle portion of the annealed rod for the microstructural characterizations. The sample surfaces were mechanically ground and further electrolytically polished using a solution of 20 % nitric acid in methanol under the voltage of 8 V at around 263 K. The microstructural examinations and crystallographic orientation investigations were performed in a field emission gun scanning electron microscope (SEM, Jeol JSM 6500 F) with an EBSD acquisition camera and the Aztec online acquisition software package (Oxford Instruments). During the EBSD measurements, the “beam-control” mode was applied. The interfaces between adjacent martensite variants were examined using a high resolution transmission electron microscope (HRTEM, JEM 2100F). The

CrystalMaker and Single-Crystal software packages (CrystalMaker software) were utilized to analyze and simulate the electron diffraction patterns.

2.1.5 Mechanical property investigations

The rectangular parallelepiped samples with a dimension of 5.5 mm × 5.5 mm × 7.5 mm were cut out of the middle portion of the annealed rod. *Ex-situ* uniaxial compression with a maximum strain of 5.44 % along the length direction of the sample was carried out using a conventional uniaxial compression machine with a strain rate of 0.02 $mm \cdot min^{-1}$.

In-situ neutron diffraction thermomechanical compressions were performed at the Heinz Maier-Leibnitz Zentrum (MLZ), Garching, Germany, with a monochromatic wavelength of 2.1 Å. The uniaxial compressive load was applied by a rotatable multifunctional (tension/ compression/ torsion) loading frame installed at STRESS-SPEX, as shown in Fig. 2. 1, under the "constant load" model to ensure a fixed load. Three different compression loads, *i.e.* -10 MPa, -40 MPa and -50 MPa, were successively applied during the cooling process across the martensitic transformation. A two-dimensional detector at 42° (2θ) was set to record the neutron diffraction signals.

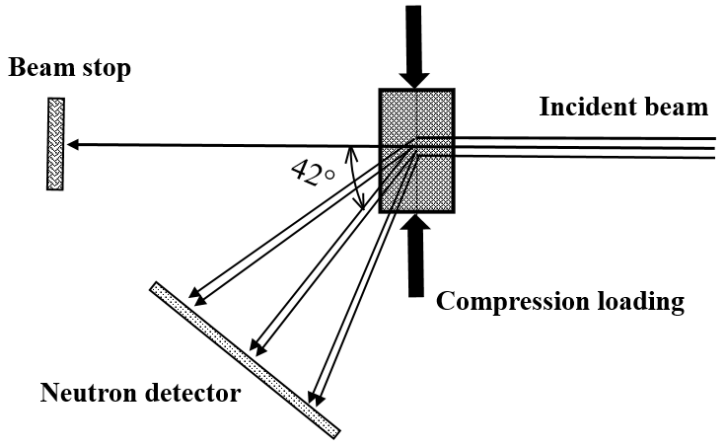

Fig. 2. 1 Illustration of *in-situ* hot-compression inspected by neutron diffraction.

2.1.6 Magnetic property examinations

Magnetization measurements were performed using the vibrating sample magnetometry in a Quantum Design cryogen-free physical properties measurement system (PPMS) Dynacool® platform of 9 T. Needle-shaped samples were cut out of the melt-spun ribbon that were wrapped

in kapton tape. An external magnetic field was applied along the rolling direction of the ribbon to minimize the demagnetization effect.

The magnetization at low- (10 mT) and high- (5 T) magnetic field as a function of temperature $M(T)$ were measured from 10 K to 400 K at a sweep rate of 1.5 $K \cdot min^{-1}$. The isothermal magnetizations were measured across the inverse martensitic transformation with a temperature interval of 1 K. The measurement protocol with a thermal cycling from 400 K to 200 K to the measurement temperature was performed prior to record each isothermal magnetization curve.

2.2 Calculation methods

2.2.1 Crystal structure determinations

The crystal structure of austenite was solved with the measured powder neutron diffraction data using the charge-flipping algorithm [237] and refined by the Rietveld method [238]. Due to the possible aperiodicity of the modulated martensite, the crystal structure of modulated martensite was determined in the frame of superspace theory. The basic idea of this theory is by adding the dimension of space to render the aperiodic structure to be periodic in mathematics, as shown in Fig. 2. 2. Then, the unit cell can be defined in a higher dimensional space, such as the (3+1)-dimensional space.

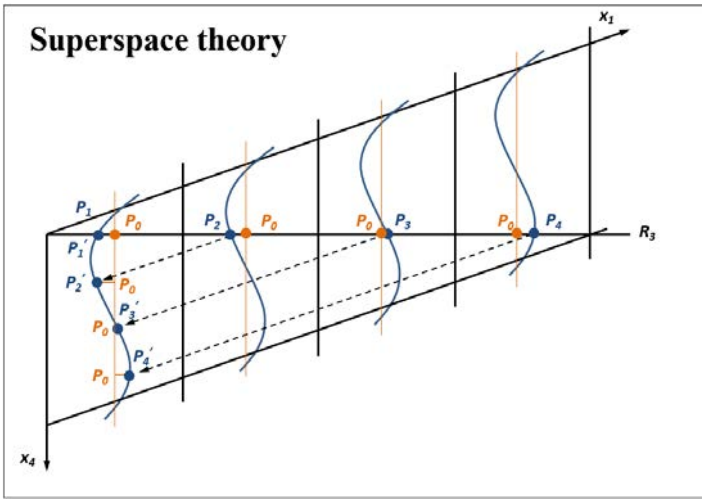

Fig. 2. 2 Illustration of the superspace theory. P_i (i = 1 ~ 4) represent the aperiodic lattice points in the three-dimensional space ($\boldsymbol{R_3}$). P_i' (i = 1 ~ 4) describe the constructed periodic lattice points in the (3+1)-dimensional space. X_1 and X_4 indicate the first and fourth dimensional base vectors, respectively.

The general procedure for the crystal structure refinement in the high-dimensional space is relatively laborious. Numerous structural parameters, including lattice parameters of average crystal structure, modulation wave vector, coefficients of modulation wave function, atomic displacement parameters and atom occupancies, *etc.*, are refined at the same time and one parameter interacts with another. Furthermore, the crystal structure determination would become particularly difficult if the experimental diffraction data are not "clean", as frequently encountered in the case of Ni-Mn-In alloys where some quantity of parent austenite is retained within the transformed microstructure. As a treatment to simplify the iteration routine for the overall refinement and to increase the determination reliability, indirect diffraction information, such as crystallographic inheritance of martensitic transformation that is well represented by diffraction peak splitting, could be effectively utilized.

With this situation, an attempt was made on the complete crystal structure determination of modulated martensite in a Mn-rich off-stoichiometric Ni-Mn-In alloy in the frame of the superspace theory. First, the average crystal structure and the modulation wave vector of the modulated martensite were determined primarily upon analyzing the diffraction peak separations induced by the martensitic transformation. The refinement of the modulated structure was performed in (3+1)-dimensional superspace with Rietveld method [238, 239].

2.2.2 *Ab-initio* calculations

The atomic sites for the off-stoichiometric elements in austenite were investigated by the first-principles calculations, in the frame of the density functional theory (DFT) using the Vienna *ab-initio* simulation package [240, 241]. The interactions between ions and electrons were described by the projector augmented wave (PAW) method [242], and the exchange correlation effects were treated by the generalized gradient approximation (GGA) in the Perdew and Wang 91 formulation [243]. The In-3d electrons were included as valence states; the kinetic energy cutoff was set to be 270 eV. The Monkhorst-Pack grid [244] with 12×12×6 k-points was employed to sample the Brillouin zone of the supercell (32 atoms). The lattice parameters and atomic positions were further optimized for all structures until the total energy decrease was less than 1 meV and the total-force was smaller than 0.02 eV/Å.

2.2.3 Basic crystallographic calculations

2.2.3.1 Coordinate system setting

Two kinds of coordinate systems are used in the present work. One is the orthonormal system ***i*-*j*-*k*** (Fig. 2. 3a). The other is the Bravais lattice basis of the corresponding phases, *i.e.* austenite cubic lattice basis $\boldsymbol{a}_A$-$\boldsymbol{b}_A$-$\boldsymbol{c}_A$ (Fig. 2. 3b) and martensite monoclinic (***b***-unique) lattice basis $\boldsymbol{a}_M$-$\boldsymbol{b}_M$-$\boldsymbol{c}_M$ (Fig. 2. 3c). The geometrical relations between the orthonormal coordinate system set to the respective Bravais lattice basis of austenite and martensite and their Bravais lattice basis are demonstrated in Fig. 2. 3b and c. For martensite, the basis vectors of the orthonormal coordinate system ***j***, ***k*** are set to parallel to $\boldsymbol{b}_M$, $\boldsymbol{c}_M$ (Fig. 2. 3c), respectively.

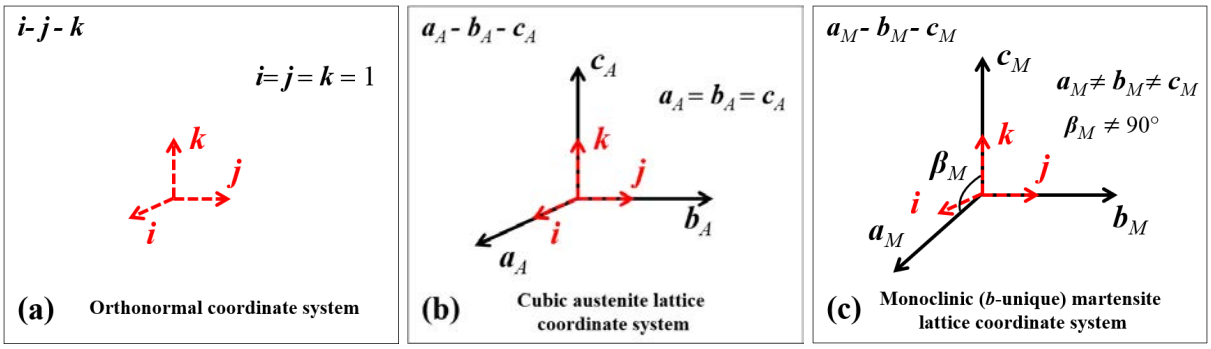

Fig. 2. 3 Various coordinate systems used in the present work. (a) Orthonormal coordinate system ***i*-*j*-*k***; (b) austenite cubic lattice basis $\boldsymbol{a}_A$-$\boldsymbol{b}_A$-$\boldsymbol{c}_A$; (c) martensite monoclinic (***b***-unique) lattice basis $\boldsymbol{a}_M$-$\boldsymbol{b}_M$-$\boldsymbol{c}_M$. The relations between the orthonormal coordinate system and the corresponding Bravais lattice basis are demonstrated in (b) and (c), respectively. All coordinate systems are of right-handedness.

2.2.3.2 Coordinate transformation

Coordinate transformation means the transformation of coordinates for vectors or planes between different reference systems. The so-called *coordinate transformation matrix* is generally utilized to describe this process in mathematics. As shown in Fig. 2. 4a, there are two arbitrary coordinate systems ***R*** and ***R'*** that are defined by the basis vectors ***X***, ***Y***, ***Z*** and ***X'***, ***Y'***, ***Z'***, respectively. ***V*** represents an arbitrary vector and its indices with respect to these two references are $[uvw]_{\boldsymbol{R}}$ and $[u'v'w']_{\boldsymbol{R'}}$, respectively. The relations between the basis vectors of references ***R*** and ***R'*** are given in Eqs. 2-1.

$$\begin{cases} \boldsymbol{X}' = a_{11}\boldsymbol{X} + a_{21}\boldsymbol{Y} + a_{31}\boldsymbol{Z} \\ \boldsymbol{Y}' = a_{12}\boldsymbol{X} + a_{22}\boldsymbol{Y} + a_{32}\boldsymbol{Z} \\ \boldsymbol{Z}' = a_{13}\boldsymbol{X} + a_{23}\boldsymbol{Y} + a_{33}\boldsymbol{Z} \end{cases} \quad (2\text{-}1)$$

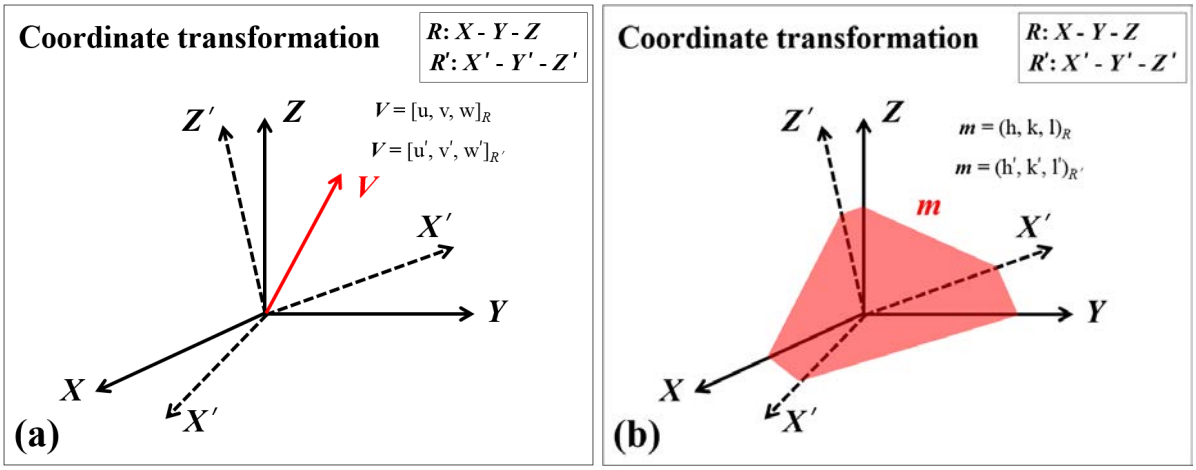

Fig. 2. 4 Illustration of coordinate transformation for vectors (a) and planes (b) between two coordinate systems ***R*** (**X- Y- Z**) and ***R'*** (**X'- Y'- Z'**).

The *coordinate transformation matrix* between references ***R*** and ***R'***, denoted $\boldsymbol{M}^{\boldsymbol{R}\to\boldsymbol{R'}}$, can be directly determined by putting the coefficients of each row of Eqs. 2-1 as column, as shown in Eq. 2-2.

$$\boldsymbol{M}^{\boldsymbol{R}\to\boldsymbol{R'}} = \begin{bmatrix} a_{11} & a_{12} & a_{13} \\ a_{21} & a_{22} & a_{23} \\ a_{31} & a_{32} & a_{33} \end{bmatrix} \quad (2\text{-}2)$$

With the *coordinate transformation matrix* of $\boldsymbol{M}^{\boldsymbol{R}\to\boldsymbol{R'}}$, the coordinate transformation for vector ***V*** (Fig. 2. 4a) from reference ***R'*** to ***R*** can by realized by Eq. 2-3.

$$\begin{bmatrix} u \\ v \\ w \end{bmatrix}_{\boldsymbol{R}} = \boldsymbol{M}^{\boldsymbol{R}\to\boldsymbol{R'}} \times \begin{bmatrix} u' \\ v' \\ w' \end{bmatrix}_{\boldsymbol{R'}} \quad (2\text{-}3)$$

The inverse of $\boldsymbol{M}^{\boldsymbol{R}\to\boldsymbol{R'}}$, denoted $\boldsymbol{M}^{\boldsymbol{R'}\to\boldsymbol{R}}$, can realize the coordinate transformation from ***R*** to ***R'***, as shown in Eq. 2-4. The determinant of $\boldsymbol{M}^{\boldsymbol{R}\to\boldsymbol{R'}}$ equal to the volume change of the parallelepipeds constituted by the basis vectors of ***R*** and ***R'***.

$$\begin{bmatrix} u' \\ v' \\ w' \end{bmatrix}_{R'} = \boldsymbol{M}^{\boldsymbol{R'}\to\boldsymbol{R}} \times \begin{bmatrix} u \\ v \\ w \end{bmatrix}_{R} \quad (2\text{-}4)$$

The inverse of transpose (or the transpose of inverse) of $\boldsymbol{M}^{\boldsymbol{R}\to\boldsymbol{R'}}$, denoted $(\boldsymbol{M}^{\boldsymbol{R}\to\boldsymbol{R'}})^{-\mathrm{T}}$, can realize the coordinate transformation for planes under these two references, as given in Eq. 2-5, where $(hkl)_{\boldsymbol{R}}$

and $(h'k'l')_{\boldsymbol{R'}}$ are the Miller indices of the plane $\boldsymbol{m}$ under $\boldsymbol{R}$ and $\boldsymbol{R'}$ (Fig. 2. 4b), respectively. The proof is given in Appendix II.

$$\begin{bmatrix} h \\ k \\ l \end{bmatrix}_{\boldsymbol{R}} = (\boldsymbol{M}^{\boldsymbol{R}\rightarrow\boldsymbol{R'}})^{-\mathbf{T}} \times \begin{bmatrix} h' \\ k' \\ l' \end{bmatrix}_{\boldsymbol{R'}} \tag{2-5}$$

2.2.3.3 Metric tensor

Suppose that $\boldsymbol{S}$ is a coordinate system defined by three non-planar basis vectors $\boldsymbol{a}$, $\boldsymbol{b}$ and $\boldsymbol{c}$. Then, the basis vectors of its correlated reciprocal space $\boldsymbol{S^*}$ can be obtained by Eqs. 2-6.

$$\boldsymbol{a}^* = \frac{\boldsymbol{b}\times\boldsymbol{c}}{\boldsymbol{a}\cdot(\boldsymbol{b}\times\boldsymbol{c})} \qquad \boldsymbol{b}^* = \frac{\boldsymbol{c}\times\boldsymbol{a}}{\boldsymbol{a}\cdot(\boldsymbol{b}\times\boldsymbol{c})} \qquad \boldsymbol{c}^* = \frac{\boldsymbol{a}\times\boldsymbol{b}}{\boldsymbol{a}\cdot(\boldsymbol{b}\times\boldsymbol{c})} \tag{2-6}$$

The *coordinate transformation matrix* between these two conjugate references $\boldsymbol{S}$ and $\boldsymbol{S^*}$, *i.e.* $\boldsymbol{M}^{\boldsymbol{S^*}\rightarrow\boldsymbol{S}}$, can be deduced, as shown in Eq. 2-7.

$$\boldsymbol{M}^{\boldsymbol{S^*}\rightarrow\boldsymbol{S}} = \begin{bmatrix} \boldsymbol{a}\cdot\boldsymbol{a} & \boldsymbol{a}\cdot\boldsymbol{b} & \boldsymbol{a}\cdot\boldsymbol{c} \\ \boldsymbol{b}\cdot\boldsymbol{a} & \boldsymbol{b}\cdot\boldsymbol{b} & \boldsymbol{b}\cdot\boldsymbol{c} \\ \boldsymbol{c}\cdot\boldsymbol{a} & \boldsymbol{c}\cdot\boldsymbol{b} & \boldsymbol{c}\cdot\boldsymbol{c} \end{bmatrix} \tag{2-7}$$

In general, this kind of special *coordinate transformation matrix* is termed as *metric tensor*. For a better distinguish, it is henceforth denoted as $\boldsymbol{G}^{\boldsymbol{S^*}\rightarrow\boldsymbol{S}}$. Since the *metric* is symmetrical (Eq. 2-7), the transpose equal to itself, *i.e.*

$$(\boldsymbol{G}^{\boldsymbol{S^*}\rightarrow\boldsymbol{S}})^{\mathbf{T}} = \boldsymbol{G}^{\boldsymbol{S^*}\rightarrow\mathbf{S}} \tag{2-8}$$

With *metric* $\boldsymbol{G}^{\boldsymbol{S^*}\rightarrow\boldsymbol{S}}$, the scalar product of two vectors, $\boldsymbol{V_1}$ $[u_1v_1w_1]_{\boldsymbol{S}}$ and $\boldsymbol{V_2}$ $[u_2v_2w_2]_{\boldsymbol{S}}$ with respect to reference $\boldsymbol{S}$, can be conveniently calculated by Eq. 2-9.

$$\boldsymbol{V_1}\cdot\boldsymbol{V_2} = [u_1\ v_1\ w_1]_{\boldsymbol{S}} \times \boldsymbol{G}^{\boldsymbol{S^*}\rightarrow\boldsymbol{S}} \times \begin{bmatrix} u_2 \\ v_2 \\ w_2 \end{bmatrix}_{\boldsymbol{S}} \tag{2-9}$$

The *metric* transformation for two references $\boldsymbol{S}$ and $\boldsymbol{S_0}$ can be realized by Eq. 2-10, where $\boldsymbol{M}^{\boldsymbol{S}\rightarrow\boldsymbol{S_0}}$ is the *coordinate transformation matrix* between references $\boldsymbol{S}$ and $\boldsymbol{S_0}$. The derivation is given in Appendix II.

$$\boldsymbol{G}^{\boldsymbol{S_0^*}\rightarrow\boldsymbol{S_0}} = (\boldsymbol{M}^{\boldsymbol{S}\rightarrow\boldsymbol{S_0}})^{\mathbf{T}} \times \boldsymbol{G}^{\boldsymbol{S^*}\rightarrow\boldsymbol{S}} \times \boldsymbol{M}^{\boldsymbol{S}\rightarrow\boldsymbol{S_0}} \tag{2-10}$$

2.2.3.4 Orientation representation

(1) Matrix

For two arbitrary coordinate systems ***S*** and ***S'***, in addition to realize the coordinate transformation for vector/ plane between these two references, their correlated *coordinate transformation matrix* $\boldsymbol{M}^{S\rightarrow S'}$ is also generally used to describe their relative orientation. In a special case, when both these two references ***S*** and ***S'*** are orthonormal, their coordinate transformation matrix $\boldsymbol{M}^{S\rightarrow S'}$ belongs to a *rotation matrix* in mathematics. For a clear description, this kind of *coordinate transformation matrix* is denoted $\boldsymbol{g}^{S\rightarrow S'}$. The determinant of $\boldsymbol{g}^{S'\rightarrow S}$ is equal to 1. The inverse of *orientation matrix* equal to its transpose, *i.e.*

$$(\boldsymbol{g}^{S\rightarrow S'})^{-1} = (\boldsymbol{g}^{S\rightarrow S'})^{T} \tag{2-11}$$

(2) Euler angles

For two orthonormal references, their relative orientation can be conveniently described by Euler angles that involves three consecutive rotations. In this work, the Euler angles under Bunge notation (φ_1, Φ, φ_2) is utilized. Moreover, the *HKL* convention - the rotation is from the macroscopic sample reference to the orthonormal reference set to the crystal lattice reference - is used, as demonstrated in Fig. 2. 5. The relation between Euler angles (φ_1, Φ, φ_2) and *orientation matrix* $\boldsymbol{g}^{S\rightarrow S'}$ is given in Eq. 2-12.

$$\boldsymbol{g}^{S\rightarrow S'} = \begin{Bmatrix} \cos\varphi_1\cos\varphi_2 - \sin\varphi_1\sin\varphi_2\cos\Phi & -\cos\varphi_1\sin\varphi_2 - \sin\varphi_1\cos\varphi_2\cos\Phi & \sin\varphi_1\sin\Phi \\ \sin\varphi_1\cos\varphi_2 + \cos\varphi_1\sin\varphi_2\cos\Phi & -\sin\varphi_1\sin\varphi_2 + \cos\varphi_1\cos\varphi_2\cos\Phi & -\cos\varphi_1\sin\Phi \\ \sin\varphi_2\sin\Phi & \cos\varphi_2\sin\Phi & \cos\Phi \end{Bmatrix} \tag{2-12}$$

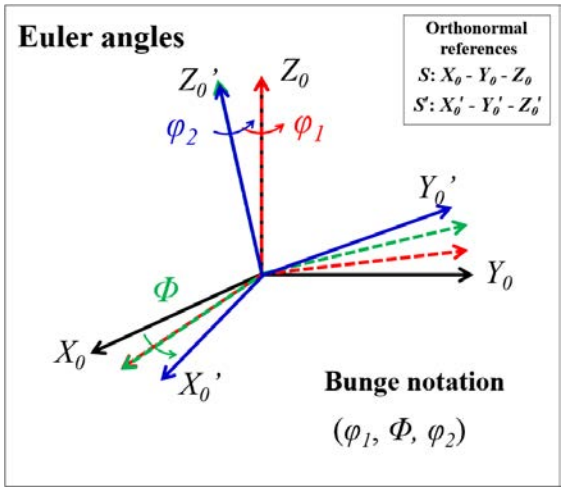

Fig. 2. 5 Definition of Euler angles under Bunge notation (φ_1, Φ, φ_2) with *HKL* convention.

2.2.3.5 Crystallographic orientation relationship

(1) Plane and in-plane direction parallelisms

The crystallographic orientation relationship (*OR*) between two crystals ***R*** and ***R'*** (grains or phases) can be intuitively described by plane and in-plane direction parallelisms, as demonstrated in Formula 2-13.

$$(hkl)_{\boldsymbol{R}} // (h'k'l')_{\boldsymbol{R'}} \qquad [uvw]_{\boldsymbol{R}} // [u'v'w']_{\boldsymbol{R'}} \tag{2-13}$$

(2) Axis/ angle pair

Axis/ angle pair is also generally used to describe crystallographic *OR*s. To determine the axis/ angle pair, the misorientation matrices $\Delta g^{\boldsymbol{R\rightarrow R'}}$ between these two crystals ***R*** and ***R'*** need to be calculated first, as demonstrated in Fig. 2. 6. It should be noted that all references, ***S*** ($\mathbf{X_0}$- $\mathbf{Y_0}$- $\mathbf{Z_0}$), ***R*** (***i***- ***j***- ***k***) and ***R'*** (***i'***- ***j'***- ***k'***), should be orthonormal. However, the crystal lattice of crystal ***R*** and /or ***R'*** are often not orthonormal, thus an orthonormal system should be used to define the crystal lattice. The setting of the orthonormal references to the crystal lattices of austenite (austenite) and martensite (monoclinic) in this study are shown in Fig. 2. 3b and c, respectively.

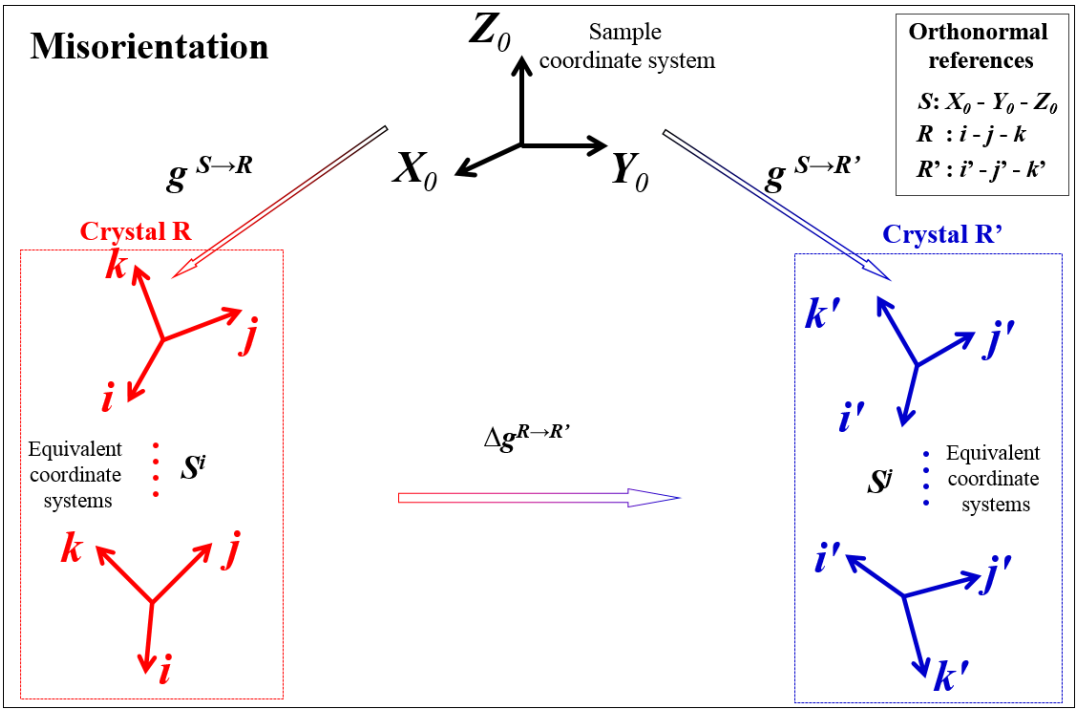

Fig. 2. 6 Misorientation matrix between two crystals ***R*** and ***R'***. $\boldsymbol{S_i}$ and $\boldsymbol{S_j}$ represent the rotational symmetry matrices of crystal ***R*** and ***R'***, respectively.

With the orientation information of domain ***R*** and ***R'***, $\boldsymbol{g}^{S\to R}$ and $\boldsymbol{g}^{S\to R'}$, their misorientation matrices $\Delta\boldsymbol{g}^{R\to R'}$ can be determined with Eq. 2-14.

$$\Delta\boldsymbol{g}^{R\to R'} = (\boldsymbol{S}^i)^{-1} \times (\boldsymbol{g}^{S\to R})^{-1} \times \boldsymbol{g}^{S\to R'} \times \boldsymbol{S}^j \tag{2-14}$$

where $\boldsymbol{S}^i$ and $\boldsymbol{S}^j$ represent the rotational symmetric matrices of domain ***R*** and ***R'***, respectively. Moreover, the misorientation can be also expressed in the form of the rotation angle ω and its related rotation axis ***d***, *i.e.*, axis/ angle pair. The relation between matrix representation and axis/ angle pair is given in Eqs. 2-15 ~ 2-18. Due to the crystallographic rotational symmetry of crystals ***R*** and ***R'***, the axis/ angle pair is generally not unique. The one with the minimum rotation angle and its correlated rotation axis is generally used to describe the crystallographic *OR* between these two crystals.

$$\omega = \arccos\left(\frac{g_{11} + g_{22} + g_{33} - 1}{2}\right) \tag{2-15}$$

(1) $\omega = 180°$

$$\mathbf{d} = (d_1,d_2,d_3) = \left(\frac{g_{11}+1}{2}, \frac{g_{22}+1}{2}, \frac{g_{33}+1}{2}\right)$$

$$\text{with} \begin{bmatrix} |d_m| = \max(|d_i|, i = 1, 2, 3) \\ d_m > 0, \quad \text{by convention} \\ \forall i \neq m, \ \operatorname{sgn}(d_i) = \operatorname{sgn}(g_{im}) \end{bmatrix} \tag{2-16}$$

(2) $\omega = 0°$

$$\boldsymbol{d} = (d_1,d_2,d_3) = (1,0,0) \tag{2-17}$$

(3) $\omega \neq 180°$ and $\omega \neq 0°$

$$\boldsymbol{d} = (d_1,d_2,d_3) = \left(\frac{g_{23}-g_{32}}{2\sin\omega}, \frac{g_{31}-g_{13}}{2\sin\omega}, \frac{g_{12}-g_{21}}{2\sin\omega}\right) \tag{2-18}$$

2.2.3.6 Stereographic projection representation

Stereographic projection is a convenient way to demonstrate the three-dimensional (3D) vectors in a two-dimensional (2D) plane for a better visualization. One of essential features of the stereographic projection is that the poles in the 2D projection plane can reflect the angle between their corresponding vectors in the 3D space. Stereographic projection with the projection plane of $\mathbf{X_0}$- $\mathbf{Y_0}$, as an example, is demonstrated in Fig. 2. 7, where ***OA*** represents an arbitrary vector with respect to the 3D orthonormal reference ***S*** **($\mathbf{X_0}$- $\mathbf{Y_0}$- $\mathbf{Z_0}$)**. Its corresponding projection pole (***A'***) is

the intersection of the projection plane ($\mathbf{X_0}$- $\mathbf{Y_0}$) with the vector of ***AS***, where ***S*** is the south pole of the projection sphere. The coordinates of ***A'*** (x_0, y_0), with respect to the 2D coordinate system of the projection plane $\mathbf{X_0}$- $\mathbf{Y_0}$, can be determined with the coordinates of ***OA*** (x, y, z) in the 3D reference ***S*** by Eq. 2-19.

$$\begin{cases} x_0 = \dfrac{x}{1+|z|} \\ y_0 = \dfrac{y}{1+|z|} \end{cases} \tag{2-19}$$

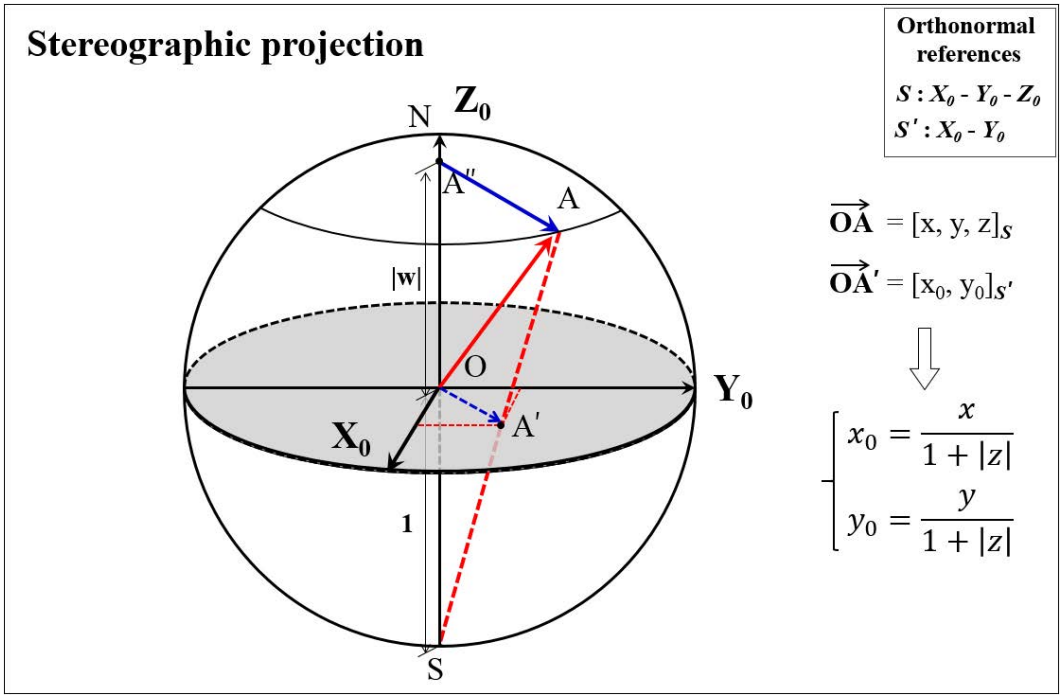

Fig. 2. 7 Illustration of stereographic projection with plane $\mathbf{X_0}$- $\mathbf{Y_0}$ as the projection plane. ***A'*** is the intersection of the projection plane ($\mathbf{X_0}$- $\mathbf{Y_0}$) with the vector of ***AS***, where ***S*** is the south pole of the projection sphere. ***A''*** is the projection of vector ***OA*** along the basis vector $\mathbf{Z_0}$.

2.2.3.7 Deformation gradient tensor

Deformation gradient tensor is generally utilized to describe a homogeneous deformation in continuum mechanics. For a clear illustration, in the present work, the *deformation gradient tensor* is denoted by $\boldsymbol{F}^{\boldsymbol{R}}_{\boldsymbol{D'\leftarrow D}}$, where the superscript ***R*** indicates the reference system, and ***D*** and ***D'*** represent the undeformed and its corresponding deformed domains. The determination of *deformation gradient tensor* is shown in Fig. 2. 8, where ***V*** represents an arbitrary undeformed

vector, and the corresponding vector after deformation is indicated by ***V'***. Reference ***R***, defined by basis vectors ***i***, ***j*** and ***k***, is an arbitrary coordinate system. ***OA***, ***OB*** and ***OC*** and ***OA'***, ***OB'*** and ***OC'*** are the resolved along the basis vectors of ***i***, ***j*** and ***k***, *i.e.*

$$\begin{cases} \boldsymbol{V} = \boldsymbol{OA} + \boldsymbol{OB} + \boldsymbol{OC} \\ \boldsymbol{V'} = \boldsymbol{OA'} + \boldsymbol{OB'} + \boldsymbol{OC'} \end{cases} \tag{2-20}$$

The deformation of vector ***V*** to ***V'*** equals the deformation of their resolved vectors, ***i.e.***, from ***OA***, ***OB***, ***OC*** to ***OA'***, ***OB'***, ***OC'***, respectively. If we suppose the coordinates of vector ***V*** with respect to reference ***R*** (***i- j- k***) are $[a\ b\ c]_{\boldsymbol{R}}$, vectors ***OA***, ***OB***, ***OC*** then equal $[a\ 0\ 0]_{\boldsymbol{R}}$, $[0\ b\ 0]_{\boldsymbol{R}}$ and $[0\ 0\ c]_{\boldsymbol{R}}$, respectively. After homogeneous deformation $\boldsymbol{F}_{\boldsymbol{D'\leftarrow D}}^{\boldsymbol{R}}$, the resultant vectors ***OA'***, ***OB'*** and ***OC'***, transformed from ***OA***, ***OB***, ***OC***, equal $[a_1\ a_2\ a_3]_{\boldsymbol{R}}$, $[b_1\ b_2\ b_3]_{\boldsymbol{R}}$ and $[c_1\ c_2\ c_3]_{\boldsymbol{R}}$, respectively. Thus, the vector ***V'***, can be expressed by $[a_{1+}\ b_{1+}\ c_1,\ a_{2+}\ b_{2+}\ c_2,\ a_{3+}\ b_{3+}\ c_3]_{\boldsymbol{R}}$. Then, the *deformation gradient tensor* $\boldsymbol{F}_{\boldsymbol{D'\leftarrow D}}^{\boldsymbol{R}}$ can be obtained, as expressed by Eq. 2-21.

$$\boldsymbol{F}_{\boldsymbol{D'\leftarrow D}}^{\boldsymbol{R}} = \frac{\partial \boldsymbol{V_i'}}{\partial \boldsymbol{V_j}} = \begin{bmatrix} \frac{\partial V_i'}{\partial V_i} & \frac{\partial V_i'}{\partial V_j} & \frac{\partial V_i'}{\partial V_k} \\ \frac{\partial V_j'}{\partial V_i} & \frac{\partial V_j'}{\partial V_j} & \frac{\partial V_j'}{\partial V_k} \\ \frac{\partial V_k'}{\partial V_i} & \frac{\partial V_k'}{\partial V_j} & \frac{\partial V_k'}{\partial V_k} \end{bmatrix} = \begin{bmatrix} \frac{\partial(a_1+b_1+c_1)}{\partial(a)} & \frac{\partial(a_1+b_1+b_1)}{\partial(b)} & \frac{\partial(a_1+b_1+b_1)}{\partial(c)} \\ \frac{\partial(a_2+b_2+c_2)}{\partial(a)} & \frac{\partial(a_2+b_2+b_2)}{\partial(b)} & \frac{\partial(a_2+b_2+b_2)}{\partial(c)} \\ \frac{\partial(a_3+b_3+c_3)}{\partial(a)} & \frac{\partial(a_3+b_3+b_3)}{\partial(b)} & \frac{\partial(a_3+b_3+b_3)}{\partial(c)} \end{bmatrix} = \begin{bmatrix} \frac{a_1}{a} & \frac{b_1}{b} & \frac{c_1}{c} \\ \frac{a_2}{a} & \frac{b_2}{b} & \frac{c_2}{c} \\ \frac{a_3}{a} & \frac{b_3}{b} & \frac{c_3}{c} \end{bmatrix} \tag{2-21}$$

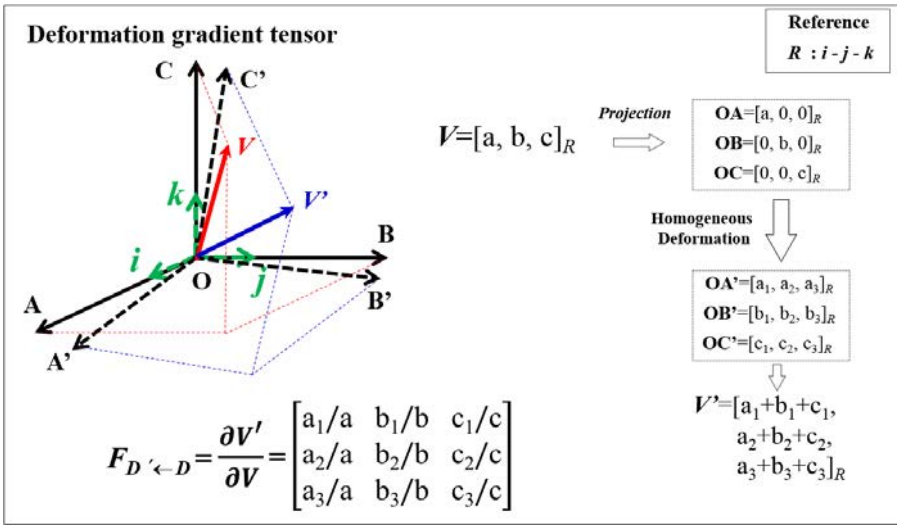

Fig. 2. 8 Definition of *deformation gradient tensor* $\boldsymbol{F}_{\boldsymbol{D'\leftarrow D}}^{\boldsymbol{R}}$. ***V*** represents an arbitrary undeformed vector, and the corresponding vector after deformation is ***V'***. Vectors ***OA***, ***OB*** and ***OC*** represent the resolved vectors of ***V*** along ***i***, ***j*** and ***k***, respectively. Their corresponding deformed vectors are indicated by ***OA'***, ***OB'*** and ***OC'***, respectively.

With the determined *deformation gradient tensor* $\boldsymbol{F}_{D'\leftarrow D}^{R}$, the deformed vector $[u'v'w']_{\boldsymbol{R}}$ can be calculated from its undeformed initial vector $[uvw]_{\boldsymbol{R}}$ with Eq. 2-22.

$$\begin{bmatrix} u' \\ v' \\ w' \end{bmatrix}_{\boldsymbol{R}} = \boldsymbol{F}_{D'\leftarrow D}^{R} \times \begin{bmatrix} u \\ v \\ w \end{bmatrix}_{\boldsymbol{R}} \tag{2-22}$$

The inverse of transpose (or the transpose of inverse) of $\boldsymbol{F}_{D'\leftarrow D}^{R}$, denoted $(\boldsymbol{F}_{D'\leftarrow D}^{R})^{-T}$, can realize the deformation for planes, as represented in Eq. 2-23, where $(hkl)_{\boldsymbol{R}}$ and $(h'k'l')_{\boldsymbol{R}}$ represent an arbitrary plane indices before and after deformation, respectively. The derivation is given in Appendix II.

$$\begin{bmatrix} h' \\ k' \\ l' \end{bmatrix}_{\boldsymbol{R}} = (\boldsymbol{F}_{D'\leftarrow D}^{R})^{-\mathrm{T}} \times \begin{bmatrix} h \\ k \\ l \end{bmatrix}_{\boldsymbol{R}} \tag{2-23}$$

Furthermore, if we consider ***OA*- *OB*- *OC*** and ***OA'*- *OB'*- *OC'*** as the coordinate systems, denoted as ***D*** and ***D'***, respectively, the *deformation gradient tensor* ($\boldsymbol{F}_{D'\leftarrow D}^{R}$) and *coordinate transformation matrices* ($\boldsymbol{M}^{R\rightarrow D'}$ and $\boldsymbol{M}^{R\rightarrow D}$) can be connected by Eq. 2-24.

$$\boldsymbol{F}_{D'\leftarrow D}^{R} = \frac{\partial V_i'}{\partial V_j} = \begin{bmatrix} \frac{a_1}{a} & \frac{b_1}{b} & \frac{c_1}{c} \\ \frac{a_2}{a} & \frac{b_2}{b} & \frac{c_2}{c} \\ \frac{a_3}{a} & \frac{b_3}{b} & \frac{c_3}{c} \end{bmatrix} = \boldsymbol{M}^{R\rightarrow D'} \times (\boldsymbol{M}^{R\rightarrow D})^{-1} \tag{2-24}$$

The change of reference for *deformation gradient tensor* can be realized by Eq. 2-25,

$$\boldsymbol{F}_{D'\leftarrow D}^{R_0} = \boldsymbol{M}^{R_0\rightarrow R} \times \boldsymbol{F}_{D'\leftarrow D}^{R} \times \boldsymbol{M}^{R\rightarrow R_0} \tag{2-25}$$

where $\boldsymbol{F}_{D'\leftarrow D}^{R_0}$ and $\boldsymbol{F}_{D'\leftarrow D}^{R}$ represent the same deformation but under different references ($\boldsymbol{R_0}$ and $\boldsymbol{R}$, respectively). $\boldsymbol{M}^{R_0\rightarrow R}$ and $\boldsymbol{M}^{R\rightarrow R_0}$ are the *coordinate transformation matrices* between these two references.

2.2.4 Predictions of twin relations

For continuous deformation of two adjacent domains ***R*** and ***R'***, as shown in Fig. 2. 9a, to keep their interface *MN* coherent after deformation, their corresponding *deformation gradient tensors* ***F*** and ***G*** must satisfy the so-called *kinematic compatibility condition* [56], *i.e.*

$$\boldsymbol{F} - \boldsymbol{G} = \boldsymbol{a} \otimes \hat{\boldsymbol{n}} \tag{2-26}$$

where $\hat{\boldsymbol{n}}$ represents the normal of interface *MN*, and $\boldsymbol{a} = (\boldsymbol{F} - \boldsymbol{G})\,\hat{\boldsymbol{n}}$. The martensitic transformation process, as illustrated in Fig. 2. 9b, generally belongs to this kind of deformation.

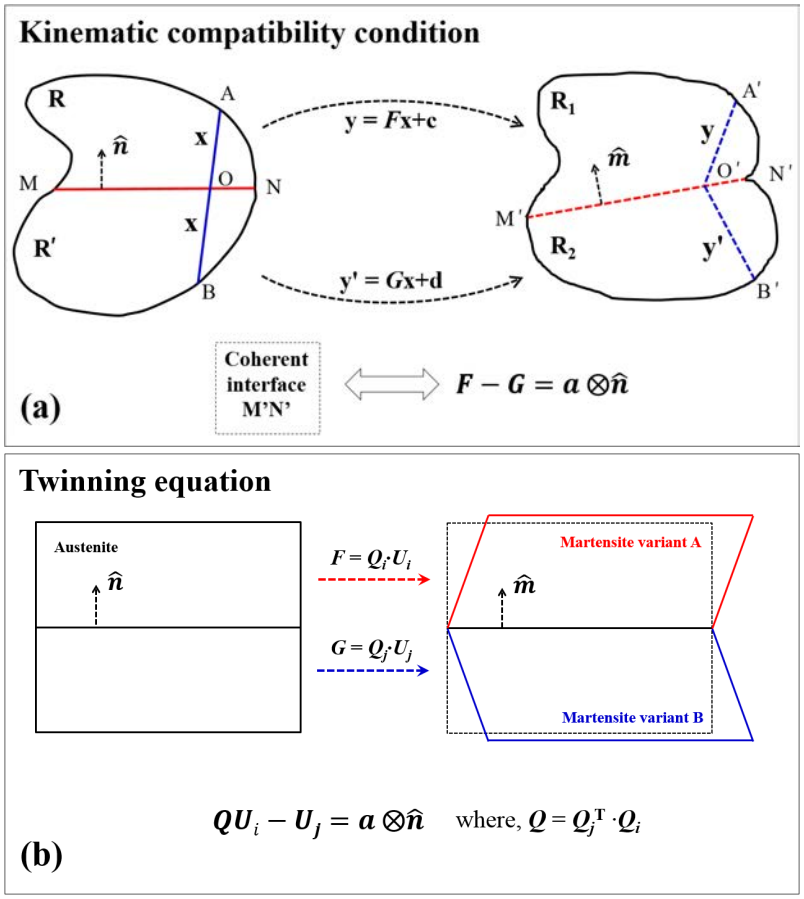

Fig. 2. 9 Illustration of the *kinematic compatibility condition* (a) and *twinning equation* (b).

With the consideration of the features of martensitic transformation, the so-called *twinning equation* can be deduced, as given in Eq. 2-27, where $\boldsymbol{U_i}$ and $\boldsymbol{U_j}$ represent the *transformation stretch tensors* of two arbitrary martensite variants during the structural transition and $\boldsymbol{Q}$ indicates the pure rotation to connect these two variants.

$$\boldsymbol{QU_i - U_j = a \otimes \hat{n}} \tag{2-27}$$

In the frame of Bain distortion model, with the crystal structure information of austenite and martensite, in combination with the crystal rotation symmetry of austenite, the *transformation stretch tensors* of different martensite variants can be obtained. Then, all possible twin relations can be predicted by solving *twinning equations* with different variant organizations. The detailed information is referred to Refs. [56, 233-235].

2.2.5 Twinning element determinations

For certain twin related crystals, their geometrical relation can be fully defined by their twinning elements, *i.e.* (1) K_1 - the twinning plane, the invariant (unrotated and undistorted) plane of simple shear; (2) η_1 - the twinning direction lying in K_1; (3) K_2 - the reciprocal or conjugate twinning plane, the second undistorted but rotated plane; (4) η_2 - the reciprocal or conjugate twinning direction lying in K_2; (5) P - the plane of shear; (6) γ - the magnitude of shear, as shown in Fig. 2. 10a. According to the rationality of Miller indices of K_1, K_2, η_1 and η_2 with respect to the parent lattice, twins are usually classified into three types: Type-I twin (K_1 and η_2 are rational), Type-II twin (K_2 and η_1 are rational) and compound twin (K_1, K_2, η_1 and η_2 are all rational).

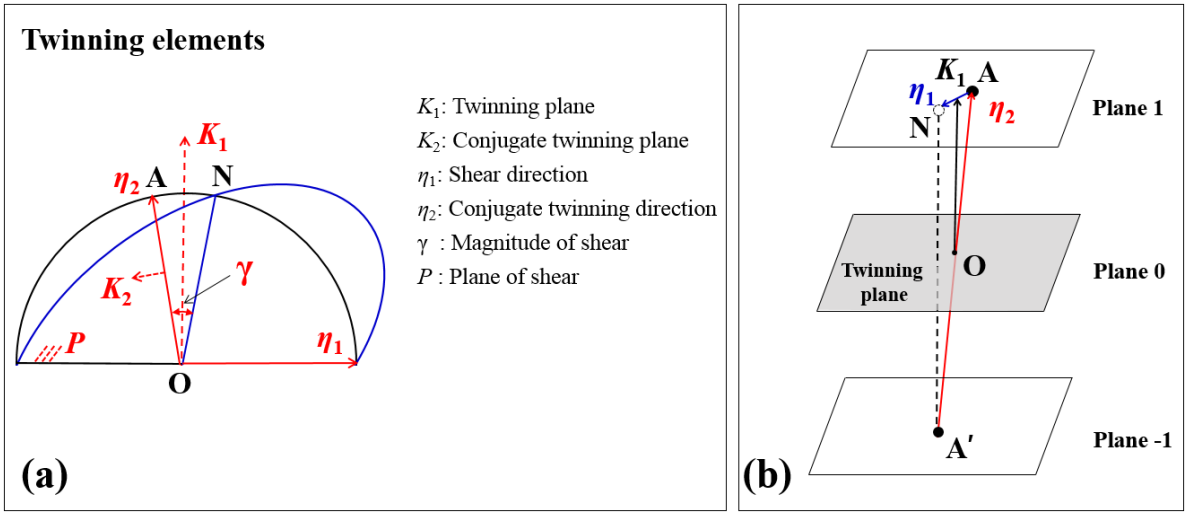

Fig. 2. 10 (a) Definition of twinning elements. (b) Illustration of the determination of twinning elements.

With the determined twinning plane K_1 (type-I and compound twins) or the shear direction η_1 (type-II twin), a direct and elegant method to determine twinning elements has been proposed by our research group. The basic idea is to first find the shortest (***AA'***) lattice vector (but not perpendicular to twinning plane) between -1 and 1 twinning planes (type-I or compound twins), as shown in Fig. 2. 10b. Under the criterion of minimum shear, it should be exactly the conjugate twinning direction η_2. Then, the complete twinning elements can be calculated based on the geometrical relations between various twinning elements. For type-II twin, the twinning elements can be determined in the reciprocal space with the same procedure. The details are described in Ref. [245].

2.2.6 Interface determinations by *indirect two-trace* method

Interface characterizations are important to materials, since both of mechanical and physical properties are closely related to their interface features. To determine the Miller indices of interfaces, an *indirect two-trace* method based on EBSD technique has been proposed by our group. Different from the traditional *two-trace* method where two perpendicular sample surfaces are needed, this method involves the preparation of only one sample surface. The determination process would be performed in two consecutive steps. First, the two independent and unparalleled traces (***AB*** and ***A'B'***) coming from crystallographically equivalent interfaces (***ABCD*** and ***A'B'C'D'***) and the crystallographic orientations of their adjacent crystals ($\boldsymbol{g_1}$, $\boldsymbol{g_2}$, $\boldsymbol{g_1}'$ and $\boldsymbol{g_2}'$), as shown in Fig. 2. 11, should be experimentally determined by SEM/ EBSD technique. Then, the interface indices can be calculated by coordinate transformation and vector cross production. The details are referred to Ref. [246].

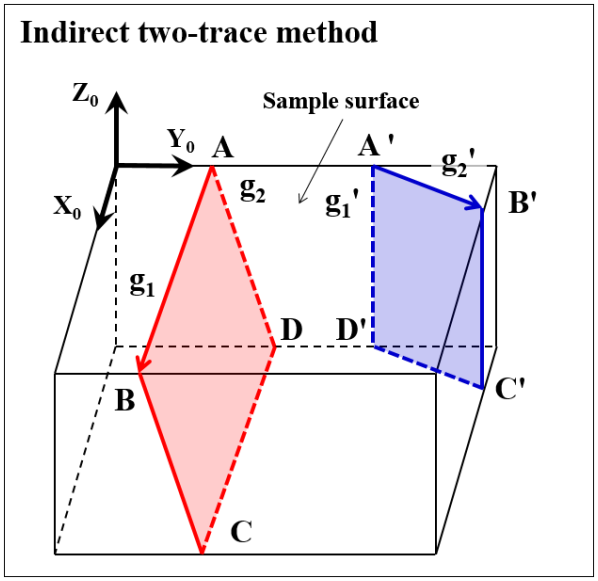

Fig. 2. 11 Illustration of indices determination for certain interface by *indirect two-trace* method. ***ABCD*** and ***A'B'C'D'*** represent two crystallographically equivalent interfaces but with differently oriented traces on the same sample surface. $\boldsymbol{g_1}$, $\boldsymbol{g_2}$, $\boldsymbol{g_1}'$ and $\boldsymbol{g_2}'$ represent the crystallographic orientations of the adjacent crystals by the two interfaces.

2.2.7 *Schmid factor* calculations

Schmid factor (*SF*) is a bridge to link the macroscopic external load with the microscopic stress resolved to certain slip, twinning/ detwinning or transformation system. It is generally used as a criterion to determine their activations. The definition of *SF* for detwinning systems that is the inverse process of twinning process is shown in Fig. 2. 12. If one twinning system is defined by K_1 and η_1, the detwinning system is thus K_1 and $-\eta_1$. It is worth emphasizing that the *SF* under the tension and compression loads are different. They should have the same value but the opposite signs.

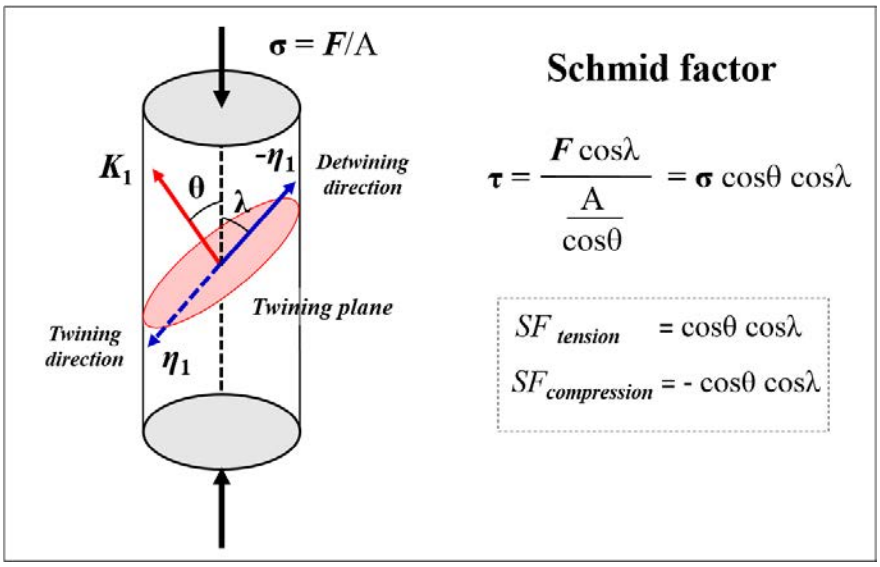

Fig. 2. 12 Illustration of *Schmid factor* (*SF*) calculation for detwinning system.

2.2.8 Magnetocaloric effect calculations

Magnetic entropy changes as a function of temperature and magnetic field can be numerically estimated using the *Maxwell relation* (Eq. 2-28) from the isothermal magnetization curves.

$$\Delta S_M (T, H) = \mu_0 \int_0^H \left(\frac{\partial M}{\partial T}\right)_H dH \qquad (2\text{-}28)$$

Magnetic hysteresis loss during magnetostructural transition can be evaluated by integrating the area between field-up and field-down magnetization curves, as illustrated in Fig. 2. 13.

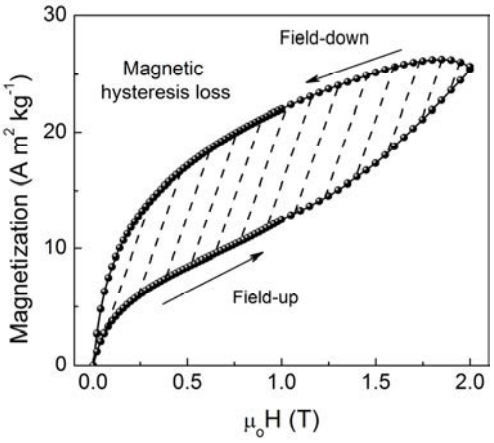

Fig. 2. 13 Magnetic hysteresis loss estimation based on field-up and field-down magnetization curves.

Chapter 3 Martensitic transformation temperature and crystal structure

In this chapter, first, the evolution of martensitic transformation temperature of $Ni_{50}Mn_{50-x}In_x$ ($0 \le x \le 25$) alloys was explored. Then, the crystal structure of austenite and various martensites (non-modulated and modulated) in these alloys were determined by means of Rietveld method with synchrotron and neutron powder diffraction techniques. For the modulated martensite, with the consideration of the possible aperiodicity of modulated structure, the crystal structure determination was carried out in the frame of superspace theory. With the accurately determined crystal structure information, its relation with the magnetic properties was discussed. Finally, in view of practical applications, such as EBSD and *ab-initio* calculation, a threefold layered superstructure model in the three-dimensional space was proposed to approximately describe the determined incommensurate 6M modulated structure.

3.1 Martensitic transformation temperatures

Fig. 3. 1 shows the evolution of the critical temperatures of martensitic transformation (M_s, M_f, A_s and A_f), detected by DSC measurements, for $Ni_{50}Mn_{50-x}In_x$ ($0 \le x \le 25$) alloys. It is seen that the martensitic transformation temperatures linearly decrease with the increase of In concentration. When $x < 15$, the martensitic transformation temperatures are above 298 K, and then the alloys should be in their martensite state at room temperature, as indicated in Fig. 3. 1. With the increase of In content, the transformation temperatures decrease and the alloys are in their austenite state. When $x > 15.5$, the martensitic transformation was not detected within the temperature range from 180 K to 800 K with DSC technique.

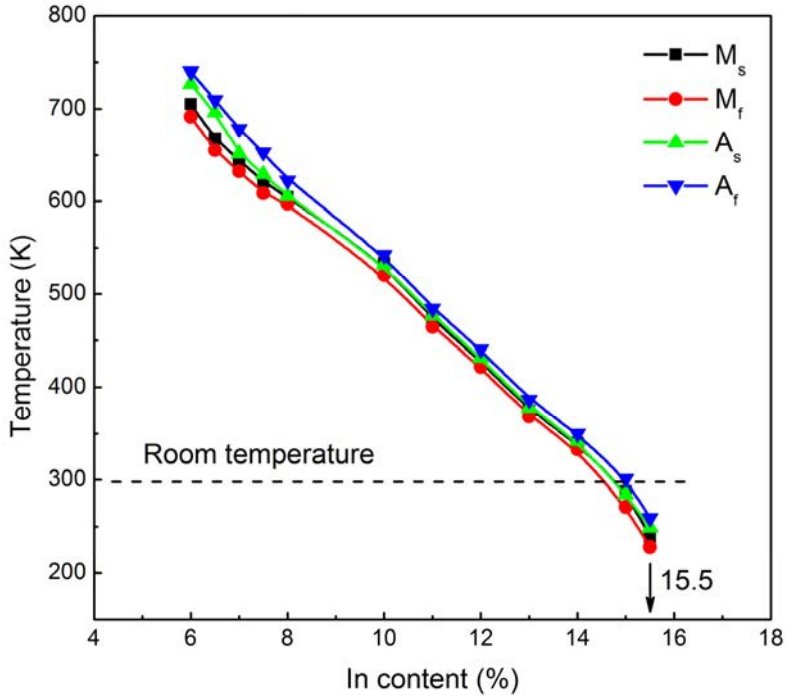

Fig. 3. 1 Evolution of the critical temperatures of the martensitic transformation for $Ni_{50}Mn_{50-x}In_x$ alloys ($0 \leq x \leq 25$). The start and finish temperatures of the forward and backward martensitic transformation are denoted as M_s, M_f, A_s and A_f, respectively.

3.2 Crystal structure

Fig. 3. 2 displays the X-ray diffraction patterns of $Ni_{50}Mn_{50-x}In_x$ ($0 \leq x \leq 25$) alloys at room temperature. It is seen that the $Ni_{50}Mn_{50-x}In_x$ alloys have a single non-modulated (NM) martensite when $x \leq 2$. With the increase of In concentration, the modulated martensite phase appears, as indicated by the black arrows in Fig. 3. 2a. The non-modulated and modulated phases coexist in the alloys with $4 \leq x \leq 10$. When $11 \leq x \leq 14$, the alloys possess a single modulated martensite state. For $Ni_{50}Mn_{35.25}In_{14.75}$ alloy, as shown in Fig. 3. 2c, it has the austenite and modulated martensite phases at room temperature. When $x \geq 15$, the alloys have a single austenite phase, as shown in Fig. 3. 2d. Furthermore, it is seen that the intensities of the satellite reflections of austenite, which represent structural ordering of alloys, are enhanced with the increase of In concentration, as indicated by the dashed box in Fig. 3. 2d.

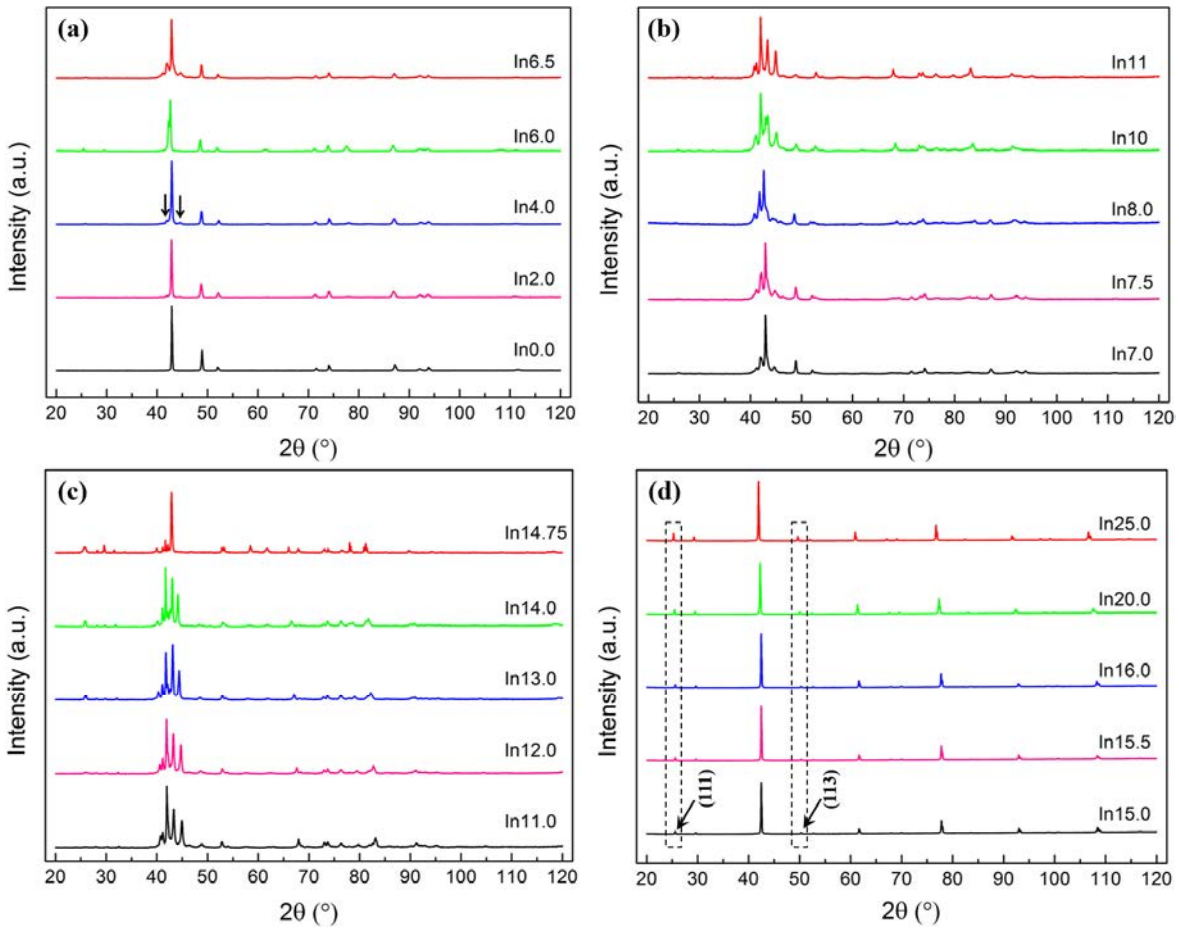

Fig. 3. 2 X-ray diffraction patterns of $Ni_{50}Mn_{50-x}In_x$ alloys ($0 \leq x \leq 25$) measured at room temperature.

3.2.1 Crystal structure determination of austenite

To accurately determine the crystal structure of austenite, a ternary Mn enriched alloy with nominal composition of $Ni_{50}Mn_{35}In_{15}$ that has austenite phase at room temperature (Fig. 3. 2), was selected. Firstly, the high-resolution powder neutron diffraction experiment was carried out to obtain high quality diffraction pattern. Then, the charge-flipping algorithm [237] and Rietveld full profile fitting approach [238] were employed to determine the statistical crystal structure data. Detailed site occupations of extra-Mn atoms, with respect to the case of the stoichiometric Ni_2MnIn alloy, were investigated by *ab-initio* calculations.

3.2.1.1 Crystal structure refinement

Fig. 3. 3 shows the powder neutron diffraction pattern of $Ni_{50}Mn_{35}In_{15}$ alloy, which is in the austenite state at room temperature. The crystal structure refinements, using the charge-flipping algorithm [237] and the Rietveld method [238], revealed that the austenitic phase possesses a cubic $L2_1$ structure with space group $Fm\bar{3}m$, as illustrated in Fig. 3. 4, being in agreement with that of the stoichiometric Ni_2MnX (X = Al, Ga and In) Heusler alloys [94]. The lattice parameter was determined to be 6.0062(7) Å. The independent atomic coordinates for the constituent elements were specified as follows: Ni atoms, *8c* (0.25, 0.25, 0.25); Mn atoms, *4a* (0, 0, 0); In (or extra-Mn) atoms, *4b* (0.5, 0.5, 0.5). Note that in the stoichiometric Ni_2MnIn case, the *4b* sites are fully occupied by In atoms. The unindexed two small peaks, as indicated by arrows in Fig. 3. 3, were confirmed resulting from the limited "surface martensite" [247, 248].

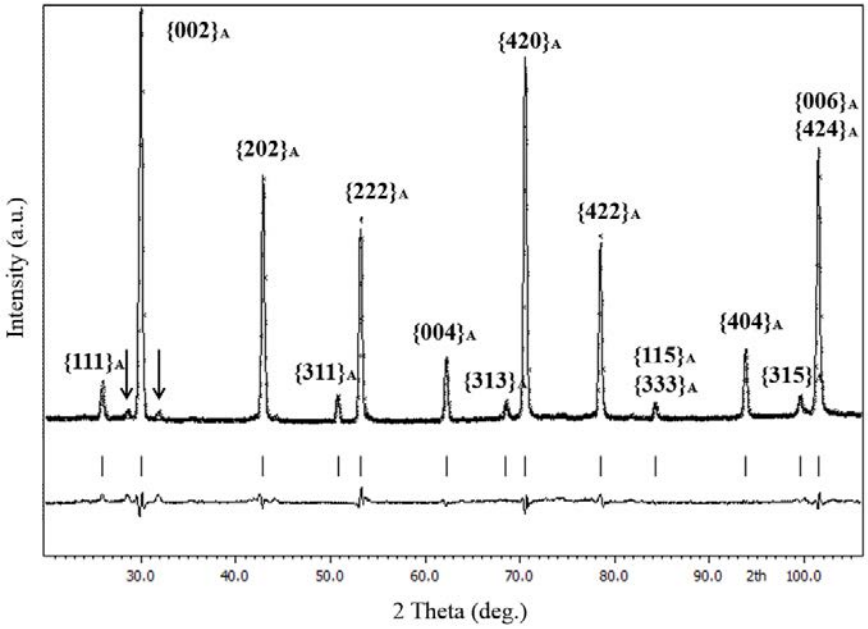

Fig. 3. 3 Powder neutron diffraction pattern (upper) of $Ni_{50}Mn_{35}In_{15}$ alloy at room temperature (dots - measured; lines - fitted with the Rietveld method), and difference (lower) between measured and calculated patterns.

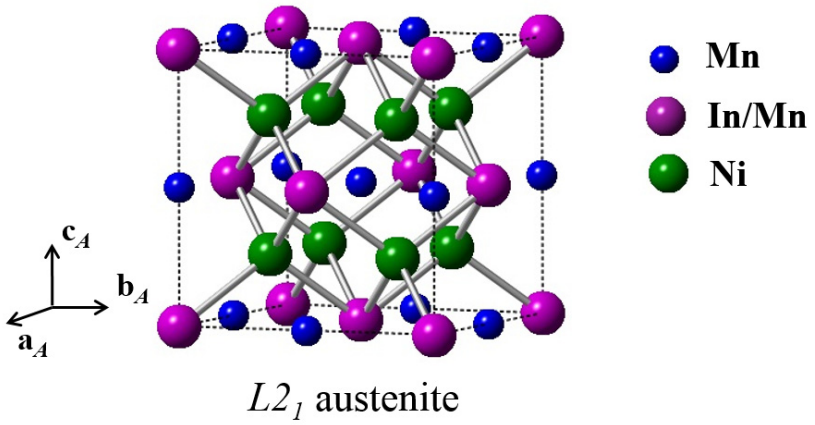

Fig. 3. 4 Illustration of cubic $L2_1$ crystal structure.

3.2.1.2 Atomic occupation investigations by *ab-initio* calculation

By means of the conventional Rietveld refinement [238, 249], one can determine statistical occupancy rates of In and extra-Mn atoms at the *4b* sites in the $L2_1$ structure, but not detailed occupational information of each species. Here, *ab-initio* calculations were performed to further figure out the distribution characteristics of extra-Mn atoms at the *4b* sites. In view of the composition of $Ni_{50}Mn_{35}In_{15}$ alloy, two unit cells containing two extra-Mn atoms were selected in the calculation scheme. There are three possible site combinations that represent different degrees of aggregation of extra-Mn atoms, as illustrated in Fig. 3. 5. The distances between the two extra-Mn atoms in the three settings are 4.22 Å (Fig. 3. 5a), 5.97 Å (Fig. 3. 5b) and 7.31 Å (Fig. 3. 5c), respectively. In each case, the formation energy E_F - taken as a measure to characterize the stability of a solid-state phase [250] - was calculated. Results show that the formation energies under the three settings were -368.51 meV, -478.64 meV and -571.71 meV, respectively. Obviously, the formation energy E_F decreases with the increase of the dispersion degree of the extra-Mn atoms, suggesting that the extra-Mn atoms tend to be dispersed from each other. Thus, it is reasonable to consider that Ni-Mn-In alloys with uniformly distributed extra-Mn atoms are more stable than those with aggregated extra-Mn atoms.

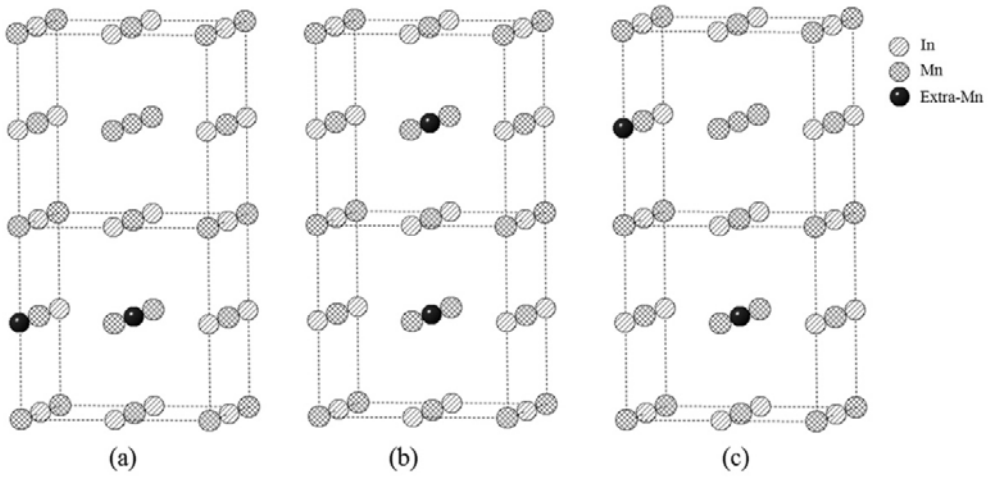

Fig. 3. 5 Three possible occupation settings for extra-Mn atoms and In atoms at the *4b* sites of the $L2_1$ structure. For a clearer illustration, Ni atoms are omitted.

3.2.2 Crystal structure determination of martensite

As shown in Fig. 3. 2, there are two kinds of martensites in $Ni_{50}Mn_{50-X}In_x$ alloys at room temperature, *i.e.* the non-modulated structure and modulated structure. For the former, the $Ni_{50}Mn_{50}$ alloy was selected to carry out the high resolution X-ray diffraction experiments and Rietveld refinements. For the latter, a ternary alloy with nominal composition of $Ni_{50}Mn_{36}In_{14}$ was selected. Synchrotron X-ray and neutron diffraction investigations were first carried out to obtain high quality diffraction patterns. With the consideration of the possible aperiodicity of modulated structures, the crystal structure determinations were performed in the frame of superspace theory by means of Rietveld method.

3.2.2.1 Crystal structure of non-modulated martensite

Fig. 3. 6 shows the powder XRD diffraction pattern of $Ni_{50}Mn_{50}$ alloy at room temperature and the pattern calculated by Rietveld refinement. Good match between the measured and the simulated diffraction patterns, R_p = 0.0448, R_{wp} = 0.0581, suggests that the non-modulated martensite has a $L1_0$ tetragonal structure with the space group of P4/mmm. The lattice parameters were refined to be a = 3.7319(2) Å, b = 3.7319(2) Å and c = 3.5211(3) Å. The independent atomic coordinates for the constituent elements were specified as follows: Ni atoms, 2e (0 0.5 0.5); Mn atoms, *1a* (0, 0, 0) and *1c* (0.5, 0.5, 0). The structural model is illustrated in Fig. 3. 7.

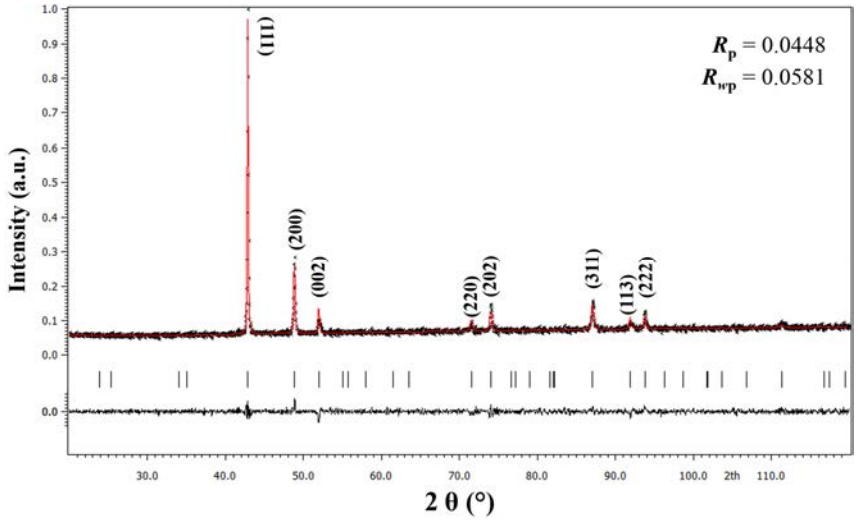

Fig. 3. 6 Powder X-ray diffraction pattern of $Ni_{50}Mn_{50}$ alloy at room temperature (dots), and the calculated pattern by Rietveld refinement (red line) and the difference between the measured and simulated pattern.

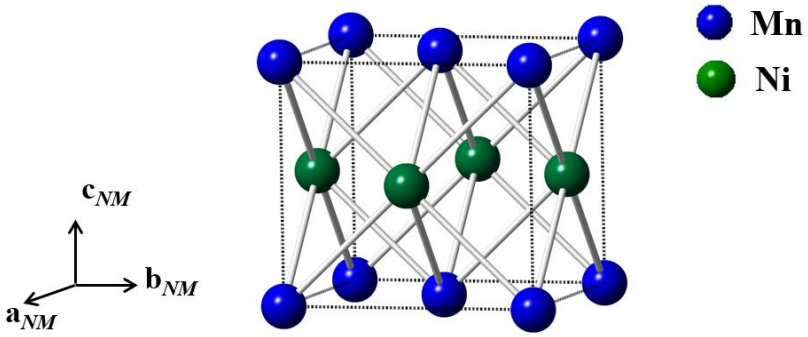

Fig. 3. 7 Illustration of the non-modulated $L1_0$ tetragonal structure of $Ni_{50}Mn_{50}$ alloy.

3.2.2.2 Crystal structure of modulated martensite

For the modulated martensite, in this work, the crystal structure determinations were performed on the following three consecutive steps. (1) The average crystal structure of modulated martensite, *i.e.* neglecting the structural modulation, was depicted by a unit cell in the three-dimensional space. The crystal system, lattice parameters and atomic positions of this average structure were obtained by analyzing the martensitic transformation-induced reflection separations in the frame of *Bain* lattice distortion and orientation inheritance, based on the collected neutron diffraction pattern of austenite and martensite and the determined crystal structure of austenite. (2)

The modulation wave vector, representing the periodicity of the modulation of atomic positions, was derived from the peak positions of satellite reflections that exist in the neutron diffraction pattern of martensite but cannot be indexed using the average structure. (3) The precise crystal structure of modulated martensite was refined with the synchrotron X-ray diffraction data, through the Rietveld refinement in the (3+1)-dimensional superspace using the JANA 2006 software [251]. In view of practical needs of experimental and theoretical studies, such as EBSD characterizations and *ab-initio* calculations, a three-dimensional superstructure model was set up to approximately describe the modulated crystal structure.

(1) Average crystal structure

The powder neutron diffraction pattern of the $Ni_{50}Mn_{36}In_{14}$ alloy collected at room temperature is displayed in black in Fig. 3. 8. As a reference, the diffraction pattern of the austenite phase of the $Ni_{50}Mn_{35}In_{15}$ alloy is also displayed in grey in Fig. 3. 8. It should be noted that for Ni-Mn-In Heusler alloys, the crystal structure of parent austenite is not sensitive to the alloy composition [44, 94]. In the present work, the compositions of the two experimental alloys are fairly close. Thus, one can reasonably ignore the composition difference between these two alloys and qualitatively approximate the diffraction pattern of the $Ni_{50}Mn_{36}In_{14}$ austenite with that of the $Ni_{50}Mn_{35}In_{15}$ austenite. As the martensitic transformation is a diffusionless phase transformation, the product martensite is generated by lattice distortion from its parent austenite. Such lattice deformation would give rise to the “symmetry breaking” of the crystal structure of the austenite and induce reflection separation or splitting. Accordingly, the crystal structure characteristics of the martensite could be deduced with the crystal structure of the austenite and the diffraction peak separations resulting from the structural transformation.

By comparing the diffraction patterns of austenite (in grey) and martensite (in black) shown in Fig. 3. 8, significant reflection splitting can be clearly detected around the $\{0\,0\,2\}_A$, $\{2\,0\,2\}_A$ and $\{2\,2\,2\}_A$ reflections of austenite. For the $\{0\,0\,2\}_A$ reflection of austenite, it splits into three martensite reflections I, II and III owing to the martensitic transformation. Notice that a set of three distinct $\{0\,0\,2\}_A$ planes can bring about only two corresponding diffraction peaks of martensite under the cubic to tetragonal or orthorhombic transformation. As a deduction, the crystal system of the average crystal structure of martensite could be either monoclinic or triclinic. For the $\{2\,0\,2\}_A$ and $\{2\,2\,2\}_A$ reflections of austenite, they split respectively into four (IV, V, VI and VII)

and two (VIII and IX) martensite reflections, rather than six and four reflections even if there are six distinct $\{2\,0\,2\}_A$ planes and four distinct $\{2\,2\,2\}_A$ planes in the cubic structure of austenite. Therefore, the crystal system of the martensite can only be monoclinic but not triclinic.

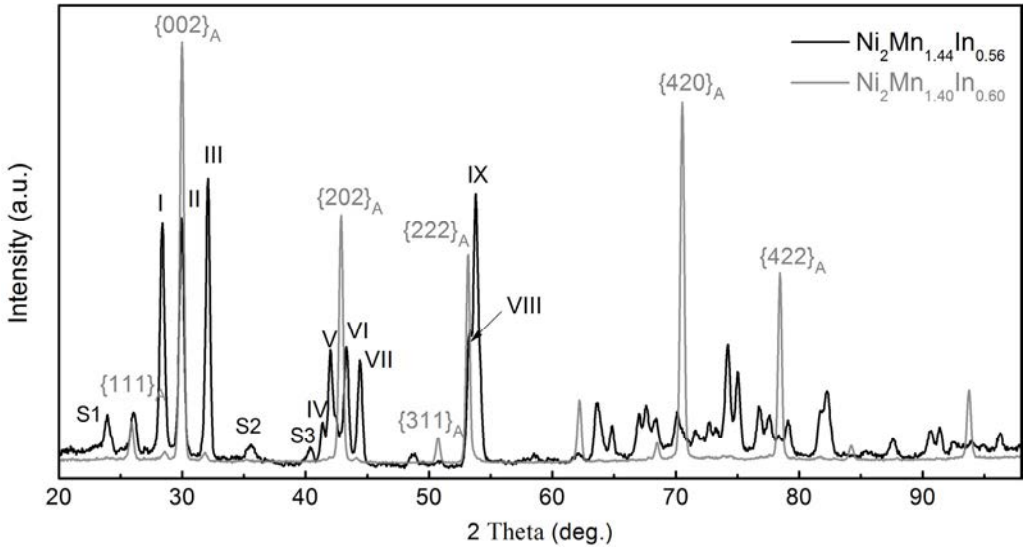

Fig. 3. 8 Powder neutron diffraction patterns of $Ni_{50}Mn_{35}In_{15}$ and $Ni_{50}Mn_{36}In_{14}$ alloys at room temperature.

Since the martensite refers to the monoclinic crystal system and the $\{0\,0\,2\}_A$ reflection splits into three reflections (I, II and III) rather than two reflections, the martensitic transformation may be ascribed to the so-called "cubic axes" [233] or "cubic-to-monoclinic II" transformation type [56], *i.e.* the twofold axis of monoclinic martensite is generated from the fourfold axes ($\langle 1\,0\,0\rangle_A$) rather than the twofold axes ($\langle 1\,1\,0\rangle_A$) of cubic austenite. Fig. 3. 9 schematically illustrates the correspondence between the lattice cells of cubic austenite and monoclinic martensite, uniquely defined in the frame of the Bain model. Here, a β_M-unique monoclinic right-handed coordinate system is chosen to represent the lattice cell of the average structure of the martensite that is in accordance with the reference setting normally used for monoclinic martensite in Heusler-type alloys [7, 31]. Under such a reference setting (Fig. 3. 9), the $[0\,0\,1]_A$ axis is contracted to be the b_M axis after martensitic transformation, whereas the $[1\,\bar{1}\,0]_A$ and $[1\,1\,0]_A$ axes are elongated and monoclinically distorted to be the c_M and a_M axes, respectively.

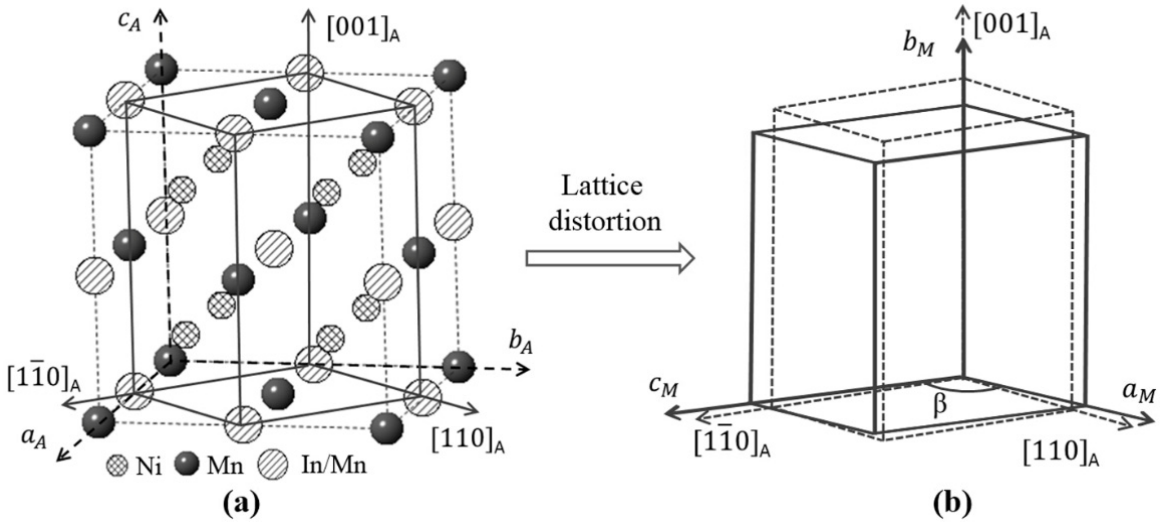

Fig. 3. 9 Illustration of lattice correspondence between (a) cubic $L2_1$ structure of austenite and (b) monoclinic structure of martensite, defined in the frame of the Bain model. The subscripts "*A*" and "*M*" denote austenite and martensite, respectively.

With the coordinate transformation under the above reference setting, the corresponding Bragg reflections of the monoclinic martensite can be predicted from the measured $\{0\,0\,2\}_A$, $\{2\,0\,2\}_A$ and $\{2\,2\,2\}_A$ reflections of the cubic austenite. The calculated results are summarized in Table 3. 1. By analyzing the peak-position correlations between the martensite and austenite phases and the lattice distortion characters of the martensitic transformation, some martensite reflections associated with the three reflection groups of the austenite could be unambiguously identified, as demonstrated below.

Table 3. 1 $\{0\,0\,2\}_A$, $\{2\,0\,2\}_A$ and $\{2\,2\,2\}_A$ reflections of austenite and corresponding reflections of martensite. The unambiguously identified reflections of martensite are highlighted in bold and italic.

Austenite reflections	$\{0\,0\,2\}_A$			$\{2\,0\,2\}_A$				$\{2\,2\,2\}_A$	
Corresponding martensite reflections	I	II	III	IV	V	VI	VII	VIII	IX
Martensite reflection planes	$(\bar{\boldsymbol{1}}\,\boldsymbol{0}\,\boldsymbol{1})_{\boldsymbol{M}}$	$(\boldsymbol{1}\,\boldsymbol{0}\,\boldsymbol{1})_{\boldsymbol{M}}$	$(\boldsymbol{0}\,\boldsymbol{2}\,\boldsymbol{0})_{\boldsymbol{M}}$	$(2\,0\,0)_M$	$(0\,0\,2)_M$	$(\bar{\boldsymbol{1}}\,\boldsymbol{2}\,\boldsymbol{1})_{\boldsymbol{M}}$ $(\boldsymbol{1}\,\boldsymbol{2}\,\bar{\boldsymbol{1}})_{\boldsymbol{M}}$	$(\boldsymbol{1}\,\boldsymbol{2}\,\boldsymbol{1})_{\boldsymbol{M}}$ $(\boldsymbol{1}\,\bar{\boldsymbol{2}}\,\boldsymbol{1})_{\boldsymbol{M}}$	$(2\,2\,0)_M$ $(2\,\bar{2}\,0)_M$	$(0\,2\,2)_M$ $(0\,2\,\bar{2})_M$

Let us consider first the case of the $\{0\,0\,2\}_A$ reflection of austenite. The corresponding I, II and III reflections of martensite are linked to the $(0\,2\,0)_M$, $(1\,0\,1)_M$ and $(\bar{1}\,0\,1)_M$ lattice planes. As mentioned above, the $[0\,0\,1]_A$ axis is contracted to be the $[0\,1\,0]_M$ axis during the austenite to martensite transformation. In consequence, the interplanar spacing of the $(0\,2\,0)_M$ plane should be smaller than that of the $\{0\,0\,2\}_A$ planes, indicating that the 2θ value for the $(0\,2\,0)_M$ peak is larger than that of the $\{0\,0\,2\}_A$ peak. Therefore, the martensite reflection III is univocally identified to be from the $(0\,2\,0)_M$ plane. For the other two martensite reflections (I and II), they can only be from the $(1\,0\,1)_M$ or $(\bar{1}\,0\,1)_M$ plane. Taking into account of the separation degree of reflection I and II from the corresponding $\{0\,0\,2\}_A$ peak, one may deduce that the monoclinic angle β_M of the martensite structure is not far from 90°. In fact, there exist two possibilities for β_M, *i.e.* $\beta_M > 90°$ or $\beta_M < 90°$, arising from an interchange of the a_M and c_M axes set for the monoclinic system. Here, the convention of $\beta_M > 90°$ (Fig. 3. 12b) is chosen to be in accordance with the traditional monoclinic cell setting for modulated martensite [25, 52, 208]. As the relative 2θ positions of the two reflections I and II (corresponding to the same $\{0\,0\,2\}_A$) are governed by the value of $\cos(\beta_M)$ (< 0), they can be uniquely indexed as the $(\bar{1}\,0\,1)_M$ and $(1\,0\,1)_M$ reflections, respectively.

For the case of the $\{2\,0\,2\}_A$ refection of austenite, the corresponding reflections IV, V, VI and VII of martensite are associated with the $(2\,0\,0)_M$, $(0\,0\,2)_M$, $\{\bar{1}\,2\,1\}_M$ ($(\bar{1}\,2\,1)_M$ and $(1\,2\,\bar{1})_M$) and $\{1\,2\,1\}_M$ ($(1\,2\,1)_M$ and $(1\,\bar{2}\,1)_M$) planes. During the structural transformation, the $[1\,1\,0]_A$ and $[1\,\bar{1}\,0]_A$ are elongated and monoclinically distorted into the a_M and c_M axes, respectively (Fig. 3. 9a).

Both the $(2\,0\,0)_M$ and $(0\,0\,2)_M$ planes have larger interplanar spacing than that of the $\{2\,0\,2\}_A$ planes. Therefore, the two reflections IV and V in Fig. 3. 8 should be from the $(2\,0\,0)_M$ and $(0\,0\,2)_M$ planes. However, it is not possible to make a one-to-one correspondence between them, since the relative 2θ positions of the reflections IV and V depend on the relative values of the a_M and c_M that are not yet known. With the method of exclusion, the other two reflections VI and VII can only be from the $\{\bar{1}\,2\,1\}_M$ and $\{1\,2\,1\}_M$ planes. One may further deduce that the reflection VI corresponds to the $\{\bar{1}\,2\,1\}_M$ planes and the reflection VII to the $\{1\,2\,1\}_M$ planes, since their relative 2θ positions are just dependent on the value of $\cos(\beta_M)$ (< 0).

As for the case of the $\{2\,2\,2\}_A$ reflection of austenite, it splits into two very close reflections VIII and IX after the martensitic transformation. These two martensite reflections could be from the $\{2\,2\,0\}_M$ ($(2\,2\,0)_M$ and $(2\,\bar{2}\,0)_M$) and $\{0\,2\,2\}_M$ ($(0\,2\,2)_M$ and $(0\,2\,\bar{2})_M$) planes. This indicates that the lattice parameters a_M and c_M are not equal but very close to each other. Again, a univocal correlation between the two martensite reflections and the corresponding lattice planes cannot be obtained, since their relative 2θ positions also depend on the relative values of the a_M and c_M.

With the peak position data of the five unambiguously identified martensite reflections, the lattice parameters of the average crystal structure were estimated to be a_M = 4.38 Å, b_M = 5.62 Å, c_M = 4.33 Å, and β_M = 93.03°. The rest reflections of the martensite, associated with the austenite reflections $\{0\,0\,2\}_A$, $\{2\,0\,2\}_A$ and $\{2\,2\,2\}_A$, can then be fully indexed, as display in Table 3. 1. Moreover, the atomic positions of the constituent Ni, Mn and In elements are attainable using the determined lattice cell of the average structure. One may consider that the austenite to martensite transformation involves a simultaneous and cooperative movement of atoms with distance less than one interatomic spacing. Thus, the atomic coordinates of the three constituent elements in the average structure of martensite can be roughly derived from those in the parent austenite by coordinate transformation under the reference setting defined in Fig. 3. 9. Based on the characteristics of the atomic arrangement of the austenite and the symmetry of the average structure of the martensite, the average structure can be appropriately described with space group *I2/m*. At this stage, the average structure of the martensite has been fully solved in the three-dimensional space.

(2) Modulation wave vector

By further examining the neutron diffraction spectrum of the $Ni_{50}Mn_{36}In_{14}$ martensite, it is found that some minor peaks, as marked by S_1, S_2 and S_3 in Fig. 3. 8, cannot be indexed with the above average structure model. Those minor peaks should belong to the so-called "satellite" reflections generated by structural modulation. Notably, the peak intensity of the $(2\ 0\ 0)_M$ plane (reflection IV) is much lower than that of the $(0\ 0\ 2)_M$ plane (reflection V) in Fig. 3. 8, in contrast to the non-modulation case where these two reflections should be comparable in intensity. This indicates that the periodicity of the $(2\ 0\ 0)_M$ planes is destroyed mainly by the atomic modulation. Therefore, the $[1\ 0\ 0]_M$ direction should be one of the principal modulation directions in the direct space. Indeed, such a deduction is in accordance with the structural modulation features found in many shape memory alloys, *i.e.* the atomic modulation is mainly associated with the periodical shuffling of the $(0\ 0\ 1)_M$ atomic layers along the $[1\ 0\ 0]_M$ direction [2, 94, 203, 205].

In order to quantitatively analyze the structural modulation of the $Ni_{50}Mn_{36}In_{14}$ martensite, a modulation wave vector $\boldsymbol{q}$ is defined in the frame of the (3+1)-dimensional superspace model [199, 200], where "3" represents the three-dimensional space and "1" stands for an extra dimension to build the superspace. Under this model, all Bragg reflections ($\boldsymbol{H}$) can be indexed with a set of four integers ($h\ k\ l\ m$) as follows:

$$\boldsymbol{H} = h\,\boldsymbol{a}^* + k\,\boldsymbol{b}^* + l\,\boldsymbol{c}^* + m\,\boldsymbol{q} \tag{3-1}$$

$$\boldsymbol{q} = k_1\,\boldsymbol{a}^* + k_2\,\boldsymbol{b}^* + k_3\,\boldsymbol{c}^* \tag{3-2}$$

where $\boldsymbol{a}^*$, $\boldsymbol{b}^*$ and $\boldsymbol{c}^*$ are the basis vectors of the reciprocal lattice of the average crystal structure. The indices ($h\ k\ l\ 0$) and ($h\ k\ l\ m$) represent the main reflections and the $|m|$ ($m \neq 0$) order satellite reflections, respectively. In view of the above-mentioned atomic modulation feature, that is mainly associated with $(0\ 0\ 1)_M$ atomic layers, the parameters k_1 and k_2 are supposed to equal zero. Then, the expression for $\boldsymbol{q}$ can be written as:

$$\boldsymbol{q} = k_3\,\boldsymbol{c}^* \tag{3-3}$$

With Eqs. 3-1 and 3-3, the interplanar spacing d_{hklm} for both main reflections and satellite reflections from the monoclinic modulated martensite can be derived as:

$$d_{hklm} = \{h^2\boldsymbol{a}^{*2} + k^2\boldsymbol{b}^{*2} + (l + m\,k_3)^2\boldsymbol{c}^{*2} + 2h\,(l + m\,k_3)\,\boldsymbol{a}^*\boldsymbol{c}^*\cos\beta^*\}^{-1/2} \tag{3-4}$$

Thus, $\boldsymbol{q}$ can be estimated with Eq. 3-4 using the peak positions of some satellite reflections. Considering that in Fig. 3. 8, the satellite reflections S_1 and S_2 are located close to the main

reflections I, II or III, they could be generated by those intense ones through structural modulation. As the atomic shuffling is not remarkable for the $(0\ 2\ 0)_M$ plane, S_1 and S_2 should be resulted from either the $(\bar{1}\ 0\ 1)_M$ reflection (peak I) or the $(1\ 0\ 1)_M$ reflection (peak II). Then, a total of four k_3 values could be obtained according to Eq. 3-4, if assuming that S_1 and S_2 are the -1 and +1 order satellite reflections of the main reflection $(\bar{1}\ 0\ 1)_M$ or $(1\ 0\ 1)_M$. The calculated k_3 values and indices of the S_1 and S_2 satellite reflections are given in Table 3. 2.

Table 3. 2 Calculated k_3 values and satellite reflection indices for S_1 and S_2.

		Satellite reflections	k_3	Satellite reflections	k_3
Peaks	S_1	$(\mathbf{\bar{1}\ 0\ 1\ \bar{1}})_M$	0.340	$(1\ 0\ 1\ \bar{1})_M$	0.457
	S_2	$(\bar{1}\ 0\ 1\ 1)_M$	0.440	$(\mathbf{1\ 0\ 1\ 1})_M$	0.341

Among the calculated k_3 values, two of them (0.340 and 0.341) are found to be almost the same, having significant discrepancy with the other two (0.457 and 0.440). It means that a common k_3 value (~0.341) may be chosen to define the real modulation wave vector, and hence to identify the exact indices for the S_1 and S_2 satellite reflections (marked in bold in Table 3. 2). The validity of this common value has been further verified using the S_3 satellite reflection, on assuming that it was generated from the main reflections IV, V, VI and VII around the $\{2\ 0\ 2\}_A$ peak. With the chosen k_3 value, the S_3 satellite reflection can be well indexed as the $(\bar{1}\ 2\ 1\ \bar{1})_M$ reflection. Hereto, the modulation wave vector of the martensite structure has been unambiguously determined.

(3) Incommensurate crystal structure

In the superspace theory [199, 200], each general atomic position is given by the atomic position $\bar{\boldsymbol{x}}^{\boldsymbol{\mu}}$ in the average crystal structure plus the deviation specified by a modulation function $\boldsymbol{u}^{\boldsymbol{\mu}}(\bar{x}_4)$, *i.e.*:

$$\boldsymbol{x}^{\boldsymbol{\mu}} = \bar{\boldsymbol{x}}^{\boldsymbol{\mu}} + \boldsymbol{u}^{\boldsymbol{\mu}}(\bar{x}_4) \tag{3-5}$$

$$\bar{\boldsymbol{x}}^{\boldsymbol{\mu}} = \boldsymbol{L} + \boldsymbol{x}_{\boldsymbol{\mu}}^{\boldsymbol{0}} \tag{3-6}$$

$$\bar{x}_4 = \boldsymbol{q}\ \bar{\boldsymbol{x}}^{\mu} + t \tag{3-7}$$

where $\boldsymbol{x}_{\boldsymbol{\mu}}^{\boldsymbol{0}}$ indicates the atomic coordinate of an independent atom μ in the unit cell of the average structure, $\boldsymbol{L}$ represents the lattice translation vector in the average structure, $\bar{x}_4$ defines the fourth coordinate in the (3+1)-dimensional superspace, and t is the phase factor. In view of the characteristics of the displacive atomic shuffling in the modulated martensite, the displacements of atomic layers can be simulated using a harmonic wave-like function, expanded in Fourier series as a function of $\bar{x}_4$:

$$\boldsymbol{u}^{\boldsymbol{\mu}}(\bar{x}_4) = \sum_{n=1}^{\infty} A_n^{\mu} \sin(2\pi n \bar{x}_4) + B_n^{\mu} \cos(2\pi n \bar{x}_4) \tag{3-8}$$

where A_n^{μ} and B_n^{μ} represent the amplitudes of the sinusoidal and cosinusoidal parts of the modulation wave function, respectively.

According to the space group of the average structure (*I2/m*) and the directional characteristics of the modulation wave vector (mainly along $\boldsymbol{c}^*$ direction), the superspace group *I2/m*($\alpha 0 \gamma$)*00* [199, 200] is considered as a good candidate to describe the symmetry of this modulated structure in the (3+1)-dimensional space. Thus, only the amplitude coefficients $A_n^{\mu}(x)$, $A_n^{\mu}(z)$ and $B_n^{\mu}(y)$ are needed to be refined, while the other coefficients $A_n^{\mu}(y)$, $B_n^{\mu}(x)$ and $B_n^{\mu}(z)$ are all equal to zero due to the symmetry restrictions of the superspace group. As previously mentioned, the structural modulation is mainly related to the shuffling of the $(0\,0\,1)_M$ atomic layers along the $[1\,0\,0]_M$ direction. Therefore, it is reasonable to assume that the *y* components $B_n^{\mu}(y)$ of the modulation wave function are zero for all atomic sites. Moreover, one may further assume that the *x* and *z* components $A_n^{\mu}(x)$ and $A_n^{\mu}(z)$ possess the same value for all atomic sites, since the three constituent elements Ni, Mn and Ga have similar shuffling behavior. These assumptions have proven to be realistic for the determination of modulated structures in Ni-Mn-Ga and Ni-Fe-Ga alloys [205, 210].

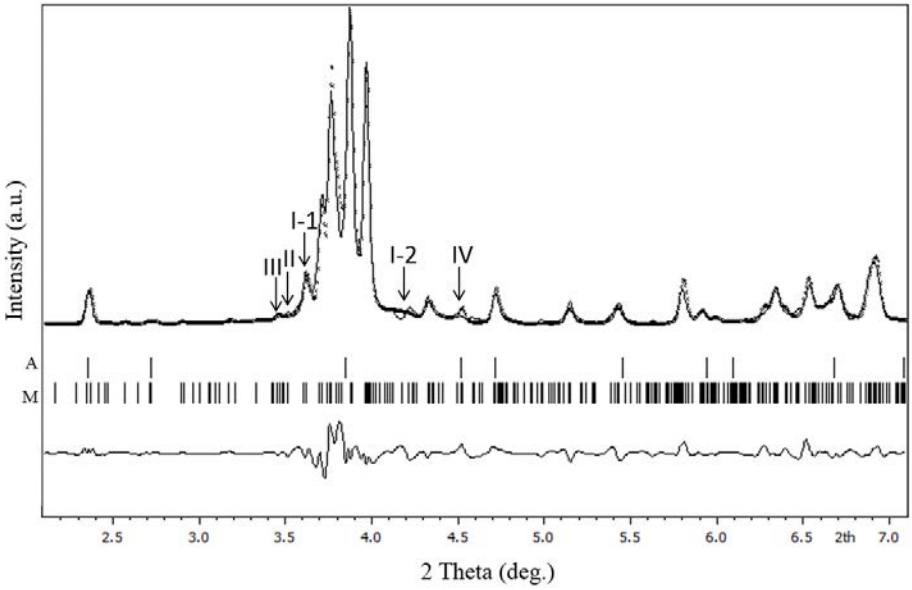

Fig. 3. 10 High-energy synchrotron XRD spectrum (upper) of $Ni_{50}Mn_{36}In_{14}$ alloy at room temperature (dots – measured; lines – fitted with the Rietveld refinement), and difference (lower) between measured and calculated spectra. The vertical arrows I-1, I-2, II and III indicate the $(\bar{1}\ 2\ 1\ \bar{1})_M$, $(\bar{1}\ 2\ 1\ 1)_M$, $(\bar{1}\ 2\ 1\ \bar{2})_M$ and $(\bar{1}\ 2\ 1\ \bar{3})_M$ satellite peaks of martensite, respectively, whereas the vertical arrow IV indicates the $\{3\ 1\ 1\}_A$ reflection of austenite.

Generally speaking, it is more appropriate to accurately determine the crystal structure of materials with complex magnetic structure using XRD data rather than neutron diffraction data. This is because XRD data contain merely crystal structure information, whereas neutron diffraction data include both nuclear and magnetic structure information. In order to obtain more details about the weak satellite reflections of the modulated martensite, the high-energy synchrotron X-ray diffraction was performed at room temperature for the $Ni_{50}Mn_{36}In_{14}$ alloy. The first-, second- and third-order satellites of the $(\bar{1}\ 2\ 1)_M$ reflection were detected, as indicated by arrows I, II and III in Fig. 3. 10. Here, the series expansion up to $n = 3$ in Eq. 3-8 is chosen to simulate the structural modulation in the Rietveld refinement. Furthermore, the effect of preferred orientation of the $(\bar{1}\ 2\ 1)_M$ reflection, resulting from the particular platelet-like microstructure of the martensitic phase [2], is approached with a March-Dollase function [252]; the atomic displacement parameters (ADP) are considered as isotropic.

Based on the above assumptions, the crystal structure of the $Ni_{50}Mn_{36}In_{14}$ modulated martensite was refined by the Rietveld method in the frame of the (3+1)-dimensional superspace

theory using the software package JANA 2006 [251]. Firstly, the modulation wave vector $\boldsymbol{q}$ was refined. Due to the symmetry of the superspace group *I2/m*(*α*0*γ*)*00*, the k_2 value should be zero. The refined modulation wave vector was given as $\boldsymbol{q} = -0.0046\,\boldsymbol{a}^* + 0.3437\,\boldsymbol{c}^*$. Since the k_1 (0.0046) is very close to zero, the first term can be neglected. This is in close agreement with the above assumption for the modulation wave vector. The output crystal structure data after the final convergence of the structural refinement are summarized in Table 3. 3 and Table 3. 4. It turns out the refinement reaches good agreement factors R_{wF}, R_p and R_{wp} [249].

Table 3. 3 Refinement details and resultant crystal structure data of $Ni_{50}Mn_{36}In_{14}$ martensite.

Radiation type	Synchrotron X-ray
Criterion for observed reflections	I > 3σ(I)
Superspace group	*I2/m*(*α*0*γ*)*00*
Modulation wave vector $\boldsymbol{q}$	0.3437(5) $\boldsymbol{c}$*
a (Å)	4.3919(4)
b (Å)	5.6202(1)
c (Å)	4.3315(7)
β (°)	93.044(1)
Volume (Å^3)	106.8
Z	2
Calculated density (g/cm^3)	8.109(4)
Calculated formula	$Ni_{50}Mn_{36}In_{14}$
Agreement factors	
- R_{wF} (main reflections)	0.0621
- R_{wF} (first-order satellite reflections)	0.0702
- R_{wF} (second-order satellite reflections)	0.0598
- R_{wF} (third-order satellite reflections)	0.0841
- *χ2*	1.66
- R_p/ R_{wp}	0.0755/ 0.1012

Table 3. 4 Atomic position (*x*, *y*, *z*), site occupancy factor (*s.o.f.*), atomic displacement parameter (U_{iso}) and amplitude (A_i) of modulation wave function of $Ni_{50}Mn_{36}In_{14}$ martensite.

Label	Atom	Wyckoff position		*x*	*y*	*z*	*s.o.f.*	U_{iso}
Mn	Mn	*2a*		0	0	0	1	0.0125(3)
In	In	*2d*		0	0.5	0	0.56	0.0115(9)
Extra-Mn	Mn	*2d*		0	0.5	0	0.44	0.0115(9)
Ni	Ni	*4h*		0.5	0.25	0	1	0.0166(7)
			A_1	0.0872(8)		-0.0009(1)		
			A_2	0.0395(8)		0.0030(8)		
			A_3	0.0238(2)		-0.0008(2)		

Apart from the good overall agreement, there are two notable local discrepancies between the measured and calculated patterns. First, one small reflection peak in Fig. 3. 10 is not recognized by the present structure of martensite. Further examination has revealed that this reflection is associated with the $\{3\,1\,1\}_A$ plane of austenite, though the martensitic transformation temperatures are significantly higher than room temperature. Very recently, a similar result was reported on $Ni_{46}Mn_{43}In_{41}$ alloy, where the retained austenite was still detected at 75 K that is far below its martensitic transformation temperature [52]. In the present work, a small amount of retained austenite, distributed in the form of island-chains, was evidenced along the boundaries of martensite platelets in the bulk $Ni_{50}Mn_{36}In_{14}$ alloy at room temperature (Fig. 4. 2c). Second, there exist obvious mismatches for the first-order satellites of the $\{\bar{1}\,2\,1\}_M$ reflection (peak I-1 and I-2 in Fig. 3. 10), especially for the I-2 satellite. This should be due to the anisotropic broadening of satellite reflections, which is commonly observed in platelets-like martensite microstructures. For instance, the broadening of the satellite reflections of the $\{\bar{1}\,2\,1\}_M$ planes was detected in the incommensurate 7M martensite of Ni-Mn-Ga alloys [205], where the $(\bar{1}\,2\,1)_M$ plane represents the inter-platelet interface plane. Further microstructure observation has confirmed that the martensitic phase in the present alloy does possess a platelet-like microstructure and the platelet interface plane refers to the $\{\bar{1}\,2\,1\}_M$ planes (This will be further discussed in Chapter 4, Section 4.2). As the

retained austenite is distributed in an island-chain form along the boundaries of martensite platelets, the distortion degree of the $\{\bar{1}\,2\,1\}_M$ planes would be further enhanced.

(4) Structure verification

For the above-determined crystal structure of the modulated martensite, it is meaningful to further verify its rationality and explore some structure-dependent magnetic properties. Fig. 3. 11 presents a two-dimensional section of the Fourier electron density map (x_2 = 0.25 and x_3 = 0.50) and the curve of the atomic modulation function (red solid lines). It can be seen that the atomic modulation function is in good accordance with the electron density map. The deviation of the modulated structure from its average structure can be estimated by comparing the atomic modulation function curve with the average atomic positions outlined by the black dashed line in Fig. 3. 11. Clearly, the atomic modulation shows a "zig-zag chain" rather than a perfect "sinusoidal wave". Such characteristics have also been revealed in various modulated martensite with different constituent elements [201, 205, 210]. Moreover, the interatomic distances between different atoms in this modulated structure were investigated. The typical atomic bond lengths are in agreement with those in the similar type of intermetallic compounds [253]. The details of the interatomic distances in this modulated structure are summarized in Table 3. 5.

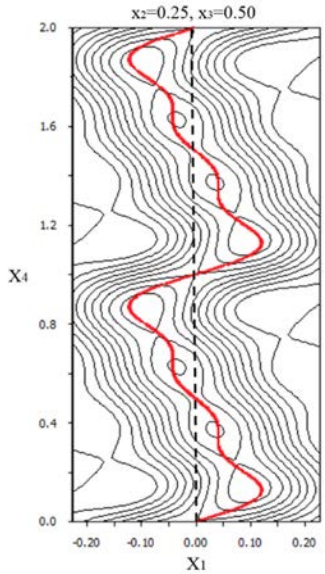

Fig. 3. 11 X_1-X_4 section of Fourier map representing a two-dimensional electron density distribution for x_2 = 0.25 and x_3 = 0.5. The atomic positions in the average structure and the modulation wave function are depicted with the black dash line and the red solid curved line, respectively. Two periods are drawn along the X_4 for a better representation.

Table 3. 5 Selected interatomic distances in incommensurate 6M modulated structure of $Ni_{50}Mn_{36}In_{14}$ martensite.

Atoms	Distance in average structure (Å)	Average distance (Å)	Minimum distance (Å)	Maximum distance (Å)
Mn - Mn	4.1153(1)	4.131(1)	3.933(1)	4.693(2)
	4.2344(1)	4.247(2)	3.82(3)	4.44(2)
Mn - In	3.0055(1)	3.020(2)	2.750(2)	3.76(2)
	3.1666(1)	3.18(2)	2.58(4)	3.43(3)
Mn - Ni	2.5826(1)	2.61(2)	2.57(2)	2.75(3)
	2.6099(1)	2.610(3)	—	—
In - In	4.1153(1)	4.131(1)	3.933(1)	4.693(2)
	4.2344(1)	4.247(2)	3.82(3)	4.44(2)
In - Ni	2.5826(1)	2.61(2)	2.57(2)	2.75(3)
	2.6099(1)	2.610(3)	—	—
Ni - Ni	3.0055(1)	3.015(2)	2.751(2)	3.76(2)
	4.1153(1)	4.131(1)	3.933(1)	4.693(2)
	4.2344(1)	4.247(2)	3.82(3)	4.44(2)

As the magnetic coupling interactions are closely related to the distances of magnetic atoms, insight into these factors is essential to the understanding of the specific magnetic properties of Ni-Mn-In alloys. By a variety of experimental studies and *ab-initio* calculations, it has been shown that the magnetic interactions in Mn-rich Ni_2MnX Heusler alloys are mainly associated with two types, Mn(*2a*) - Mn(*2a*) (ferromagnetic coupling) and Mn(*2a*) - Mn(*2d*) (ferromagnetic or antiferromagnetic coupling) [250, 254]. For Ni-Mn-In alloys, a weak-magnetic martensite phase is considered as the prerequisite for inducing inverse martensitic transformation by magnetic field. To reveal the weak-magnetism of the present modulated martensite, the atomic distances between the Mn(*2a*) - Mn(*2d*) atoms were further investigated.

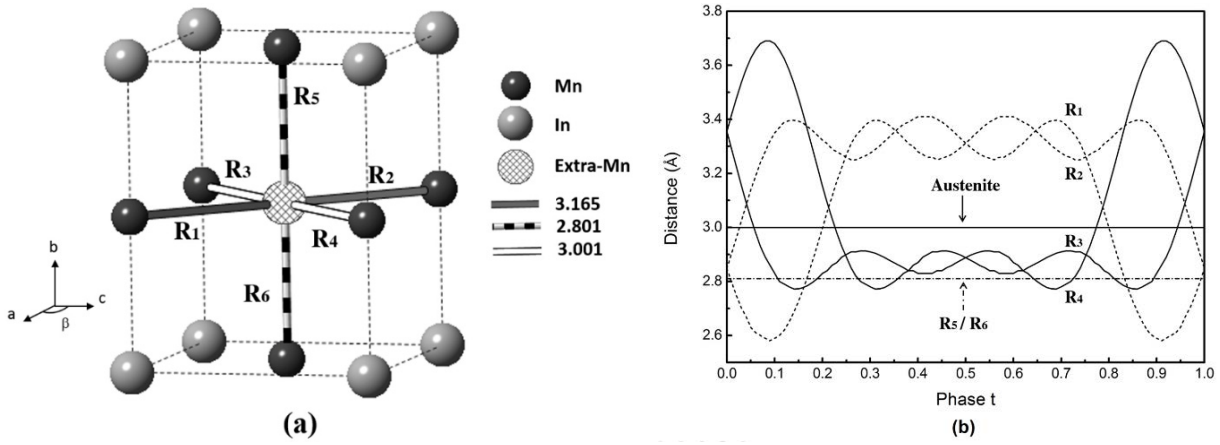

Fig. 3. 12 Schematic illustration of *2a*-Mn and *2d*-extra-Mn positions in the average structure. (b) Plots of the distances between Mn and extra-Mn atoms in the modulated structure as a function of the phase factor *t* in one modulation period. For reference, the distances between Mn and extra-Mn atoms in austenite are also displayed.

Fig. 3. 12a shows the atomic positions of the *2a*-Mn atoms and the *2d*-extra-Mn atoms in the average structure of the martensite. Around one extra-Mn atom, there are six first-neighbor Mn atoms with distances R_i (i = 1~6) to the extra-Mn atom. The evolutions of these atomic distances with atomic modulation are plotted in Fig. 3. 12b. As a reference, the corresponding atomic distance in the austenite phase is displayed with a black solid line. Compared with the average structure case, the atomic distances R_5 and R_6 (along the $[0\ 1\ 0]_M$) with a length of 2.801 Å are reduced after the structural transformation, and they are completely unvaried with the atomic modulation since the modulation components along the $[0\ 1\ 0]_M$ equal to zero. However, the atomic distances R_1, R_2, R_3 and R_4 are significantly affected by the atomic modulation, as shown in Fig. 3. 12b. These four distances are either reduced or increased with respect to the corresponding atomic distances in the austenite. It is clear that during the martensitic transformation, the symmetry of the magnetic interaction environment of the extra-Mn atoms is severely broken. Some Mn - Mn atomic distances become shorter, which results in a strong hybridization interaction and an increase of the antiferromagnetic coupling. Thus, in general, the magnetism of martensitic should be reduced with respect to that of austenitic [27, 28]. Besides, the ferromagnetic and antiferromagnetic couplings may coexist in modulated martensite with Mn-rich non-stoichiometric composition. This could be the origin of the exchange bias effect detected in Ni-Mn-In alloy [34].

Furthermore, since the environment of magnetic atoms keeps changing with atomic modulation, the spin orientation becomes locally canted in the modulated martensite. As a consequence, the magnetic structure of the modulated martensite should be highly anisotropic and complicated. This may be the reason why the nuclear structure refinements based on neutron diffraction data are very difficult, as the diffraction data contain the mixed nuclear and magnetic structure information. Despite this, the lattice parameters and the modulation wave vector, estimated from the neutron diffraction data, are found to be in good agreement with those determined from the synchrotron X-ray diffraction data in Table 3. 3.

(5) Superstructure approximation

In view of the needs for the practical experimental and theoretical studies, such as EBSD, TEM crystallographic orientation analyses and *ab-initio* calculations, it is essential to establish a three-dimensional structural model to represent the structural characteristics of the incommensurate modulated structure as accurately as possible. Here, the modulation wave vector could be expressed as $\boldsymbol{q} = 1/3(1+\delta)\ \boldsymbol{c^*}$, where δ represents the incommensurate degree of the modulated structure and is equal to 0.0104. Hence, a three-dimensional superstructure with three consecutive unit cells of the average structure can be employed to approximate the incommensurate structure, as displayed in Fig. 3. 13. However, it is worth emphasizing that this superstructure is just an approximation rather than the real crystal structure. The atomic shuffling directions of modulated atomic layers in this superstructure are similar to the $(2\bar{1})_2$ stacking sequence in the frame of Zhdanov model [255]. For the latter, two consecutive layers shift towards a specific direction and the remaining layers shift in the opposite direction (denoted one block), and the subscript "2" refers to the number of blocks in the unit cell. Under the present superstructure model, the incommensurate modulated structure was identified to belong to the monoclinic space group *P2/m*, with lattice parameters a = 4.3919(4) Å, b = 5.6202(1) Å, c = 12.9947(1) Å, and β = 93.044(1)°. The fractional coordinates of atoms are displayed in Table 3. 6.

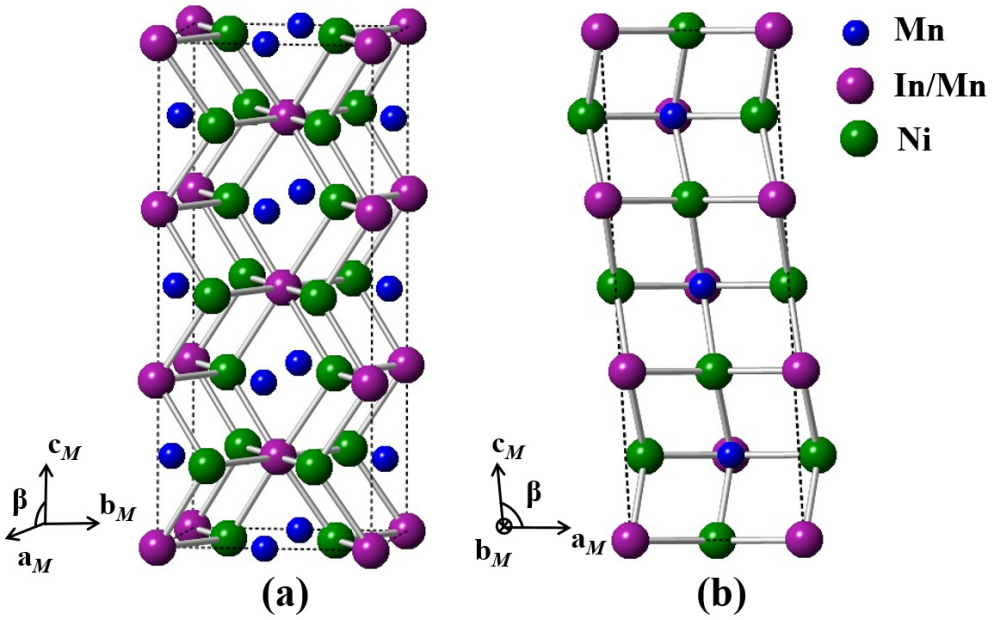

Fig. 3. 13 Schematic illustration of 3-dimensional superstructure with three consecutive unit cells.

Table 3. 6 Atomic positions of three-fold layered superstructure of $Ni_{50}Mn_{36}In_{14}$ martensite derived from the incommensurate 6M modulated structure.

Atom type	Wyckoff position	*x*	*y*	*z*	s.o.f.	U*iso*
Mn	*1a*	0	0	0	1.00	0.0125
Mn	*1h*	1/2	1/2	1/2	1.00	0.0125
Mn	*2m*	0.0416	0	0.3319	1.00	0.0125
Mn	*2n*	0.6107	1/2	0.1676	1.00	0.0125
In/ Mn	*1b*	0	1/2	0	0.56/ 0.44	0.0116
In/ Mn	*1g*	1/2	0	1/2	0.56/ 0.44	0.0116
In/ Mn	*2m*	0.6107	0	0.1676	0.56/ 0.44	0.0116
In/ Mn	*2n*	0.0416	1/2	0.3319	0.56/ 0.44	0.0116
Ni	*2j*	1/2	3/4	0	1.00	0.0167
Ni	*2k*	0	1/4	1/2	1.00	0.0167
Ni	*4o*	0.5416	3/4	0.3319	1.00	0.0167
Ni	*4o*	0.1107	1/4	0.1676	1.00	0.0167

In order to examine the rationality of the above three-dimensional superstructure model, the EBSD measurements were performed on a bulk sample of the $Ni_{50}Mn_{36}In_{14}$ alloy. Fig. 3. 14a present a typical EBSD pattern acquired at room temperature. The calculated Kikuchi lines based on this superstructure model are displayed in red solid lines in Fig. 3. 14b. The exact matches for the main reflections and the satellite reflections (highlighted with the white dash line as one example in Fig. 3. 14a) have confirmed the validity of the suggested superstructure model. Furthermore, the simulated single crystal diffraction pattern, projected along the $[0\ 1\ 0]_M$ axis, is displayed in Fig. 3. 14c. Five satellite spots are predicted between the two main reflections $(2\ 0\ 0)_M$ and $(2\ 0\ 6)_M$. Similar satellite reflections were detected in $Ni_{45}Mn_{36.5}Co_5In_{13.5}$ single crystal, using the high-energy synchrotron X-ray diffraction [25]. With the notation of Otsuka [55] (*i.e.* "*n*M" is referred to the relationship $n = s + 1$ where *s* represent the number of satellite spots between the main reflections and M stands for the crystal system "monoclinic") this modulated structure can be defined as the incommensurate 6M modulated structure. In addition, the present 6M superstructure model was verified with several off-stoichiometric Ni-(Co)-Mn-In alloys, in terms of X-ray and EBSD-based crystal structure analyses. It is found that it is representative for Ni-Mn-In alloys with martensitic transformation around room temperature that are of particular importance in view of practical applications.

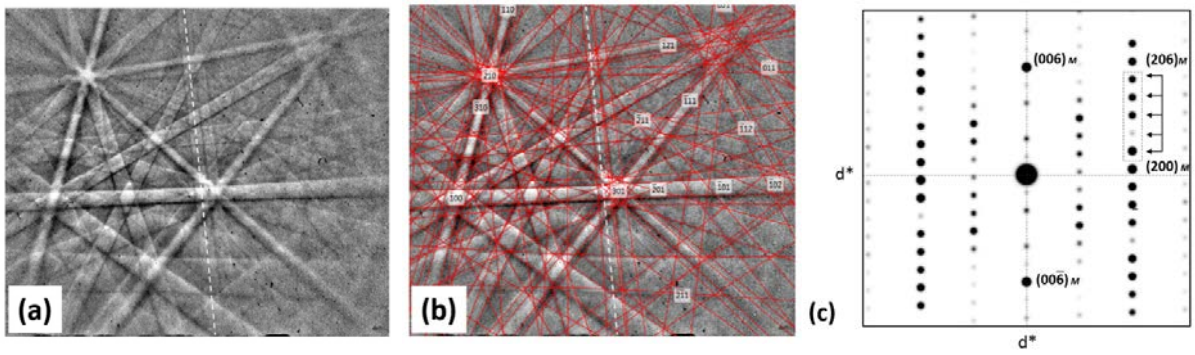

Fig. 3. 14 (a) Measured and (b) simulated EBSD Kikuchi patterns. One of the satellite reflections is highlighted with the white dash line. (c) $[0\ 1\ 0]_M$ projection of the simulated single crystal diffraction pattern.

Clearly, the present superstructure model is different from those reported in the literature for the alloys with similar composition. It is known that the crystal structure of martensite in Ni-Mn-In alloys are sensitive to internal stress and external environments (pressure and temperature) [94].

Different kinds of martensite may be observed for samples undergoing different preparation processes. Thus, the preparation of stress-free sample is a prerequisite for correct determination of modulated structure. In addition, the existence of preferred crystallographic orientation has significant impact on the intensity of reflections [256], affecting the relative intensity of different reflections. This effect is especially prominent for satellite reflections that bear the information of structural modulation. Obviously, distinct preferential orientations can be expected in bulk and ribbon samples. It implies that the determination of modulation structure may be disturbed by the texture effect. Furthermore, it is not rigorous to determine the modulated crystal structure by comparing the diffraction patterns of Ni-Mn-In alloys with those reported for other Heusler alloys such as Ni-Mn-Ga and Ni-Mn-Al alloys. This is because the type of modulation is associated with the modulation wave vector that is defined by the positions of satellite reflections. In consequence, the modulated structure determined by mere comparison may bear large inaccuracy.

3.3 Summary

In this chapter, first, the evolution of martensitic transformation temperature of $Ni_{50}Mn_{50-x}In_x$ ($0 \leq x \leq 25$) alloys were studied. With the increase of In concentration, the martensitic transformation linearly decrease. When $x < 15$, the alloys are in martensite state at room temperature. With the increase of In concentration, the alloys are in their austenite state at room temperature. The martensitic transformation was not detected for the alloys with In concentration higher than 15.5 % in the temperature range from 180 K to 800 K.

Then, the crystal structure of austenite and various martensites (non-modulated and modulated) in $Ni_{50}Mn_{50-x}In_x$ alloys ($0 \leq x \leq 25$) were determined. The austenite of Ni-Mn-In alloys possesses a highly ordered cubic $L2_1$ structure belonging to the space group $Fm\bar{3}m$. The extra-Mn atoms have a preference to be uniformly dispersed. The non-modulated martensite has a tetragonal $L1_0$ structure belonging to the space group P4/mmm. For the modulated martensite, with the consideration of the possible aperiodicity of modulated structure, the crystal structure determination was performed in the frame of superspace theory. Refinements show that it has an incommensurate 6M modulated structure with the superspace group $I2/m(\alpha 0\gamma)00$. With the accurately determined crystal structure of the modulated martensite, its relation with the magnetic properties was discussed. A three-fold layered superstructure in the three-dimensional space was

proposed to approximately describe the incommensurate modulated structure. This 6M superstructure model is considered to be representative for off-stoichiometric Ni-(Co)-Mn-In modulated martensite with martensitic transformation around room temperature. This part of work is expected to offer an important basis for reliable crystallographic and microstructural characterizations on Ni-Mn-In alloys, so as to understand the underlying mechanisms of their multifunctional magneto-responsive properties.

Chapter 4 Microstructure characterization

In this chapter, the morphological and crystallographic features of 6M modulated martensite of Ni-Mn-In alloys were studied theoretically and experimentally. First, the possible twin relations between martensite variants were theoretically explored in the frame of the crystallographic theories of martensitic transformation (CTMTs) [56, 222-225, 233-235]. Then, the microstructure features, such as variant types, crystallographic orientation relationships between adjacent variants, variant organization manner and variant interfaces, were experimentally investigated by electron backscatter diffraction (EBSD) and high resolution transmission electron microscopy (HRTEM). Finally, a comparative analysis on the results of theoretical predictions and experimental investigations were carried out. In this work, the ternary Mn enriched polycrystalline bulk samples with nominal composition of $Ni_{50}Mn_{36}In_{14}$ was selected.

4.1 Theoretical prediction of twin relations

So far, many kinds of crystallography based theories of martensitic transformation have been developed to predict twin relations between martensite variants, such as the classical phenomenological theories of martensitic transformation (PTMTs) [222-226] and the nonlinear elasticity theory [56, 233-235]. In these theories, all possible twin relations are determined with the crystal structures of the corresponding phases (austenite and martensite). In this work, with the determined crystal structure information in Chapter 3, all possible twin relations of 6M modulated martensite of Ni-Mn-In based alloy were first explored theoretically.

4.1.1 Determination of *transformation stretch tensors*

In this work, the ternary Mn enriched $Ni_{50}Mn_{36}In_{14}$ alloy having the martensitic transformation temperatures are close to room temperature (Fig. 3. 2) was selected. The high temperature phase, austenite, has a cubic $L2_1$ structure with the lattice parameter of 5.9890 Å. The low temperature phase, martensite, possesses an incommensurate 6M modulated structure that can be approximated by a three-fold superstructure model in the three-dimensional space (Fig. 3. 13) [257]. As only lattice distortion across the structural transition is considered in the frame of crystallographic theories of martensitic transformation rather than the individual movements of atoms [222-226],

the average structure model (Fig. 3. 12a), henceforth termed "1M", was used to represent the three-fold superstructure for simplicity. The lattice parameters of the average structure are a_{1M} = 4.3919(4) Å, b_{1M} = 5.6202(1) Å, c_{1M} = 4.3316(1) Å, and β_{1M} = 93.044(1)°.

In the frame of CTMTs [56, 233], as shown in Fig. 4. 1, there are two possible Bain distortions from cubic austenite to monoclinic martensite, *i.e.* "cubic-to-monoclinic I" (Fig. 4. 1a) and "cubic-to-monoclinic II" (Fig. 4. 1b). Their discrepancy is the different origins of the two-fold axis $\langle 010 \rangle_M$ of the monoclinic (***b***-unique) martensite. In the former, it is transformed from a two-fold axis $\langle 110 \rangle_A$ of austenite (Fig. 4. 1a), whereas it is from a four-fold axis $\langle 100 \rangle_A$ of austenite (Fig. 4. 1b) in the latter. In the investigated material, considering the lattice parameter of the two-fold axis (b_{1M}, 5.6202 Å) is largely different from the others (a_{1M}, 4.3919 Å; c_{1M}, 4.3316 Å), the lattice distortion of $Ni_{50}Mn_{36}In_{14}$ alloy should belong to the "cubic-to-monoclinic II" type under the minimum distortion criterion.

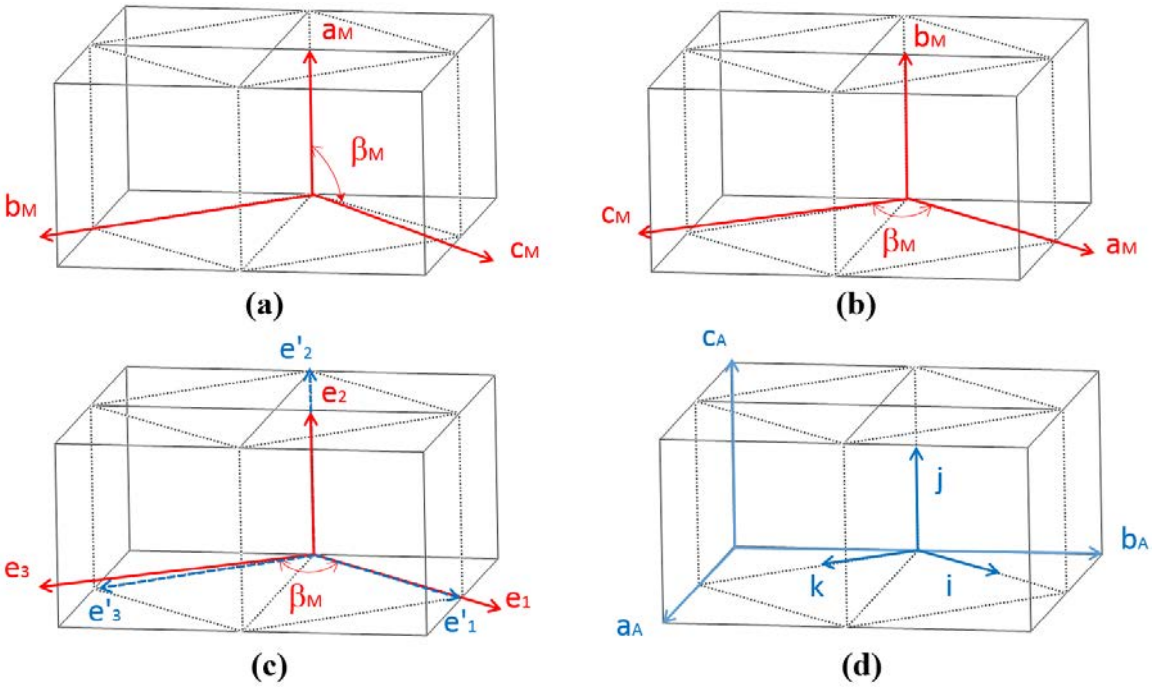

Fig. 4. 1 Schematic representations of the two types of Bain distortions in cubic-to-monoclinic martensitic transformation, *i.e.* "cubic-to-monoclinic I" (a) and "cubic-to-monoclinic II" (b). (c) Vector correspondence under the "cubic-to-monoclinic II" (b) type Bain distortion. (d) Illustration of two kinds of coordinate systems, *i.e.* austenite lattice reference $\boldsymbol{a_A}$- $\boldsymbol{b_A}$- $\boldsymbol{c_A}$ and orthonormal reference ***i***- ***j***- ***k***.

First, based on the correspondence of vectors under the "cubic-to-monoclinic II" type Bain distortion (Fig. 4. 1c), with Eqs. 2-24 and 2-25, the correlated *deformation gradient tensor* $\boldsymbol{F}^{\boldsymbol{A}}_{\boldsymbol{D'}\leftarrow\boldsymbol{D}}$ with respect to the austenite lattice reference $\boldsymbol{A}$ (Fig. 4. 1d) can be determined by Eq. 4-1.

$$\boldsymbol{F}^{\boldsymbol{A}}_{\boldsymbol{D'}\leftarrow\boldsymbol{D}} = \boldsymbol{M}^{\boldsymbol{A}\rightarrow\boldsymbol{R}} \times \boldsymbol{F}^{\boldsymbol{R}}_{\boldsymbol{D'}\leftarrow\boldsymbol{D}} \times \boldsymbol{M}^{\boldsymbol{R}\rightarrow\boldsymbol{A}} = \boldsymbol{M}^{\boldsymbol{A}\rightarrow\boldsymbol{R}} \times \boldsymbol{M}^{\boldsymbol{R}\rightarrow\boldsymbol{D'}} \times (\boldsymbol{M}^{\boldsymbol{R}\rightarrow\boldsymbol{D}})^{-1} \times \boldsymbol{M}^{\boldsymbol{R}\rightarrow\boldsymbol{A}} \tag{4-1}$$

Then, the *transformation stretch tensor* $\boldsymbol{U}^{\boldsymbol{A}}$ can be resolved from the *deformation gradient tensor* $\boldsymbol{F}^{\boldsymbol{A}}_{\boldsymbol{D'}\leftarrow\boldsymbol{D}}$ by polar decomposition [56], as given in Eq. 4-2. Moreover, under the consideration of the rotational symmetry of cubic system (Appendix I), the *transformation stretch tensors* for all martensite variants can be determined, as summarized in Table 4. 1.

$$\boldsymbol{U}^{\boldsymbol{A}} = \begin{bmatrix} 1.0022 & 0.0071 & 0 \\ 0.0071 & 1.0570 & 0 \\ 0 & 0 & 0.9384 \end{bmatrix} \tag{4-2}$$

4.1.2 Predication of twin relations

With the determined *transformation stretch tensors* $\boldsymbol{U}^{\boldsymbol{A}}$ for all martensite variants (Table 4. 1), the possible twin types of all combined variant pairs can be obtained by solving the *twinning equations* (Eq. 2-27), as summarized in Table 4. 1. It is seen that there are maximum 14 possible distinct twins, denoted I, II, … XIV, respectively, that can be classified into four categories: type-I, type-II, compound and non-conventional twins [56, 233-235]. Different from the generally observed type-I, type-II and compound twins of which the twinning elements are partially (even fully) rational, as shown in Table 4. 1, the twinning plane (K_1), twinning direction (η_1), conjugate twinning plane (K_2) and conjugate twinning direction (η_2) are fully irrational for the non-conventional twin. The type-I and type-II twins might be each generated by the two-fold or four-fold rotational cubic symmetries. Compound twins are generated by two-fold rotational cubic symmetries. The non-conventional twins are from the four-fold rotational cubic symmetries. The three-fold rotational cubic symmetries cannot result in twins in the investigated materials.

Table 4. 1 *Transformation stretch tensors* $\boldsymbol{U^A}$ of various variants under Bain distortion and all possible distinct twin relations in $Ni_{50}Mn_{36}In_{14}$ alloys. $\boldsymbol{\mathcal{P}}$ indicates the corresponding rotational symmetry of various variants. $\boldsymbol{\lambda_2}$ is the middle eigenvalue of $(\boldsymbol{U_j})^{-T}(\boldsymbol{U_i})^{T}\boldsymbol{U_i}(\boldsymbol{U_j})^{-1}$ that represents the relative deformation of variant $\boldsymbol{j}$ with respect to $\boldsymbol{i}$. The indices of twinning planes K_1 and twinning directions η_1 are expressed in the reference of austenite lattice basis.

Variant pair	$\mathcal{P}$	transformation stretch tensor U^A	λ_2	Twinning plane normal, K_1	Twinning direction, η_1	*Shear*		Twin type
V1:V1	1 x,y,z	$\begin{bmatrix}1.0022 & 0.0071 & 0\\ 0.0071 & 1.0570 & 0\\ 0 & 0 & 0.9384\end{bmatrix}$	—	—	—	—	—	—
V1:V2	2 -x,-y,z			—	—	—	—	—
V1:V3	2 x,-y,-z	$\begin{bmatrix}1.0022 & -0.0071 & 0\\ -0.0071 & 1.0570 & 0\\ 0 & 0 & 0.9384\end{bmatrix}$	1.0	[-1,0,0]	[0,-1,0]	0.0277	I	Compound
V1:V4	2 -x,y,-z			[0,1,0]	[1,0,0]		II	Compound
V1:V5	2 -y,-x,-z	$\begin{bmatrix}1.0570 & 0.0071 & 0\\ 0.0071 & 1.0022 & 0\\ 0 & 0 & 0.9384\end{bmatrix}$	1.0	$1/\sqrt{2}$[1,1,0]	$1/\sqrt{2}$[-1,1,0]	0.1064	III	Compound
V1:V6	2 y,x,-z			$1/\sqrt{2}$[1,-1,0]	$1/\sqrt{2}$[-1,-1,0]		IV	Compound
V1:V7	4^- y,-x,z	$\begin{bmatrix}1.0570 & -0.0071 & 0\\ -0.0071 & 1.0022 & 0\\ 0 & 0 & 0.9384\end{bmatrix}$	1.0	[0.7912,0.6116,0]	[-0.6116,0.7912,0]	0.1099	V	Non-conventional
V1:V8	4^+ -y,x,z			[0.6116,-0.7912,0]	[-0.7912,-0.6116,0]		VI	Non-conventional
V1:V9	3^+ z,x,y	$\begin{bmatrix}1.0570 & 0 & 0.0071\\ 0 & 0.9384 & 0\\ 0.0071 & 0 & 1.0022\end{bmatrix}$	0.9	—	—	—		—
V1:V10	3^+ -z,-x,y			—	—			—
V1:V11	3^+ -z,x,-y	$\begin{bmatrix}1.0570 & 0 & -0.0071\\ 0 & 0.9384 & 0\\ -0.0071 & 0 & 1.0022\end{bmatrix}$	0.9	—	—			—
V1:V12	3^+ z,-x,-y			—	—			—
V1:V13	2 -x,-z,-y	$\begin{bmatrix}1.0022 & 0 & 0.0071\\ 0 & 0.9384 & 0\\ 0.0071 & 0 & 1.0570\end{bmatrix}$	1.0	[-0.0873,-0.7044,-0.7044]	$1/\sqrt{2}$[0,-1,1]	0.2392	VII	Type I
V1:V14	4^- x,z,-y			$1/\sqrt{2}$[0,1,-1]	[0.0767,0.7050,0.7050]		VIII	Type II
V1:V15	4^+ x,-z,y	$\begin{bmatrix}1.0022 & 0 & -0.0071\\ 0 & 0.9384 & 0\\ -0.0071 & 0 & 1.0570\end{bmatrix}$	1.0	[0.0873,0.7044,-0.7044]	$1/\sqrt{2}$[0,1,1]		IX	Type II
V1:V16	2 -x,z,y			$1/\sqrt{2}$[0,-1,-1]	[-0.0767,-0.7050,0.7050]		X	Type I
V1:V17	3^- y,z,x	$\begin{bmatrix}0.9384 & 0 & 0\\ 0 & 1.0022 & 0.0071\\ 0 & 0.0071 & 1.0570\end{bmatrix}$	1.1	—	—	—		—
V1:V18	3^- -y,-z,x			—	—			—
V1:V19	3^- y,-z,-x	$\begin{bmatrix}0.9384 & 0 & 0\\ 0 & 1.0022 & -0.0071\\ 0 & -0.0071 & 1.0570\end{bmatrix}$	1.1	—	—			—
V1:V20	3^- -y,z,-x			—	—			—
V1:V21	2 -z,-y,-x	$\begin{bmatrix}0.9384 & 0 & 0\\ 0 & 1.0570 & 0.0071\\ 0 & 0.0071 & 1.0022\end{bmatrix}$	1.0	$1/\sqrt{2}$[1,0,-1]	[0.7010,0.1310,0.7010]	0.1331	XI	Type I
V1:V22	4^+ z,y,-x			[-0.6974,-0.1651,-0.6974]	$1/\sqrt{2}$[-1,0,1]		XII	Type II
V1:V23	4^- -z,y,x	$\begin{bmatrix}0.9384 & 0 & 0\\ 0 & 1.0570 & -0.0071\\ 0 & -0.0071 & 1.0022\end{bmatrix}$	1.0	[0.6974,0.1651,-0.6974]	$1/\sqrt{2}$[1,0,1]		XIII	Type II
V1:V24	2 z,-y,x			$1/\sqrt{2}$[-1,0,-1]	[-0.7010,-0.1310,0.7010]		XIV	Type I

4.2 Experimental investigation on microstructure features

4.2.1 Morphological features of martensite

The band contrast and crystallographic orientation micrographs of modulated martensite in the bulk $Ni_{50}Mn_{36}In_{14}$ alloy - measured by EBSD at room temperature - are displayed in Fig. 4. 2a and b, respectively. It can be seen that the martensite is in plate shape and organized in colonies or groups within initial austenite grains. In each colony, thin plates are alternately distributed with four different crystallographic orientations.

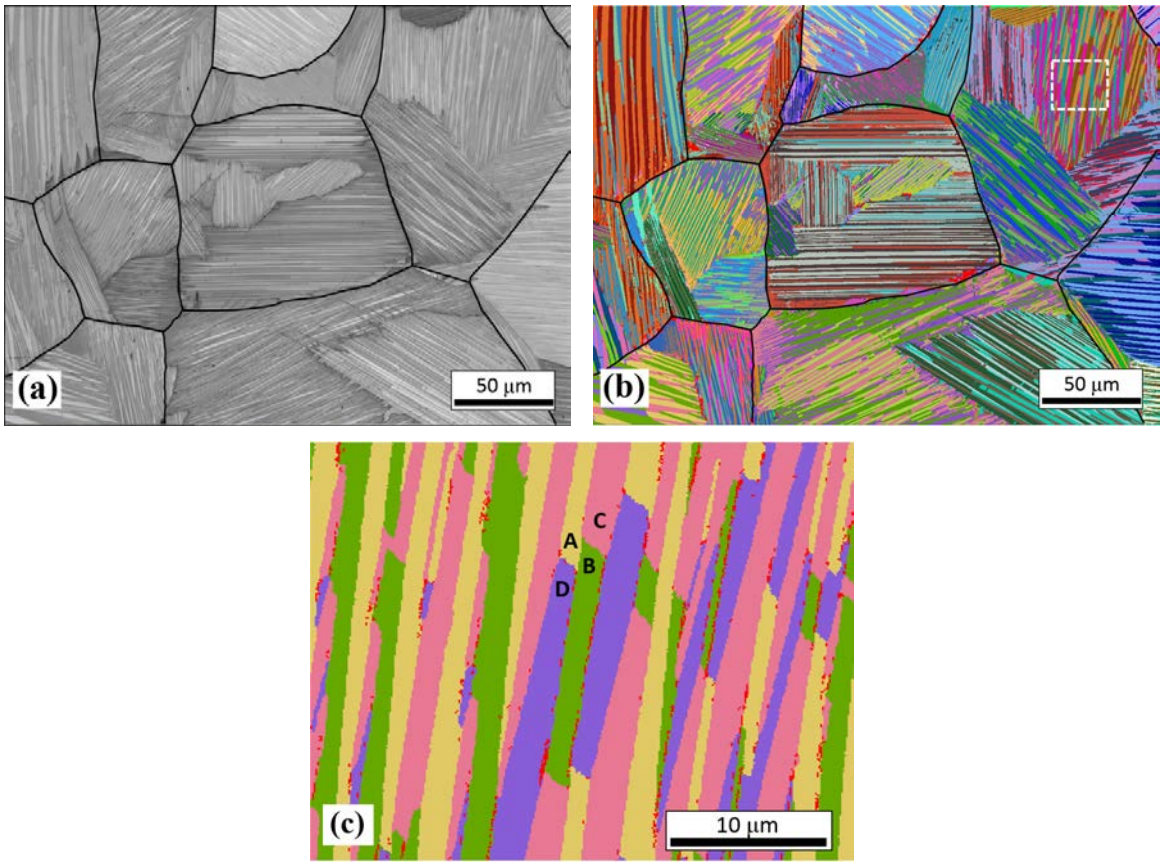

Fig. 4. 2 (a) Band contrast micrograph and (b) crystallographic orientation micrograph of $Ni_{50}Mn_{36}In_{14}$ alloy measured by EBSD at room temperature. Thick black lines in (a) and (b) outline original austenite grain boundaries. (c) Zoomed crystallographic orientation micrograph of the area enclosed with the dashed white rectangle in (b). Four differently oriented martensite plates (orientation variants) are labeled as A, B, C and D. The discretely distributed red points in (c) were indexed as the $L2_1$ cubic austenite phase.

As an example, Fig. 4. 2c presents the zoomed orientation micrograph of the area outlined with the dashed white rectangle in Fig. 4. 2b, where A, B, C and D denote four differently oriented martensite plates (variants). Adjacent martensite plates are separated by two kinds of interfaces in terms of the interface trace orientation. One refers to those interfaces with trace roughly paralleled to the plate length direction (termed interplate interfaces), *i.e.* the boundaries between variants A and B, A and C, B and D, and C and D. The other refers to those interfaces with trace across the plates (termed intraplate interfaces), *i.e.* the boundaries between variants A and D, and B and C. Furthermore, some limited amount of austenite phases distributed as the form of "island-chain" were also detected, as shown in Fig. 4. 2c. In this chapter, we focus only on the microstructure features of the martensite phase.

With the measured EBSD orientation data of the four martensite variants A, B, C and D in Fig. 4. 2c, the mean and maximum deviations from their mean orientations were calculated. The results are displayed in Table 4. 2. It is seen that the mean and maximum angular deviations are respectively less than 0.3° and 1°, suggesting a homogeneous orientation for each kind of variant. The small orientation deviations could be ascribed to the retained strains associated with the martensitic transformation as well as the EBSD imprecision in orientation measurements. Thus, each martensite variant is considered as a nearly perfect crystal with negligible lattice distortion. For the subsequent crystallographic calculations, the determined mean orientation data were used as the input to get better accuracy.

Table 4. 2 Mean and maximum orientation deviations from the mean orientations of four martensite variants A, B, C and D in Fig. 4. 2c, represented in minimum rotation angle.

Variant	Mean orientation (φ_1, ϕ, φ_2)	Mean deviation	Maximum deviation
A	(167.4367°, 7.9514°, 246.3696°)	0.2784°	0.9620°
B	(14.6294°, 107.6467°, 213.8242°)	0.2792°	0.7975°
C	(90.2600°, 59.4931°, 21.9914°)	0.2810°	0.7677°
D	(143.2065°, 100.2620°, 87.3843°)	0.2997°	0.9955°

4.2.2 Crystallographic features of martensite

For the present $Ni_{50}Mn_{36}In_{14}$ alloy, each colony of martensite plates consists of four variants (denoted as A, B, C and D in Fig. 4. 2c). The misorientations among various variants were calculated from their mean orientations, and the results are summarized in Table 4. 3. It can be seen that there exists at least one 180° rotation (with a small deviation) with the rotation axis either close to a normal to a rational plane or a rational direction (also with a small deviation) for each variant pair. According to the classical definition of twin [233, 258, 259], all these martensite variants are twin-related one another. More specifically, variant pairs A: C and B: D belong to type-I type twin with the $(\bar{1}23)_M$ plane as the twinning plane K_1, A: B and C: D to type-II type twin with the $[\bar{3}\bar{3}1]_M$ direction as the twinning direction η_1, and A: D and B: C to compound twin with the $(103)_M$ plane as the twinning plane K_1 and the $[30\bar{1}]_M$ direction as the twinning direction η_1.

Table 4. 3 Misorientation angles and corresponding rotation axes between four martensite variants A, B, C and D. The subscripts "*Ortho*" and "*M*" represent the orthonormal coordinate frame and the monoclinic superlattice frame, respectively. The geometrical relationship between the two coordinate frames is consistent with the notation defined in *Oxford Channel 5*.

Variant pair	Misorientation angle ω	Rotation axis		Twin type
		Rotation axis ***d***	Deviation angle	
A:C	83.4766°	$[\overline{0.7288}\ \overline{0.0036}\ \overline{0.6847}]_{Ortho}$	0.1730° from $[\bar{3}0\bar{1}]_M$	Type-I
	179.7258°	$[\overline{0.4559}\ 0.7462\ 0.4852]_{Ortho}$	0.2200° from normal to $(\bar{1}23)_M$	
B:D	83.1465°	$[\overline{0.7300}\ \overline{0.0017}\ \overline{0.6835}]_{Ortho}$	0.0790° from $[\bar{3}0\bar{1}]_M$	
	179.8741°	$[\overline{0.4535}\ 0.7481\ 0.4844]_{Ortho}$	0.0094° from normal to $(\bar{1}23)_M$	
A:B	179.9569°	$[\overline{0.5157}\ \overline{0.6654}\ 0.5397]_{Ortho}$	0.1945° from $[\bar{3}\bar{3}1]_M$	Type-II
	96.5670°	$[0.7230\ 0.0005\ 0.6908]_{Ortho}$	0.0411° from normal to $(103)_M$	
C:D	96.8185°	$[0.7198\ 0.0010\ 0.6942]_{Ortho}$	0.0543° from normal to $(103)_M$	
	179.9123°	$[\overline{0.5192}\ \overline{0.6638}\ 0.5383]_{Ortho}$	0.0667° from $[\bar{3}\bar{3}1]_M$	
A:D	179.7104°	$[0.7253\ \overline{0.0055}\ 0.6884]_{Ortho}$	0.5415 from [301] 0.4718° from normal to $(103)_M$	Compound
	179.3718°	$[0.6884\ 0.0025\ \overline{0.7254}]_{Ortho}$	0.3807° from $[30\bar{1}]_M$ 0.5415 from normal to $(10\bar{3})_M$	
B:C	179.9587°	$[0.7245\ 0.0060\ 0.6893]_{Ortho}$	0.6179° from $[301]_M$ 0.4465° from normal to $(103)_M$	
	179.3070°	$[0.6893\ \overline{0.0004}\ \overline{0.7245}]_{Ortho}$	0.2824° from $[30\bar{1}]_M$ 0.5120° from normal to $(10\bar{3})_M$	

The determined twinning elements (K_1, the twinning plane; η_1, the twinning direction; K_2, the reciprocal or conjugate twinning plane; η_2, the reciprocal or conjugate twinning direction; P, the plane of shear; s, the magnitude of shear) are summarized in Table 4. 4. Notably, the twinning shears for type-I and type-II twins are exactly the same (0.2392), being almost one order of magnitude higher than that of compound twin (0.0277).

Table 4. 4 Twinning elements of type-I, type-II and compound twins identified for 6M modulated martensite in $Ni_{50}Mn_{36}In_{14}$ alloy. The theoretical minimum rotation angles (ω) and corresponding rotation axes (***d***) associated with the three twin types are also given.

Twinning elements	Type-I twin	Type-II twin	Compound twin
K_1	$\{\bar{1}23\}_M$	$\{1.1240\ \bar{2}\ \overline{2.6280}\}_M$	$\{103\}_M$
K_2	$\{1.1240\ 2\ \overline{2.6280}\}_M$	$\{\bar{1}\bar{2}3\}_M$	$\{\bar{1}03\}_M$
η_1	$<3.3264\ 3\ \overline{0.8912}>_M$	$<\bar{3}\bar{3}1>_M$	$<\bar{3}01>_M$
η_2	$<\bar{3}31>_M$	$<3.3264\ \bar{3}\ \overline{0.8912}>_M$	$<301>_M$
P	$\{1\ \overline{0.1150}\ 3.3451\}_M$	$\{1\ 0.1150\ 3.3451\}_M$	$\{010\}_M$
s	0.2392	0.2392	0.0277
Theoretical ω/ ***d***	83.20°/ $<301>_M$	96.80°/ normal to $(103)_M$	180°/ $<\bar{3}01>_M$

Based on the *indirect two-trace* method [246], the interface planes connecting the twin-related martensite variants of the same group and their deviations from the corresponding twinning plane K_1 were calculated, and the results are summarized in Table 4. 5. It is seen that all the interface planes are well consistent with their respective K_1. The angular deviations of compound twin interface planes from K_1 are relatively larger than those of type-I and type-II twin interface planes. This is ascribed to the relative short length and “stepped” feature of compound twin interfaces.

Table 4. 5 Interface planes between various martensite variants of the same colony and their deviations from the corresponding twinning planes K_1.

Twin type	K_1	Variant pair	Interface plane	Deviation from K_1
Type-I	$\{\bar{1}23\}_M$	A: C	$(1.3051\ \overline{2.5541}\ \overline{3.9843})_M$	0.9432°
			$(1.2739\ \overline{2.5556}\ 3.7714)_M$	0.3838°
		B: D	$(1.2452\ 2.5852\ \overline{3.8277})_M$	0.8556°
			$(\overline{1.3119}\ 2.5617\ 3.8681)_M$	0.5571°
Type-II	$\{1.1240\ \bar{2}\ \overline{2.6280}\}_M$	A: B	$(1.5576\ \overline{2.7012}\ \overline{3.6795})_M$	0.8684°
			$(1.4967\ 2.7387\ \overline{3.5321})_M$	0.7186°
		C: D	$(\overline{1.1677}\ \overline{2.0000}\ 2.6877)_M$	0.9707°
			$(\overline{1.1276}\ \overline{2.0000}\ 2.5333)_M$	0.8395°
Compound	$\{103\}_M$	A: D	$(\overline{1.0000}\ \overline{0.0025}\ \overline{3.0540})_M$	0.4901°
			$(\overline{1.0000}\ 0.0225\ \overline{2.8650})_M$	1.4353°
		B: C	$(1.0000\ 0.0369\ 2.9088)_M$	1.4206°
			$(1.0000\ \overline{0.0094}\ 2.9984)_M$	0.2875°

Fig. 4. 3a presents the stereographic projections of interface planes in the macroscopic sample coordinate frame for the three twin types, where the overlapping poles are enlarged in the dashed line boxes. The poles of the interface planes of type-I twin pairs (A: C and B: D) are very close to each other, as represented by the filled circles in Fig. 4. 3a. This means that the type-I twin interfaces are parallel. The poles of the interface planes of type-II twin pairs (A: B and C: D), as indicated by the filled diamonds in Fig. 4. 3a, are distributed around those of type-I twin pairs (A: C and B: D) with a deviation of about 5°, suggesting that there is a small angular deviation between the interfaces of type-I and type-II twins. This is in accordance with that observed on the 5M and 7M modulated martensite in Ni-Mn-Ga alloys [260-264]. As for the interfaces of compound twin pairs (A: D and B: C), they are also almost parallel. These compound twin interfaces are oriented roughly perpendicular to the type-I twin interfaces. To obtain an overview of variant organization in one martensite colony, the interface traces of the twin-related variants are illustrated in a two-dimensional sample section, as shown in Fig. 4. 3b.

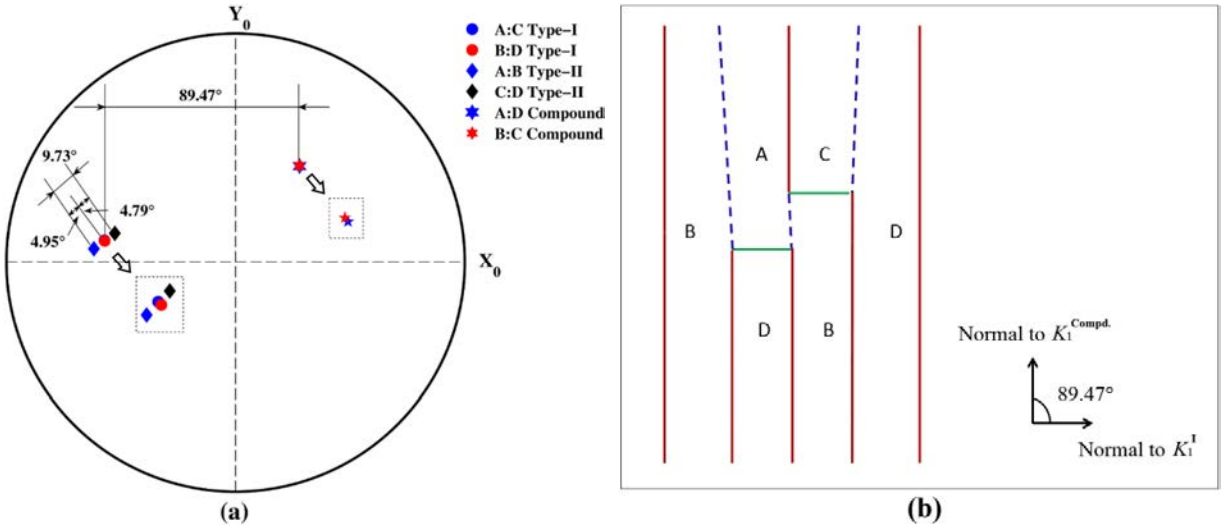

Fig. 4. 3 (a) Stereographic projections of interface planes of various variant pairs (from one martensite colony) in the macroscopic sample coordinate frame. The overlapped poles are enlarged in the dashed line boxes. The interfaces associated with type-I, type-II and compound twins are denoted by filled circles, diamonds and stars, respectively. (b) Illustration of variant organization within one martensite colony. The interface traces associated with type-I, type-II and compound twins are highlighted in red solid, blue dashed and green solid lines, respectively. K_1^{I} and $K_1^{Compd.}$ represent the twinning planes of type-I and compound twins, respectively.

According to the HRTEM observations, the three types of twins are associated with different interface characters at atomic scale, as shown in Fig. 4. 4. More specifically, the type-I twin pair A: C possesses a straight interface (outlined with the dashed white horizontal line in Fig. 4. 4a), whereas the type-II twin pair A: B has a stepped interface (outlined with the dashed white zigzag line in Fig. 4. 4b).Thus, different stress-response behaviors could be expected for the type-I and type-II twins, although they have the same amount of twinning shear. The interface of the compound twin pair A: D also possesses step feature (Fig. 4. 4c), just like that of the type-II twin pair but with larger step size.

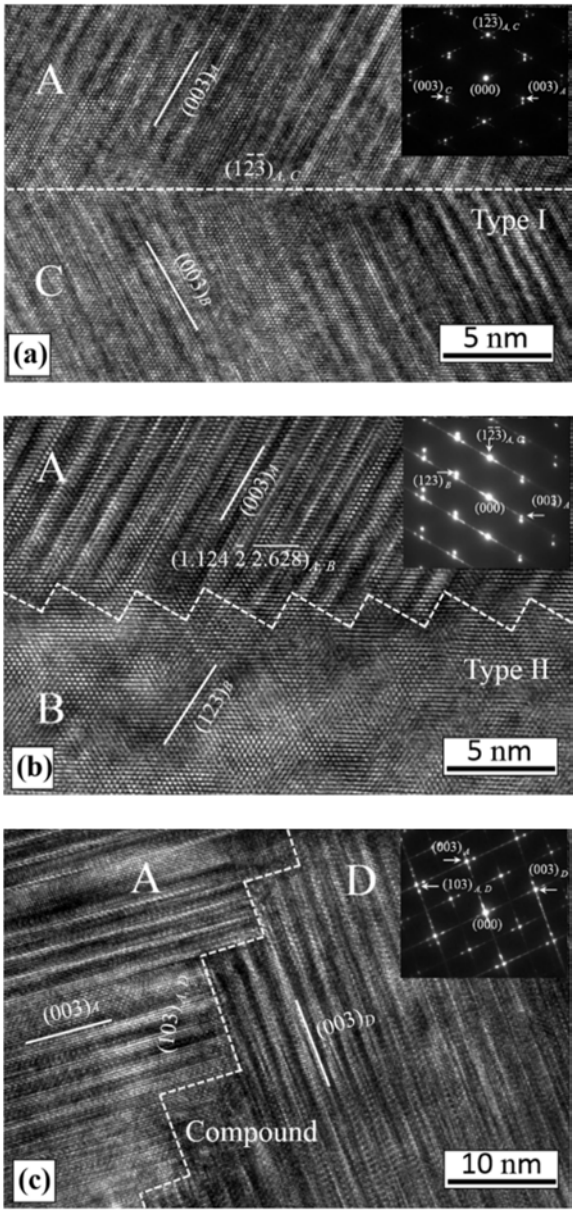

Fig. 4. 4 HRTEM lattice images and corresponding diffraction patterns of (a) type-I, (b) type-II and (c) compound twins. The directions of incident electron beam are along $<210>_M$ in (a), ~ $<210>_M$ in (b) and $<010>_M$ in (c) with respect to the lattice reference of variant A. The type-I twin interface is indicated in dashed white straight line, and the type-II and compound twin interfaces in dashed white zigzag lines.

4.3 Comparative analysis of the theoretical and experimental results

As revealed in Section 4.1 and Section 4.2, there are 14 possible twin relations in the investigated material (Table 4. 1). However, only three twin relations, *i.e.* type-I (A: C or B: D), type-II (A: B or C: D) and compound twin (A: D or B: C), were generally observed between adjacent variants in each variant colony (Fig. 4. 2). The experimentally observed type-I, type-II and compound twins (Table 4. 4) correspond to the predicted twin pairs X/ VIII, VII/ IX, and I/ II (Table 4. 1), respectively. The predicted non-conventional twin is not detected. This situation should be ascribed to the defined variant organization manner in Ni-Mn-In based alloys, as shown in Fig. 4. 2 and Fig. 4. 3. In the frame of CTMTs, twin relations are predicted with consideration of all possible variant pairs in mathematics. However, in reality, the microstructure of martensite would generally self-organize in a particular way to minimize the transformation elastic strains. Thus, some variants could never be adjacent physically although theoretically they are of twin relation. The underlying mechanism of variant organization in Ni-Mn-In based alloys will be discussed in detailed in Chapter 5.

4.4 Summary

Crystallographic theories of martensitic transformation suggest that there are in maximum 14 distinct twin relations in 6M modulated $Ni_{50}Mn_{36}In_{14}$ alloy that can be classified into four twin types, *i.e.* type-I, type-II, compound and non-conventional twins. Type-I and type-II twins might exist between the two-fold or four-fold cubic rotational symmetry related variants. Compound twins are between the two-fold rotational cubic symmetry related variants. Non-conventional twins only exist between the four-fold rotational cubic symmetry related variants. It is not possible to be of twins for the three-fold rotational cubic symmetry related variants.

Microstructural characterizations by electron backscatter diffraction (EBSD) technique show that the martensite is in plate shape and self-organized in colonies within which the plates stretch roughly in the same direction. Each colony has four types of orientation variants. Due to the unique variant organization manner in Ni-Mn-In alloys, only three twin relations are experimentally evidenced, *i.e.* type-I (A: C, B: D), type-II (A: B, C: D) and compound twin (A: D, B: C). The twinning shears of type-I and type-II twins are the same and equal to 0.2392 that is around one order of magnitude higher than that of compound twin (0.0277). Variant interfaces are defined by

their corresponding twinning plane K_1 in the mesoscopic scale. HRTEM investigations show that the type-I twin is of a coherent interface at atomic scale, whereas the type-II and compound twins have “stepped” interfaces. The step heights of the compound twin interface are much larger than those of the type-II twin interface. In view of variant organization, there are only one oriented type-I and compound twin interfaces but two distinct type-II interfaces that have a theoretical angular deviation of about 5° from the type-I twin interface orientation.

Chapter 5 Martensitic transformation crystallography

In this chapter, the crystallographic orientation relationship (*OR*) between austenite and 6M modulated martensite, martensitic transformation strain path and its effect on microstructure, and geometrical compatibility between austenite and martensite were studied. First, the crystallographic *OR* between austenite (***A***) and the correlated 6M modulated martensite, $(hkl)_A // (h'k'l')_{6M}$ and $[uvw]_A // [u'v'w']_{6M}$, was investigated based on EBSD technique with a sample having the coexisting two-phases. Then, with the determined crystal structure, microstructure and crystallographic *OR*, the martensitic transformation strain path and its effect on microstructure of martensite were explored. Finally, the geometrical compatibilities between austenite and 6M modulated martensite were examined theoretically by means of crystallographic theories of martensitic transformation (CTMTs) and experimentally by EBSD and high resolution transmission electron microscopy (HRTEM).

5.1 Orientation relationship between austenite and martensite

In this work, the polycrystalline bulk sample of $Ni_{50}Mn_{36}In_{14}$ alloy that has coexisting austenite and martensite at room temperature (Fig. 3. 10 and Fig. 4. 2c) was selected. The alloys were prepared by arc-melting. The as-cast ingots were further injected into a copper mould to obtain dense specimens. The experimental details are described in Chapter 2. For convenience of figure consultation, the microstructure shown in Fig. 4. 2c is represented here in Fig. 5. 1. As shown in Fig. 5. 1, apart from four martensite variants A, B, C and D in each colony, some residual austenite phase as “island-chains” along martensite variant interfaces can be detected, as represented with the red discrete points in the figure. The observation of the residual austenite below its martensitic transformation temperatures should be attributed to the kinetic arrest (KA) effect in these materials [40, 41, 128, 132]. The coexistence of martensite and austenite allow experimentally exploring of the crystallographic *OR* between these two phases.

Here, the determinations were performed in three steps. First, with the consideration of crystal structure features of austenite ($L2_1$ cubic) and martensite (modulated monoclinic), the possible *ORs* were selected by consulting the literature. Second, the possibilities of various *ORs* were qualitatively evaluated by comparing their parallelism degree of *OR* planes, $(hkl)_A$ & $(h'k'l')_{6M}$,

and *OR* directions, $[uvw]_A$ & $[u'v'w']_{6M}$. Finally, the misorientations between the austenite and the martensite variants deduced from the theoretical *ORs* are compared with those calculated from the measured orientations of the austenite and the martensite variants. The *OR* provides the highest match is estimated as the effective *OR* to analyze the transformation strain path.

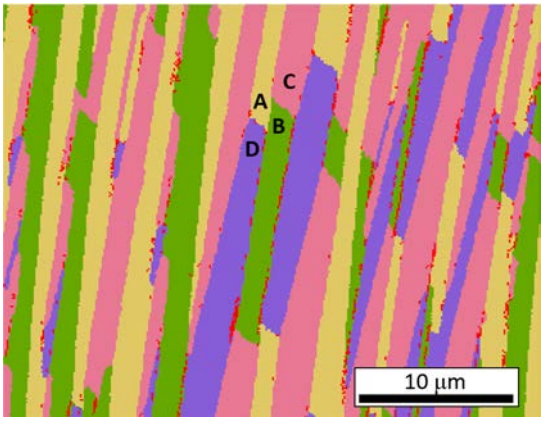

Fig. 5. 1 Crystallographic orientation micrograph of the area enclosed with the dashed white rectangle in Fig. 4. 2b. A, B, C and D represent the four distinct variants. The discretely distributed red points represent the cubic austenite phase.

Table 5. 1 Possible *ORs* and their corresponding plane and in-plane direction parallelisms. Subscript "A", and "1M" and "6M" represent the austenite, and the average structure and the six-layered superstructure of martensite, respectively.

Possible *ORs*	Parallel planes and in-plane directions	
	Simple crystal structure	Six-layered superstructure
Bain relation	$\{001\}_A//\{010\}_{1M}$ & $<010>_A//<101>_{1M}$	$\{001\}_A//\{010\}_{6M}$ & $<010>_A//<301>_{6M}$
N-W relation	$\{111\}_A//\{011\}_{1M}$ & $<11\bar{2}>_A//<0\bar{1}1>_{1M}$	$\{111\}_A//\{013\}_{6M}$ & $<11\bar{2}>_A//<0\bar{3}1>_{6M}$
K-S relation	$\{111\}_A//\{011\}_{1M}$ & $<10\bar{1}>_A//<\bar{1}\bar{1}1>_{1M}$	$\{111\}_A//\{013\}_{6M}$ & $<10\bar{1}>_A//<\bar{3}\bar{3}1>_{6M}$
Pitsch relation	$\{101\}_A//\{1\bar{2}\bar{1}\}_{1M}$ & $<10\bar{1}>_A//<\bar{1}\bar{1}1>_{1M}$	$\{101\}_A//\{1\bar{2}\bar{3}\}_{6M}$ & $<10\bar{1}>_A//<\bar{3}\bar{3}1>_{6M}$

In consideration of the crystal structure features of austenite ($L2_1$ cubic) and modulated monoclinic martensite, it was found that *Bain* [265], *Nishiyama- Wassermann* (*N-W*) [266, 267], *Kurdjumov- Sachs* (*K-S*) [268] and *Pitsch* relations [269] might be possible in the investigated material. Their *OR* expressed in plane and in-plane direction parallelisms are summarized in Table 5. 1. It should be noted that the published *OR*s are generally defined in simple structures (relative

to modulated structure), whereas the martensite in the present material possesses a 6M modulated structure. Thus, the reported Miller indices of *OR* planes and directions of martensite in the literature cannot directly be utilized. Considering that the 6M modulated structure in this study can be approximated by a six-layered superstructure with three unit cells of the average structure along ***c*** axis [257], the corresponding *OR* indices of martensite are re-expressed with respect to the lattice of the six-layered superstructure. The results are listed in Table 5. 1.

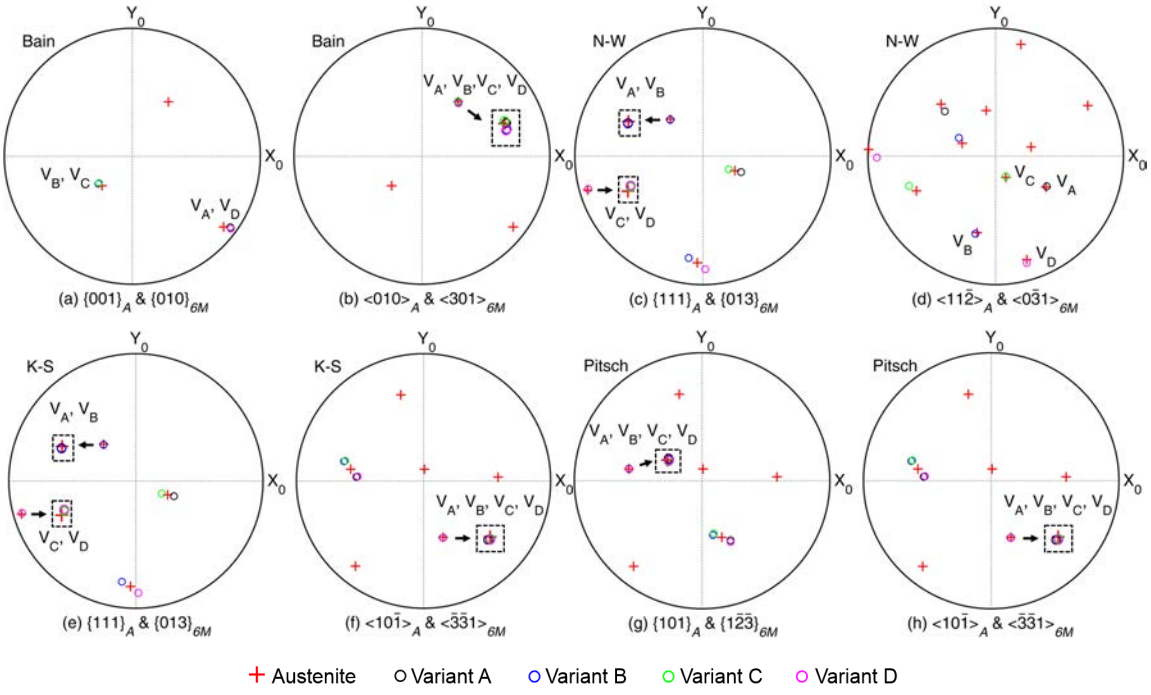

Fig. 5. 2 Pole figures of *OR* planes and directions in *Bain* (a and b), *N-W* (c and d), *K-S* (e and f) and *Pitsch* (g and h) relations. The poles of austenite are highlighted with red crosses. Variants A, B, C and D are indicated with V_A, V_B, V_C and V_D, respectively. The poles of V_A, V_B, V_C and V_D are indicated with the black, blue, green and magenta circles, respectively. The overlapped poles are enlarged within the dashed rectangle boxes.

To evaluate the possibilities of various *ORs*, their pole figures of *OR* planes and directions were plotted with the measured orientations of the microstructural constituents in Fig. 5. 1, and displayed in Fig. 5. 2. To avoid accidental matches, the mean orientations of austenite and martensite were utilized [270]. Fig. 5. 2a shows the joint pole figure of *OR* planes under *Bain* relation, *i.e.* $\{001\}_A$ of austenite and $\{010\}_{6M}$ of martensite. It is seen that the $\{010\}_{6M}$ poles of

martensite variant pairs V_A: V_D and V_B: V_C roughly coincide with two distinct $\{001\}_A$ poles of austenite. Pole figure of *OR* directions under *Bain* relation, *i.e.* $<010>_A$ of austenite and $<301>_{6M}$ of martensite, is displayed in Fig. 5. 2b. It is seen that the $<301>_{6M}$ poles of V_A, V_B, V_C and V_D almost coincide with one $<010>_A$ pole of austenite. With a similar analysis of Fig. 5. 2c ~ h, all good coincidence of *OR* planes and directions can be observed for *N-W*, *K-S* and *Pitsch* relations.

To further differentiate the match of these four *ORs* with the experimental results, the misorientations between the austenite and the martensite generated under each *OR* is calculated and expressed in Euler angles with respect to the lattice basis of austenite, as displayed in Table 5. 2, and compared with the misorientations calculated from the measured orientations of the austenite and the martensite variants. The comparisons are expressed in disorientation angle (ω) for each martensite variant, and displayed in the same table. For the *Bain* and the *N-W ORs*, it is seen that the disorientation angles for most of the martensite variants are larger than 1°, whereas for the *K-S* and the *Pitsch ORs*, the differences between the experimental and theoretical misorientations for the four variants are around 0.5°. For V_A and V_B, the differences under the *Pitsch* relation are slightly larger than those of the *K-S* relation, while their differences under *Pitsch* relation are smaller than those under the *K-S* relation for V_C and V_D. The mean deviations under the *Pitsch* and the *K-S* relations are very close to each other, and are comparable to the measurement error of EBSD techniques (± 0.5°). Thus, both *K-S* and *Pitsch* relations could be possible to describe the lattice correspondence between austenite and martensite in the present material.

Table 5. 2 The theoretical misorientation between austenite and martensite under the *Bain*, *N-W*, *K-S* and *Pitsch ORs* are expressed in Euler angles with respect to the lattice basis of austenite. The comparison between the theoretical misorientation and the experimental misorientation between austenite and martensite expressed in disorientation angle and the mean disorientation angles over the four martensite variants.

ORs	Euler angles of theoretical orientation relations	Minimal rotation angle of the experimental and theoretical *OR* (°)				
		V_A	V_B	V_C	V_D	Mean angle
Bain	(133.06, 90.00, 0.00)	3.2923	3.4033	3.2650	3.7029	3.4159
N-W	(133.09, 92.38, 1.39)	0.7994	1.4227	1.0866	1.7560	1.2662
K-S	(133.84, 92.41, 2.40)	0.5390	0.3561	0.5724	0.7282	0.5489
Pitsch	(3.18, 136.41, 94.93)	0.5793	0.3651	0.2798	0.4517	0.4190

To reveal the geometrical difference between the *K-S* and the *Pitsch* relation, the *OR* planes and directions are illustrated in austenite lattice (orange) and the *Pitsch* relation-related martensite lattice (green), as shown in Fig. 5. 3. For a clear illustration, here, the average structure of martensite is utilized [257]. It is seen that *K-S* and *Pitsch* relations share the same *OR* directions, *i.e.* $[0\bar{1}\bar{1}]_A$ and $[\bar{3}\bar{3}1]_{6M}$, as indicated with the bold black arrows in Fig. 5. 3a. The projection of Fig. 5. 3a along the *OR* direction is given in Fig. 5. 3b. The normal of the *OR* planes are indicated in the dashed arrow lines. It is seen that the corresponding *K-S* planes, $\{1\bar{1}1\}_A$ and $\{013\}_{6M}$, is just deviated by 0.33° when *Pitsch* relation is exactly satisfied. This small angular deviation between *OR* planes should be the geometrical difference between the *K-S* and the *Pitsch* relations in the investigated material. Such a situation arises from the specific geometric features of the crystal structures of the parent and the product phases. During the structure transformation, when one *OR* is followed, the other is almost satisfied.

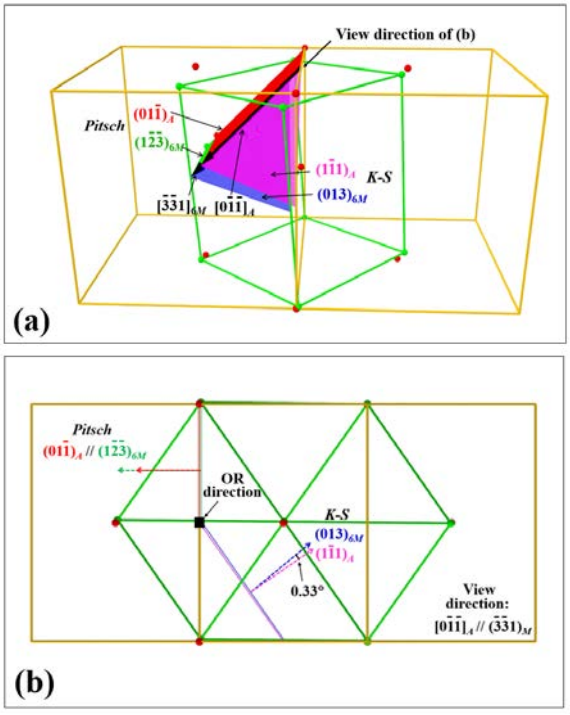

Fig. 5. 3 Illustration of *OR* planes and directions of *K-S* and *Pitsch* relations in austenite lattice (orange) and *Pitsch* relation-related martensite lattice (green). For a better illustration, the average structure of martensite is utilized. The common *OR* directions are indicated with the bold black arrows. Various *OR* planes with *K-S* and *Pitsch* relations are highlighted in different colors. Projection of (a) along the *OR* direction ($[0\bar{1}\bar{1}]_A$ or $[\bar{3}\bar{3}1]_{6M}$) is given in (b).

5.2 Martensitic transformation strain path

For a transformation, the *OR* not only describes the geometrical relation between the parent and the product phase but also provides useful information on the transformation process. Thus together with the crystal structure information of the two phases, it can be used to analyze the specific lattice distortion associated with the structure transformation (transformation path) to understand the transformation resistance and its impact on the resultant microstructural configuration. It is well known that the martensitic transformation is involved in a diffusionless and coordinate atomic movement with the relative displacement of atoms, in general, smaller than the length of atomic band. Consequently, the *OR* planes of the austenite and the martensite, $(hkl)_A$ and $(h'k'l')_{\acute{o}M}$, and the *OR* directions, $[uvw]_A$ and $[u'v'w']_{\acute{o}M}$ could be used as boundary conditions or confinements to identify the transformation strain path, as the two are not rotated during the transformation. The lattice distortion under a specific *OR* thus can be figured out, as illustrated in Fig. 5. 4, where the *OR* planes, $(hkl)_A$ and $(h'k'l')_{\acute{o}M}$, and the *OR* directions, $[uvw]_A$ and $[u'v'w']_{\acute{o}M}$, in austenite and martensite lattices are represented in red and blue, respectively. It should be noted that the $(hkl)_A$ plane is not the so-called invariant plane (or *habit plane*), as the in-plane direction $[uvw]_A$ might be involved in a dilatational deformation during structural transformation. According to the lattice distortion in Fig. 5. 4, with the crystal structures of austenite and martensite, the *deformation gradient tensor* of martensitic transformation under a certain *OR* can be obtained, using Eqs. 2-24 and 2-25, for further transformation path analysis.

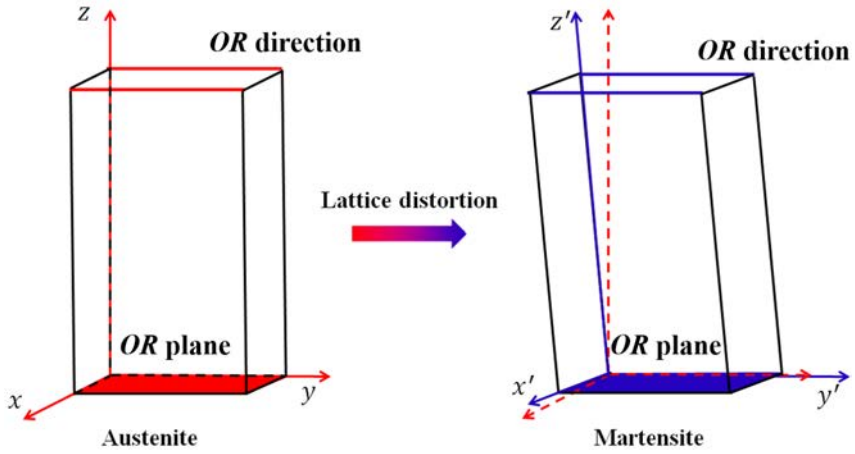

Fig. 5. 4 Illustration of lattice distortion under certain crystallographic orientation relationship (*OR*) between austenite and martensite across the structural transition.

5.2.1 Strain components of lattice distortion

Since both the *K-S* and the *Pitsch* relations are possible in the investigated material, in this work, their corresponding transformation paths, henceforth termed *K-S* and *Pitsch* path, may be identified. In this work, the average structure of martensite [257] is utilized for simplicity, as the atomic position modulation does not affect the lattice distortion during martensitic transformation. The lattice distortions under the *K-S* and the *Pitsch* paths are illustrated in Fig. 5. 5.

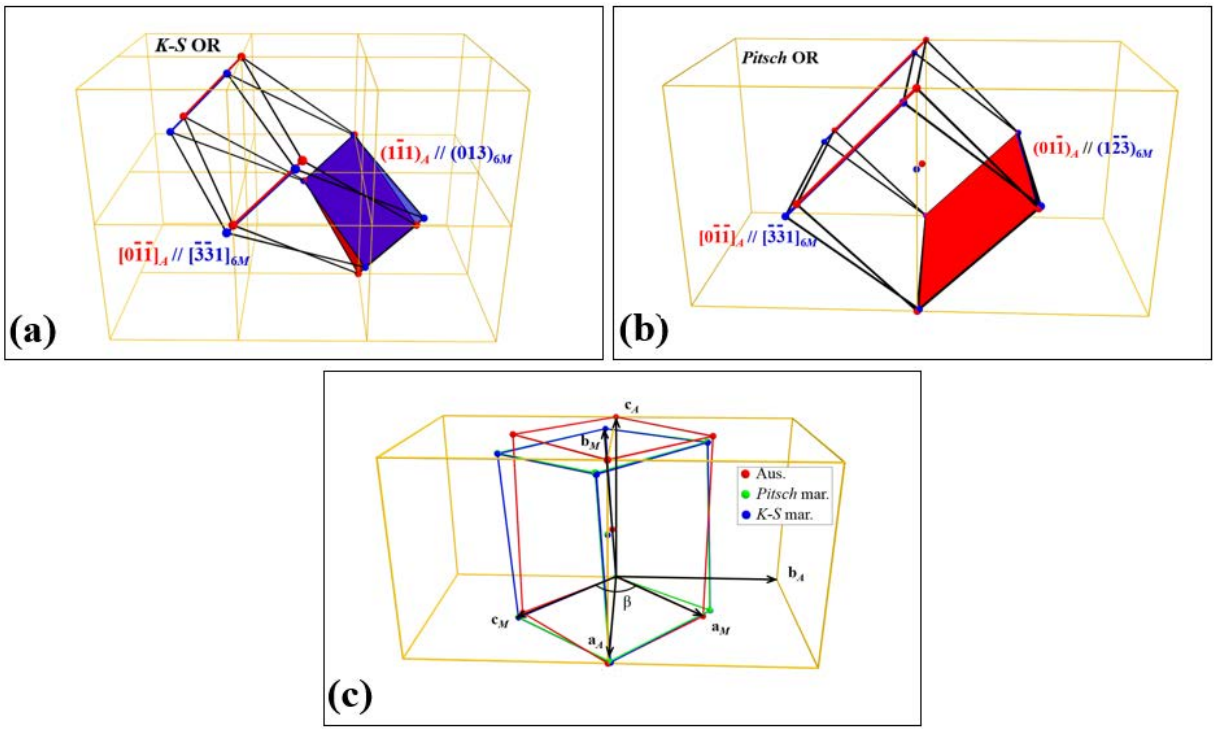

Fig. 5. 5 Illustration of lattice distortions under the *K-S* (a) and the *Pitsch* (b) relations. *OR* plane and direction of austenite and martensite are represented in red and blue, respectively. The unit cells of martensite (average structure) under the *K-S* and the *Pitsch* paths are shown in (c).

The strain components of their related *deformation gradient tensors* are summarized in Table 5. 3. It is seen that the normal strain components (dilation) under the *K-S* path are larger than those of the *Pitsch* path, whereas the shear strain components under the *K-S* path are smaller than those that under the *Pitsch* path. It should be noted that the amount of all normal and shear strains of the *K-S* and the *Pitsch* paths are comparable to each other and also comparable to those reported in other shape memory alloys [271], which implies that both the *K-S* and the *Pitsch* paths are possible in the present material. The corresponding theoretical unit cells of martensite under the *Pitsch*

(green) and the *K-S* (blue) path are demonstrated in Fig. 5. 5c. It is seen that these two unit cells seem to largely overlap, although they are associated with two different transformation strains (Fig. 5. 5a and b). The disorientation between these two lattices is as small as 0.44°.

Table 5. 3 Components of lattice distortion from austenite to martensite under *K-S* and *Pitsch* paths.

K-S path		*Pitsch* path	
Dilation in $[\bar{2}\bar{1}1]_A$	-0.5114 %	Dilation in $[100]_A$	0.4058 %
Dilation in $[0\bar{1}\bar{1}]_A$	-0.1299 %	Dilation in $[0\bar{1}\bar{1}]_A$	0.1298 %
Dilation in $[1\bar{1}1]_A$	0.6832 %	Dilation in $[01\bar{1}]_A$	-0.5788 %
Shear in $(1\bar{1}1)_A[\bar{2}\bar{1}1]_A$	0.0061	Shear in $(0\bar{1}1)_A[100]_A$	0.0091
Shear in $(\bar{2}\bar{1}1)_A[0\bar{1}\bar{1}]_A$	-0.0769	Shear in $(0\bar{1}\bar{1})_A[0\bar{1}\bar{1}]_A$	-0.0103
Shear in $(1\bar{1}1)_A[0\bar{1}\bar{1}]_A$	-0.0908	Shear in $(0\bar{1}1)_A[0\bar{1}\bar{1}]_A$	-0.1185

5.2.2 Relation between martensitic transformation strain path and microstructure of martensite

Due to the singularity of crystal symmetry involved in different transformation path (the *OR* plane and the *OR* directions), the microstructures of the product phase, such as the number of martensite variant, variant organization manner and variant interface, could be different and should be explored.

5.2.2.1 Theoretical martensite variants under *K-S* and *Pitsch* paths

With the crystal structure of the austenite and the martensite, all possible martensite variants within one austenite grain under the *K-S* and the *Pitsch* path were first theoretically deduced. Results show that the numbers of the distinct orientation variants under the two paths, henceforth termed as *K-S* and *Pitsch* variants, are the same and equal to 24, as demonstrated in Fig. 5. 6, where the *K-S* and the *Pitsch* variants were indicated with blue open circles and red solid crosses, respectively. It is seen that the orientations of the 24 *K-S* variants are almost equivalent with their corresponding *Pitsch* variants with a small misorientation angle of 0.44°. For a clear identification, the predicted variants are numbered 1 ~ 24, as shown in Fig. 5. 6. The counterpart variants with

similar orientations under the *K-S* and the *Pitsch* path, such as variant 1, are termed as *K-S* 1 and *Pitsch* 1, respectively. The specific transformation strain paths for the 24 *K-S* and the 24 *Pitsch* variants were detailed and listed in Table 5. 4. It is seen that for the counterpart *K-S* and *Pitsch* variants, they conserve the same direction but different planes during transformation.

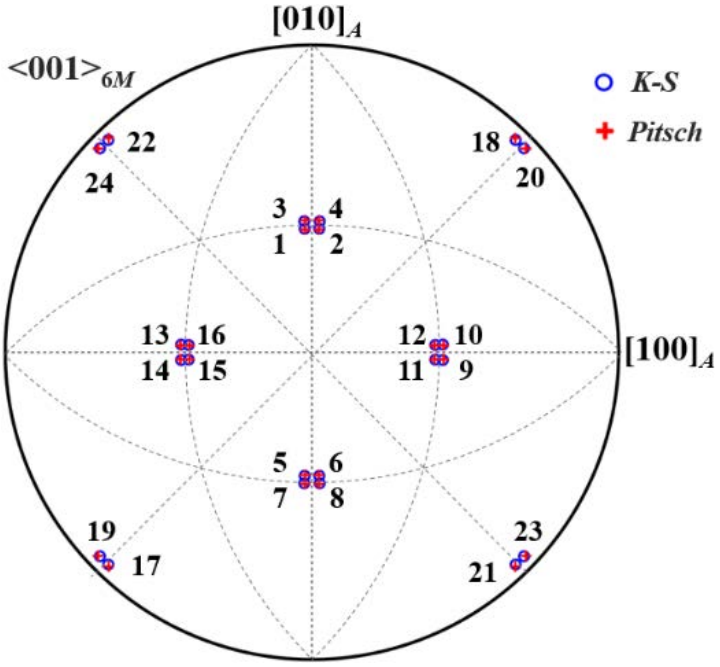

Fig. 5. 6 $\langle 001 \rangle_{6M}$ stereographic projection representing all theoretical martensite variants under the *K-S* and the *Pitsch* path. The crystal lattice basis of their corresponding austenite is utilized as the projection reference.

Table 5. 4 Martensitic transformation strain paths for various *K-S* and *Pitsch* variants and their related crystallographic rotational symmetry elements. For *K-S* variants, their corresponding Bishop-Hill notation [272, 273] for each variant are also listed, where ***a***, ***b***, ***c*** and ***d*** represent four kinds of $\{111\}_A$ shear planes and *I*, *II* and *III* indicate the distinct shear directions.

Variant type	Rotational symmetry	*K-S* transformation path			*Pitsch* transformation path	
		Plane	direction	Bishop-Hill notation	Plane	direction
1	**(x, y, z)**	$(\bar{1}\ \bar{1}\ \bar{1})$	$[1\ 0\ \bar{1}]$	aII	(1 0 1)	$[1\ 0\ \bar{1}]$
2	**(x, -y, -z)**	$(\bar{1}\ 1\ 1)$	[1 0 1]	cII	$(1\ 0\ \bar{1})$	[1 0 1]
3	**(-x, -z, -y)**	(1 1 1)	$[\bar{1}\ 1\ 0]$	-aIII	$(\bar{1}\ \bar{1}\ 0)$	$[\bar{1}\ 1\ 0]$
4	**(-x, z, y)**	$(1\ \bar{1}\ \bar{1})$	$[\bar{1}\ \bar{1}\ 0]$	-cIII	$(\bar{1}\ 1\ 0)$	$[\bar{1}\ \bar{1}\ 0]$
5	**(-x, y, -z)**	$(1\ \bar{1}\ 1)$	$[\bar{1}\ 0\ 1]$	dII	$(\bar{1}\ 0\ \bar{1})$	$[\bar{1}\ 0\ 1]$
6	**(-x, -y, z)**	$(1\ 1\ \bar{1})$	$[\bar{1}\ 0\ \bar{1}]$	bII	$(\bar{1}\ 0\ 1)$	$[\bar{1}\ 0\ \bar{1}]$
7	**(x, -z, y)**	$(\bar{1}\ 1\ \bar{1})$	[1 1 0]	-dIII	$(1\ \bar{1}\ 0)$	[1 1 0]
8	**(x, z, -y)**	$(\bar{1}\ \bar{1}\ 1)$	$[1\ \bar{1}\ 0]$	-bIII	(1 1 0)	$[1\ \bar{1}\ 0]$
9	**(z, x, y)**	$(\bar{1}\ \bar{1}\ \bar{1})$	$[\bar{1}\ 1\ 0]$	aIII	(1 1 0)	$[\bar{1}\ 1\ 0]$
10	**(-z, x, -y)**	$(1\ \bar{1}\ 1)$	[1 1 0]	dIII	$(\bar{1}\ 1\ 0)$	[1 1 0]
11	**(-y, -x, -z)**	(1 1 1)	$[0\ \bar{1}\ 1]$	-aI	$(0\ \bar{1}\ \bar{1})$	$[0\ \bar{1}\ 1]$
12	**(y, -x, z)**	$(\bar{1}\ 1\ \bar{1})$	$[0\ \bar{1}\ \bar{1}]$	-dI	$(0\ \bar{1}\ 1)$	$[0\ \bar{1}\ \bar{1}]$
13	**(-z, -x, y)**	$(1\ 1\ \bar{1})$	$[1\ \bar{1}\ 0]$	bIII	$(\bar{1}\ \bar{1}\ 0)$	$[1\ \bar{1}\ 0]$
14	**(z, -x, -y)**	$(\bar{1}\ 1\ 1)$	$[\bar{1}\ \bar{1}\ 0]$	cIII	$(1\ \bar{1}\ 0)$	$[\bar{1}\ \bar{1}\ 0]$
15	**(-y, x, z)**	$(1\ \bar{1}\ \bar{1})$	$[0\ 1\ \bar{1}]$	-cI	(0 1 1)	$[0\ 1\ \bar{1}]$
16	**(y, x, -z)**	$(\bar{1}\ \bar{1}\ 1)$	[0 1 1]	bIII	$(0\ 1\ \bar{1})$	[0 1 1]
17	**(y, z, x)**	$(\bar{1}\ \bar{1}\ \bar{1})$	$[0\ \bar{1}\ 1]$	aI	(0 1 1)	$[0\ \bar{1}\ 1]$
18	**(-y, -z, x)**	$(1\ 1\ \bar{1})$	[0 1 1]	bI	$(0\ \bar{1}\ 1)$	[0 1 1]
19	**(-z, -y, -x)**	(1 1 1)	$[1\ 0\ \bar{1}]$	-aII	$(\bar{1}\ 0\ \bar{1})$	$[1\ 0\ \bar{1}]$
20	**(z, y, -x)**	$(\bar{1}\ \bar{1}\ 1)$	$[\bar{1}\ 0\ \bar{1}]$	-bII	$(1\ 0\ \bar{1})$	$[\bar{1}\ 0\ \bar{1}]$
21	**(y, -z, -x)**	$(\bar{1}\ 1\ 1)$	$[0\ 1\ \bar{1}]$	cI	$(0\ \bar{1}\ \bar{1})$	$[0\ 1\ \bar{1}]$
22	**(-y, z, -x)**	$(1\ \bar{1}\ 1)$	$[0\ \bar{1}\ \bar{1}]$	dI	$(0\ 1\ \bar{1})$	$[0\ \bar{1}\ \bar{1}]$
23	**(-z, y, x)**	$(1\ \bar{1}\ \bar{1})$	[1 0 1]	-cII	$(\bar{1}\ 0\ 1)$	[1 0 1]
24	**(z, -y, x)**	$(\bar{1}\ 1\ \bar{1})$	$[\bar{1}\ 0\ 1]$	-dII	(1 0 1)	$[\bar{1}\ 0\ 1]$

5.2.2.2 Theoretical variant organization features under *K-S* and *Pitsch* paths

To explore the relation of the martensite variants with their related "transformation plane" (the *OR* plane), the stereographic projection of the transformation planes for the *K-S* ($\{103\}_{6M}$) and the *Pitsch* ($\{1\bar{2}\bar{3}\}_{6M}$) variants were plotted and illustrated in Fig. 5. 7. For the *K-S* path, it is seen that the 24 variants are gathered into four variant clusters (Fig. 5. 7a). The pole of each variant cluster that consists of six *K-S* variants perfectly coincide with one $\{111\}_A$ pole of austenite. As a consequence, each $\{111\}_A$ plane of austenite would generate six *K-S* variants across the structural transition. For example, *K-S* variants 1, 3, 9, 11, 17 and 19 correspond to the same transformation plane $(111)_A$, as shown in Fig. 5. 7a. Different from the *K-S* path, the 24 *Pitsch* variants are located into six variant clusters and each cluster is composed of four variants (Fig. 5. 7b). It implies that each $\{110\}_A$ plane could produce four *Pitsch* variants.

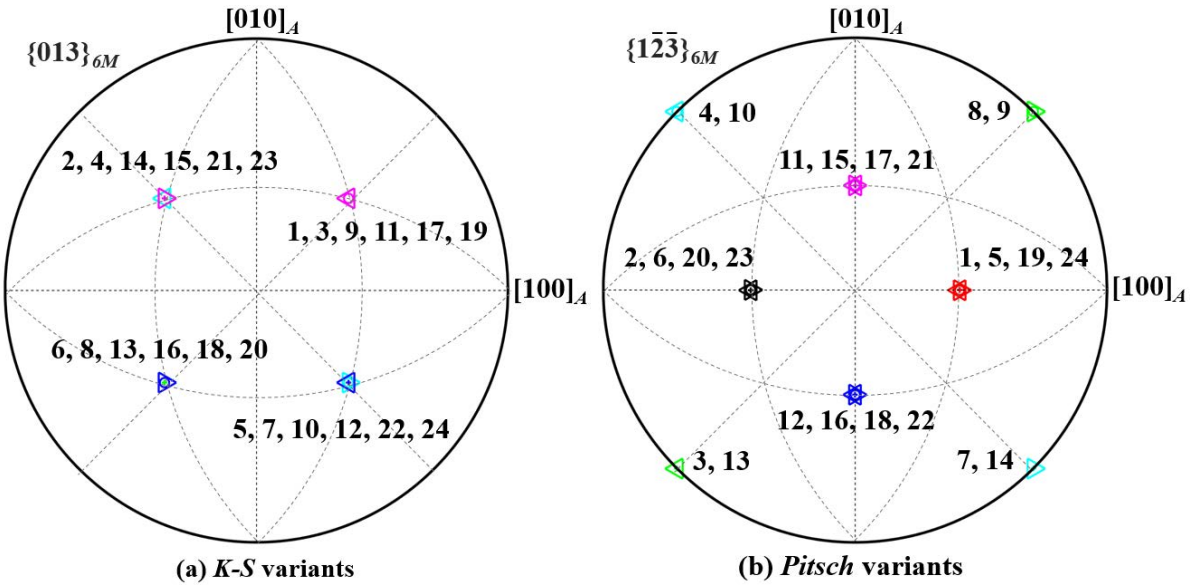

Fig. 5. 7 (a) Stereographic projections of $\{103\}_{6M}$ for 24 *K-S* variants; (b) Stereographic projections of $\{1\bar{2}\bar{3}\}_{6M}$ for 24 *Pitsch* variants. The lattice basis of their related austenite is utilized as the projection reference. The numbering of *K-S* and *Pitsch* variants is consistent with that in Table 5. 4.

The *K-S* and the *Pitsch* path with respect to the $L2_1$ austenite lattice are illustrated in Fig. 5. 8. For a better illustration, only one transformation plane in each path, *e.g.* $(111)_A$ under *K-S* path and

$(10\bar{1})_A$ under *Pitsch* path, is plotted. The normal of transformation plane and transformation direction are indicated with the green and red arrow, respectively. It is seen that there are three distinct <110>$_A$ transformation directions, $[01\bar{1}]_A$, $[\bar{1}10]_A$ and $[0\bar{1}1]_A$, on one transformation plane under the *K-S* path. However, there is only one <110>$_A$ transformation direction, $[101]_A$, in each transformation plane, for the *Pitsch* path, as shown in Fig. 5. 8b. The specific transformation paths of the six $(111)_A$ plane-related *K-S* variants 1, 3, 9, 11, 17 and 19, and the four $(\bar{1}01)_A$ plane related-*Pitsch* variants 2, 6, 20, 23, are illustrated in Fig. 5. 9 and Fig. 5. 10, respectively. Under the *K-S* path, it is seen that one certain transformation direction together with the transformation plane will generate two distinct martensite variants. For example, $[10\bar{1}]_A$ direction with $(111)_A$ plane will generate *K-S* variant of 1 (Fig. 5. 9a) and 19 (Fig. 5. 9f) by changing the sign of the normal of the transformation plane. Thus, three distinct transformation directions ($[01\bar{1}]_A$, $[\bar{1}10]_A$ and $[0\bar{1}1]_A$) would generate six *K-S* variants (1, 3, 9, 11, 17 and 19), as shown in Fig. 5. 9a ~ f. Different from the *K-S* path, one certain transformation direction together with the transformation plane will generate four distinct *Pitsch* variants. For instance, the transformation direction $[101]_A$ would generate *Pitsch* variants 2 (Fig. 5. 10a), 6 (Fig. 5. 10b), 20 (Fig. 5. 10c) and 23 (Fig. 5. 10d) by changing the sign of the normal of the transformation plane and that of the transformation directions. This difference in crystallographic symmetry of transformation plane and direction between the *K-S* and the *Pitsch* path would result in different variant organization.

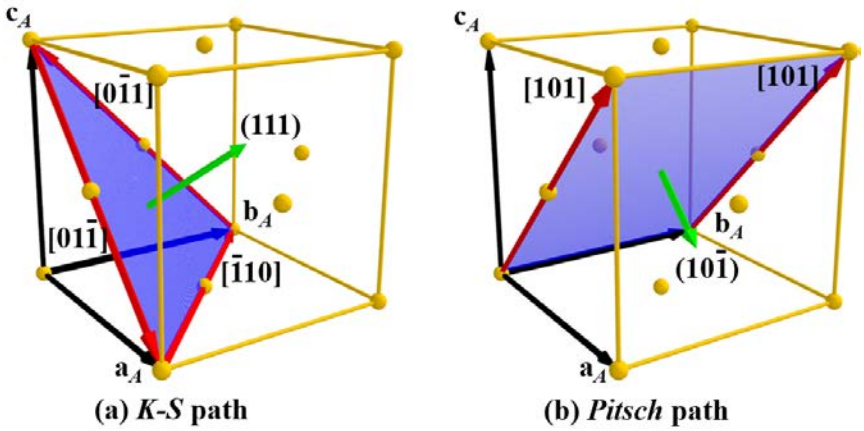

Fig. 5. 8 Illustration of *K-S* (a) and *Pitsch* (b) transformation strain path with respect to $L2_1$ austenite lattice. The transformation planes and directions are highlighted with the blue planes and the red arrows, respectively. The normal of the transformation planes are indicated with the green arrows. For a clear illustration, only Mn atoms (in orange) are plotted.

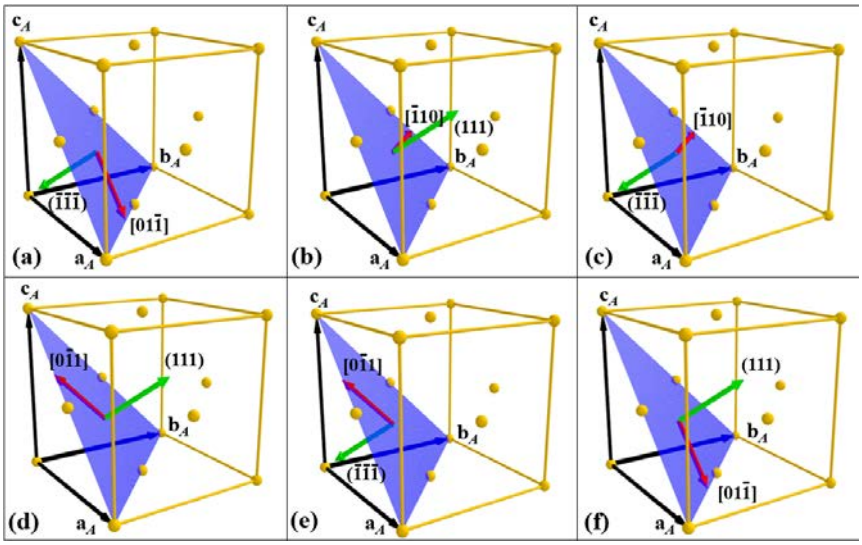

Fig. 5. 9 Illustration of the specific transformation paths for six *K-S* variants within $(111)_A$ cluster. (a) 1; (b) 3; (c) 9; (d) 11; (e) 17; (f) 19. The normal of transformation planes and directions are highlighted with the green and red arrows, respectively. For a clear illustration, only Mn atoms (in orange) are plotted.

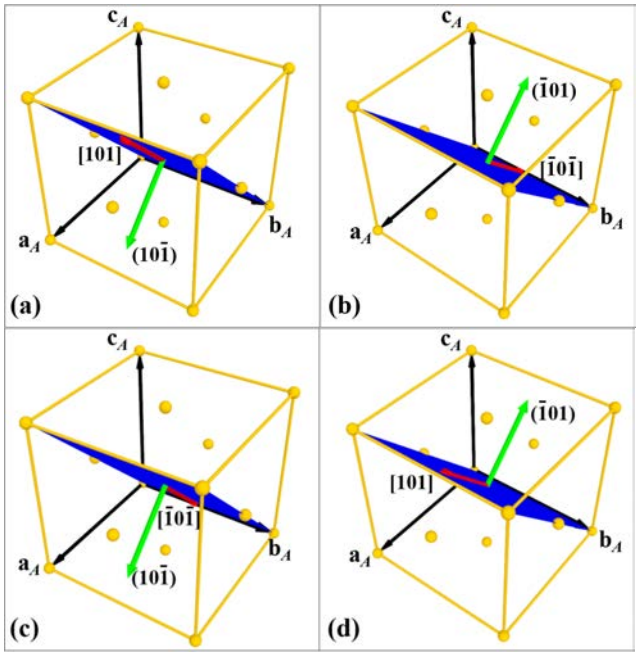

Fig. 5. 10 Illustration of specific transformation paths of the four *Pitsch* variants within $(10\bar{1})_A$ cluster. (a) 2; (b) 6; (c) 20; (d) 23. The normal of transformation planes and directions are highlighted with the green and red arrows, respectively. For a clear illustration, only Mn atoms (in orange) are plotted.

It is known that the evolution of the microstructure across the martensitic transformation is involved in a self-accommodated manner. Thus, variant organization should simultaneously satisfy the strain and stress compatibility requirements. The former guaranty that the material is continuous and no crack is created between variant interfaces. The latter insure that the stress in the vicinity of the interface varies continuously and no stress mutation occurs. In theory, the satisfaction of these two conditions in variant interface requires that the two adjacent variants are generated from the same (or opposite) transformation plane and direction of the parent phase. Under the *K-S* path, since one pair of transformation plane and direction can only generate two martensite variants, the self-accommodated "sandwich-like" structure with two alternately distributed variants (*AB…AB*) should be observed in the material. However, for the *Pitsch* path, one pair of transformation plane and direction can produce four different martensite variants, as shown in Fig. 5. 10. Thus, it should be possible to form four variants that are alternately distributed to form a self-accommodated cluster in a local area of the material.

Moreover, the microstructural evolution across the structural transition should also satisfy the minimum interfacial and bulk elastic strain energy. First, the interfacial energy of possible variant organization is analyzed. As examples, variant organizations of the six $(111)_A$ plane-related *K-S* variants (V_1, V_3, V_9, V_{17}, V_{11} and V_{19}) and the four $(10\bar{1})_A$ plane-related *Pitsch* variants (V_2, V_6, V_{20} and V_{23}) are analyzed. Based on the misorientation calculations, we found that only 3 variants are twin-related with one arbitrary variant under the *K-S* path. For instance, only V_3, V_{11} and V_{19} are twin-related with V_1. Then, the interfaces of variant pairs V_1: V_3, V_1: V_{11} and V_1: V_{19} could be the twinning plane between each pair and thus could be coherent low-energy interfaces, whereas the interfaces of V_1: V_9 and V_1: V_{17}) could not be coherent low-energy interfaces. Thus, only three twin-related variant organizations are possible in view of minimum interface energy. Different from the *K-S* variants, all the four *Pitsch* variants are mutually twin-related and could have their twinning planes as variant interfaces to achieve low-energy interfaces.

Second, the bulk elastic strain energy of variant formation is analyzed. In theory, the bulk elastic strain energy across the structural transition should be closely related to the volume change between the parent and the product phase. The three eigenvalues of the combined *deformation gradient tensor* of the variant group of (Eq. 5-1) should be close to 1 for a minimum elastic strain for the transformation. The combined *deformation gradient tensor* of two variants can be expressed as follows:

$$\boldsymbol{F}^{\mathbf{A}} = \mathrm{x} \times \boldsymbol{F}_{\mathrm{i}}^{\mathbf{A}} + (1\text{-}\mathrm{x}) \times \boldsymbol{F}_{\mathrm{j}}^{\mathbf{A}} \qquad (0 \le \mathrm{x} \le 1) \tag{5-1}$$

where $\boldsymbol{F}_{\mathrm{i}}^{\mathbf{A}}$ and $\boldsymbol{F}_{\mathrm{j}}^{\mathbf{A}}$ represent the *deformation gradient tensors* of variant *i* and *j*, and x is their relative volume fraction. The evolution of the eigenvalues for the *K-S* and the *Pitsch* organization are shown in Fig. 5. 11 and Fig. 5. 12, respectively. Under the *K-S* path, it is seen that the three eigenvalues significantly increase with the organization of V_1: V_3 and V_1: V_{11}. Thus, these two kinds of organizations are not unfavorable. For the organization of V_1: V_{19}, all the three eigenvalues are close to 1 and stay constant with the variation of their relative volume. Thus, this variant organization could be possible. Under the *Pitsch* path, as shown in Fig. 5. 12, the three eigenvalues for any arbitrary two variants are close to 1 and stay constant with the variation of their relative volume, suggesting that one variant can freely organize with other three variants under the *Pitsch* path without increasing the volume change. The results are in good agreement with the analysis based on the strain and stress compatibility conditions.

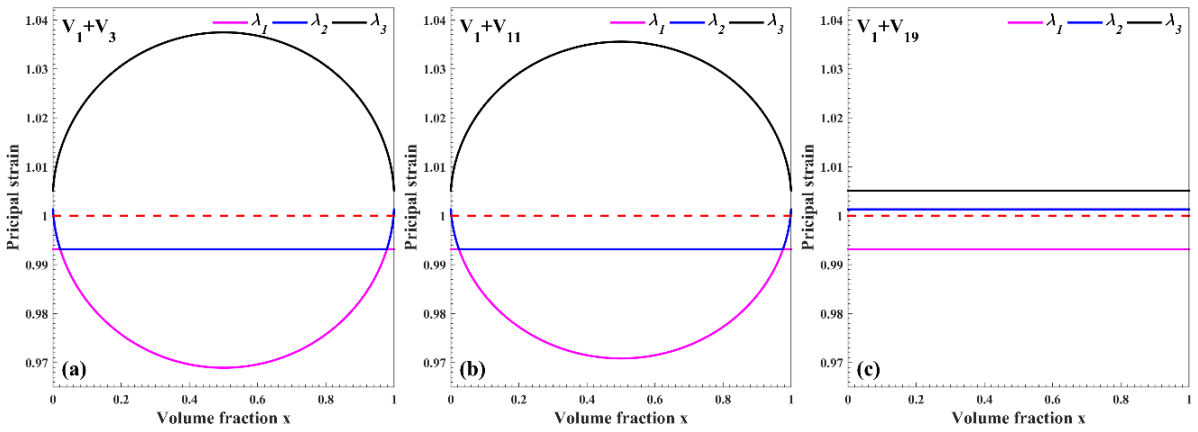

Fig. 5. 11 Eigenvalue evolution of the combined *deformation gradient tensor* for the twin-related *K-S* variant organizations with volume fraction x. (a) Variant 1 and 3; (b) Variant 1 and 11; (c) Variant 1 and 19. As a reference, the principal strain equals to zero is illustrated with the dashed red line.

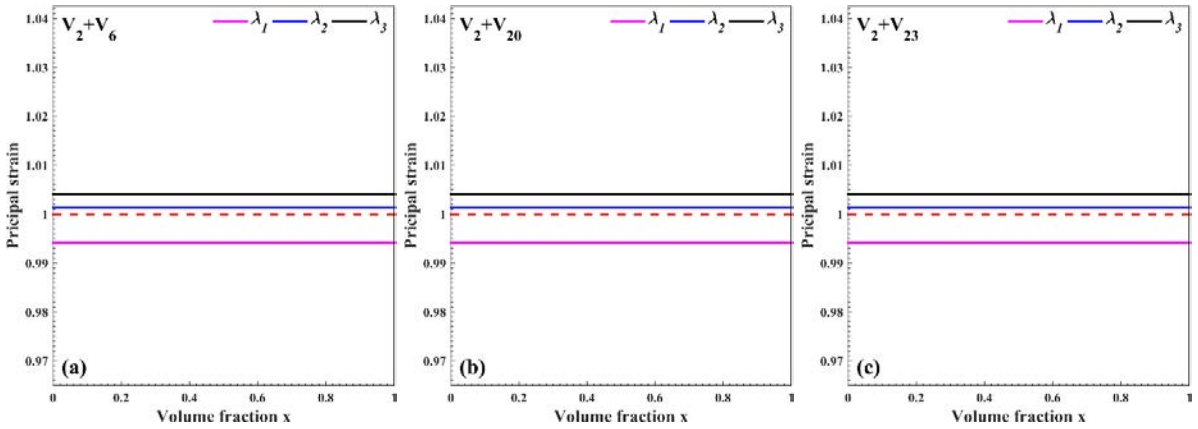

Fig. 5. 12 Eigenvalue evolution of the combined *deformation gradient tensor* for the twin-related *Pitsch* variant organizations with volume fraction x. (a) Variant 2 and 6; (b) Variant 2 and 20; (c) Variant 2 and 23. For a comparison, the scale of the vertical axes are set to be equal to those in Fig. 5. 11.

5.2.2.3 Determination of martensitic transformation strain path

With the predicted variant organization features under the *K-S* and the *Pitsch* path, in combination with the observed microstructure features, the transformation path in Ni-Mn-In alloys can be uniquely determined. As shown in Fig. 5. 1, there are always four kinds of martensite variants rather than two in the local areas and the "sandwich-like" structure has never been observed. It implies that the *Pitsch* path should be the effective transformation path for Ni-Mn-In alloys. Fig. 5. 13 shows the $\langle 001 \rangle_{6M}$ stereographic projection of the measured four kinds of variants in Fig. 5. 1. It is seen that they are in good accordance with the predicted *Pitsch* variants 2, 23, 20 and 6 (Fig. 5. 6a). As shown in Fig. 5. 7b, these variants exactly come from the same $\{101\}_A$ variant cluster under the *Pitsch* path. It is in good agreement with our deductions that the self-accommodated four variants should be associated with the same transformation plane and direction in the investigated material. Moreover, the interfaces between V_A and V_C or (V_B and V_D) is $\{1\bar{2}\bar{3}\}_{6M}$ that corresponds to the transformation plane $\{10\bar{1}\}_A$ of the austenite phase. This further confirms that the *Pitsch* path is the transformation path in Ni-Mn-In alloys.

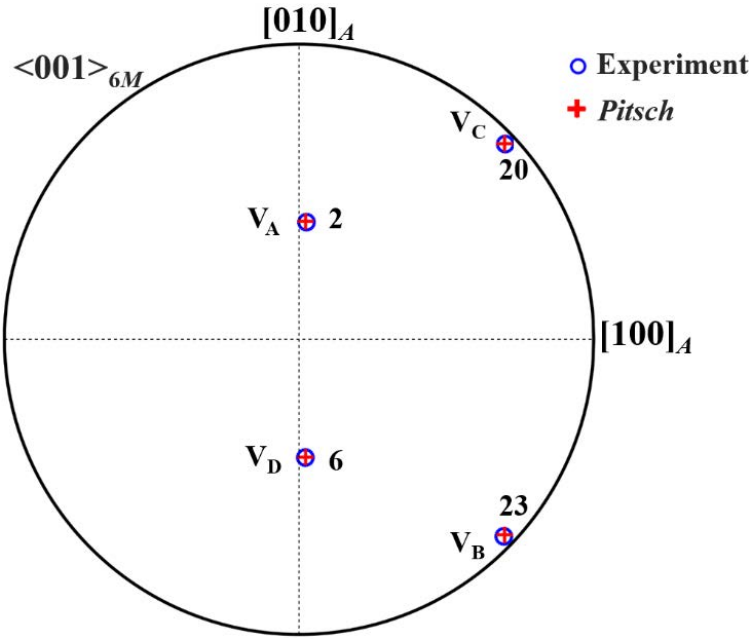

Fig. 5. 13 $\langle 001 \rangle_{6M}$ stereographic projection of experimental and theoretical martensite variants. The blue solid circles represent the measured martensite variants within one martensite colony in Fig. 5. 1. The red markers indicate the corresponding predicted *Pitsch* variants.

5.2.3 Mechanism of martensite variant organization

With the determined transformation strain path of the structural transition, the underlying mechanism of variant organization in Ni-Mn-In alloys can be revealed. It is clear now that the four distinct variants within one colony are generated from the same (or opposite) transformation plane and direction. Due to the crystallographic symmetry of austenite (cubic), there are six groups of independent transformation systems. Thus, in theory, it should generate at maximum six distinct martensite colonies and 24 distinct orientation variants within one austenite grain. It is in good agreement with the observed experimental results, as shown in Fig. 5. 14. Independent martensite colonies are highlighted in different colors and labeled in G1 ~ G6 in Fig. 5. 14b.

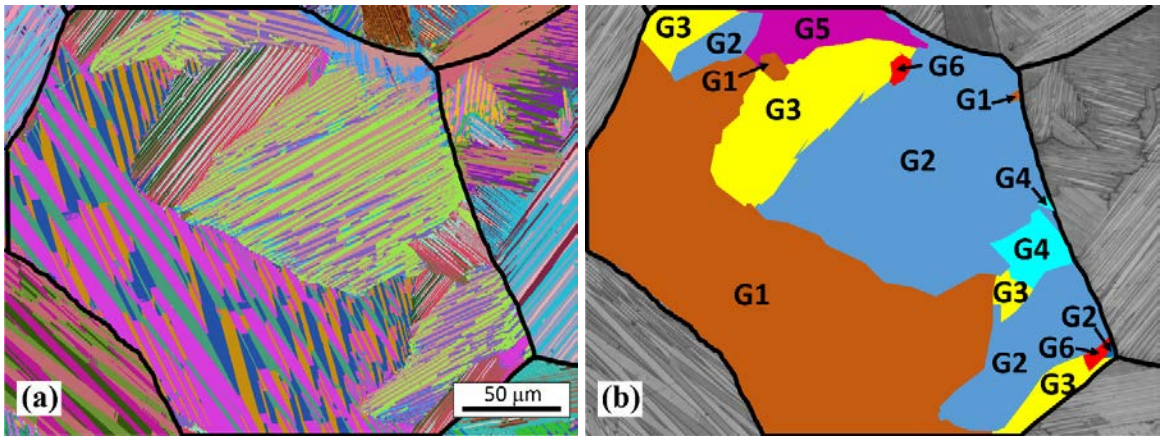

Fig. 5. 14 Crystallographic orientation (a) and band contrast (b) micrograph of $Ni_{50}Mn_{36}In_{14}$ at room temperature. Individual martensite colonies in (b) are highlighted in different colors and labeled in G1 ~ G6.

5.3 Geometrical compatibility between austenite and martensite

For Ni-Mn-In based alloys, the relatively large hysteresis loss, associated with the magnetostructural transition, is an important negative factor limiting their pratical application. It is well recongnized that the hysteresis loss across the magnetostructral transition is closely related to the stressed transition layer between austenite and martensite that would give rise to an energy barrier to cause energy consumption [139, 274]. The general strategy to eliminate the stressed transition layer is to increase the geometrical compitability between the corresponding phases. Thus, the study on geometrical compatiblity between austenite and martensite in Ni-Mn-In based alloys should be meanningful.

In this work, a Co-doped quaternary $Ni_{45}Co_5Mn_{36.8}In_{13.2}$ alloy that has coexisting two-phases at room temperature was chosen. The ingots were fabricated by arc-melting. The as-cast rods were further annealed in a sealed quartz tube under Ar atmosphere at 1173 K for 24 hours followed by water quenching. The experimental details are described in Chapter 2. The lattice parameters of austenite was determined to be a = 5.9823 Å. The lattice parameters of the average structure of martensite was refined to be a = 4.3969Å, b = 5.5769Å, c = 4.3269 Å, and β = 93.6774°. Then, with the determined transformation path, the *deformation gradient tensor* $\boldsymbol{F}_{D'\leftarrow D}^{OR}$ and *transformation stretch tensor* $\boldsymbol{U}^{OR}$ for lattice distortion across the structural transition can be determined, as given in Eq. 5-1 and 5-2, respectively, where *OR* represents the orthonormal

coordinate system defined by the *OR* direction, the *OR* plane normal and the cross product of these two vectors as the basis vectors.

$$\boldsymbol{F}_{\boldsymbol{D'\leftarrow D}}^{\boldsymbol{OR}} = \begin{bmatrix} 0.99750 & 0 & 0.01051 \\ -0.01207 & 1.00015 & -0.13122 \\ 0 & 0 & 0.99145 \end{bmatrix} \quad (5\text{-}1)$$

$$\boldsymbol{U}^{\boldsymbol{OR}} = \begin{bmatrix} 0.99754 & -0.00586 & 0.00586 \\ -0.00586 & 0.99797 & -0.06574 \\ 0.00586 & -0.06574 & 0.99797 \end{bmatrix} \quad (5\text{-}2)$$

The three eigenvalues of the *transformation stretch tensor* $\boldsymbol{U}^{\boldsymbol{OR}}$ were determined to be $\lambda_1 = 0.93223$, $\lambda_2 = 0.99652$ and $\lambda_3 = 1.06473$. Unexpectly, it is seen that the λ_2 is very close to 1, suggesting the austenite and martensite phase has a relative good geometrical compitablitiy in the present material. It seems that this is not the origin of the large hysteresis losses that has been observed in the materials with similar compositions [28, 59, 137, 138]. Fig. 5. 15a shows an EBSD crystallograhic orientation micrograph of $Ni_{45}Co_5Mn_{36.8}In_{13.2}$ alloy at room temperature. It is seen that two phases, austenite and modulated martensite, coexist. The *habit plane* is bordered by single martensite variant with austenite, rather than the generally observed “sandwich-like” two variants. It is in good agreement with the theoretical result that the λ_2 is very close to 1. However, with high resolution transmission electron microscopy (HRTEM), a stressed transition layer with a thickness of about 20 nm between austenite and martensite was detected, as shown in Fig. 5. 15b. This could be one of the reason of the relative large hysteresis loss in the investigated materials [28, 59, 137, 138]. Furthermore, it implies that the criterion of $\lambda_2 = 1$ is not sufficient to guarantee the well geometric compatibility between the austenite and the martensite. The more effective criteria to evaluate the geometric compatibility are still in need.

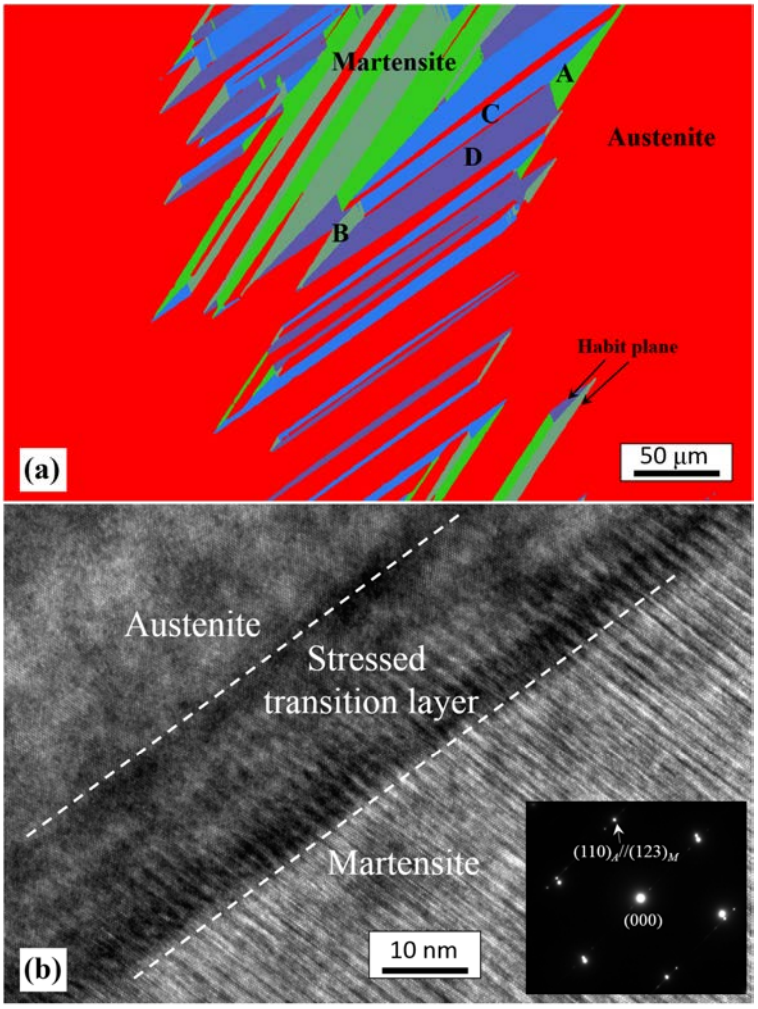

Fig. 5. 15 (a) SEM/ EBSD orientation micrograph of $Ni_{45}Co_5Mn_{36.8}In_{13.2}$ alloy measured at room temperature showing two coexisting phases and (b) HRTEM phase contrast micrograph demonstrating the transition layer at the *habit plane* region.

5.4 Summary

In this chapter, the crystallographic orientation relationship (*OR*) between austenite and martensite, martensitic transformation strain path and its effect on the microstructure of martensite, and geometrical compatibility between austenite and martensite were investigated. With the measured crystallographic orientation information of austenite and martensite by EBSD technique, Both *Kurdjumov- Sachs* (*K-S*) and *Pitsch* relations are found to be possible to describe the lattice correspondence between austenite and martensite. The magnetostructural transition in Ni-Mn-In alloys follow *Pitsch* type of transformation path, *i.e.* $\{101\}_A \langle 10\bar{1}\rangle_A$. Investigations show that four

distinct martensite variants within one colony are transformed from the same (or opposite) transformation plane and direction of austenite. Due to cubic symmetry, a maximum 6 distinct martensite colonies and 24 distinct variants within one austenite grain can be obtained. With the determined martensitic transformation strain path, the geometrical compatibility between austenite and martensite are explored. The middle eigenvalue of the *transformation stretch tensor* across the structural transition is close to 1 (0.99652) and the *habit plane* is bordered by single martensite variant with austenite, suggesting a relative good geometrical compatibility between the austenite and the martensite. A stressed transition layer of around 20 nm near the *habit plane* evidenced by HRTEM implies that the criterion of $\lambda_2 = 1$ is not sufficient to guarantee the geometric compatibility.

Chapter 6 Performance

For Ni-Mn-In based alloys, metamagnetic shape memory effect (MMSME) and magnetocaloric effect (MCE) are two important properties. With the determined information on crystal structure, microstructure and martensitic transformation, these two effects were further studied in this chapter. For the former, we focused on variant rearrangement/ selection under external mechanical loading. Two kinds of loading strategies, *i.e.* loading at martensite state and loading across the structural transition, were investigated by means of *ex-situ* SEM/ EBSD and *in-situ* neutron diffraction (ND). Schmid factor for martensitic transformation strain path was introduced to evaluate the efficiency of martensite variant selection during loading across the structural transition. For the latter, the influences and correlated underlying mechanisms of heat treatment on MCE and its related hysteresis loss were explored.

6.1 Martensite variant rearrangement under external mechanical loads

To obtain shape memory effects in SMAs, an appropriate prestrain to martensite is generally required, prior to applying an actuating temperature/ magnetic field to induce the inverse martensitic transformation and realize the shape recovery. In fact, this process is realized by rearranging martensite variants under external loads [2, 7, 56]. In this section, the behaviors and mechanisms of variant rearrangement under mechanical loading in martensite state and across the structural transition were studied.

6.1.1 Mechanical loading in martensite state

Mechanical loading in martensite state, generally utilized to induce a prestrain for SMAs, were first studied. The investigations were performed in two steps. First, with determined morphological and crystallographic information of modulated martensite in Ni-Mn-In based alloys, all favorable loading orientations were explored theoretically by means of Schmid factor (*SF*) calculations. Then, *ex-situ* microstructure examinations were carried out by electron backscatter diffraction (EBSD). In this work, the polycrystalline $Ni_{50}Mn_{36}In_{14}$ bulk samples was selected. The alloys were prepared by arc-melting technique and injected into a copper mould to obtain dense specimens. The as-cast rods were further annealed in a sealed quartz tube under Ar atmosphere at

1173 K for 24 hours followed by water quenching. The experimental details are described in Chapter 2.

6.1.1.1 Favorable loading direction predictions by Schmid factor calculations

As shown in Chapter 5, at most 24 orientation variants of the 6M modulated martensite can form in one initial austenite grain (Fig. 5. 14). These 24 orientation variants are self-accommodated into 6 distinct groups. Although the absolute crystallographic orientations of the 4 intra-colony orientation variants vary from one group to another, their interrelationships (*i.e.* the three twin relations) and boundary characteristics keep constant over the entire martensite microstructure. In this sense, individual groups (colonies) are crystallographically equivalent and can be treated as mechanical units to an external load. Considering the fact that martensite variants within one colony are twin-related one another, the variant rearrangement under external loading should be attributed to the so-called "detwinning" process [275]. Due to the specific variant organization illustrated in Fig. 4. 3b, the loading orientations with respect to the detwinning systems of the variants would play an important role during variant reorientation. Here, an attempt was made to explore possible effective loading orientations for the detwinning of the three types of twins.

First, we take one variant (variant A) as the host crystal of the other three variants (variants B, C and D). This implies that B, C and D could be regarded as the twins of A realized *via* the respective type-II, type-I and compound twinning, as summarized in Table 6. 1. Fig. 6. 1 presents the stereographic projections of the twinning planes K_1 and twinning directions η_1 of the three twinning systems in an orthonormal reference frame set to the Bravais lattice basis of variant A. In view of the polarity of twinning process [276], we specially select the projection plane that allows the K_1 and η_1 of the three twinning systems to be stereographically projected from the same hemisphere. It is seen that for the type-I and type-II twins, the respective K_1 and η_1 are very close to each other. For the compound twin, its K_1 is approximately perpendicular to the twinning planes of the type-I and type-II twins.

Table 6. 1 Twinning systems and twin types required for the formation of variants B, C and D *via* twinning of variant A. The twinning planes K_1 and twinning directions η_1 are referenced to the lattice basis of the 6M superstructure.

Twin variant	K_1	η_1	Twin type
B	$\{1.1240\ \bar{2}\ \overline{2.6280}\}_{6M}$	$<3.3264\ 3\ \overline{0.8912}>_{6M}$	Type-II
C	$\{\bar{1}\ 2\ 3\}_{6M}$	$<\bar{3}\ \bar{3}\ 1>_{6M}$	Type-I
D	$\{1\ 0\ 3\}_{6M}$	$<\bar{3}\ 0\ 1>_{6M}$	Compound

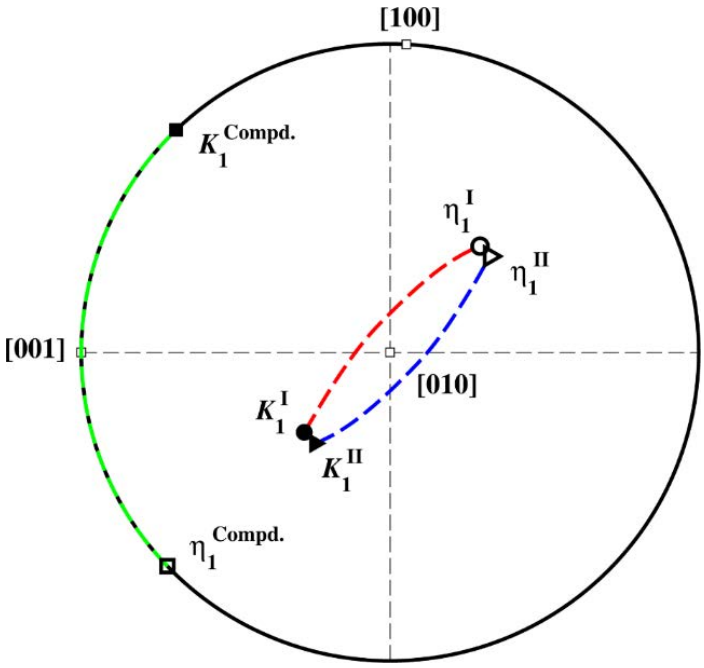

Fig. 6. 1 Stereographic projections of twinning planes K_1 and twinning directions η_1 of type-I, type-II and compound twins of variant A. The orthonormal basis set to the monoclinic lattice basis of variant A under the *Oxford Channel 5* convention is chosen as the projection reference. The poles of twinning planes (K_1^{I}, K_1^{II} and $K_1^{Compd.}$) and twinning directions (η_1^{I}, η_1^{II} and $\eta_1^{Compd.}$) of type-I, type-II and compound twins are represented in filled and open circles, triangles and squares, respectively.

With the specified twinning systems of one variant to produce the other three variants, it is possible to find out the optimum loading orientations for the reverse (detwinning) process to obtain single variant state. This can be done by applying an external load in all possible orientations with

respect to the host crystal. In what follows, we shall consider only the uniaxial compression mode due to its convenience for practical operation. If one twinning system is denoted by K_1 and η_1, the detwinning system is thus K_1 and $-\eta_1$. The Schmid factors (*SF*s) of the three detwinning systems were calculated as a function of loading orientation, as shown in stereographic projections in Fig. 6. 2.

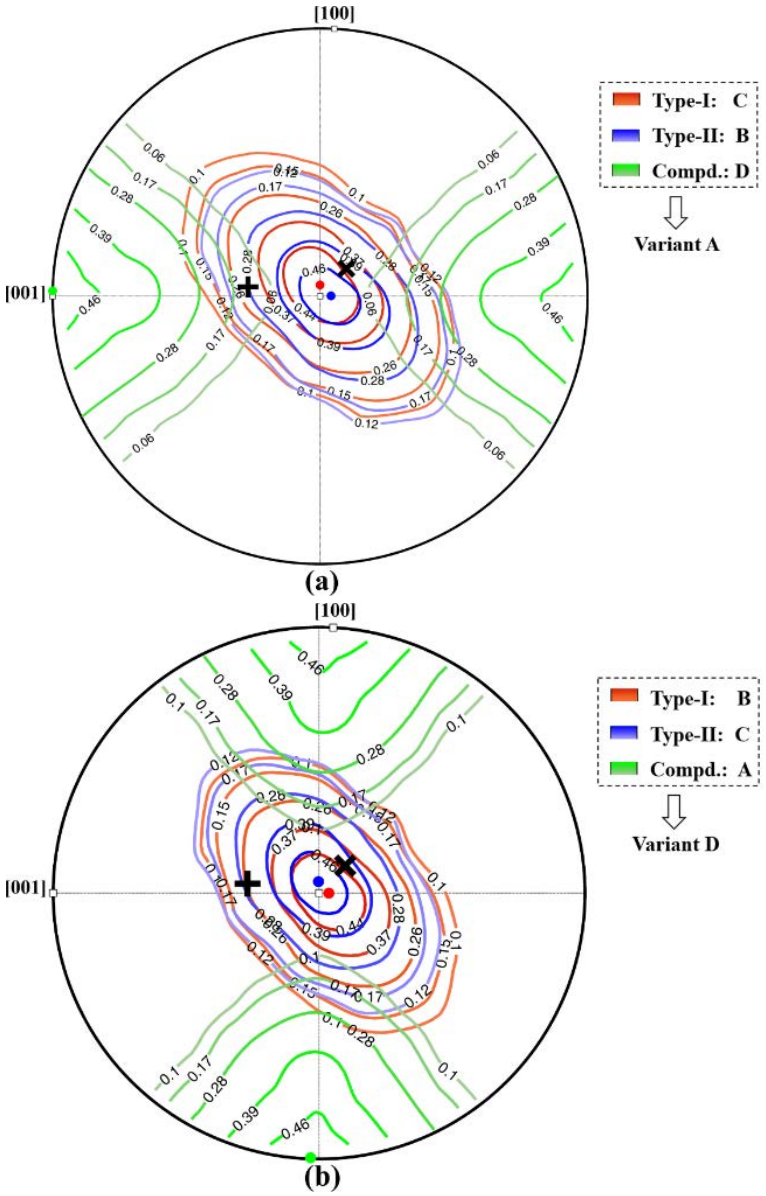

Fig. 6. 2 *SF* distributions of (a) variants B, C and D (host crystal A) and (b) variants A, B and C (host crystal D) under uniaxial compression. Contour lines for type-I, type-II and compound detwinning systems are plotted with gradient red, blue and green lines, respectively. The cross and the rotated cross indicate two different loading orientations for the *ex-situ* compression tests.

For the case of variant A as the host crystal (Fig. 6. 2a), the efficient *SF* zones for the type-I and type-II detwinning systems overlap to a large extent. It suggests that variant C (type-I twin) and variant B (type-II twin) could be simultaneously transformed into variant A under the same favorable loading orientation. Moreover, if choosing variant D as the host crystal of variants A, B and C (Fig. 6. 2b), the efficient loading orientations to eliminate variants B and C are the same as the above case. This means that under a favorable loading orientation to obtain variant A, variant D could also become favorable. Interestingly, in either case, there are two common zones where the detwinning of three variants (variants B, C and D for host variant A or variants B, C and A for host variant D) has positive *SF* values. However, in the two cases, the common zones are not the same in terms of loading orientations. It should be noted that in the above analyses, the choice of variant A or D as the host crystal is arbitrary. The rest variants can also be taken as the host crystal, and the analysis procedures remain the same.

6.1.1.2 *Ex-situ* microstructure examinations

Based on the above theoretical analyses, *ex-situ* uniaxial compression tests were performed on the polycrystalline $Ni_{50}Mn_{36}In_{14}$ bulk samples. Two special martensite colonies with different variant orientations with respect to the compressive loading orientations, as shown in Fig. 6. 3a and c, were presented to verify the above analyses. For the former (Fig. 6. 3a), the uniaxial loading direction was along one orientation with high *SF* for both type-I and type-II detwinning systems (marked with the rotated cross in Fig. 6. 2). For the latter (Fig. 6. 3c), the uniaxial loading direction was located within one common orientation zone with positive *SF* for all the three detwinning systems (marked with the cross in Fig. 6. 2).

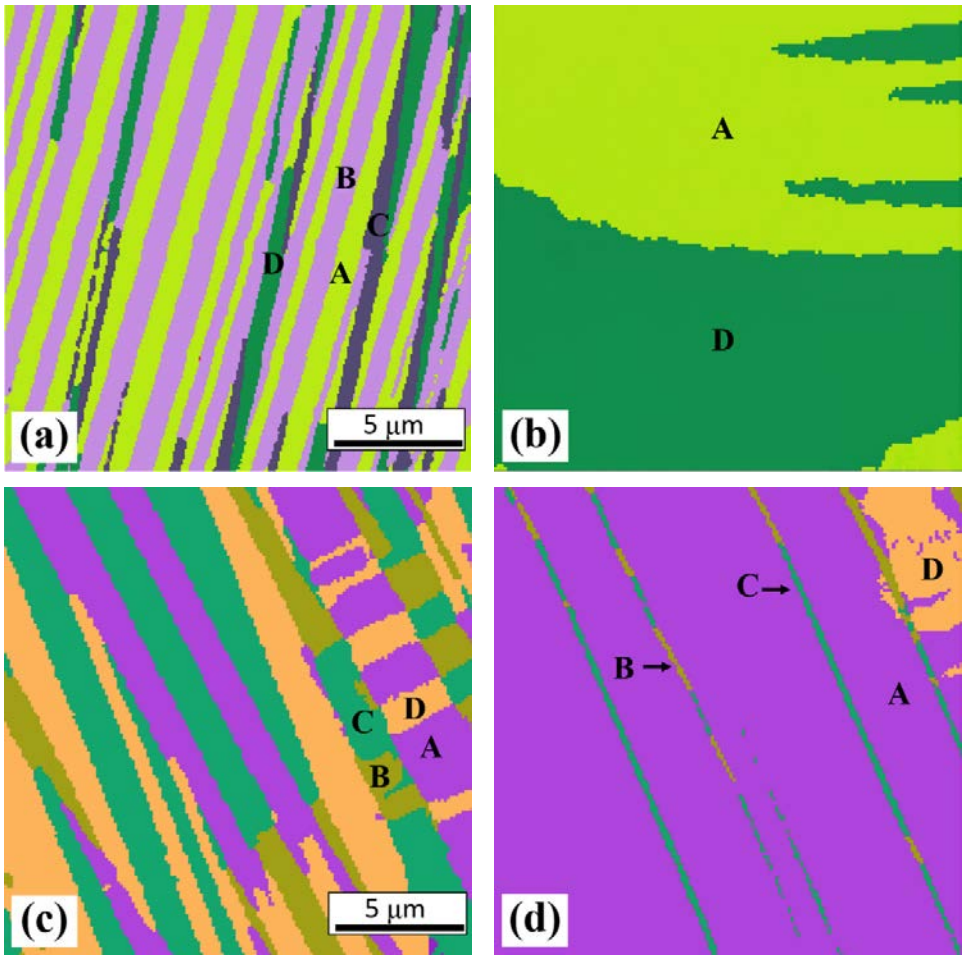

Fig. 6. 3 (a and c) Initial configurations of martensite variants within one colony and (b and d) corresponding microstructures after uniaxial compression. The loading orientation in (b) is approximately along the optimum orientation with high *SF* for both type-I and type-II detwinning systems, and that in (d) is within the common zone with positive *SF* for type-I, type-II and compound detwinning systems.

In both cases, the area fractions of the four martensite variants A, B, C and D are comparable before compression but greatly changed after compression depending on the loading orientations. When the loading orientation is favored only for the type-I and type-II detwinning systems, variants B and C disappear while variants A and D are left with almost the same area fraction (Fig. 6. 3b), as we predicted above. Such a loading orientation is not beneficial to eliminate variant D or A, since the *SF* value for the compound detwinning system is nearly zero. When the loading orientation falls into the common zone with positive *SF* for all the three detwinning systems, the situation changes drastically. As evidenced in Fig. 6. 3d, most part of the variant colony is occupied

by variant A and only very small area fractions of variants B, C and D are present. Clearly, the most efficient loading orientation to obtain the single variant configuration is the one located in the common positive *SF* detwinning zone, although it does not provide the highest *SF* for any detwinning system.

Taking into account the remaining variants B, C and D in Fig. 6. 3d, one can further explore the detwinning behaviors of the three different types of twins. It is seen that variant B (in type-II twin relation with variant A) has a less remaining area fraction than variant C (in type-I twin relation with variant A), although the type-II detwinning system possesses a smaller *SF* value (0.31) than that of the type-I detwinning system (0.35). This suggests that type-I twin has a larger detwinning resistance, which is in good accordance with the results obtained in Cu-Al-Ni and Ni-Mn-Ga alloys that the type-II twin requires a much smaller twinning stress [260, 277-281]. This small twinning stress for type-II twin might be associated with the step feature of the twinning plane, as evidenced in Fig. 4. 4b. Besides, most of variant D that is of compound twin relation with variant A has also been detwinned as shown in Fig. 6. 3d, although the associated *SF* value is only 0.10. This implies that compound twin possesses very small detwinning resistance, which could be attributed to its tiny shear amount (0.0277) and highly stepped interface, as displayed in Fig. 4. 4c. In addition, the shape of variant D becomes irregular after the uniaxial compression, as indicated in Fig. 6. 3b and d. The heavily curved interfaces between variants A and D further confirm the high mobility of the compound twin interface. Thus, in addition to the loading orientation, the intrinsic resistance of detwinning system plays an important role during detwinning.

It is worth noting that under mechanical loading, martensite variants do react within colonies through detwinning of unfavorably oriented and less resistant variants. In some circumstances, it is possible to obtain single variant state in some colonies by one uniaxial compression. The efficient loading orientation is one located in the common zone where the *SF* values for the type-I, type-II and compound detwinning systems are all positive, profiting the different detwinning behaviors of different twins. If knowing the loading orientation with respect to a chosen colony, the detwinning process and the efficiency of variant reorientation can be deduced.

6.1.2 Mechanical loading across the structural transition

In addition to load in martensite state, the appropriate mechanical loading across martensitic transformation, henceforth termed thermomechanical loading, is another alternative to induce

prestrain to martensite. In this part of work, *in-situ* neutron diffraction investigations and microstructural examinations by electron backscatter diffraction (EBSD) were performed. Schmid factor for martensitic transformation strain path was introduced to evaluate the efficiency of variant selection during loading at martensite state and during loading across structural transition.

6.1.2.1 *In-situ* neutron diffraction investigations

In this part of work, the polycrystalline bulk sample of $Ni_{51}Mn_{34}In_{16}$ alloy with the martensitic transformation temperature slightly above room temperature, T_{TM} = 316 K, was chosen. The alloys were fabricated using arc-melting technique. The as-cast ingots were further injected into a copper mould to obtain dense specimens. Three compression loads, *i.e.* -10 MPa, -40 MPa and -50 MPa, were successively applied across martensitic transformation. The experimental details are described in Chapter 2. Under consideration that the $\{002\}_A$ reflection of austenite splits into three distinct reflections of martensite $\{10\bar{3}\}_{6M}$, $\{103\}_{6M}$ and $\{020\}_{6M}$, as shown in Fig. 6. 4, the splitting of $\{002\}_A$ reflection, was thus utilized to inspect the transformation and variant selection.

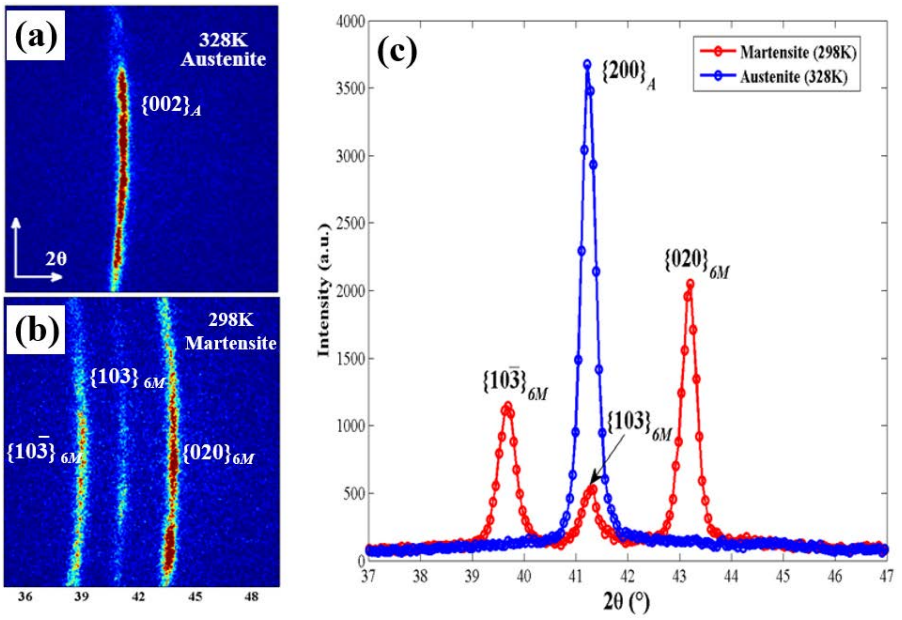

Fig. 6. 4 Neutron diffraction images of austenite (a) and martensite (b) at 2θ from 35° to 50°. Their corresponding diffraction patterns against 2θ (37° to 47°) in intensity profiles are displayed in (c).

By comparing peak positions of austenite and martensite around $\{002\}_A$ reflection (Fig. 6. 4c), one can see that the $\{002\}_A$ planes suffer a large negative or a positive normal strain, to form the

$\{020\}_{6M}$ or the $\{10\bar{3}\}_{6M}$ planes during martensitic transformation, whereas those for the $\{103\}_{6M}$ planes involves a very small normal strain since its interplaner spacing is almost the same as that of $\{002\}_A$ planes. If the external compressive load is applied along $\langle 001\rangle_A$ direction, the splitting to $\{020\}_{6M}$ might be favored, but that to $\{10\bar{3}\}_{6M}$ might be eliminated.

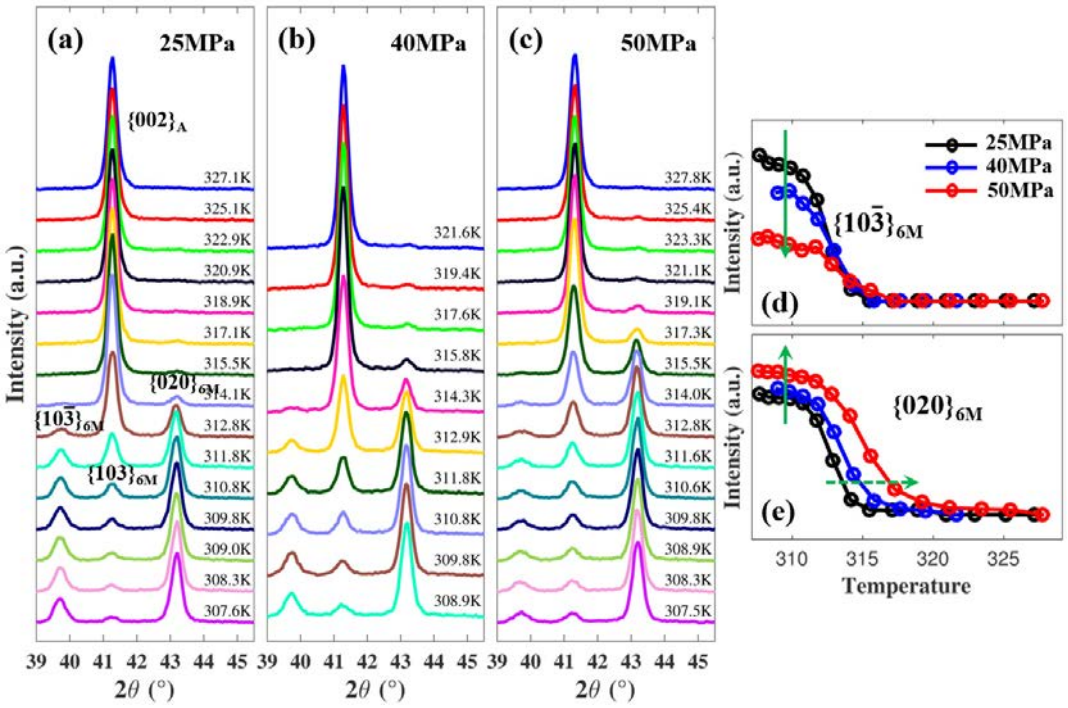

Fig. 6. 5 Temperature dependent neutron diffraction patterns across the structural transition under different loads, *i.e.* (a) -25 MPa; (b) -40 MPa; (c) -50 MPa. Intensity variations of $\{10\bar{3}\}_{6M}$ (d) and $\{020\}_{6M}$ (e) reflections with temperature.

Fig. 6. 5 shows temperature dependent diffraction patterns across the structural transition under the loads, *i.e.* -25 MPa, -40 MPa and -50 MPa, and the temperature resolved intensity variations of $\{10\bar{3}\}_{6M}$ and $\{020\}_{6M}$ reflections under these three loads. It is seen that with the increase of the load, the transformation start temperature shifts toward the higher temperature, as indicated with the green dashed arrow in Fig. 6. 5e, indicating the occurrence of stress induced transformation. Meanwhile, with the increase of the load, the intensity of the $\{10\bar{3}\}_{6M}$ reflection decrease (Fig. 6. 5d), whereas that of $\{020\}_{6M}$ reflection increases (Fig. 6. 5e), indicating an orientation selection during the transformation. With the changes of the relative intensities of these two

reflections, the macroscopic strain gradually increases, as shown in Fig. 6. 6, *i.e.* 1.08 %, 1.30 % and 1.89 % under the loads of -20 MPa, -40 MPa and -50 MPa, respectively.

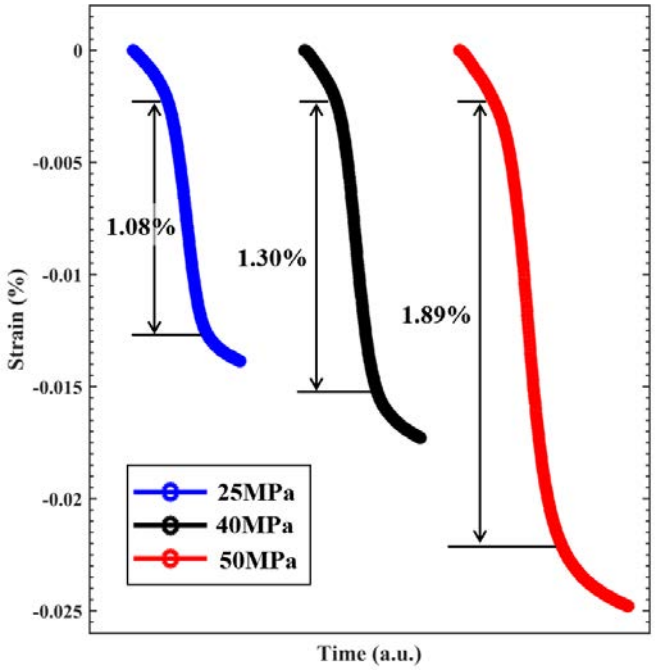

Fig. 6. 6 Macroscopic strains across the structural transition under the three successively compressive loads -20 MPa, -40 MPa and -50 MPa.

6.1.2.2 Variant selection under thermomechanical process

To explore the microscopic process of the orientation selection during the thermomechanical loading revealed above, the morphological and crystallographic features of martensite after the thermomechanical treatment were investigated by SEM/ EBSD. Fig. 6. 7a and b show band contrast and orientation micrographs of the specimen after hot compression under 50 MPa in which the grain boundaries of austenite are marked with the black solid lines. It is seen that only one or two martensite colonies, outlined by the black dashed lines, are observed within initial austenite grains, which is significantly different from the microstructure of the undeformed polycrystalline samples where many martensite colonies are generally observed within austenite grains, as shown in Fig. 4. 2 and Fig. 5. 14. The traces of the variant interfaces in Fig. 6. 7a is generally at about 45° from the compression direction.

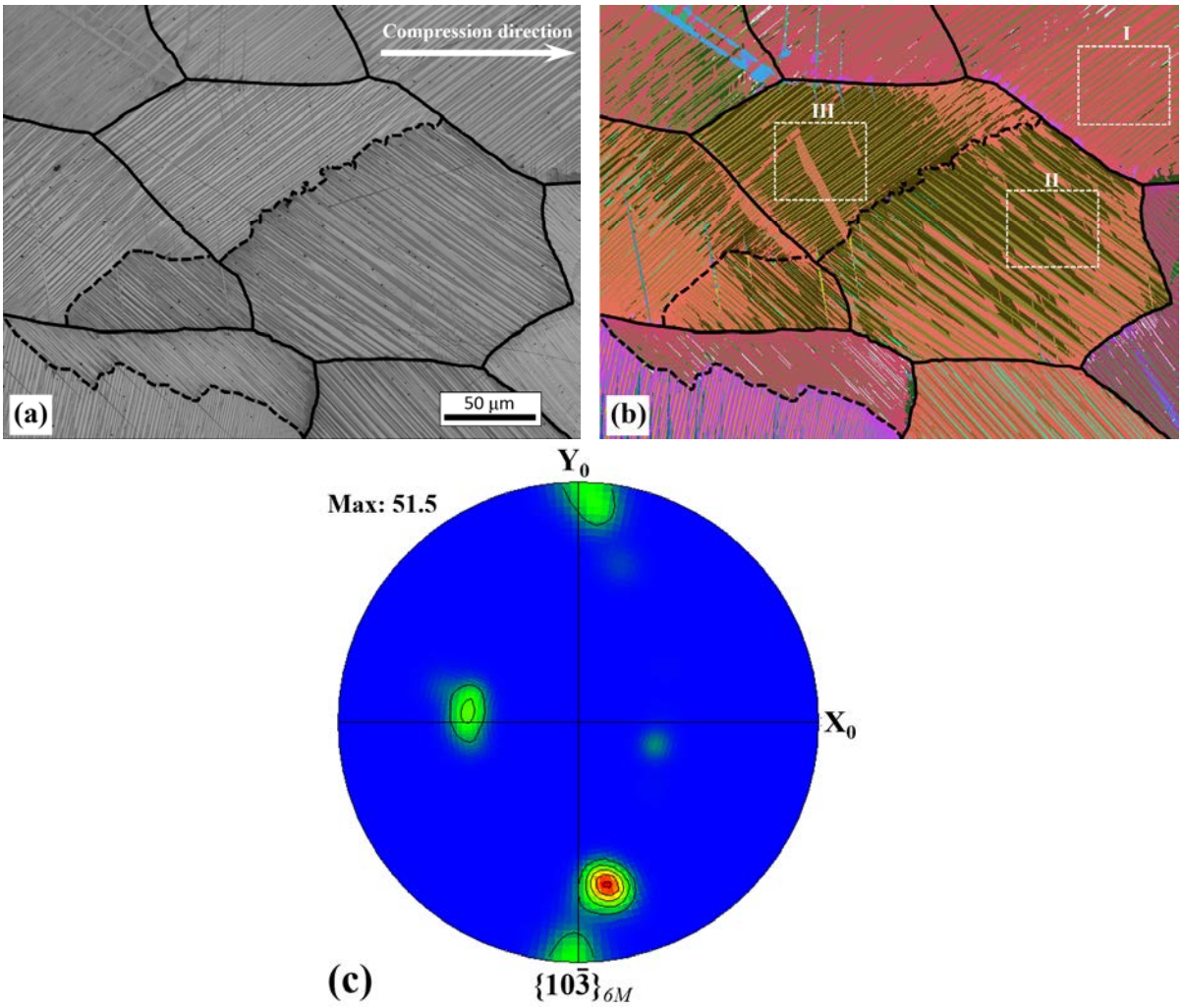

Fig. 6. 7 Microstructure feature of the polycrystalline sample after hot compression (-50 MPa). (a) band contrast micrograph; (b) crystallographic orientation micrograph; (c) $\{10\bar{3}\}_{6M}$ pole figure. The compression axis is parallel to $\mathbf{X_0}$.

The pole figures of $\{10\bar{3}\}_{6M}$ planes, derived from the orientation information in Fig. 6. 7b, are plotted in Fig. 6. 7c. It is seen that after the hot compression most of the variants are oriented with their $\{10\bar{3}\}_{6M}$ planes, resulting from the extended $\{002\}_A$ plane across the structural transition (Fig. 6. 4c), perpendicular to the compression direction ($\mathbf{X_0}$). Furthermore, three characteristic martensite colonies, indicated in the white dashed boxes I, II and III in Fig. 6. 7b, are chosen and zoomed in Fig. 6. 8a_1, b_1 and c_1, respectively. The area faction histogram of the four variants in each colony is inserted in the figure. It is seen that the area fractions of the four variants within different colonies are significantly different, which is different from the cases of the undeformed polycrystalline

samples in which the four variants are of comparable area fractions (Fig. 5. 14 and Fig. 6. 3a and c).

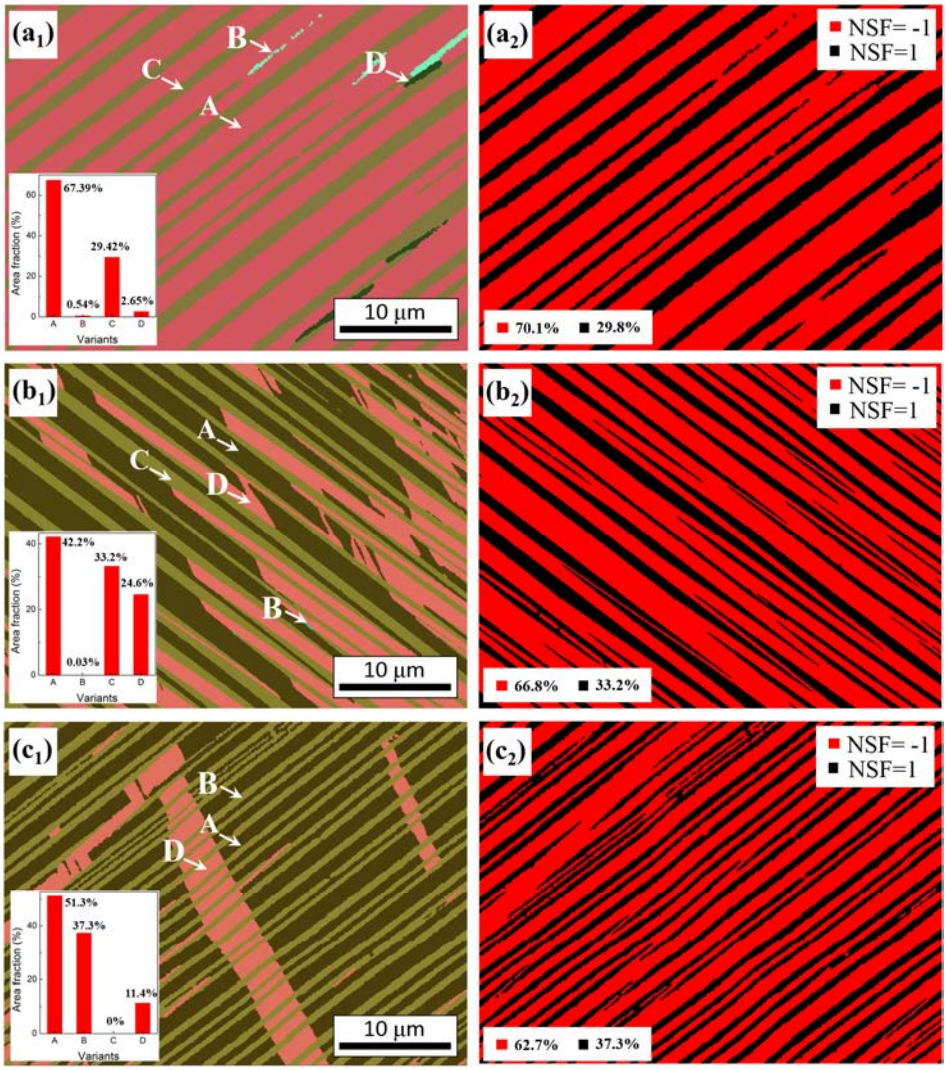

Fig. 6. 8 Zoomed orientation maps of the dashed boxes in Fig. 6. 7b where the area faction histogram of the four variants is inserted, and their corresponding micrograph of normalized Schmid factor (*NSF*) of the transformation path. (a_1 and a_2) colony I; (b_1 and b_2) colony II; (c_1 and c_2) colony III.

Despite the change of the microstructures induced by the hot compression (Fig. 6. 8a_1, b_1 and c_1), it was found that the variant interfaces still coincide with the twinning plane of type I twin or the $\{101\}_A$ plane of austenite (the *Pitch OR* plane), suggesting that the martensitic transformation under the compressive load still obeys the *Pitch* type strain path, *i.e.* $\{101\}_A$ & $\langle 10\bar{1}\rangle_A$. The specific transformation paths for variants in colonies of Fig. 6. 8a_1, b_1 and c_1 were determined and listed in

Table 6. 2. As shown in Fig. 5. 5b and Table 5. 3, under the *Pitsch* strain path, the highest lattice distortion of the structural transition is the $\{101\}_A$ / $\langle 10\bar{1}\rangle_A$ shear component, hence this deformation could be dominant for the structure transition, and the path having the highest the resolved shear stress may have the largest chance to be activated. Based on such a consideration, the Schmid factor (*SF*) of the strain paths for the formation of the variants in Fig. 6. 8a_1, b_1 and c_1 were evaluated, using Eq. 6-1.

$$SF = \cos\alpha \cdot \cos\gamma \tag{6-1}$$

where α and γ are the angles of the loading orientation with respect to the respective transformation path plane and direction. The *SFs* are further normalized with the maximum *SF* of all the 24 possible variants within the same austenite grain and termed as normalized Schmid factor (*NSF*). Due to the negative magnitude (-0.1185) of the shear component $\{101\}_A$ / $\langle 10\bar{1}\rangle_A$, as shown in Table 5. 3, the variants with the largest negative *SFs* should be the one receiving the highest resolved shear stress from the external load.

Table 6. 2 The martensitic transformation paths, their corresponding Schmid factors (*SF*) and normalized Schmid factors (*NSF*), and the observed area fractions for variants in Fig. 6. 8a_1, b_1 and c_1. Euler angles of austenite, deduced with the *Pitsch* orientation relationship, for these three martensite colonies are also listed.

Colonies	Euler angles of austenite	Variants	Martensitic transformation path	*SF*	*NSF*	Area fraction (%)
I	(88.8, 128.4, 176.1)	A	$(\bar{1}0\bar{1})[10\bar{1}]$	-0.31	-1	67.4
		B	$(101)[10\bar{1}]$	0.31	1	0.5
		C	$(\bar{1}0\bar{1})[\bar{1}01]$	0.31	1	29.4
		D	$(101)[\bar{1}01]$	-0.31	-1	2.7
II	(258.4, 47.2, 29.5)	A	$(\bar{1}0\bar{1})[10\bar{1}]$	-0.25	-1	42.2
		B	$(101)[10\bar{1}]$	0.25	1	0.03
		C	$(\bar{1}0\bar{1})[\bar{1}01]$	0.25	1	33.2
		D	$(101)[\bar{1}01]$	-0.25	-1	24.6
III	(258.4, 47.2, 29.5)	A	$(10\bar{1})[\bar{1}0\bar{1}]$	-0.25	-1	51.3
		B	$(\bar{1}01)[\bar{1}0\bar{1}]$	0.25	1	37.3
		C	$(10\bar{1})[101]$	0.25	1	0
		D	$(\bar{1}01)[101]$	-0.25	-1	11.4

Table 6. 2 displays the results of the *SFs* and the *NSFs* for the martensite variants in the three colonies in Fig. 6. 8a_1, b_1 and c_1. The distribution maps of *NSFs* for colonies in Fig. 6. 8a_1, b_1 and c_1 are shown in Fig. 6. 8a_2, b_2 and c_2, respectively. It is seen that all the three colonies are mainly occupied by variants with the largest *NSFs* (-1), as highlighted in red. It shows that the martensite colonies with certain variants having the largest *SFs* are preferred to be generated under the mechanical loading across the structural transition. This might be the reason why the number of martensite colonies within one austenite grain is significantly reduced by compression.

However, it should be noted that in all the three colonies some variants, occupied around 1/3, with positive maximum *NSF* is also selected, as highlighted in black in Fig. 6. 8a_2, b_2 and c_2. It may be related to the self-accommodation requirement of martensitic transformation to decrease the transformation elastic strain energy. Thus the *displacement gradient tensors* of the structure distortion from austenite to martensite expressed in the sample reference $\mathbf{X_0}$-$\mathbf{Y_0}$-$\mathbf{Z_0}$ ($\mathbf{X_0}$// compression axis) for variants A, B, C and D in the three colonies in Fig. 6. 8, as an example, were analyzed. The *displacement gradient tensors* of variant A, B, C and D in colony I in Fig. 6. 8$a_1$were given in Eqs. 6-2 ~ 6-5.

$$D_A = \begin{bmatrix} -0.0359 & 0.0424 & 0.0212 \\ -0.0459 & 0.0523 & 0.0244 \\ 0.0403 & -0.0450 & -0.0202 \end{bmatrix} \quad (6\text{-}2)$$

$$D_B = \begin{bmatrix} 0.0399 & -0.0445 & -0.0197 \\ 0.0519 & -0.0598 & -0.0283 \\ -0.0269 & 0.0320 & 1.0161 \end{bmatrix} \quad (6\text{-}3)$$

$$D_C = \begin{bmatrix} 0.0273 & -0.0375 & -0.0236 \\ 0.0430 & -0.0598 & -0.0384 \\ -0.0288 & 0.0421 & 0.0286 \end{bmatrix} \quad (6\text{-}4)$$

$$D_D = \begin{bmatrix} -0.0355 & 0.0506 & 0.0336 \\ -0.0380 & 0.0537 & 0.0353 \\ 0.0269 & -0.0359 & -0.0220 \end{bmatrix} \quad (6\text{-}5)$$

It is seen that the signs of all strain components for variants with negative *SFs* (A and D) are opposite to those with positive *SFs* (B and C). Element $\boldsymbol{e_{1j}}$ have particular importance, as "$\boldsymbol{1}$" is the compression direction and the specimen is subject to a dimension reduction in this direction. Thus variants with $\boldsymbol{e_{11}} < 0$ can accommodate the macroscopic reduction and could be selected. Thus variant A and D could be selected by the macroscopic strain. However, the large $\boldsymbol{e_{12}}$ and $\boldsymbol{e_{13}}$ that means shears in the compression direction will increase the dimension in the compression direction when these variants are formed and should be compensated. Thus, the generation of variants B and C can just compensate these two shears for variants A and D. This is why A and C or D and B appear in pairs. Moreover, A/ C and B/ D are type I twins. Their interfaces are the coherent $\boldsymbol{K_1}$

plane and should possess low interfacial energy. Consequently, the generation of twin-related variants with positive *SFs* could greatly reduce the transformation elastic energy and further promote the structural transition. For a detailed exploration about the variant selections, the strain compatibilities between the macroscopic strain and the microscopic accommodations, between different austenite grains, and between different colonies, should be further considered.

Consequently, it could be concluded that the mechanical loading across the structural transition is an effective approach to apply prestrains at martensite by decreasing the number of martensite colonies and changing the self-accommodated microstructure features within colonies for the polycrystalline Ni-Mn-In alloys. The colonies or variants with large transformation *SFs* should have preference to be generated. However, to compensate the transformation strains for variants with large transformation *SFs*, some variants with unfavorable *SFs* could also be generated.

6.2 Influence of annealing on magnetocaloric effects

With the determined information of crystal structure, microstructure and martensitic transformation crystallography, the effect of annealing on magnetocaloric effect (MCE) and its related magnetic hysteresis loss were explored. In this work, the as-spun and annealed quaternary $Ni_{45}Co_5Mn_{36.8}In_{13.2}$ ribbons were studied. The as-spun ribbons were melt spun using a single copper roller with a wheel-rotating speed of 15 m/s. Part of ribbons were annealed at 1173 K for 24 hours in a sealed quartz tube.

6.2.1 Magnetic property investigations

Fig. 6. 9a shows the magnetization variations of the as-spun and annealed ribbons as a function of temperature. It is seen that with the decrease of the temperature, both specimens transform from the paramagnetic austenite to the ferromagnetic austenite, and further to the weak-magnetic martensite. The martensitic transformation temperature (T_{TM}) of the annealed ribbon is about 34.5 K lower than that of the as-spun ribbon. It shows that the heat treatment could significantly stabilize the austenite phase, implying that the annealed ribbon need a larger drive force to trigger the structural transition than that of the as-spun ribbons. Different from the martensitic transformation temperature, it is seen that the heat treatment can greatly increase the magnetic transition temperature (by 17.1 K), as shown in Fig. 6. 9a. It shows that the heat treatment is favorable to

stabilize the ferromagnetic state of austenite, suggesting that the magnetic interaction is enhanced with the annealing process. This is further confirmed with the increased saturation magnetizations of the austenite of the annealed ribbon under a magnetic field of 5 mT.

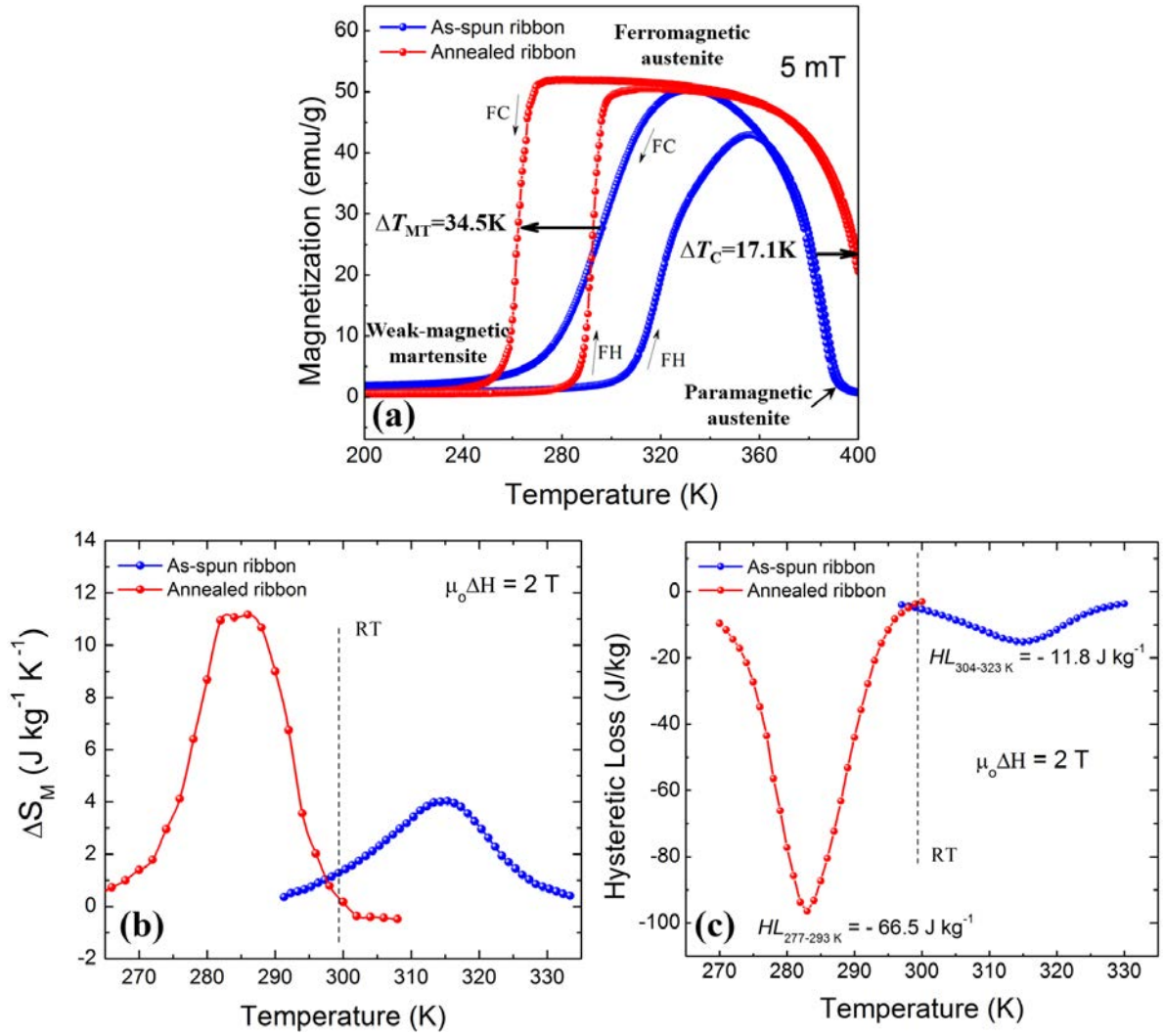

Fig. 6. 9 Temperature dependence of magnetization (a) under a magnetic field of 5 mT; Variations of magnetic entropy change ΔS_M (b) and magnetic hysteresis loss (c) against temperature across magnetostructural transition for as-spun and annealed ribbons under a magnetic field of 2 T.

Fig. 6. 9b displays the variations of magnetic entropy change ΔS_M against temperature, estimated from the isothermal magnetization curves across the inverse martensitic transformation under a magnetic field of 2 T, using the *Maxwell equations* (Eq. 2-28). It is seen that the ΔS_M, generally used to represent the MCEs in Heulser alloys, is significantly enhanced by the heat treatment from 4.5 J·kg^{-1}·K^{-1} to 11.5 J·kg^{-1}·K^{-1}. The variations of hysteresis loss against temperature

across the inverse martensitic transformation, calculated by integrating the areas between the field-up and the field-down isothermal magnetization curves, are given in Fig. 6. 9c. It is seen that the as-spun ribbon has a relative small hysteresis loss of -11.8 $J \cdot kg^{-1}$. For the annealed sample, the magnetic hysteresis loss is greatly increased and equal to -66.5 $J \cdot kg^{-1}$. As a consequence, despite the enhancement of the magnetic entropy change after heat treatment, the correlated magnetic hysteresis loss is also greatly increased simultaneously. Thus, the explorations on the underlying mechanisms of annealing effect on the magnetic entropy change and the hysteresis loss should be meaningful for further property optimizations.

6.2.2 Crystal structure and microstructure characterizations

Fig. 6. 10 shows the X-ray diffraction patterns of the as-spun and the annealed ribbons. It is seen that the as-spun ribbon has two-phases *i.e.* austenite and martensite, coexisting at room temperature, whereas the annealed ribbon has only austenite phase. This difference should be associated with the significant decrease of the martensitic transformation temperatures with the annealing (Fig. 6. 9a). Moreover, the superlattice reflections of $(111)_A$ and $(113)_A$ of austenite, representing ordering degree of the constituent elements, are clearly observed in the X-ray pattern of the annealed ribbon (Fig. 6. 10b), but they do not appear in the as-spun ribbon (Fig. 6. 10a), as marked with the dashed box in Fig. 6. 10. This suggests that the as-annealed ribbon possesses a highly ordered $L2_1$ structure ($Fm\bar{3}m$), whereas the as-spun ribbon seems to have a *B2* structure ($Pm\bar{3}m$). The peak positions of the other reflections of the austenite in the two ribbons are almost the same, suggesting that the lattice parameters are not sensitive to the heat treatment.

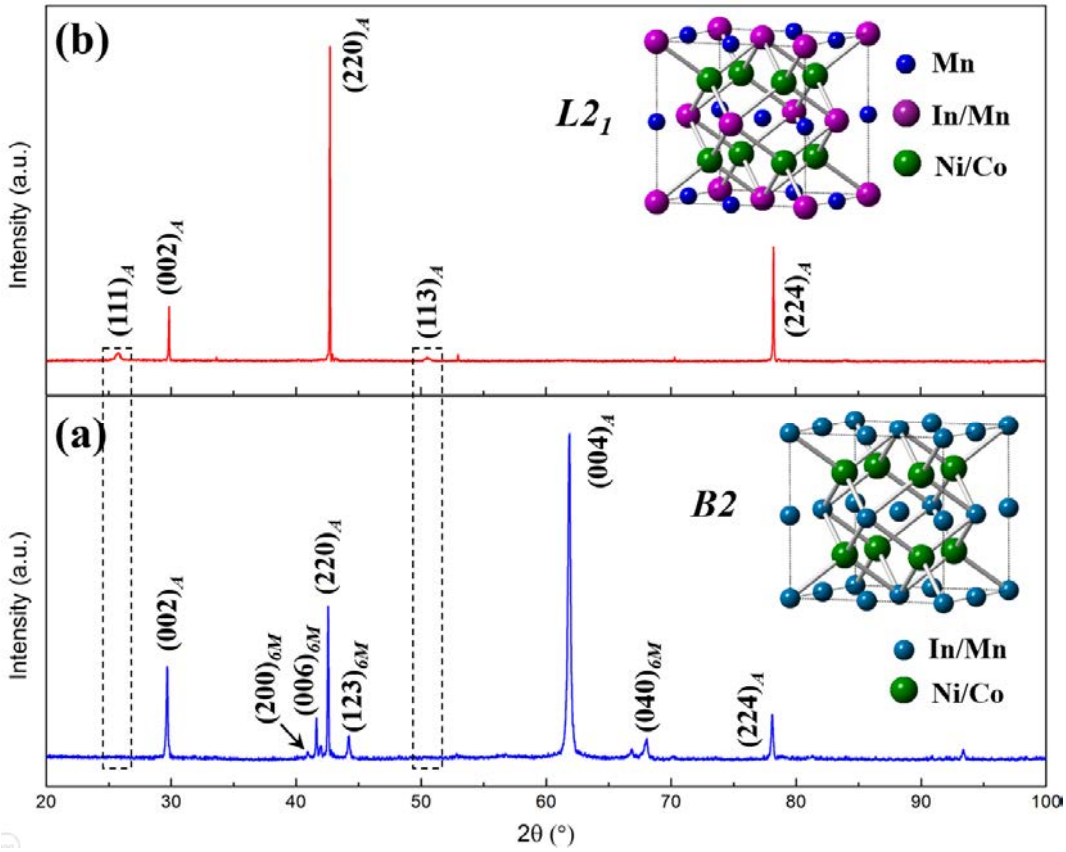

Fig. 6. 10 X-ray diffraction patterns of as-spun (a) and annealed ribbons (b) measured at room temperature.

Fig. 6. 11 displays the BSE images of the as-spun and the annealed ribbons. For the as-spun ribbon, it is seen that the austenite (with flat surface) and the martensite (with corrugated surface) are present (Fig. 6. 11a). For the as-spun ribbon, the grain sizes of the austenite are relatively small (around 10 μm). Fine plate shaped martensite can be observed in many austenite grains. After the heat treatment, the grains of austenite are greatly coarsened (about 100 μm), as shown in Fig. 6. 11b. Very limited amount of martensite plates appear in some austenite grains. The orientation micrographs of the as-spun and the annealed ribbons are shown in Fig. 6. 11. It is seen that the *habit planes* between austenite and martensite in both ribbons are bordered by single martensite variant. These results are in good agreement with those observed in bulk specimens with the same alloy composition, as shown in Fig. 5. 15a.

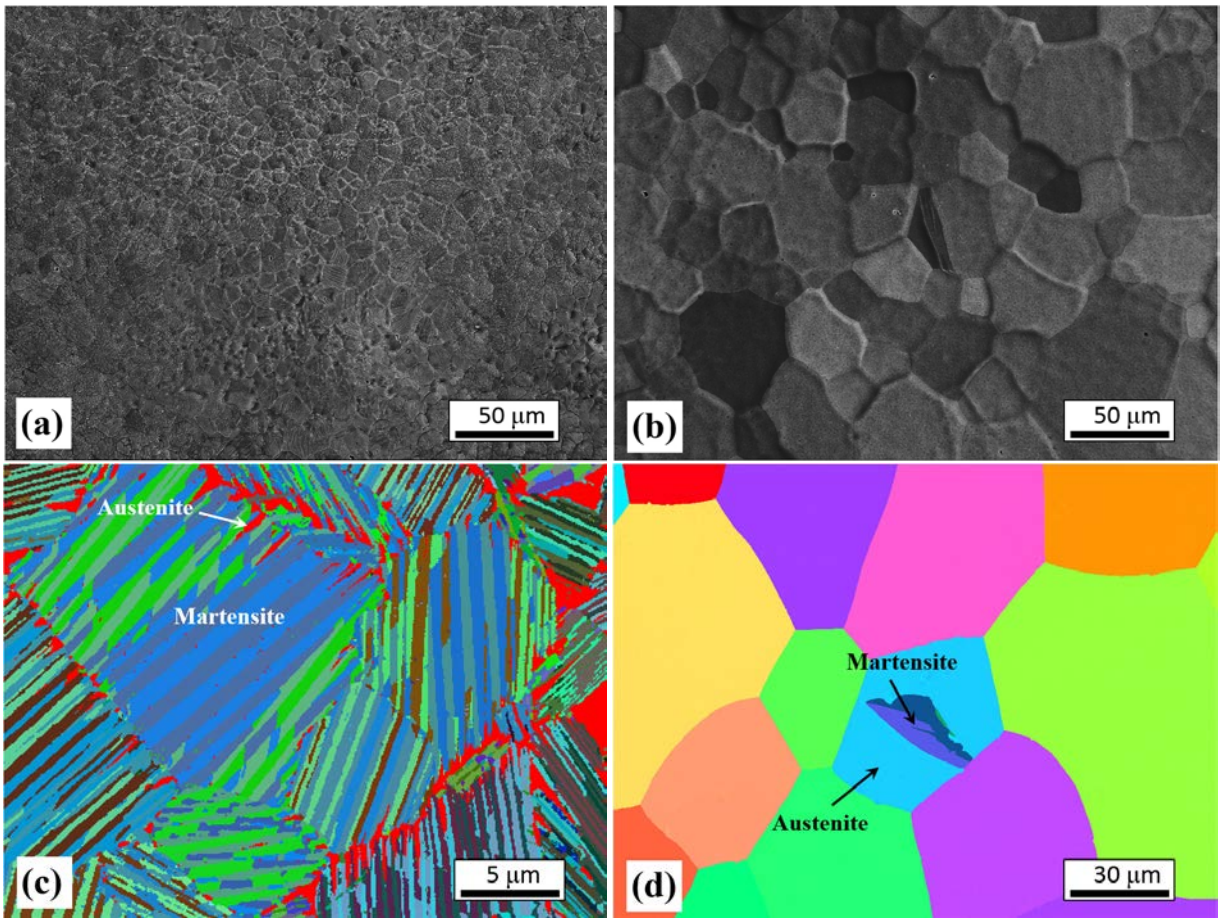

Fig. 6. 11 BSE images of as-spun (a) and annealed ribbons (b) at room temperature. (c) Orientation micrograph of martensite in the as-spun ribbon in which the residual austenite is highlighted in red. (d) Orientation map of austenite and martensite in the annealed ribbon where the two phases are colored according to their crystallographic orientations.

6.2.3 Discussions

With the information of the crystal structure, the microstructre and the magnetic properties, the influence of the heat treatment on the MCE can be further analyzed. The increased entropy change by heat treatment (Fig. 6. 9b) should be ascribed to the enhanced magnetic interactions resulting from the increased chemical ordering, as shown in Fig. 6. 10. The enhanced magnetic interaction is also experimentally evidenced by the increase of the magnetic transition temperature of austenite (T_c) after annealing (Fig. 6. 9). Thus, the enhancement of chemical order should be an effective way to increase MCEs.

Unfortunately, the hysteresis loss across the magnetostructuaral transition is also greatly enhanced with the heat treatment (Fig. 6. 9c). As discussed in Section 1.2.3.2, two types of material parameters would have influence on hysteresis loss. One is the resistance of martensitic transformation, such as the geometrical compitability between austenite and martensite. The other is material factors to promote the magnetostructural transition, such as crystal defects. As shown in Fig. 6. 10, the lattice paramters of austenite in the ribbon samples are not very sensitive to heat treatment. Both the as-spun and the annealed ribbons hae good geometrical compitability between austenite and martensite, as shown in Fig. 6. 11c and d, just like the case in bulk specimens as discussed in Section 5.3 (Fig. 5. 15a). Thus, the variations of geometrical compitabilities between austenite and martensite should be not the prominent factors to influence hysteresis loss.

Furthermore, as shown in Fig. 6. 11 a and b, the heat treatments can significantly promote the growth of grains. The average grain diameter of as-spun ribbon (around 10 μm) is about 10 times samller than that of annealed ribbon (around 100 μm). The big grain of annealed ribbons could be one of the important reasons for the large hysteresis. The similar effect of grain size on hysteresis loss was also found in Gd_5Ge_4 alloy [282]. The influence of grain size on hysteresis loss could be ascribed to the promotion of grain boundary on nucleation for phase transformation. Crystal defects constituted by grain boundaries offer numerous favorable nucleation sites for phase transformation. Thus, the refined microstructure should promote structural transition. It could be indirectly evidenced by the microstructure feature that only one martensite colony is generally observed in one initial austenite grain (Fig. 6. 11 c), which is significantly different from samples with a larger austenite grain in which many martensite colonies are generally observed within one austenite grain (Fig. 4. 2 and Fig. 5. 14). Moreover, some other crystal defects, such as dislocation and vacancy should have a simlar effect like grain boundaries.

As discussion above, the materials parameters to dominate the magentic entropy change and the hysteresis loss are different in the investigated material. For the magentic entropy change, the chemical ordered degree should play a prominent role. For hysteresis loss, the grain boundaries could be one of the most important parameters. Due to the different origins of these two effects, it could be possible to find an appropriate treatment process, such as rapidly heat treatment, to enhance MCE but to keep low hysteresis loss.

6.3 Summary

In this chapter, first, the behaviors and underlying mechanisms of variant rearrangement under external compressive loads were investigated. Two kinds of loading strategies are considered, *i.e.* loading in martensite state and across the structural transition. For the former, Schmid factor (*SF*) predictions and *ex-situ* microstructural investigations were carried out. *SF* calculations show that under uniaxial compression condition, the loading orientation zones with high *SF*s for type-I and type-II detwinning systems are close to each other, being at about 90° away from those of compound detwinning system. The detwinning resistances of different types of twins are considered to be associated with their twinning shears and twin boundary structures. Type-I twin possesses much larger detwinning resistance than that of type-II twin, although they have the same amount of twinning shear (0.2392). Compound twin has the smallest detwinning resistance, which is benefited from its tiny twinning shear (0.0277) and "stepped" twin interface. Under external loading, martensite variants react locally within colonies through detwinning if the loading orientation is favorable. It is possible to obtain single variant state in some colonies when the loading orientation is in the common positive *SF* zone of the three detwinning systems.

For loading across the structural transition, *in-situ* neutron diffraction investigations and microstructural examinations were performed. Results show that the thermomechanical loading can significantly reduce the number of martensite colonies and change the self-accommodated microstructure within colonies for Ni-Mn-In polycrystalline alloys. The martensite colonies/ variants with large transformation *SF*s appear preferentially, however, to accommodate the transformation strains generated by variants with large transformation *SFs*, their twin-related variants could also be generated even though they possess unfavorable *SFs*. The combination of these two loading strategies might produce complimentary effects to induce a prestrain in the materials. The treatment could be performed into two consecutive steps. First, the uniaxial compression load is applied across structural transition to decrease martensite colonies and variant numbers within colonies by variant selections. Then, loading in martensite state along some characteristics directions to obtain the single variant state by detwinning processes.

In addition to variant rearrangement/ selection under different mechanical loadings, the influence of annealing on MCE and its related hysteresis loss were explored. It is found that the heat treatment can significantly enhance the magnetic entropy change ΔS_M, but increase the

magnetic hysteresis loss simultaneously. For the ΔS_M, the enhanced chemical ordered degree should play a prominent role. Thus the treatments to increase chemical ordered degree should be an effective way to promote the MCE. The magnetic hysteresis loss might be closely related to the crystal defects. Fine grained microstructures could be favorable to promote the nucleation for structural transition and then result in a low hysteresis loss. Due to the different dominating parameters of these two effects, it might be possible to find an approach that could increase MCE but keep a low hysteresis loss simultaneously.

The results of this part of work are expected to be served as a basis to understand the underlying mechanisms of these two properties and to guide subsequent performance optimizations.

Chapter 7 Conclusions and perspectives

7.1 Conclusions

From the above theoretical and experimental investigations, the following conclusions can be drawn:

Evolution of martensitic transformation temperatures in $Ni_{50}Mn_{50-x}In_x$ ($0 \leq x \leq 25$) alloys

With the increase of In concentration, the martensitic transformation temperatures linearly decrease. When $x < 15$, the alloys are in martensite state at room temperature. The alloys are in their austenite state at room temperature for the compositions $x \geq 15$. The martensitic transformation was not detected for the alloys with In concentration higher than 15.5 % in the temperature range from 180 K to 800 K.

Refinements of crystal structures of austenite and various martensites in Mn enriched Ni-Mn-In alloys

The austenite of Ni-Mn-In alloys possesses an ordered cubic $L2_1$ structure belonging to space group $Fm\bar{3}m$. The extra-Mn atoms have a preference to be uniformly dispersed. The non-modulated martensite has a tetragonal $L1_0$ structure belonging to space group P4/mmm. For the modulated martensite, with the consideration of the possible aperiodicity of modulated structure, the crystal structure determination was performed in the frame of superspace theory. Refinements show that it has an incommensurate 6M modulated structure with the superspace group $I2/m(\alpha 0\gamma)00$. With the determined crystal structure information, its relation with the magnetic properties was discussed. A three-fold layered superstructure in the three-dimensional space was proposed to approximately describe this incommensurate structure. This 6M superstructure model is considered to be representative for off-stoichiometric Ni-(Co)-Mn-In modulated martensite with martensitic transformation around room temperature.

Investigations of the morphological and crystallographic features of 6M Ni-Mn-In modulated martensite

Crystallographic theories of martensitic transformation suggest that there are in maximum 14 distinct twin relations in 6M Ni-Mn-In modulated martensite that can be classified into four twin types, *i.e.* type-I, type-II, compound and non-conventional twins. Type-I and type-II twins might exist between the two-fold or four-fold cubic rotational symmetry related variants. Compound twins are between the two-fold rotational cubic symmetry related variants. Non-conventional twins only exist between the four-fold rotational cubic symmetry related variants. It is not possible to be of twins for the three-fold rotational cubic symmetry related variants in the investigated materials.

The microstructure of martensite is in plate shape and self-organized in colonies within which the plates stretch roughly in the same direction. Due to the unique variant organization manner in Ni-Mn-In alloys, only three twin relations are experimentally evidenced, *i.e.* type-I (A: C, B: D), type-II (A: B, C: D) and compound twin (A: D, B: C). Variant interfaces are defined by their corresponding twinning plane K_1 in the mesoscopic scale. However, at atomic scale, the type-I twins have a coherent interface, whereas the type-II and compound twins have "stepped" interfaces. The step heights of the compound twin interface are much larger than those of the type-II twin interface. In view of variant organization, there are only one oriented type-I and compound twin interfaces but two distinct type-II interfaces that have a theoretical angular deviation of about 5° from the type-I twin interface orientation.

Studies on crystallographic orientation relationship (OR), transformation strain path and geometric compatibility of the martensitic transformation

Both *Kurdjumov- Sachs* (*K-S*) and *Pitsch* relations are found to be possible to describe the lattice correspondence between austenite and martensite in 6M Ni-Mn-In alloys. However, the strain path related to the *Pitsch* relation is evidenced to be the effective one to realize the structural distortion. With the *Pitsch* transformation path, four distinct martensite variants within one colony are transformed from the same (or opposite) transformation plane and direction of austenite. Due to cubic symmetry, the maximum 6 distinct martensite colonies and 24 distinct variants within one austenite grain can be obtained. The middle eigenvalue of the *transformation stretch tensor* across the structural transition is close to 1 (0.99652) and the *habit plane* is bordered by single martensite variant with austenite, suggesting a relative good geometrical compatibility between the austenite

and the martensite. A stressed transition layer of about 20 nm near the *habit plane*, evidenced by HRTEM, implies that the criterion of $\lambda_2 = 1$ is not sufficient to guarantee the geometric compatibility.

Exploration of the behavior and the mechanism of martensite variant rearrangement/ selection under compressive loadings in martensite state and across the structural transition

For the compressive loading in martensite state, variant arrangement is realized by the detwinning processes. *SF* calculations show that under uniaxial compression condition, the loading orientation zones with high *SFs* for type-I and type-II detwinning systems are close to each other, being at about 90° away from those of compound detwinning system. The detwinning resistances of different types of twins are considered to be associated with their twinning shears and twin boundary structures. Type-I twin possesses much larger detwinning resistance than that of type-II twin, although they have the same amount of twinning shear. Compound twin has the smallest detwinning resistance, which is benefited from its tiny twinning shear and stepped twin interface. Under external loading, martensite variants react locally within colonies through detwinning if the loading orientation is favorable. It is possible to obtain single variant state in some colonies when the loading orientation is in the common positive *SF* zone of the three detwinning systems.

For loading across the structural transition, the prestrain is obtained by variant selection in which the number of colonies is significantly reduced and the variant organization within colony is greatly changed. The *SF* for transformation strain path is introduced to evaluate the possible selection of variants. The martensite colonies/ variants with large transformation *SFs* appear preferentially, due to the self-accommodation requirement of the transformation, their twin-related variants with unfavorable *SFs* could also be generated to compensate the transformation strain and guarantee the transformation.

Exploration of the influence of heat treatment on magnetocaloric effect and its related hysteresis loss

Heat treatment can significantly enhance the magnetic entropy change ΔS_M but simultaneously increase the magnetic hysteresis loss. For ΔS_M, the chemical ordered degree should play a prominent role. The treatments that increase chemical order should be effective to enhance the ΔS_M. The hysteresis loss might be closely related to the crystal perfectness of austenite. Crystal defects,

such as grain boundaries, could be favorable to promote the nucleation for structural transition and then result in a low hysteresis loss.

7.2 Perspectives

Since 2004, studies on Ni-Mn-In based alloys have well been developed both in experimental investigations and theoretical explorations. Plenty of excellent properties, such as large magnetic-field-induced strain, giant magnetocaloric effect and giant magnetoresistance, and their related underlying mechanisms have been revealed. However, some basic knowledge is still not available, and some properties, such as the large hysteresis loss, are still need to be improved before large-scaled applications of these materials. With the studies on this PhD work, we see some new perspectives on the study of Ni-Mn-In alloys that are summarized as follows:

(1) For Ni-Mn-In based alloys, all their multifunctional properties are found to be closely related to the modulated crystal structure features of their martensite. However, until now, the origin of modulation of the crystal structures in these alloys is still unclear. Detailed information on the nature of structure modulation is needed. The investigations with molecular dynamic simulation might offer some useful clues.

(2) The multiple magnetoresponsive behaviors of Ni-Mn-In alloys mainly originate from the magnetic-field-induce inverse martensitic transformation. Thus, the detailed knowledge on martensitic transformation will be quite essential. However, little attention has been devoted to study on the nucleation and growth processes of martensitic transformation in these materials.

(3) As revealed in Section 6.1.1, the structures of variant interfaces are closely related to the applied prestrain and the resultant metamagnetic shape memory effect. So far, the precise crystallographic components of the interfacial segments between martensite variants with type-II and compound twin relations are still not unclear. Knowledge on these two kinds of interface could be helpful to further optimize the metamagnetic shape memory effect. The atomic scale interface characterizations and theoretical analysis with the consideration of geometrical misfit could provide us some useful information.

(4) As revealed in Section 6.1, the mechanical loading in martensite state along some characteristic directions could obtain a single martensite variant state in some colonies, and the mechanical loading across the structural transition can significantly reduce the number of

martensite colonies. Thus, the combination of these two loading strategies might produce complimentary effects to achieve low number variant state for polycrystalline materials. The treatment could be performed into two consecutive steps. First, the uniaxial compression load is applied during the structural transition to decrease the number of martensite colonies and variant numbers within colonies by variant selections. Then, loading in martensite state along some characteristics directions to obtain the single variant state by detwinning processes.

(5) For a detailed exploration on martensite variant reactions under the mechanical loading in martensite state, or variant selections under the mechanical loading across the structural transition, the strain compatibilities between the macroscopic deformation and the microscopic structural distortion, between different austenite grains, and between different colonies, should be considered. The crystal plasticity finite-element approaches could be an efficient tool.

(6) For hysteresis effect, as revealed in Section 5.3, the criterion of $\lambda_2 = 1$ is not sufficient to guarantee good geometric compatibility between the austenite and the martensite. A more realistic criterion to evaluate the geometric compatibility beteen the parent and product phase is still in need. Apart from the geometrical compatibility, a comrehensive criterion, containning the related material parameters, such as crystal structure and microstructrue, to evaluate the hysteresis loss across the structural transition is in still need.

(7) As revealed in Section 6.2, the magnetic entropy change ΔS_M across the magnetostructural transition, generally used to characterize the magnetic refrigeration capacity, is closely related to chemical ordered degree, but the correlated magnetic hysteresis loss could be associated with the crystal defects, such as grain boundaries. Due to the different dominating parameters of these two effects, it might be possible to find an approach that could increase magnetic refrigeration capacity but simultaneously keep a low hysteresis loss.

Appendix

Appendix I: Symmetry matric of cubic and monoclinic crystal system

Table A.1 Symmetry elements of cubic crystal system.

Element	Rotation	Euler angles of rotation	Matrix	Element	Rotation	Euler angles of rotation	Matrix
1	(x, y, z)	(0,0,0)	$\begin{pmatrix}1&0&0\\0&1&0\\0&0&1\end{pmatrix}$	4+ x, 0,0	(x, $\bar{z}$, y)	(0,90,0)	$\begin{pmatrix}1&0&0\\0&0&-1\\0&1&0\end{pmatrix}$
2 x, 0,0	(x, $\bar{y}$, $\bar{z}$)	(0,180,0)	$\begin{pmatrix}1&0&0\\0&-1&0\\0&0&-1\end{pmatrix}$	4+ 0, y, 0	(z, y, $\bar{x}$)	(90,90,270)	$\begin{pmatrix}0&0&1\\0&1&0\\-1&0&0\end{pmatrix}$
2 0, y, 0	($\bar{x}$, y, $\bar{z}$)	(180,180,0)	$\begin{pmatrix}-1&0&0\\0&1&0\\0&0&-1\end{pmatrix}$	4+ 0,0, z	($\bar{y}$, x, z)	(90,0,0)	$\begin{pmatrix}0&-1&0\\1&0&0\\0&0&1\end{pmatrix}$
2 0,0, z	($\bar{x}$, $\bar{y}$, z)	(180,0,0)	$\begin{pmatrix}-1&0&0\\0&-1&0\\0&0&1\end{pmatrix}$	4- x, 0,0	(x, z, $\bar{y}$)	(180,90,180)	$\begin{pmatrix}1&0&0\\0&0&1\\0&-1&0\end{pmatrix}$
3+ $\bar{x}$, x, $\bar{x}$	(z, x, y)	(90,90,0)	$\begin{pmatrix}0&0&1\\1&0&0\\0&1&0\end{pmatrix}$	4- 0, y, 0	($\bar{z}$, y, x)	(270,90,90)	$\begin{pmatrix}0&0&-1\\0&1&0\\1&0&0\end{pmatrix}$
3+ $\bar{x}$, $\bar{x}$, x	($\bar{z}$, x, $\bar{y}$)	(270,90,180)	$\begin{pmatrix}0&0&-1\\1&0&0\\0&-1&0\end{pmatrix}$	4- 0,0, z	(y, $\bar{x}$, z)	(270,0,0)	$\begin{pmatrix}0&1&0\\-1&0&0\\0&0&1\end{pmatrix}$
3+ x, $\bar{x}$, $\bar{x}$	($\bar{z}$, $\bar{x}$, y)	(270,90, 0)	$\begin{pmatrix}0&0&-1\\-1&0&0\\0&1&0\end{pmatrix}$	2 x, x, 0	(y, x, $\bar{z}$)	(90,180,0)	$\begin{pmatrix}0&1&0\\1&0&0\\0&0&-1\end{pmatrix}$
3+ $\bar{x}$, x, $\bar{x}$	(z, $\bar{x}$, $\bar{y}$)	(90,90,180)	$\begin{pmatrix}0&0&1\\-1&0&0\\0&-1&0\end{pmatrix}$	2 x, $\bar{x}$, 0	($\bar{y}$, $\bar{x}$, $\bar{z}$)	(270,180,0)	$\begin{pmatrix}0&-1&0\\-1&0&0\\0&0&-1\end{pmatrix}$
3- x, x, x	(y, z, x)	(180,90,90)	$\begin{pmatrix}0&1&0\\0&0&1\\1&0&0\end{pmatrix}$	2 x, 0, x	(z, $\bar{y}$, x)	(90,90,90)	$\begin{pmatrix}0&0&1\\0&-1&0\\1&0&0\end{pmatrix}$
3- $\bar{x}$, $\bar{x}$, x	(y, $\bar{z}$, $\bar{x}$)	(0,90,270)	$\begin{pmatrix}0&1&0\\0&0&-1\\-1&0&0\end{pmatrix}$	2 0, y, y	($\bar{x}$, z, y)	(180,90,0)	$\begin{pmatrix}-1&0&0\\0&0&1\\0&1&0\end{pmatrix}$
3- x, $\bar{x}$, $\bar{x}$	($\bar{y}$, z, $\bar{x}$)	(180,90,270)	$\begin{pmatrix}0&-1&0\\0&0&1\\-1&0&0\end{pmatrix}$	2 $\bar{x}$, 0, x	($\bar{z}$, $\bar{y}$, $\bar{x}$)	(270,90,270)	$\begin{pmatrix}0&0&-1\\0&-1&0\\-1&0&0\end{pmatrix}$
3- $\bar{x}$, x, $\bar{x}$	($\bar{y}$, $\bar{z}$, x)	(0,90,90)	$\begin{pmatrix}0&-1&0\\0&0&-1\\1&0&0\end{pmatrix}$	2 0, y, $\bar{y}$	($\bar{x}$, $\bar{z}$, $\bar{y}$)	(0,90,180)	$\begin{pmatrix}-1&0&0\\0&0&-1\\0&-1&0\end{pmatrix}$

Table A.2 Symmetry elements of monoclinic crystal system.

Element	Rotation	Euler angles of rotation	Matrix	Element	Rotation	Euler angles of rotation	Matrix
1	(x, y, z)	(0,0,0)	$\begin{pmatrix} 1 & 0 & 0 \\ 0 & 1 & 0 \\ 0 & 0 & 1 \end{pmatrix}$	$2\ 0, y, 0$	$(\bar{x}, y, \bar{z})$	(180,180,0)	$\begin{pmatrix} -1 & 0 & 0 \\ 0 & 1 & 0 \\ 0 & 0 & -1 \end{pmatrix}$

Appendix II: Deformation gradient tensor in the reciprocal space

Fig. II. A demonstrates the *metric transformation* between $\boldsymbol{G}^{\boldsymbol{S_0^*\rightarrow S_0}}$ and $\boldsymbol{G}^{\boldsymbol{S^*\rightarrow S}}$, where $\boldsymbol{S}$ and $\boldsymbol{S_0}$ represent the two arbitrary reference systems and $\boldsymbol{M}^{\boldsymbol{S_0\rightarrow S}}$ indicates the *coordinate transformation matrix* between the references $\boldsymbol{S}$ and $\boldsymbol{S_0}$. With the equations of the magnitude of vector $\vec{r}$ under these two references (Fig. II. A), the relation of *metric transformation* can be determined, as shown in Eq. II-A.

$$\boldsymbol{G}^{\boldsymbol{S_0^*\rightarrow S_0}}=(\boldsymbol{M}^{\boldsymbol{S\rightarrow S_0}})^{\mathrm{T}}\times\boldsymbol{G}^{\boldsymbol{S^*\rightarrow S}}\times\boldsymbol{M}^{\boldsymbol{S\rightarrow S_0}} \tag{II-A}$$

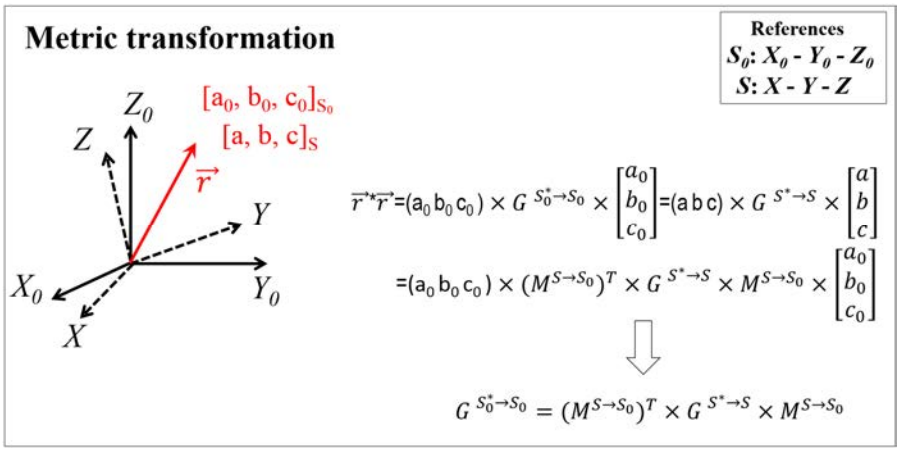

Fig. II. A Matric transformation between references $\boldsymbol{S_0}$ and $\boldsymbol{S}$.

The coordinate transformation for crystal plane under two different references $\boldsymbol{S_0}$ and $\boldsymbol{S}$ can be realized using the transformation matrix between their correlated reciprocal spaces $\boldsymbol{S_0^*}$ and $\boldsymbol{S^*}$, as demonstrated in Eq. II-B.

$$\begin{bmatrix}h_0\\k_0\\l_0\end{bmatrix}_{\boldsymbol{S_0}}=\boldsymbol{M}^{\boldsymbol{S_0^*\rightarrow S^*}}\times\begin{bmatrix}h\\k\\k\end{bmatrix}_{\boldsymbol{S}} \tag{II-B}$$

With the equation of *matric transformation* (Eq. II-A), the relation between the *coordinate transformation matrices* for references under the direct and reciprocal spaces can be determined, as given in Eq. II-C.

$$\boldsymbol{M}^{\boldsymbol{S}_0^*\rightarrow\boldsymbol{S}^*} = \boldsymbol{G}^{\boldsymbol{S}_0^*\rightarrow\boldsymbol{S}_0} \times \boldsymbol{M}^{\boldsymbol{S}_0\rightarrow\boldsymbol{S}} \times \boldsymbol{G}^{\boldsymbol{S}\rightarrow\boldsymbol{S}^*}$$

$$= (\boldsymbol{M}^{\boldsymbol{S}\rightarrow\boldsymbol{S}_0})^{\mathbf{T}} \times \boldsymbol{G}^{\boldsymbol{S}^*\rightarrow\boldsymbol{S}} \times \boldsymbol{M}^{\boldsymbol{S}\rightarrow\boldsymbol{S}_0} \times \boldsymbol{M}^{\boldsymbol{S}_0\rightarrow\boldsymbol{S}} \times \boldsymbol{G}^{\boldsymbol{S}\rightarrow\boldsymbol{S}^*}$$

$$= (\boldsymbol{M}^{\boldsymbol{S}_0\rightarrow\boldsymbol{S}})^{-\mathbf{T}} \qquad \text{(II-C)}$$

With Eqs. II-B and II-C, the *coordinate transformation* for crystal plane between references $\boldsymbol{S_0}$ and $\boldsymbol{S}$ can be obtained, as shown in Eq. II-D.

$$\begin{bmatrix} h_0 \\ k_0 \\ l_0 \end{bmatrix}_{\boldsymbol{S_0}} = (\boldsymbol{M}^{\boldsymbol{S}_0\rightarrow\boldsymbol{S}})^{-\mathbf{T}} \times \begin{bmatrix} h \\ k \\ k \end{bmatrix}_{\boldsymbol{S}} \qquad \text{(II-D)}$$

Like the *coordinate transformation*, the *homogeneous deformation* for crystal plane can be determined in the reciprocal space, *i.e.*

$$\begin{bmatrix} h' \\ k' \\ l' \end{bmatrix}_{\boldsymbol{R}} = \boldsymbol{F}_{\boldsymbol{D}'^*\leftarrow\boldsymbol{D}^*}^{\boldsymbol{R}^*} \times \begin{bmatrix} h \\ k \\ l \end{bmatrix}_{\boldsymbol{R}} \qquad \text{(II-E)}$$

With Eqs. II-C and 2-24, the relation for the *deformation gradient tensors* under the direct and reciprocal space can be obtained, as given in Eq. II-F.

$$\boldsymbol{F}_{\boldsymbol{D}'^*\leftarrow\boldsymbol{D}^*}^{\boldsymbol{R}^*} = \boldsymbol{M}^{\boldsymbol{R}^*\rightarrow\boldsymbol{D}'^*} \times (\boldsymbol{M}^{\boldsymbol{R}^*\rightarrow\boldsymbol{D}^*})^{-1}$$

$$= (\boldsymbol{M}^{\boldsymbol{R}\rightarrow\boldsymbol{D}'})^{-\mathrm{T}} \times ((\boldsymbol{M}^{\boldsymbol{R}\rightarrow\boldsymbol{D}})^{-1})^{-\mathrm{T}}$$

$$= (\boldsymbol{M}^{\boldsymbol{R}\rightarrow\boldsymbol{D}'} \times (\boldsymbol{M}^{\boldsymbol{R}\rightarrow\boldsymbol{D}})^{-1})^{-\mathrm{T}}$$

$$= (\boldsymbol{F}_{\boldsymbol{D}'\leftarrow\boldsymbol{D}}^{\boldsymbol{R}})^{-\mathrm{T}} \qquad \text{(II-F)}$$

Thus, the *homogeneous deformation* for crystal plane can be realized by Eq. II-G.

$$\begin{bmatrix} h' \\ k' \\ l' \end{bmatrix}_{\boldsymbol{R}} = (\boldsymbol{F}_{\boldsymbol{D}'\leftarrow\boldsymbol{D}}^{\boldsymbol{R}})^{-\mathbf{T}} \times \begin{bmatrix} h \\ k \\ l \end{bmatrix}_{\boldsymbol{R}} \qquad \text{(II-G)}$$

References

[1] C. M. Wayman, *Introduction to the crystallography of martensitic transformations*, New York: Macmillan, 1964.

[2] Z. Nishiyama, *Martensitic Transformation*, New York: Academic Press, 1978.

[3] J. W. Christian, *The theory of transformations in metals and alloys*, London: Pergamon Press, 2002.

[4] R. Kainuma, K. Oikawa, W. Ito, *et al.*, **J. Mater. Chem.**, 2008, 18 (16): 1837-1842.

[5] L. Chang, T. Read, **T. Am. I. Min. Met. Eng.**, 1951, 191 (1): 47-52.

[6] W. J. Buehler, J. Gilfrich, R. Wiley, **J. Appl. Phys.**, 1963, 34 (5): 1475-1477.

[7] K. Otsuka, X. Ren, **Prog. Mater. Sci.**, 2005, 50 (5): 511-678.

[8] C. Chluba, W. Ge, R. Lima de Miranda, *et al.*, **Science**, 2015, 348 (6238): 1004-1007.

[9] K. Otsuka, C. Wayman, K. Nakai, *et al.*, **Acta Metall.**, 1976, 24 (3): 207-226.

[10] K. Otsuka, H. Sakamoto, K. Shimizu, **Acta Metall.**, 1979, 27 (4): 585-601.

[11] H. Otsuka, H. Yamada, T. Maruyama, *et al.*, **ISIJ Int.**, 1990, 30 (8): 674-679.

[12] A. Sato, E. Chishima, Y. Yamaji, *et al.*, **Acta Metall.**, 1984, 32 (4): 539-547.

[13] Y. Tanaka, Y. Himuro, R. Kainuma, *et al.*, **Science**, 2010, 327 (5972): 1488-1490.

[14] P. Entel, V. Buchelnikov, M. E. Gruner, *et al.*, **Mater. Sci. Forum**, 2008, 583: 21-41.

[15] W. Huang, Z. Ding, C. Wang, *et al.*, **Mater. Today**, 2010, 13 (7): 54-61.

[16] M. V. Gandhi, B. Thompson, *Smart materials and structures*, London: Springer, 1992.

[17] K. Ullakko, J. Huang, C. Kantner, *et al.*, **Appl. Phys. Lett.**, 1996, 69 (13): 1966-1968.

[18] I. Takeuchi, O. Famodu, J. Read, *et al.*, **Nat. Mater.**, 2003, 2 (3): 180-184.

[19] A. Sozinov, A. A. Likhachev, N. Lanska, *et al.*, **J. Phys. IV**, 2003, 112: 955-958.

[20] A. Sozinov, N. Lanska, A. Soroka, *et al.*, **Appl. Phys. Lett.**, 2013, 102 (2): 021902.

[21] H. E. Karaca, I. Karaman, B. Basaran, *et al.*, **Acta Mater.**, 2006, 54 (1): 233-245.

[22] A. Sozinov, A. A. Likhachev, N. Lanska, *et al.*, **Appl. Phys. Lett.**, 2002, 80 (10): 1746-1748.

[23] R. Chulist, W. Skrotzki, C. G. Oertel, *et al.*, **Scripta Mater.**, 2010, 63 (5): 548-551.

[24] S. J. Murray, M. Marioni, S. M. Allen, *et al.*, **Appl. Phys. Lett.**, 2000, 77 (6): 886-888.

[25] H. E. Karaca, I. Karaman, B. Basaran, *et al.*, **Adv. Funct. Mater.**, 2009, 19 (7): 983-998.

[26] Y. Sutou, Y. Imano, N. Koeda, *et al.*, **Appl. Phys. Lett.**, 2004, 85 (19): 4358-4360.

[27] R. Kainuma, Y. Imano, W. Ito, *et al.*, **Nature**, 2006, 439 (7079): 957-960.

[28] J. Liu, T. Gottschall, K. P. Skokov, *et al.*, **Nat. Mater.**, 2012, 11 (7): 620-626.

[29] S. Singh, L. Caron, S. W. D'Souza, *et al.*, **Adv. Mater.**, 2016, 28 (17): 3321-3325.

[30] E. Stern-Taulats, A. Planes, P. Lloveras, *et al.*, **Acta Mater.**, 2015, 96: 324-332.

[31] L. Mañosa, D. Gonzalez-Alonso, A. Planes, *et al.*, **Nat. Mater.**, 2010, 9 (6): 478-481.

[32] Y. J. Huang, Q. D. Hu, N. M. Bruno, *et al.*, **Scripta Mater.**, 2015, 105: 42-45.

[33] B. Lu, F. Xiao, A. Yan, *et al.*, **Appl. Phys. Lett.**, 2014, 105 (16): 161905.

[34] B. Wang, Y. Liu, P. Ren, *et al.*, **Phys. Rev. Lett.**, 2011, 106 (7): 077203.

[35] A. K. Pathak, M. Khan, B. R. Gautam, *et al.*, **J. Magn. Magn. Mater.**, 2009, 321 (8): 963-965.

[36] V. K. Sharma, M. K. Chattopadhyay, K. H. B. Shaeb, *et al.*, **Appl. Phys. Lett.**, 2006, 89 (22): 222509.

[37] T. Samanta, A. U. Saleheen, D. L. Lepkowski, *et al.*, **Phys. Rev. B**, 2014, 90 (6): 064412.

[38] I. Dubenko, A. K. Pathak, S. Stadler, *et al.*, **Phys. Rev. B**, 2009, 80 (9): 092408.

[39] A. Granovskii, V. Prudnikov, A. Kazakov, *et al.*, **J. Exp. Theor. Phys.**, 2012, 115 (5): 805-814.

[40] V. K. Sharma, M. K. Chattopadhyay, S. B. Roy, **Phys. Rev. B**, 2007, 76 (14): 140401.

[41] W. Ito, K. Ito, R. Y. Umetsu, *et al.*, **Appl. Phys. Lett.**, 2008, 92 (2): 021908.

[42] J. Liu, N. Scheerbaum, S. Kauffmann-Weiss, *et al.*, **Adv. Eng. Mater.**, 2012, 14 (8): 653-667.

[43] J. L. Sánchez Llamazares, T. Sanchez, J. D. Santos, *et al.*, **Appl. Phys. Lett.**, 2008, 92 (1): 012513.

[44] T. Krenke, M. Acet, E. F. Wassermann, *et al.*, **Phys. Rev. B**, 2006, 73 (17): 174413.

[45] B. Hernando, J. L. S. Llamazares, J. D. Santos, *et al.*, **J. Magn. Magn. Mater.**, 2009, 321 (7): 763-768.

[46] A. P. Kazakov, V. N. Prudnikov, A. B. Granovsky, *et al.*, **Appl. Phys. Lett.**, 2011, 98 (13): 131911.

[47] A. K. Pathak, M. Khan, I. Dubenko, *et al.*, **Appl. Phys. Lett.**, 2007, 90 (26): 262504.

[48] T. Krenke, E. Duman, M. Acet, *et al.*, **Phys. Rev. B**, 2007, 75 (10): 104414.

[49] K. Oikawa, W. Ito, Y. Imano, *et al.*, **Appl. Phys. Lett.**, 2006, 88 (12): 122507.

[50] J. Liu, N. Scheerbaum, D. Hinz, *et al.*, **Appl. Phys. Lett.**, 2008, 92 (16): 162509.

[51] J. Liu, T. G. Woodcock, N. Scheerbaum, *et al.*, **Acta Mater.**, 2009, 57 (16): 4911-4920.

[52] K. Abematsu, R. Y. Umetsu, R. Kainuma, *et al.*, **Mater. Trans.**, 2014, 55 (3): 477-481.

[53] W. Ito, Y. Imano, R. Kainuma, *et al.*, **Metall. Mater. Trans. A**, 2007, 38 (4): 759-766.

[54] W. Ito, M. Nagasako, R. Y. Umetsu, *et al.*, **Appl. Phys. Lett.**, 2008, 93 (23): 232503.

[55] K. Otsuka, T. Ohba, M. Tokonami, *et al.*, **Scripta Metall. Mater.**, 1993, 29 (10): 1359-1364.

[56] K. Bhattacharya, *Microstructure of Martensite: Why it Forms and How it Gives Rise to the Shape-Memory Effect*, Oxford: Oxford University Press, 2003.

[57] S.-H. Kim, H. Kim, N. J. Kim, **Nature**, 2015, 518 (7537): 77-79.

[58] V. M. Schastlivtsev, Y. V. Kaletina, E. A. Fokina, *et al.*, **Phys. Met. Metallogr.**, 2011, 112 (1): 61-71.

[59] T. Gottschall, K. P. Skokov, B. Frincu, *et al.*, **Appl. Phys. Lett.**, 2015, 106 (2): 021901.

[60] W. Cai, Y. Feng, J. H. Sui, *et al.*, **Scripta Mater.**, 2008, 58 (10): 830-833.

[61] S. Aksoy, **J. Magn. Magn. Mater.**, 2015, 373: 236-239.

[62] K. Singh, S. K. Singh, D. Kaur, **J. Appl. Phys.**, 2014, 116 (11): 114103.

[63] A. Sokolov, L. Zhang, I. Dubenko, *et al.*, **Appl. Phys. Lett.**, 2013, 102 (7): 072407.

[64] B. Erkartal, V. Duppel, R. Niemann, *et al.*, **Adv. Eng. Mater.**, 2012, 14 (8): 710-715.

[65] S. Rios, I. Karaman, X. Zhang, **Appl. Phys. Lett.**, 2010, 96 (17): 173102.

[66] Y. J. Huang, Q. D. Hu, J. W. Hou, *et al.*, **Scripta Mater.**, 2014, 87: 21-24.

[67] Y. J. Huang, Q. D. Hu, J. Liu, *et al.*, **Acta Mater.**, 2013, 61 (15): 5702-5712.

[68] T. Miyamoto, M. Nagasako, R. Kainuma, **J. Alloy Compd.**, 2013, 549: 57-63.

[69] S. Y. Yang, Y. D. Liu, C. P. Wang, *et al.*, **J. Alloy Compd.**, 2015, 619: 498-504.

[70] A. Turabi, H. Karaca, H. Tobe, *et al.*, **Scripta Mater.**, 2016, 111: 110-113.

[71] J. A. Monroe, I. Karaman, B. Basaran, *et al.*, **Acta Mater.**, 2012, 60 (20): 6883-6891.

[72] T. Sakon, S. Yamazaki, Y. Kodama, *et al.*, **Jpn. J. Appl. Phys.**, 2007, 46 (3): 995-998.

[73] Y. D. Wang, Y. Ren, E. W. Huang, *et al.*, **Appl. Phys. Lett.**, 2007, 90 (10): 101917.

[74] H. E. Karaca, I. Karaman, A. Brewer, *et al.*, **Scripta Mater.**, 2008, 58 (10): 815-818.

[75] L. Jian, S. Aksoy, N. Scheerbaum, *et al.*, **Appl. Phys. Lett.**, 2009, 95 (23): 232515.

[76] A. M. Tishin, Y. I. Spichkin, *The magnetocaloric effect and its applications*, Bristol: CRC Press, 2003.

[77] V. Franco, J. S. Blazquez, B. Ingale, *et al.*, **Annu. Rev. Mater. Res.**, 2012, 42: 305-342.

[78] E. Warburg, **Ann. Phys.**, 1881, 249 (5): 141-164.

[79] P. Debye, **Ann. Phys.**, 1926, 386 (25): 1154-1160.

[80] W. Giauque, **J. Am. Chem. Soc.**, 1927, 49 (8): 1864-1870.

[81] W. F. Giauque, D. P. MacDougall, **Phys. Rev.**, 1933, 43 (9): 768.

[82] N. P. Kolmakova, R. Z. Levitin, A. I. Popov, *et al.*, **Phys. Rev. B**, 1990, 41 (10): 6170-6178.

[83] R. Li, T. Numazawa, T. Hashimoto, *et al.*, *Magnetic and Thermal Properties of $Dy_3Al_5O_{12}$ as a Magnetic Refrigerant*, in *Advances in Cryogenic Engineering Materials*, K. D. Timmerhaus, R. W. Fast, A. F. Clark, R. P. Reed, Editors. 1986, Springer: New York. p. 287-294.

[84] R. D. McMichael, J. J. Ritter, R. D. Shull, **J. Appl. Phys.**, 1993, 73 (10): 6946-6948.

[85] G. Brown, **J. Appl. Phys.**, 1976, 47 (8): 3673-3680.

[86] V. K. Pecharsky, K. A. Gschneidner Jr., **Phys. Rev. Lett.**, 1997, 78 (23): 4494-4497.

[87] K. A. Gschneidner Jr., V. K. Pecharsky, A. O. Tsokol, **Rep. Prog. Phys.**, 2005, 68 (6): 1479-1539.

[88] A. Fujita, S. Fujieda, Y. Hasegawa, *et al.*, **Phys. Rev. B**, 2003, 67 (10): 104416.

[89] O. Tegus, E. Bruck, K. H. J. Buschow, *et al.*, **Nature**, 2002, 415 (6868): 150-152.

[90] J. Pons, E. Cesari, C. Seguí, *et al.*, **Mater. Sci. Eng. A**, 2008, 481-482: 57-65.

[91] L. Min, Y. Bing-feng, **J. Cent. South. Univ. T.**, 2009, 16 (1): 1-12.

[92] A. Planes, L. Mañosa, M. Acet, **J. Phys. Condens. Matter**, 2009, 21 (23): 233201.

[93] J. R. Sun, B. G. Shen, F. X. Hu, *Magnetocaloric Effect and Materials*, in *Nanoscale Magnetic Materials and Applications*, J. P. Liu, E. Fullerton, O. Gutfleisch, D. J. Sellmyer, Editors. 2009, Springer: London. p. 441-483.

[94] M. Acet, L. Mañosa, A. Planes, *Magnetic-Field-Induced Effects in Martensitic Heusler-Based Magnetic Shape Memory Alloys*, in *Handbook of Magnetic Materials*, K. H. J. Buschow, Editor. 2011, Elsevier Science B. V.: Amsterdam. p. 231-289.

[95] V. D. Buchelnikov, V. V. Sokolovskiy, **Phys. Met. Metallogr.**, 2011, 112 (7): 633-665.

[96] S. Aksoy, M. Acet, T. Krenke, *et al.*, *Magnetic Interactions Governing the Inverse Magnetocaloric Effect in Martensitic Ni–Mn-Based Shape-memory Alloys*, in *Disorder and Strain-Induced Complexity in Functional Materials*. 2012, Springer. p. 67-77.

[97] I. Dubenko, T. Samanta, A. K. Pathak, *et al.*, **J. Magn. Magn. Mater.**, 2012, 324 (21): 3530-3534.

[98] S. Y. Yu, Z. H. Liu, G. D. Liu, *et al.*, **Appl. Phys. Lett.**, 2006, 89 (16): 162503.

[99] Z. D. Han, D. H. Wang, C. L. Zhang, *et al.*, **Solid. State. Commun.**, 2008, 146 (3-4): 124-127.

[100] A. K. Pathak, B. R. Gautam, I. Dubenko, *et al.*, **J. Appl. Phys.**, 2008, 103 (7): 07F315.

[101] A. K. Pathak, I. Dubenko, C. Pueblo, *et al.*, **J. Appl. Phys.**, 2010, 107 (9): 09A907.

[102] V. K. Sharma, M. K. Chattopadhyay, S. B. Roy, **J. Phys. D: Appl. Phys.**, 2010, 43 (22): 225001.

[103] V. K. Sharma, M. K. Chattopadhyay, L. S. S. Chandra, *et al.*, **J. Phys. D: Appl. Phys.**, 2011, 44 (14): 145002.

[104] L. Chen, F. X. Hu, J. Wang, *et al.*, **Appl. Phys. Lett.**, 2012, 101 (1): 012401.

[105] Y. Feng, J. H. Sui, H. B. Wang, *et al.*, **J. Magn. Magn. Mater.**, 2012, 324 (12): 1982-1984.

[106] J.-P. Camarillo, E. Stern-Taulats, L. Mañosa, *et al.*, **J. Phys. D: Appl. Phys.**, 2016, 49 (12): 125006.

[107] M. Ovichi, H. Elbidweihy, E. Della Torre, *et al.*, **J. Appl. Phys.**, 2015, 117 (17): 17D107.

[108] X. Zhao, J. Yang, X. Wang, *et al.*, **IEEE Trans. Magn.**, 2011, 47 (10): 2455-2458.

[109] T. Paramanik, I. Das, **J. Alloy Compd.**, 2016, 654: 399-403.

[110] Z. G. Guo, L. Q. Pan, M. Y. Rafique, *et al.*, **J. Alloy Compd.**, 2013, 577: 174-178.

[111] T. D. Thanh, W. Z. Nan, G. Nam, *et al.*, **Curr. Appl. Phys.**, 2015, 15 (10): 1200-1204.

[112] Z. H. Liu, S. Aksoy, M. Acet, **J. Appl. Phys.**, 2009, 105 (3): 033913.

[113] A. Kazakov, V. Prudnikov, A. Granovsky, *et al.*, **J. Nanosci. Nanotechnol.**, 2012, 12 (9): 7426-7431.

[114] Z. Li, K. Xu, H. Yang, *et al.*, **J. Appl. Phys.**, 2015, 117 (22): 223904.

[115] S. Pandey, A. Quetz, A. Aryal, *et al.*, **J. Appl. Phys.**, 2015, 117 (17): 17A737.

[116] S. Pandey, A. Quetz, I. Rodionov, *et al.*, **J. Appl. Phys.**, 2015, 117 (18): 183905.

[117] V. Sánchez-Alarcos, J. Pérez-Landazábal, V. Recarte, *et al.*, **J. Phys. D: Appl. Phys.**, 2015, 48 (44): 445006.

[118] V. K. Sharma, M. K. Chattopadhyay, S. B. Roy, **J. Phys. D: Appl. Phys.**, 2007, 40 (7): 1869-1873.

[119] M. K. Chattopadhyay, V. K. Sharma, S. B. Roy, **Appl. Phys. Lett.**, 2008, 92 (2): 022503.

[120] V. V. Sokolovskiy, V. D. Buchelnikov, V. V. Khovaylo, *et al.*, **Int. J. Refrig.**, 2014, 37: 273-280.

[121] C. S. Mejia, A. K. Nayak, J. A. Schiemer, *et al.*, **J. Phys. Condens. Matter**, 2015, 27 (41): 415402.

[122] M. Ghorbani Zavareh, C. Salazar Mejía, A. K. Nayak, *et al.*, **Appl. Phys. Lett.**, 2015, 106 (7): 071904.

[123] A. K. Pathak, I. Dubenko, S. Stadler, *et al.*, **J. Phys. D: Appl. Phys.**, 2008, 41 (20): 202004.

[124] T. Kihara, X. Xu, W. Ito, *et al.*, **Phys. Rev. B**, 2014, 90 (21): 214409.

[125] Z. B. Li, J. L. Sánchez Llamazares, C. F. Sánchez-Valdés, *et al.*, **Appl. Phys. Lett.**, 2012, 100 (17): 174102.

[126] Z. B. Li, Y. D. Zhang, C. F. Sánchez-Valdés, *et al.*, **Appl. Phys. Lett.**, 2014, 104 (4): 044101.

[127] H. Li, S. Feng, J. Ren, *et al.*, **J. Magn. Magn. Mater.**, 2015, 391: 17-21.

[128] F. Lino-Zapata, J. Llamazares, D. Ríos-Jara, *et al. Magnetization study of the kinetic arrest of martensitic transformation in as-quenched $Ni_{52.2}Mn_{34.3}In_{13.5}$ melt spun ribbons*. in *MRS Proceedings*. 2012. Cambridge Univ Press. p. 149-154.

[129] J. L. Llamazares, C. Garcia, B. Hernando, *et al.*, **Appl. Phys. A**, 2011, 103 (4): 1125-1130.

[130] B. Hernando, J. L. Sánchez Llamazares, V. Prida, *et al.*, **Appl. Phys. Lett.**, 2009, 94 (22): 222502.

[131] J. Sánchez Llamazares, B. Hernando, V. Prida, *et al. Magnetocaloric properties of rapidly solidified $Ni_{51.1}Mn_{31.2}In_{17.7}$ Heusler alloy ribbons*. in *MRS Proceedings*. 2009. Cambridge Univ Press. p. 1200-G1207-1205.

[132] J. S. Llamazares, B. Hernando, J. Sunol, *et al.*, **J. Appl. Phys.**, 2010, 107 (9): 09A956.

[133] R. Caballero-Flores, T. Sanchez, W. O. Rosa, *et al.*, **J. Alloy Compd.**, 2012, 545: 216-221.

[134] X. Zhao, B. Li, C.-C. Hsieh, *et al.*, **IEEE Trans. Magn.**, 2012, 48 (11): 3742-3745.

[135] X. G. Zhao, C. C. Hsieh, J. H. Lai, *et al.*, **Scripta Mater.**, 2010, 63 (2): 250-253.

[136] X. G. Zhao, C. C. Hsieh, W. C. Chang, *et al.*, **J. Phys. Conf. Ser.**, 2011, 266: 012128.

[137] C. S. Mejía, M. G. Zavareh, A. Nayak, *et al.*, **J. Appl. Phys.**, 2015, 117 (17): 17E710.

[138] L. Jian, N. Scheerbaum, J. Lyubina, *et al.*, **Appl. Phys. Lett.**, 2008, 93 (10): 102512.

[139] Y. Song, X. Chen, V. Dabade, *et al.*, **Nature**, 2013, 502 (7469): 85-88.

[140] M. Brokate, *Hysteresis and phase transitions*, New York: Springer-Verlag, 1996.

[141] Y. Y. Gong, D. H. Wang, Q. Q. Cao, *et al.*, **Adv. Mater.**, 2015, 27 (5): 801-805.

[142] M. Gueltig, H. Ossmer, M. Ohtsuka, *et al.*, **Mater. Today**, 2015, 2: S883-S886.

[143] E. Stern-Taulats, P. O. Castillo-Villa, L. Mañosa, *et al.*, **J. Appl. Phys.**, 2014, 115 (17): 173907.

[144] D. V. Ragone, *Thermodynamics of materials*, New York: Wiley, 1995.

[145] V. K. Pecharsky, K. A. Gschneidner Jr., Y. Mudryk, *et al.*, **J. Magn. Magn. Mater.**, 2009, 321 (21): 3541-3547.

[146] V. K. Sharma, M. K. Chattopadhyay, R. Kumar, *et al.*, **J. Phys. Condens. Matter**, 2007, 19 (49): 496207.

[147] X. X. Zhang, B. Zhang, S. Yu, *et al.*, **Phys. Rev. B**, 2007, 76 (13): 132403.

[148] A. K. Pathak, I. Dubenko, C. Pueblo, *et al.*, **Appl. Phys. Lett.**, 2010, 96 (17): 172503.

[149] A. K. Pathak, I. Dubenko, Y. Xiong, *et al.*, **J. Appl. Phys.**, 2011, 109 (7): 07A916.

[150] S. Dwevedi, B. Tiwari, **J. Alloy Compd.**, 2012, 540: 16-20.

[151] F. S. Liu, Q. B. Wang, W. Q. Ao, *et al.*, **J. Magn. Magn. Mater.**, 2012, 324 (4): 514-518.

[152] J. H. Chen, N. M. Bruno, I. Karaman, *et al.*, **J. Appl. Phys.**, 2014, 116 (20): 203901.

[153] A. Kamantsev, V. Koledov, E. Dilmieva, *et al.*, **EPJ Web Conf.**, 2014, 75: 04008.

[154] J. Ren, H. Li, S. Feng, *et al.*, **Intermetallics**, 2015, 65: 10-14.

[155] I. Rodionov, Y. S. Koshkid'ko, J. Cwik, *et al.*, **Jetp Lett.**, 2015, 101 (6): 385-389.

[156] X. Zhang, M. Qian, R. Su, *et al.*, **Mater. Lett.**, 2016, 163: 274-276.

[157] E. Bonnot, R. Romero, L. Mañosa, *et al.*, **Phys. Rev. Lett.**, 2008, 100 (12): 125901.

[158] L. Mañosa, D. González-Alonso, A. Planes, *et al.*, **Nat. Commun.**, 2011, 2: 595.

[159] D. Matsunami, A. Fujita, K. Takenaka, *et al.*, **Nat. Mater.**, 2015, 14 (1): 73-78.

[160] S. A. Nikitin, G. Myalikgulyev, M. P. Annaorazov, *et al.*, **Phys. Lett. A**, 1992, 171 (3-4): 234-236.

[161] Y. Liu, I. C. Infante, X. J. Lou, *et al.*, **Adv. Mater.**, 2014, 26 (35): 6132-6137.

[162] J. Cui, Y. Wu, J. Muehlbauer, *et al.*, **Appl. Phys. Lett.**, 2012, 101 (7): 073904.

[163] L. Mañosa, S. Jarque-Farnos, E. Vives, *et al.*, **Appl. Phys. Lett.**, 2013, 103 (21): 211904.

[164] L. Mañosa, E. Stern-Taulats, A. Planes, *et al.*, **Phys. Status Solidi B**, 2014, 251 (10): 2114-2119.

[165] B. Lu, P. Zhang, Y. Xu, *et al.*, **Mater. Lett.**, 2015, 148: 110-113.

[166] M. N. Baibich, J. M. Broto, A. Fert, *et al.*, **Phys. Rev. Lett.**, 1988, 61 (21): 2472-2475.

[167] S. Parkin, N. More, K. Roche, **Phys. Rev. Lett.**, 1990, 64 (19): 2304-2307.

[168] R. von Helmolt, J. Wecker, B. Holzapfel, *et al.*, **Phys. Rev. Lett.**, 1993, 71 (14): 2331-2333.

[169] P. A. Algarabel, M. R. Ibarra, C. Marquina, *et al.*, **Appl. Phys. Lett.**, 1995, 66 (22): 3061-3063.

[170] S. Yuasa, T. Nagahama, A. Fukushima, *et al.*, **Nat. Mater.**, 2004, 3 (12): 868-871.

[171] J. S. Moodera, L. R. Kinder, T. M. Wong, *et al.*, **Phys. Rev. Lett.**, 1995, 74 (16): 3273-3276.

[172] P. M. Levy, S. Zhang, A. Fert, **Phys. Rev. Lett.**, 1990, 65 (13): 1643-1646.

[173] N. Garcia, A. Hernando, **J. Magn. Magn. Mater.**, 1991, 99 (1-3): L12-L19.

[174] L. Morellon, J. Stankiewicz, B. Garcia-Landa, *et al.*, **Appl. Phys. Lett.**, 1998, 73: 3462-3464.

[175] J. Mira, F. Rivadulla, J. Rivas, *et al.*, **Phys. Rev. Lett.**, 2003, 90 (9): 097203.

[176] S. Chatterjee, S. Majumdar, R. K. Mukhopadhyay. *Large magnetoresistance in Ni-Mn-In alloy*. in *Solid State Physics: 56th DAE Solid State Physics Symposium*. 2012. USA: American Institute of Physics. p. 1161-1162.

[177] I. D. Rodionov, D. E. Mettus, A. P. Kazakov, *et al.*, **Phys. Solid State**, 2013, 55 (9): 1861-1865.

[178] M. Kiwi, **J. Magn. Magn. Mater.**, 2001, 234 (3): 584-595.

[179] J. Nogues, I. K. Schuller, **J. Magn. Magn. Mater.**, 1999, 192 (2): 203-232.

[180] P. Nordblad, **Nat. Mater.**, 2015, 14 (7): 655-656.

[181] V. Skumryev, S. Stoyanov, Y. Zhang, *et al.*, **Nature**, 2003, 423 (6942): 850-853.

[182] W. H. Meiklejohn, C. P. Bean, **Phys. Rev.**, 1956, 102 (5): 1413-1414.

[183] J. Nogues, J. Sort, V. Langlais, *et al.*, **Phys. Rep.**, 2005, 422 (3): 65-117.

[184] A. K. Pathak, I. Dubenko, S. Stadler, *et al.*, **IEEE Trans. Magn.**, 2009, 45 (10): 3855-3857.

[185] Wikipedia. *Hall effect*. 2016, Available from: https://en.wikipedia.org/wiki/Hall_effect.

[186] E. H. Hall, **Am. J. Math.**, 1879, 2 (3): 287-292.

[187] R. Karplus, J. Luttinger, **Phys. Rev.**, 1954, 95 (5): 1154-1160.

[188] M. Zelený, L. Straka, A. Sozinov. *Ab initio study of Ni_2MnGa under shear deformation*. in *MATEC Web of Conferences*. 2015. EDP Sciences. p. 05006.

[189] I. Dubenko, A. K. Pathak, N. Ali, *et al.*, **J. Phys. Conf. Ser.**, 2010, 200 (5): 052005.

[190] V. Prudnikov, A. Kazakov, I. Titov, *et al.*, **Jetp Lett.**, 2010, 92 (10): 666-670.

[191] V. K. Sharma, M. K. Chattopadhyay, S. K. Nath, *et al.*, **J. Phys. Condens. Matter**, 2010, 22 (48): 486007.

[192] R. Y. Umetsu, W. Ito, K. Ito, *et al.*, **Scripta Mater.**, 2009, 60 (1): 25-28.

[193] M. Chattopadhyay, S. Roy, P. Chaddah, **Phys. Rev. B**, 2005, 72 (18): 180401.

[194] J. Kurchan, **Nature**, 2005, 433 (7023): 222-225.

[195] P. G. Debenedetti, F. H. Stillinger, **Nature**, 2001, 410 (6825): 259-267.

[196] P. W. Anderson, **Science**, 1995, 267 (5204): 1617-1617.

[197] V. Martynov, V. Kokorin, **J. Phys. III**, 1992, 2 (5): 739-749.

[198] A. G. Khachaturyan, S. M. Shapiro, S. Semenovskaya, **Phys. Rev. B**, 1991, 43 (13): 10832-10843.

[199] T. Janssen, A. Janner, A. Looijenga-Vos, *et al.*, *Incommensurate and commensurate modulated structures*, in *International Tables for Crystallography*, E. Prince, Editor. 2004, Springer: New York. p. 907-955.

[200] S. Van Smaalen, *Incommensurate Crystallography*, Oxford: Oxford University Press, 2007.

[201] S. Morito, K. Otsuka, **Mater. Sci. Eng. A**, 1996, 208 (1): 47-55.

[202] G. Mogylnyy, I. Glavatskyy, N. Glavatska, *et al.*, **Scripta Mater.**, 2003, 48 (10): 1427-1432.

[203] J. Pons, R. Santamarta, V. A. Chernenko, *et al.*, **J. Appl. Phys.**, 2005, 97 (8): 083516.

[204] J. Pons, R. Santamarta, V. A. Chernenko, *et al.*, **Mater. Sci. Eng. A**, 2006, 438-440: 931-934.

[205] L. Righi, F. Albertini, E. Villa, *et al.*, **Acta Mater.**, 2008, 56 (16): 4529-4535.

[206] D. Shechtman, I. Blech, D. Gratias, *et al.*, **Phys. Rev. Lett.**, 1984, 53 (20): 1951-1953.

[207] A. Mironov, A. Abakumov, E. Antipov, **Rigaku J.**, 2003, 19: 20-23.

[208] A. Pramanick, X. Wang, K. An, *et al.*, **Phys. Rev. B**, 2012, 85 (14): 144412.

[209] S. Singh, J. Nayak, A. Rai, *et al.*, **J. Phys. Condens. Matter**, 2013, 25 (21): 212203.

[210] L. Righi, P. Lázpita, J. Gutierrez, *et al.*, **Scripta Mater.**, 2010, 62 (6): 383-386.

[211] C. M. Wayman, **Annu. Rev. Mater. Sci.**, 1971, 1 (1): 185-218.

[212] G. Meyrick, G. W. Powell, **Annu. Rev. Mater. Sci.**, 1973, 3 (1): 327-362.

[213] J. Ball, R. James, **Arch. Ration. Mech. Anal.**, 1987, 100: 13-52.

[214] T. Tadaki, K. Otsuka, K. Shimizu, **Annu. Rev. Mater. Sci.**, 1988, 18 (1): 25-45.

[215] C. M. Wayman, **Prog. Mater. Sci.**, 1992, 36: 203-224.

[216] W. Lojkowski, H.-J. Fecht, **Prog. Mater. Sci.**, 2000, 45 (5): 339-568.

[217] M. X. Zhang, P. M. Kelly, **Prog. Mater. Sci.**, 2009, 54 (8): 1101-1170.

[218] J. P. Hirth, R. C. Pond, **Prog. Mater. Sci.**, 2011, 56 (6): 586-636.

[219] I. Beyerlein, X. Zhang, A. Misra, **Annu. Rev. Mater. Res.**, 2014, 44 (1): 329-363.

[220] H. K. D. H. Bhadeshia, *Worked examples in the Geometry of Crystals*, London: Institute of Materials, 2006.

[221] Y. M. Jin, G. J. Weng, **Acta Mater.**, 2002, 50 (11): 2967-2987.

[222] M. Wechsler, D. Lieberman, T. Read, **Trans. Am. Inst. Min. Metall. Petrol. Engrs.**, 1953, 197: 1503-1515.

[223] J. K. Mackenzie, J. S. Bowles, **Acta Metall.**, 1957, 5 (3): 137-149.

[224] J. K. Mackenzie, J. S. Bowles, **Acta Metall.**, 1954, 2 (1): 138-147.

[225] J. S. Bowles, J. K. Mackenzie, **Acta Metall.**, 1954, 2 (2): 224-234.

[226] J. S. Bowles, J. K. Mackenzie, **Acta Metall.**, 1954, 2 (1): 129-137.

[227] J. M. Ball, R. D. James, **Phil. Trans. R. Soc. A**, 1992, 338 (1650): 389-450.

[228] K. F. Hane, T. W. Shield, **Mater. Sci. Eng. A**, 2000, 291 (1): 147-159.

[229] K. F. Hane, T. W. Shield, **J. Elasticity**, 2000, 59 (1): 267-318.

[230] K. F. Hane, T. W. Shield, **Philos. Mag. A**, 1998, 78 (6): 1215-1252.

[231] D. Bernardini, T. J. Pence, *Mathematical Models for Shape-Memory Materials*, in *Smart materials*, M. Schwartz, Editor. 2009, CRC Press: Boca Raton. p. 20.17-20.28.

[232] K. F. Hane, T. Shield, **Acta Mater.**, 1999, 47 (9): 2603-2617.

[233] M. Pitteri, G. Zanzotto, *Continuum Models for Phase Transitions and Twinning in Crystals*, Boca Raton: Chapman & Hall/CRC, 2002.

[234] G. Dolzmann, *Variational methods for crystalline microstructure-analysis and computation*, Berlin: Springer, 2003.

[235] S. Müller, *Variational models for microstructure and phase transitions*, Berlin: Springer, 1999.

[236] M. Hoelzel, A. Senyshyn, N. Juenke, *et al.*, **Nucl. Instr. Meth. Phys. Res. A**, 2012, 667: 32-37.

[237] L. Palatinus, **Acta Crystallogr. Sect. B**, 2013, 69 (1): 1-16.

[238] H. Rietveld, **J. Appl. Cryst.**, 1969, 2 (2): 65-71.

[239] D. Chateigner, *Combined Analysis*, London: Wiley-ISTE, 2013.

[240] G. Kresse, J. Furthmüller, **Phys. Rev. B**, 1996, 54: 11169.

[241] G. Kresse, D. Joubert, **Phys. Rev. B**, 1999, 59: 1758-1775.

[242] P. E. Blöchl, **Phys. Rev. B**, 1994, 50 (24): 17953-17979.

[243] J. P. Perdew, K. Burke, M. Ernzerhof, **Phys. Rev. Lett.**, 1996, 77: 3865-3869.

[244] H. J. Monkhorst, J. D. Pack, **Phys. Rev. B**, 1976, 13 (12): 5188-5192.

[245] Y. D. Zhang, Z. B. Li, C. Esling, *et al.*, **J. Appl. Cryst.**, 2010, 43: 1426-1430.

[246] Y. D. Zhang, C. Esling, X. Zhao, *et al.*, **J. Appl. Cryst.**, 2007, 40: 436-440.

[247] J. Klostermann, W. Burgers, **Acta Metall.**, 1964, 12 (4): 355-360.

[248] F. C. Lovey, J. Ferron, L. S. De Bernardez, *et al.*, **Scripta Metall.**, 1983, 17 (4): 501-504.

[249] G. Will, *Powder Diffraction: The Rietveld method and the two-stage method*, Berlin: Springer, 2006.

[250] N. Xu, J. M. Raulot, Z. B. Li, *et al.*, **Appl. Phys. Lett.**, 2012, 100 (8): 084106.

[251] V. Petříček, M. Dušek, L. Palatinus, **Z. Kristallogr. Cryst. mater.**, 2014, 229 (5): 345-352.

[252] W. A. Dollase, **J. Appl. Cryst.**, 1986, 19 (4): 267-272.

[253] A. Taylor, B. J. Kagle, *Crystallographic data on metal and alloy structures*, New York: Dover Publications, 1963.

[254] P. Lázpita, J. M. Barandiarán, J. Gutiérrez, *et al.*, **New J. Phys.**, 2011, 13 (3): 033039.

[255] G. Zhdanov, **C. R. Dokl. Acad. Sci. URSS**, 1945, 48: 39-42.

[256] H. Klein, **Adv. Eng. Mater.**, 2009, 11 (6): 452-458.

[257] H. L. Yan, Y. D. Zhang, N. Xu, *et al.*, **Acta Mater.**, 2015, 88: 375-388.

[258] R. W. Cahn, **Adv. Phys.**, 1954, 3 (12): 363-445.

[259] B. A. Bilby, A. G. Crocker, **Proc. R. Soc. A**, 1965, 288 (1413): 240-255.

[260] L. Straka, O. Heczko, H. Seiner, *et al.*, **Acta Mater.**, 2011, 59 (20): 7450-7463.

[261] Z. Li, Y. Zhang, C. Esling, *et al.*, **J. Appl. Cryst.**, 2010, 43: 617-622.

[262] Z. B. Li, Y. D. Zhang, C. Esling, *et al.*, **Acta Mater.**, 2012, 60 (20): 6982-6990.

[263] M. Matsuda, Y. Yasumoto, K. Hashimoto, *et al.*, **Mater. Trans.**, 2012, 53 (5): 902-906.

[264] M. Nishida, T. Hara, M. Matsuda, *et al.*, **Mater. Sci. Eng. A**, 2008, 481-482: 18-27.

[265] E. C. Bain, N. Y. Dunkirk, **Trans. AIME**, 1924, 70 (1): 25-35.

[266] Z. Nishiyama, **Sci. Rep.**, 1934, 23: 637-664.

[267] G. Wassermann, K. Mitt, **Inst. Eisenforsch.**, 1935, 17: 149-155.

[268] G. Kurdjumov, G. Sachs, **Z. Phys.**, 1930, 64: 325-343.

[269] W. Pitsch, **Acta Metall.**, 1962, 10 (9): 897-900.

[270] M. Humbert, N. Gey, J. Muller, *et al.*, **J. Appl. Cryst.**, 1996, 29: 662-666.

[271] Z. B. Li, Y. D. Zhang, C. Esling, *et al.*, **Acta Mater.**, 2011, 59 (7): 2762-2772.

[272] J. Bishop, R. Hill, **Philos. Mag.**, 1951, 42 (327): 414-427.

[273] J. Bishop, R. Hill, **Philos. Mag.**, 1951, 42 (334): 1298-1307.

[274] Z. Y. Zhang, R. D. James, S. Müller, **Acta Mater.**, 2009, 57 (15): 4332-4352.

[275] Z. Li, Y. Zhang, C. Esling, *et al.*, **Appl. Phys. Lett.**, 2014, 105 (2): 021907.

[276] J. W. Christian, S. Mahajan, **Prog. Mater. Sci.**, 1995, 39 (1-2): 1-157.

[277] L. Straka, N. Lanska, K. Ullakko, *et al.*, **Appl. Phys. Lett.**, 2010, 96 (13): 131903.

[278] V. Novak, P. Šittner, S. Ignacova, *et al.*, **Mater. Sci. Eng. A**, 2006, 438-440: 755-762.

[279] S. Kaufmann, R. Niemann, T. Thersleff, *et al.*, **New J. Phys.**, 2011, 13 (5): 053029.

[280] Y. Ge, H. Jiang, A. Sozinov, *et al.*, **Mater. Sci. Eng. A**, 2006, 438-440: 961-964.

[281] Y. Liu, Z. L. Xie, **Acta Mater.**, 2003, 51 (18): 5529-5543.

[282] J. D. Moore, G. K. Perkins, Y. Bugoslavsky, *et al.*, **Appl. Phys. Lett.**, 2006, 88 (7): 072501.

Publication list

I: Publications in international journals

[1] **Haile Yan**, Yudong Zhang, Nan Xu, Anatoliy Senyshyn, Heinz-Günter Brokmeier, Claude Esling, Xiang Zhao, and Liang Zuo, *Crystal structure determination of incommensurate modulated martensite in Ni-Mn-In Heusler alloys*, **Acta Mater.**, 88, 375 (2015).

[2] **Haile Yan**, Bo Yang, Yudong Zhang, Zongbin Li, Claude Esling, Xiang Zhao, and Liang Zuo, *Variant organization and mechanical detwinning of modulated martensite in Ni-Mn-In alloy*, **Acta Mater.**, 111,75 (2016).

[3] **Haile Yan**, Xiang Zhao, Nan Jia, Yiran Zheng, and Tong He, *Influence of shear banding on the formation of brass-type textures in polycrystalline fcc metals with low stacking fault energy*, **J. Mater. Sci. Technol.**, 408 (2014).

[4] **Haile Yan**, Zongbin Li, Chunyang Zhang, Yudong Zhang, Claude Esling, Xiang Zhao, and Liang Zuo, *The phase transformation and magnetic properties in Ni-Mn-In alloys*, **Adv. Mat. Res.**, 712-715, 54 (2013).

[5] **Haile Yan**, Chunyang Zhang, Yudong Zhang, Xinli Wang, Claude Esling Xiang Zhao, and Liang Zuo, *Crystallographic insights into Ni-Co-Mn-In metamagnetic shape memory alloy*, **J. Appl. Cryst.**, under review.

[6] Chunyang Zhang, **Haile Yan**, Yudong Zhang, Claude Esling, Xiang Zhao, and Liang Zuo, *Crystal structure and crystallographic characteristics of martensite in $Ni_{50}Mn_{38}Sb_{12}$ alloy*, **J. Appl. Cryst.**, 49, 513 (2016).

[7] Chunqing Lin, **Haile Yan**, Yudong Zhang, Claude Esling, Xiang Zhao, and Liang Zuo, *Microstructure and crystallographic features of modulated martensite in $Ni_{50}Mn_{38}Sn_{12}$ alloy*, **J. Appl. Cryst.**, under review.

II: Contributions to International Conferences

[1] **Haile Yan**, Yudong Zhang, Claude Esling, Xiang Zhao, and Liang Zuo, *Crystallography of martensitic transformation of Ni-Mn based alloys and its impact on martensite variant selection*, **The 24th International Materials Research Congress,** 2015.08, Cancun, Mexico. (**Invited lecture**).

[2] **Haile Yan**, Yudong Zhang, Claude Esling, Xiang Zhao, and Liang Zuo, *Crystal structure and microstructure of martensite in Ni-Mn-In alloys and the behavior of variant rearrangement under uniaxial loading*, **The 9th International Conference on Processing & Manufacturing of Advanced Materials (Thermec)**, 2016.05, Graz, Austria. (**Invited lecture**).

[3] **Haile Yan**, Yudong Zhang, Nan Xu, Anatoliy Senyshyn, Heinz-Günter Brokmeier, Claude Esling, Xiang Zhao, and Liang Zuo, *Incommensurate 6M modulated crystal structure in Ni-Mn-In martensite phase, 2015.03,* **Anisotropy and Texture 2015**, Metz, France. (**Oral presentation**).

[4] **Haile Yan**, Yudong Zhang, Claude Esling, Xiang Zhao, and Liang Zuo, *Crystal structure, microstructure and martensitic transformation path in Ni-Mn-In alloys*, **The 9th International Conference on Processing & Manufacturing of Advanced Materials (Thermec)**, 2016.05, Graz, Austria. (**Poster**).

[5] Yudong Zhang, **Haile Yan**, Nan Xu, Anatoliy Senyshyn, Heinz-Günter Brokmeier, Claude Esling, Xiang Zhao, and Liang Zuo, *Crystal structure, microstructure and the detwinning behavior of Ni-Mn-In metamagnetic shape memory alloy*, 2016.03, **Anisotropy and Texture 2016**, Dresden, German. (**Invited lecture**).

Acknowledgements

The work presented in this dissertation is mainly completed at the Laboratoire d'étude des Microstructures et de Mécanique des Matériaux (LEM3), UMR CNRS 7239, Université de Lorraine, Metz, France, and the Key Laboratory for Anisotropy and Texture of Materials (ATM), Northeastern University, Shenyang, China. I would like to give my hearted thanks to all the members for their kind help.

I am grateful to the China Scholarship Council (CSC) for providing a Ph.D. scholarship for two years, and the French State for financially supporting my Ph.D. study for 6 months through the Program “Investment in the future” operated by the National Research Agency and referenced by ANR-11-LABX-0008-01 (LabEx DAMAS). The present work has been supported by the National Natural Science Foundation of China (Grant No. 51431005), the 863 Program of China (Grant No. 2015AA034101), the 111 Program of China (Grant No. B07015), the Program for Liaoning Innovative Research Team in University (Grant No. LT2013007), and the Fundamental Research Funds for Central Universities of China (Grant No. N130110001).

I would like to give my sincerely thanks to my supervisors, Dr. Yudong ZHANG and Prof. Claude ESLING at Université de Lorraine, France, and Prof. Xiang ZHAO at Northeastern University, China, for guiding me into this amzaing and fruitful research field, and for their constant help and support on my research work and daily life. I would also like to express my appreciation to Prof. Liang ZUO at Northeastern University, China, for his insightful guidance and inspiring discussions. From them, I have not only learn knowledge but also precise scientific attitude towards work and persistence to overcome difficulties.

I would like to express my thanks to Prof. Heinz-Günter BROKMEIER at Technische Universität Clausthal, Germany, Dr. Weimin GAN and Dr. Anatoliy SENYSHYN at FRM II, Germany, Dr. José Luis SANCHEZ LLAMAZARES and Mr. César Fidel SANCHEZ VALDES at Instituto Potosino de Investigación Científica y Tecnológica, Mexico, and Dr. Xinli WANG at Northeastern University, China, for their kind help on synchrotron X-ray diffraction, neutron diffraction, magnetic property, and transmission electron microscopy investigations. I would also like to express my appreciation to Dr. Zongbin LI, Dr. Bo YANG, and Dr. Nan XU at Northeastern

University, China, for their helpful and fruitful discussions on crystallography, shape memory effect, magnetocaloric effect, and *ab inito* calculations.

I am also grateful to all the staffs and students of LEM3 and ATM who shared their experiences with me and offered help to my study and daily life, especially to Ms. Xiaorui LIU, Prof. Nan JIA, Dr. Changshu HE, Dr. Dong WANG, Mr. Hao WANG, Mr. Chunyang ZHANG, Mr. Naifu ZOU, Mr. Shun XU, Ms. Chunqing LIN, Mr. Jiangkun FAN, Dr. Komi SOHO, and Mr. Amen SOGAH. Special thanks give to my young friend Ms. Pengru ZHAO for her help in the language of French.

I would like to sincerely appreciate all the jury members Dr. José Luis SANCHEZ LLAMAZARES at Instituto Potosino de Investigación Científica y Tecnológica, Mexico, Prof. Zhidong ZHANG at Institute of Metal Research, Chinese Academy of Sciences, China, Prof. Werner SKROTZKI at Technische Universität Dresden, Germany, and Prof. Zheng LIU at Shenyang University of Technology, China, for taking time out of their busy schedules to review my dissertation and achieve my Ph.D. defense.

At last, I would like to thank my endlessly loving parents, grandmother, brother, and other relatives. Without their understanding and support from my childhood to now, I would never have made it through. I dedicate this dissertation to them.

25/05/2016

Metz, France